



**HAL**  
open science

# Borosilicate glasses : from viscoplasticity to indentation cracking ?

Matthieu Bourguignon

► **To cite this version:**

Matthieu Bourguignon. Borosilicate glasses : from viscoplasticity to indentation cracking?. Material chemistry. Sorbonne Université, 2024. English. NNT : 2024SORUS247 . tel-04797848

**HAL Id: tel-04797848**

**<https://theses.hal.science/tel-04797848v1>**

Submitted on 22 Nov 2024

**HAL** is a multi-disciplinary open access archive for the deposit and dissemination of scientific research documents, whether they are published or not. The documents may come from teaching and research institutions in France or abroad, or from public or private research centers.

L'archive ouverte pluridisciplinaire **HAL**, est destinée au dépôt et à la diffusion de documents scientifiques de niveau recherche, publiés ou non, émanant des établissements d'enseignement et de recherche français ou étrangers, des laboratoires publics ou privés.

# Sorbonne Université

Ecole doctorale 397 : Physique et Chimie des Matériaux

*Laboratoire Sciences et Ingénierie de la Matière Molle*

## **Borosilicate glasses - from viscoplasticity to indentation cracking?**

Par **Mathieu Bourguignon**

Thèse de doctorat de Physique Chimie des matériaux

Dirigée par Etienne Barthel

Prévue le 23 Octobre 2024

Devant un jury composé de :

M. Hosni Idrissi	Professeur, Ecole Polytechnique de Louvain	Président du Jury
M. Jean-Pierre Guin	Directeur de recherche, Université de Rennes	Rapporteur
Mme. Cindy Lynn Rountree	Directrice de recherche, CEA Saclay	Rapporteur
Mme. Ekaterina Burov	Ingénieur de recherche, Saint-Gobain Recherche	Examineur
M. Morgan Rusinowicz	Maître assistant, Mines de Saint-Etienne	Examineur
M. Matteo Ciccotti	Professeur, ESPCI	Co-encadrant de thèse
M. Etienne Barthel	Directeur de recherche, CNRS	Directeur de thèse



# Contents

<b>Contents</b>	<b>iii</b>
<b>1 Structure and mechanical properties of oxide glasses: state of the art</b>	<b>7</b>
1.1 Silicate glass : structure and general mechanical properties . . . . .	8
1.1.1 Mechanical properties of oxide glasses . . . . .	8
1.1.1.a General discussion about oxide glasses . . . . .	8
1.1.1.b A model to predict the mechanical properties . . . . .	9
1.1.2 Structure of oxide glasses . . . . .	10
1.1.2.a The pure amorphous silica system . . . . .	10
1.1.2.b Multi-component glasses: glass formers and network modifiers . .	12
1.1.3 Fracture properties of oxide glasses . . . . .	14
1.1.3.a Fracture toughness . . . . .	14
1.1.3.b Intrinsic strength of glass . . . . .	17
1.2 Plasticity in oxide glasses . . . . .	19
1.2.1 Brittle to ductile transition: lengthscales . . . . .	19
1.2.2 First approach to the indentation stress fields - Yoffe model . . . . .	20
1.2.3 Plastic deformation mechanisms: densification vs shear flow . . . . .	21
1.2.3.a Structural changes induced by densification . . . . .	21
1.2.3.b Experimental techniques to characterize densification under inden-	
tation . . . . .	24
1.2.3.c Shear flow . . . . .	25
1.2.3.d Role of Poisson ratio . . . . .	27
1.2.3.e Role of the glass composition . . . . .	28
1.2.3.f Role of the indenter geometry . . . . .	29
1.2.4 Indentation cracking . . . . .	30
1.2.4.a Cracking morphology . . . . .	30
1.2.4.b Crack resistance . . . . .	32
1.2.5 Constitutive relations and other numerical models developed for oxide glasses	33
1.2.5.a Constitutive relations . . . . .	34
1.2.5.b Finite Element Analysis (FEA) to understand indentation of glasses	36
1.2.5.c Molecular dynamics simulations . . . . .	37
<b>2 Effect of irradiation on silicate glass plasticity - In-situ micromechanical testing</b>	<b>41</b>
2.1 Material and methods . . . . .	44
2.2 In situ micropillar compression . . . . .	49

2.2.1	Mechanical behavior under irradiation and strain rate sensitivity . . . . .	49
2.2.2	Residual geometry of compressed micropillars with and without electron irradiation . . . . .	51
2.3	Electron irradiation and viscoplastic deformation . . . . .	53
2.3.1	Relaxation tests . . . . .	53
2.3.1.a	Rescaling time with current density . . . . .	53
2.3.1.b	Time description - the stretched exponential model . . . . .	55
2.3.2	Strain rate description . . . . .	56
2.3.3	Application and comparison with other glass compositions . . . . .	58
2.4	Physical description of the phenomenon . . . . .	59
2.4.1	Glass plasticity and activation model . . . . .	59
2.4.2	Impact of irradiation . . . . .	61
2.4.3	Two relaxation mechanisms: analogy with dynamic measurements . . . . .	63
2.4.4	From strain rate to relaxation . . . . .	65
<b>3</b>	<b>Characterization of indentation cracking in alkaline-earth aluminoborosilicate glasses: densification vs plastic shear flow</b>	<b>69</b>
3.1	Material and methods . . . . .	71
3.2	Glass properties . . . . .	79
3.2.1	Thermal properties . . . . .	79
3.2.2	Mechanical properties . . . . .	80
3.2.2.a	Elastic moduli . . . . .	80
3.2.2.b	Hardness and flow stress . . . . .	81
3.2.3	Crack resistance measurements . . . . .	83
3.3	Indentation cross-sections and plastic flow characterization . . . . .	84
3.4	Roughness measurements of the plastically deformed region . . . . .	87
3.5	Understanding what rules indentation cracking . . . . .	90
3.5.1	Impact of the volumetric change on crack resistance . . . . .	90
3.5.2	Shear localizations and cracking susceptibility . . . . .	93
3.5.2.a	Shear bands formations . . . . .	93
3.5.2.b	Crack initiation . . . . .	95
3.5.3	Composition dependence of local rearrangements and crack resistance . . . . .	98
<b>4</b>	<b>Appendices</b>	<b>119</b>
1	Appendix: Time - Irradiation superposition . . . . .	120
2	Appendix: CMABS glass properties . . . . .	122
3	Appendix: Full mapping of indentation cross-sections . . . . .	124
4	Appendix: Roughness measurements of indentation cross-sections . . . . .	127
5	Appendix: Characterization of the densification ability by thermal recovery measurements . . . . .	128

# Acknowledgements

This work was conducted at ESPCI Paris, the Soft Matter and Engineering Laboratory (SIMM), at Mines de Saint-Etienne in the Georges Friedel laboratory, and finally in Japan in the NEG company. The project was directed by Etienne Barthel who made this PhD an inspiring and joyful experience. I dearly thank him for his availability and precious scientific and mental support. This manuscript is the result of fructuous discussions and valuable supervision that guided me throughout this wide exciting journey. I am extremely grateful for the opportunity I had to present my work at various national and international conferences. The project was also co-directed by Matteo Ciccotti. I would like to thank him, especially for the very interesting discussions we had at the beginning of the PhD about glassy polymers. I would like to acknowledge Agence National de la Recherche who agreed to finance the GaLAaD project I belonged to and consequently my research.

Many thanks to my committee members, Jean-Pierre Guin and Cindy Lynn Rountree who accepted to report this manuscript. My sincere thanks to Ekaterina Burov and Morgan Rusinowicz for examining this work. Deep thanks to Hosni Idrissi for the honor of being the president of the jury.

This work was enriched by many discussions and collaborations at various levels. As this project was chosen to be pluridisciplinar, I am very thankful for all the people who share their expertise. First, I thank the permanent researchers at SIMM laboratory for discussions about amorphous glassy polymers mechanics and chemistry in particular Artem Kovalenko for his precious help in the formulation of epoxy. Thanks to Bruno Bresson for his expertise in microscopy techniques (ESEM) and Mohamed Hannafi for his help with thermal measurements and all the training. I would be remiss in not mentioning the help of the ESPCI workshop in particular Jean-Claude Mancier and Ludovic Olanier for fixing mechanical apparatus and designing homemade setups.

Secondly, I wish to thank all the people who helped with the irradiation part of my work. Thanks to Sergio Sao-Joao for his help and work on the compression of silicate glass micropillars under SEM as well as their trimming with FIB. I deeply thank Guillaume Kermouche, who generously provided knowledge and expertise in the analysis, data processing, and scientific discussion. I am also grateful to Morgan Rusinowicz, who joined the project near the end of the PhD, for numerous discussions about the interpretation of physical phenomena related to electronic irradiation. Thanks should also go to Gergely Molnàr for his availability and help with FEM calculations and discussions on plasticity theory. More generally, I would like to thank all the members of the GaLAaD project with whom I was able to present my work and discuss it during the bi-annual meetings (Christine Martinet, Alice Bertholet, Thierry Deschamps, Anne Tanguy,

Guillaume Kermouche, Gergely Molnàr, Etienne Barthel).

Finally, conducting a part of my PhD at Nippon Electric Glass Co.,Ltd., was also an opportunity to be closely aligned with the challenges encountered in the development and production of silicate glasses on an industrial scale. This experience underscored the importance of collaboration between academia and industry in driving innovation and addressing complex material challenges. I would like to thank all the people who helped me during this doctoral internship in Japan, starting first with Gustavo Rosales-Sosa. A huge thank you to him for his support throughout this intense 6-month project, which was rich in scientific results. I particularly appreciated his guidance and the knowledge he provided me, whether it was about glass manufacturing during the first months or the various characterization methods used in the company. Thank you also for all the moments spent outside the company; my integration in Japan was all the more enjoyable because of it! I would also like to thank Kato-san and Nakane-san for their extensive knowledge in the field. The scientific discussions we had during various meetings often helped to bring many answers to the problems we encountered. Thank you for also taking me to visit some parts of Shiga Prefecture; I will cherish the memories of discovering Shigaraki and the pottery session with them. I would also like to thank Yamazaki-san for his scientific expertise and the good places he recommended me to discover, particularly around Toyama and Kanazawa. I would also like to thank Shimatani-san, Yama-chan, and Jun, first for the many ping pong sessions during lunchtime, but also for the tennis sessions on Sundays and the good times spent in various izakaya. Finally, I would like to thank Séverin Barthel, with whom I shared the first three months of the internship in the company and with whom I visited a significant part of Japan, for his moral support and enthusiasm. A big thanks also for his valuable help on the numerical simulation aspect of birefringence.

I am also grateful to my non-permanent colleagues at the SIMM lab who contributed to make this journey very unique and unforgettable. I'll keep warm memories of conferences, lab-week ends, and many fun events. I thank you all for your moral support. Warm thanks to my cohort members, "Ze best PhD year" (Maxime, Gabriel, Perrine, Svetlana, Sixtine, Martin, Marion, Edwige, Léa, Grégoire, Ombeline, Paula, Lazare, and Donghao)! Special thanks to Perrine and Lazare for the great moments spent at SFL. A big thanks go to my office mates, Léa, Hiam, and Lorenzo for all their help, good mood, and enthusiasm (and long discussions about Japan). A huge thanks to Julie, first for welcoming me into the best office in the old building (especially after 6 p.m.), but also for her kindness and daily good cheer in the lab as well as outside, with all the activities we shared. I also want to thank the third-floor members for the fun and trustful atmosphere (special thanks to Bruno, Artem, Maxime, Théo). I would also like to thank the volleyball team for our delightful sportive Fridays (especially Jean-Francois, Fakhr, and Thomas).

Last but not least, I would like to deeply thank my family, especially my parents and my brother. Their belief in me has kept my motivation high during this process. I would like to warmly thank all my friends, from Phelma and, of course, the Montmorency dream team I have known since childhood, middle school, and high school. Thank you all for being here around me, I am very lucky to have you in my life.

Elisa, thank you for your kindness and your support during these 5 years.

I will conclude by thanking you, the reader, for the interest that led you to read this work, built from results obtained in various parts of the world (Because did you know? I've been to Japan)



# Introduction and outline of the manuscript

Silicate glasses are among the most widely used materials across the widest range of human activity due to their unique combination of optical clarity, mechanical strength, and chemical durability. Composed primarily of silicon dioxide ( $\text{SiO}_2$ ), often with the addition of other oxides such as sodium oxide ( $\text{Na}_2\text{O}$ ) and calcium oxide ( $\text{CaO}$ ), these glasses are integral to numerous applications. In architecture, they are used in windows, facades, and insulation, providing both light, structural support, and energy efficiency. In electronics, silicate glasses are critical for the manufacture of displays and screens, where their hardness and scratch resistance are essential. Additionally, in the optics industry, glasses are employed in lenses, prisms, and optical fibers, owing to their low optical dispersion and high transparency. The versatility of silicate glasses extends to their use in packaging, particularly for food and pharmaceuticals, where their impermeability and chemical inertness offer unmatched protection. Moreover, in the automotive and aerospace industries, silicate glasses are used for windshields and cockpit windows, but also as reinforcement fibers in polymer composites, where their combination of lightweight and mechanical strength is highly valued.

Despite their widespread application, silicate glasses are not without limitations, particularly in their mechanical performance under stress. Their use is often limited by their low fracture resistance, despite their remarkably high intrinsic strength. It has long been understood that surface defects dramatically reduce the mechanical strength of silicate glasses. Remarkably, among various silicate glasses, which otherwise share similar mechanical properties (their elastic, plastic, and resistance to fracture *propagation* are very close), some exhibit significantly better resistance to crack *formation* than others. Understanding how surface defects form in silicate glasses and how sensitivity to surface damage is related to composition remains an open question in materials' mechanics and a significant technological challenge.

It has been more or less explicitly suggested for some time that material damage resulting from shear-induced plastic flow, particularly the formation of shear bands, plays a crucial role in the initiation of fractures [1]. However, this hypothesis has yet to gain traction in the literature and has not been systematically tested, primarily due to challenges in modeling the plastic response of these materials at the continuum scale, and thereby accurately representing the plastic deformations that occur during indentation.

In this thesis, we therefore attempted to characterize this plasticity experimentally at the local scale as well as the dynamics of the physical processes involved. The manuscript is organized in an introductory chapter followed by two results chapters which can be read independently, like articles.

- **Chapter 1: Structure and mechanical properties of oxide glasses: state of the art**

This chapter provides a short review of the structure and mechanical properties of oxide glasses, especially borosilicate glasses. We explore the basic principles governing the behavior of silicate glasses, including their brittleness and the mechanisms of plastic deformation and in particular densification and shear flow, and especially the impact of glass composition, offering a detailed exploration of how different oxides contribute to the overall mechanical performance. Special attention is given to the constitutive relations that predict the behavior of oxide glasses under various conditions.

- **Chapter 2: Effect of irradiation on silicate glasses plasticity – in-situ micromechanical testing**

This chapter focuses on the experimental investigation of the effects of electron irradiation on the plasticity of silicate glasses. It presents a detailed account of in-situ microcompression tests performed on micropillars under irradiation, including the morphology observed in micropillars after compression and stress relaxation experiments. It explores the relation between the strain rate sensitivity of the plasticity of silicates and irradiation, providing insights into the composition dependence of the mechanisms driving plasticity.

- **Chapter 3: Characterization of indentation cracking in alkaline-earth aluminoborosilicate glasses: densification vs plastic shear flow**

The chapter investigates the mechanisms of indentation cracking in alkaline-earth aluminoborosilicate glasses, with a specific focus on the quantification of shear localization. Starting from the observation of cross-sections of indents, we propose a new approach to characterize the morphology of the shear bands and their distribution by measuring roughness in the plastically deformed region. This method quantifies the extent of shear flow localization and offers new insights into how different glass compositions influence the formation and propagation of cracks. Comparing with more usual parameters such as thermal recovery measurements and Poisson ratio, this chapter highlights the significance of shear flow to better understand the relationship between composition and crack resistance.

The characterization methods and data processing routines are detailed at the beginning of each chapter.

## Chapter 1

# Structure and mechanical properties of oxide glasses: state of the art

### Contents

---

<b>1.1 Silicate glass : structure and general mechanical properties . . . . .</b>	<b>8</b>
1.1.1 Mechanical properties of oxide glasses . . . . .	8
1.1.2 Structure of oxide glasses . . . . .	10
1.1.3 Fracture properties of oxide glasses . . . . .	14
<b>1.2 Plasticity in oxide glasses . . . . .</b>	<b>19</b>
1.2.1 Brittle to ductile transition: lengthscales . . . . .	19
1.2.2 First approach to the indentation stress fields - Yoffe model . . . . .	20
1.2.3 Plastic deformation mechanisms: densification vs shear flow . . . . .	21
1.2.4 Indentation cracking . . . . .	30
1.2.5 Constitutive relations and other numerical models developed for oxide glasses . . . . .	33

---

## 1.1 Silicate glass : structure and general mechanical properties

### 1.1.1 Mechanical properties of oxide glasses

#### 1.1.1.a General discussion about oxide glasses

In an Ashby diagram (Fig. 1.1), oxide glasses are classified as "Technical ceramics". They have relatively high rigidity, with Young's modulus values of around 50 to 90 GPa and densities ranging from 2000 to 3000 kg/m<sup>3</sup>. But what is even more striking is that the region covered by oxide glasses is relatively tiny on this diagram, which implies that in most cases and for most glass compositions, their mechanical properties will be more or less similar. This places silicate glasses in a group of materials that offer good rigidity for their weight. This combination enables oxide glass to withstand stress without deforming too much while remaining relatively light. This is an advantage in applications where it is important to limit weight while retaining a degree of rigidity. In the design of structural elements, vehicle components, or applications where weight efficiency is crucial (such as aerospace or portable devices), glass can be a wise choice. For example, a lighter material with high rigidity can allow thinner or less dense structures to be built without compromising mechanical performance, which can also contribute to better fuel economy in vehicles or reduced structural loads in buildings.

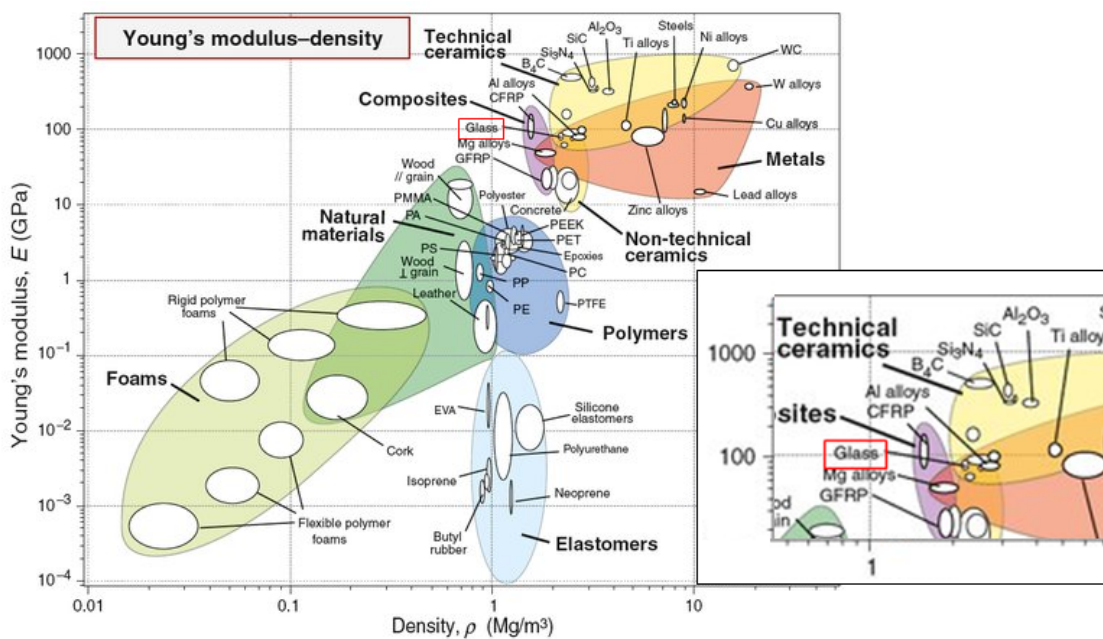


FIGURE 1.1: Ashby diagram displaying Young's modulus ( $E$ ) as a function of density ( $\rho$ ) (from [2]).

Another significant property of oxide glasses is the hardness which measures their resistance to permanent deformation or scratching. A quantitative measure of hardness is the Vickers hardness test, carried out by applying a specific force  $F$  to a square diamond tip and measuring the area  $A$  of the indent left on the material. Vickers hardness is then defined as  $H_v \equiv F/A$  and values for oxide glasses are generally in the range of 2 to 8 GPa [3, 4] which is relatively high compared with metals, for example, most of which have a hardness of around hundreds of MPa or lower.

On the other hand, oxide glasses also exhibit thermal properties that play a role just as crucial as mechanical properties in their behavior and exploitation. Two of the most significant thermal properties are the glass transition temperature ( $T_g$ ) and the coefficient of thermal expansion (CTE). Upon reaching the glass transition temperature from below, the amplitude of atomic and molecular movement within the amorphous structure is enhanced. For multicomponent oxide glasses, the  $T_g$  generally ranges between 500°C and 800°C [5, 6] but can reach up to 1200°C for pure amorphous silica. This wide range is dependent on the specific composition of the glass. Finally, the coefficient of thermal expansion measures the tendency of a material to change volume in response to a temperature change. The CTE typically ranges from 5 to  $10 \times 10^{-6}$  °C for oxide glasses. A low CTE is often desirable as it means the material expands or contracts little with temperature changes. Finally, oxide glasses are renowned for their remarkable transparency, a property that significantly contributes to their widespread use in various applications. This optical transparency is primarily due to the glass's wide band gap, which prevents visible light's absorption, allowing it to pass through the material with minimal scattering or absorption. The inherent transparency of silicate glasses makes them ideal for windows, lenses, and other optical devices, as they provide clear and undistorted views while maintaining structural integrity. This unique combination of transparency and durability underscores the essential role of silicate glasses in both everyday products and advanced technological applications.

### 1.1.1.b A model to predict the mechanical properties

One of the simplest glass properties to measure is the density ( $\rho$ ), as the previous diagram exposed. Archimedes' method [7] consists in immersing the glass sample in water and measuring the displaced volume. It can easily determine the volume of odd-shaped samples. Density  $\rho$  is then obtained by dividing the mass ( $m$ ) of the glass sample by the volume ( $V$ ). This property is useful for calculating the atomic packing density ( $V_t$ ) (defined in the conventional way as the ratio between the total volumes summed over all atoms based on known atomic radii and the actual volume calculated from measured density and composition). In the '70s, Makishima and Mackenzie [8] developed a model to predict Young's modulus ( $E$ ) by using this atomic packing density and the dissociation energy per unit volume ( $G$ ) (or inter-atomic bonding strength) with the following equation:

$$E = 2V_t G \quad (1.1)$$

With the assumption of a multicomponent glass, (1.1) becomes:

$$E = 2V_t G = 2 \left( \frac{\rho}{M} \sum_{i=1}^n V_i X_i \right) \left( \sum_{i=1}^n G_i X_i \right) \quad (1.2)$$

where  $M$  is the effective molar weight,  $G_i$  is the dissociation energy of oxide  $i$ ,  $X_i$  is the mole fraction of oxide  $i$  and  $V_i$  is the packing factor of the oxide  $i$ . For an oxide  $A_X O_Y$ ,  $V_i$  and  $G_i$  have also been determined by Inaba [9] with the following equations:

$$V_i = 6.023 \times 10^{23} \frac{4}{3} \pi (X R_A^3 + Y R_O^3) \quad (1.3)$$

$$G_i = \frac{\rho_i}{M_i} [X\Delta H_f(A, gas) + Y\Delta H_f(O, gas) - \Delta H_f(A_XO_Y, crystal) - (X + Y)RT] \quad (1.4)$$

$R_A$  and  $R_O$  are the respective ionic radius of cation and oxygen.  $M_i$  and  $\rho_i$  are the molecular weight and the density of the oxide  $i$ , and  $\Delta H_f$  are the molar heats of formation from the elements in their standard states of the oxide and gaseous atoms. In his paper, Inaba provided  $V_i$  and  $G_i$  values for a wide range of oxides. Subsequently, Makishima and Mackenzie [10] further developed their model to calculate the bulk modulus ( $K$ ), the shear modulus ( $G$ ), and the Poisson ratio ( $\nu$ ) of oxide glasses:

$$K = 2.4V_t^2G \quad (1.5)$$

$$G = \frac{7.2V_t^2G}{10.8V_t - 1} \quad (1.6)$$

$$\nu = 0.5 - \frac{1}{7.2V_t} \quad (1.7)$$

This Makishima-Mackenzie (MM) model is therefore relatively easy to use to quickly estimate the stiffness and the Poisson ratio of any oxide glass from its previously measured density.

## 1.1.2 Structure of oxide glasses

### 1.1.2.a The pure amorphous silica system

Amorphous silica, or more generally oxide glasses are completely long-range disordered materials, as described by Zachariassen [11, 12]. Their structures do not display any periodicity or symmetry with the repetition of a unit cell (Fig. 1.2.a) in comparison with crystalline structures from metals for instance. The only reproducible pattern within the structure is a short-range order of chemical nature, with one silicon atom in the center of the tetrahedron structure and four oxygen atoms located at each corner of the tetrahedron (Fig. 1.2.b).

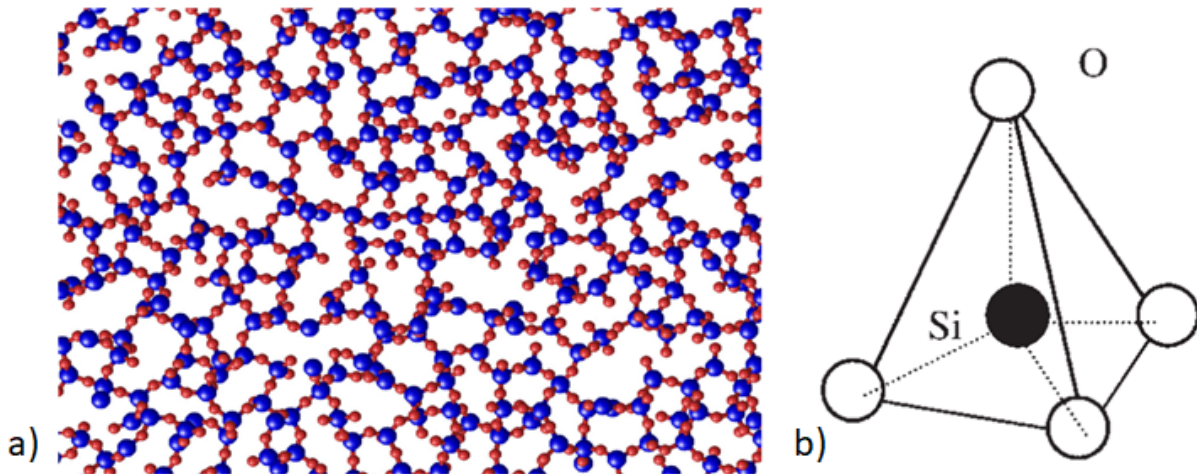


FIGURE 1.2: (a) Sectional view of a 3D MD simulations from [13]. It shows a typical pure-amorphous silica structure where red spheres correspond to O atoms and blue spheres correspond to Si atoms. (b) Tetrahedron structure of silicon atom bonded to four oxygens.

Therefore, each oxygen atom is shared by two silicon atoms, and another tetrahedron shares each corner of one tetrahedron. This relatively open structure (there are no shared edges) results in

a distribution of bond angles. The first data on this short-range glass structure comes from Mozzi and Warren's X-ray diffraction measurements [14]. Other methods such as neutron scattering have enabled the estimation of the interatomic distances Si-Si, Si-O, and O-O [15] and are gathered in Table 1.1.

TABLE 1.1: Bond lengths in pure amorphous silica

Bond	Length( Å)	Technique	Reference
Si-O	$1.608 \pm 0.004$	Neutrons scattering	[15]
Si-Si	$3.077 \pm 0.111$	Neutrons scattering	[15]
O-O	$2.626 \pm 0.006$	Neutrons scattering	[15]
Si-O	$1.62 \pm 0.02$	Molecular Dynamics	[16]
Si-Si	$3.05 \pm 0.02$	Molecular Dynamics	[16]
O-O	$2.64 \pm 0.02$	Molecular Dynamics	[16]

An interaction potential for  $\text{SiO}_2$ , designed and calibrated by Vashishta *et al.* [16] has been used in molecular dynamics to reproduce with accuracy a structure similar to that observed in experiments (Table 1.1). Molecular dynamics thus provides access to an intimate vision of the material model and makes it possible to provide a distribution of its structure such as an approximation of the O-Si-O angle and the Si-O-Si angle which correspond respectively to an angle in the tetrahedron and the interlink angle between two tetrahedra. From XRD experiments, it has also been found the distribution of the Si-O-Si angle peaked around  $146^\circ$  and the O-Si-O angle around  $109^\circ$ .

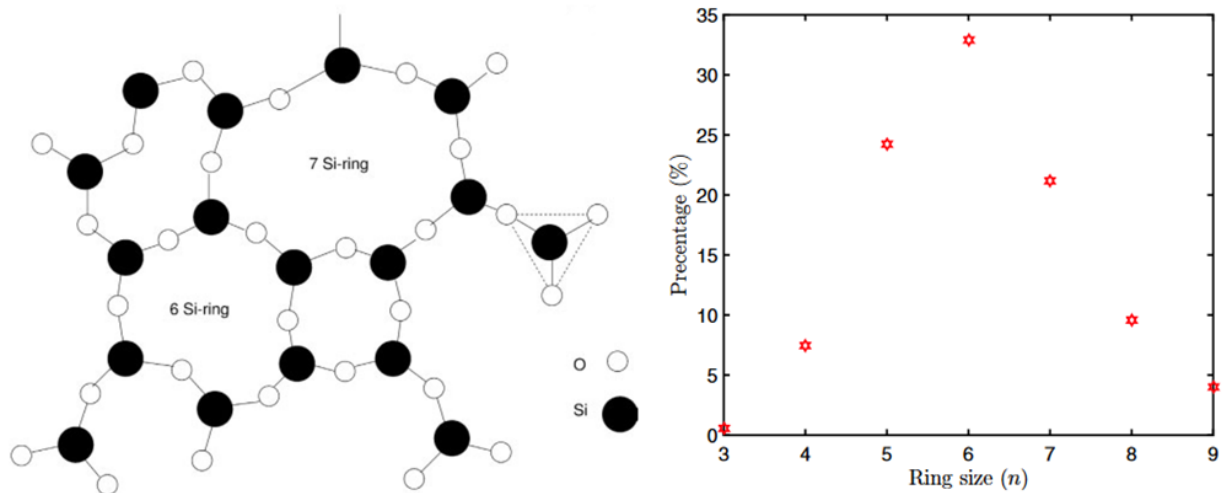


FIGURE 1.3: (a) 2D projections of structures showing the glassy structure of pure silica with a 6 Si-ring and a 7 Si-ring from [17], (b) Distribution of rings of pure-amorphous silica from molecular dynamic simulations from [13, 18].

At a larger scale than the short-range order, it is difficult to describe the amorphous structure. Following Zachariassen [11] we can try to identify patterns where  $\text{SiO}_4$  tetrahedra are connected to form rings with  $n$  silica atoms and  $n$  oxygen atoms. For example, thanks to molecular dynamics, Fig. 1.3.a shows a 2D structure of pure-amorphous silica displaying 6-member and 7-member rings. More recently, scanning electron microscope (SEM) and transmission electron microscope

(TEM) measurements from [19] provided images of the silica network in 2D which support this description. In practice, this description is mostly used in simulations [18], described in 1.2.5.c, (Fig. 1.3.b) in which it is fairly easy to count the proportion of n-member rings: in silica, it shows a maximum percentage of 6-member rings in the pure amorphous silica.

### 1.1.2.b Multi-component glasses: glass formers and network modifiers

Pure amorphous silica is one of the simplest glasses. However, in the industrial field, it is common practice to include additional oxides to adjust the properties (mechanical, thermal, optical, electrical, etc...) of the resulting glasses, for example, to lower their glass transition temperature or improve their mechanical strength. These components of oxide glasses can be distributed into three different categories: (1) glass formers, (2) modifiers, and (3) intermediate [12]. A glass former is an oxide that naturally forms an amorphous structure. It typically has a 3D network of covalent bonds whose bond strength is greater than 80 kcal per mole according to Sun [20]. In silicate glasses, the Si-O bond is the primary glass former. In contrast, network modifiers (typically an alkaline or an alkaline-earth oxide, characterized by ionic bonding) modify the Si-O network. Adding a glass modifier to a glass former typically results in non-bridging oxygen (NBO) atoms within the glass structure and an associated ion nearby to maintain charge neutrality.

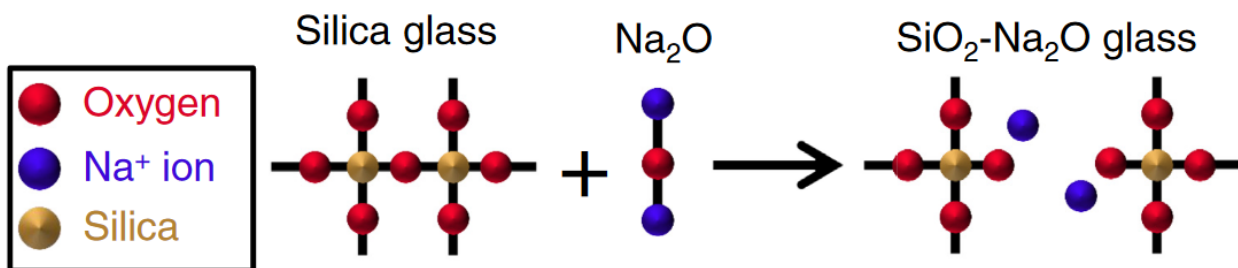


FIGURE 1.4: Diagram of what happens when the glass modifier  $\text{Na}_2\text{O}$  is added to a pure amorphous silica system taken from [13].

Let us consider the binary system  $\text{SiO}_2\text{-Na}_2\text{O}$  as an example (see Fig. 1.4 above): when a molecule of  $\text{Na}_2\text{O}$  is added to a pure silica system, one Si-O-Si bond is broken and one NBO is formed on each of the adjacent silica tetrahedra. Each NBO is charge-compensated by a  $\text{Na}^+$ .

The terminology  $Q^x$  with  $x$  the number of bridging oxygens (BO) on a tetrahedron is generally used to describe the structure:  $Q^4$  means each oxygen atom of the tetrahedron is shared by another tetrahedron *i.e.* all four corners are bridged. A network only composed of  $Q^4$  silica is fully polymerized. On the other hand,  $Q^2$ , for example, corresponds to a silicon atom surrounded by two NBO and two BO. It has been shown that the relative amount of NBO has a direct impact on the mechanical and thermal properties of glasses [21, 22]. The effect of increasing NBO content is mainly network depolymerization. Consequently, the mobility in the network is improved, resulting in a higher atomic packing density, a lower glass transition, and a lower hardness. For example, the addition of network modifiers, such as sodium, tends to decrease the  $T_g$  due to NBOs since less energy is required to activate the partial mobility of the network.

To go further, in 1942, Dietzel [23] proposed a classification of several oxides as a function of their cation field to describe their ability to form or modify the glass network. We can also find

this parameter as cation field strength ( $FS$ ) in the literature. The field strength is defined according to the following equation:

$$FS = \frac{z_M}{(r_M + r_O)^2} \quad (1.8)$$

where  $z_M$  is the cation effective charge, and  $r_M$  and  $r_O$  are respectively the radii of the network modifier and its associated oxygen.  $FS$  is indicative of the magnitude of the electrostatic attractive force between the cation and its associated oxygen. According to Table 1.2, when  $FS > 1$ , the oxide is considered as a glass former while for  $FS < 0.32$ , the oxide is more likely to modify the network than form it. In Chapter 3, we will see that substituting calcium, the ion network modifier with the highest field strength, by an intermediate ion like magnesium, which has a relatively low field strength for its category, can significantly impact the fracture properties of the glass. However, for a given oxide, Shannon [24] shed light on multiple possible values for cation radii which depend on its coordination number in the network. Thus, Dietzel's classification and  $FS$  could be slightly modified depending on the glass composition.

TABLE 1.2: Role of cation in glass and their field intensity ( $r_O = 1.4\text{\AA}$ ) adapted from [17].

Role	Cation	Z	$r_c$ ( $\text{\AA}$ )	FS
Glass formers	Si	4	0.4	1.23
	B	3	0.25	1.10
	Ge	4	0.53	1.07
Intermediates	Ti	4	0.74	0.87
	Al	3	0.53	0.80
	Zr	4	0.86	0.78
	Be	2	0.41	0.61
	Mg	2	0.86	0.39
	Zn	2	0.88	0.38
Modifiers	Ca	2	1.14	0.31
	Pb	2	1.33	0.27
	Li	1	0.9	0.19
	Na	1	1.16	0.15
	K	1	1.52	0.11

The third group of oxides is the glass intermediates. Depending on the composition, these oxides act either as glass modifiers or as glass formers. The traditional example is the aluminum oxide ( $\text{Al}_2\text{O}_3$ ). When this oxide is added to the binary system  $\text{SiO}_2$ - $\text{Na}_2\text{O}$ , Al atoms (with an initial 3-coordination) replace Si atoms in tetrahedra and form covalent bonds with oxygen. Therefore, they are negatively charged and  $\text{Na}^+$  ions in their vicinity allow charge compensation. As a result, the number of NBOs gradually decreases in favor of network connectivity with the amount of  $\text{Al}_2\text{O}_3$ , and  $T_g$  increases. When the full network is recovered, the  $T_g$  is still lower than for pure silica because of the added mobility due to the  $\text{Na}^+$ . When the molar concentration of  $\text{Al}_2\text{O}_3$  exceeds the molar concentration of  $\text{Na}_2\text{O}$ , some Al atoms will then act as charge compensators and will form ionic bonds in the glass network. Consequently, the coordination number of Al can

also be modified (4-, 5- or 6- coordinated) [25].

A final essential glass-forming element worth highlighting is boron. Boron plays a crucial role in the composition of borosilicate glass, where it is present as boron oxide  $B_2O_3$ . Within the glass structure, boron can form two types of coordination: trigonal  $BO_3$  and tetrahedral  $BO_4$ . This structural versatility allows boron to significantly enhance the properties of the glass. The addition of  $B_2O_3$  alters the silicate network by introducing  $BO_3$  units, which reduce the viscosity of the molten glass [26], demonstrating higher mobility than the silicate network. Additionally,  $BO_4$  units, formed in the presence of certain modifiers, improve the connectivity of the system. On the other hand, in other systems without silica, like the  $25Na_2O \cdot xAl_2O_3 \cdot (75-x)B_2O_3$  system, the  $Al_2O_3/B_2O_3$  ratio may also affect the boron coordination [27]. Indeed, network modifiers tend to preferentially charge-balance Al-tetrahedra than B-tetrahedra. It results in a gradual decrease of the average boron coordination number by adding more  $Al_2O_3$ .

### 1.1.3 Fracture properties of oxide glasses

#### 1.1.3.a Fracture toughness

Mechanical properties also include fracture. Quantitative assessment of fracture properties helps evaluate the stress level at which a piece of glass breaks, which must be considered when manufacturing devices with glass components. Various approaches have been developed, which complement each other.

An important early work is due to C. Inglis, who introduced, in 1913, an analytical approach to understanding the phenomenon of stress concentration around defects in structures [28]. He showed that elliptic holes lead to significant increases in local stresses in high-curvature regions. He formulated the equation for the stress  $\sigma_f$  concentration at the apex of an elliptical flaw in an infinite plate under applied stress  $\sigma$  (at infinity):

$$\sigma_f = \sigma \left( 1 + 2\sqrt{\frac{a}{\rho}} \right) \quad (1.9)$$

where  $a$  is the semi-major axis length of the ellipse and  $\rho$  is the radius of curvature at the flaw tip. Clearly, a smaller radius of curvature results in higher stress near the crack tip.

In 1921, A.A. Griffith provided a complementary viewpoint to Inglis's work. Griffith introduced an energy-based fracture theory for brittle materials [29]. He demonstrated that crack propagation is governed by a balance between the elastic energy released by the propagation of the crack and the surface energy created. He formulated a criterion for fracture, known as Griffith's criterion and expressed as:

$$\sigma = \sqrt{\frac{2\gamma E}{\pi a}} \quad (1.10)$$

where,  $\gamma$  is the rupture energy per unit area of the material,  $E$  is the Young's modulus of the material, and  $a$  is the half-length of the crack. A larger defect leads to a lower rupture stress: this result is analogous to the effect of a large curvature at the tip. Although the fracture energy  $\gamma$  of silicate glasses is relatively low (between 5 and 10 J/m<sup>2</sup>), especially when compared to metals or polymers, it has been observed that this fracture energy is still ten times higher than the surface

energy. This suggests the existence of additional energy dissipation mechanisms, beyond the simple breaking of chemical bonds, such as local plastic deformation.

Finally, in the 1950s, George R. Irwin unified these concepts by introducing the notion of stress intensity factor  $K$  [30] which quantifies the stress enhancement around a perfectly sharp tip *ie* for an infinite tip curvature ( $\rho \rightarrow 0$ ). Irwin's equation for the stress intensity factor is given by:

$$K = \sigma\sqrt{\pi a} \quad (1.11)$$

for a penny shaped crack of length  $2a$ . Just as Griffith's rupture energy, Irwin's fracture toughness defines the ability of the glass (or other material) to resist the propagation of this pre-existing crack. In fact,  $\gamma = \frac{K^2}{2E}$ . When the stress intensity factor, associated with this mode, reaches the critical value  $K_c$ , the crack propagates within the materials. This parameter  $K_c$  defines the condition for the onset of a rapid, or unstable, crack extension [31, 32].

But it turns out that most glasses are susceptible to undergo slow crack extension, often environmentally-assisted, over  $K$  values below  $K_c$ , called the sub-critical crack growth. Fig. 1.5.a describes this phenomenon with three regimes of sub-critical crack propagation [33, 34]:

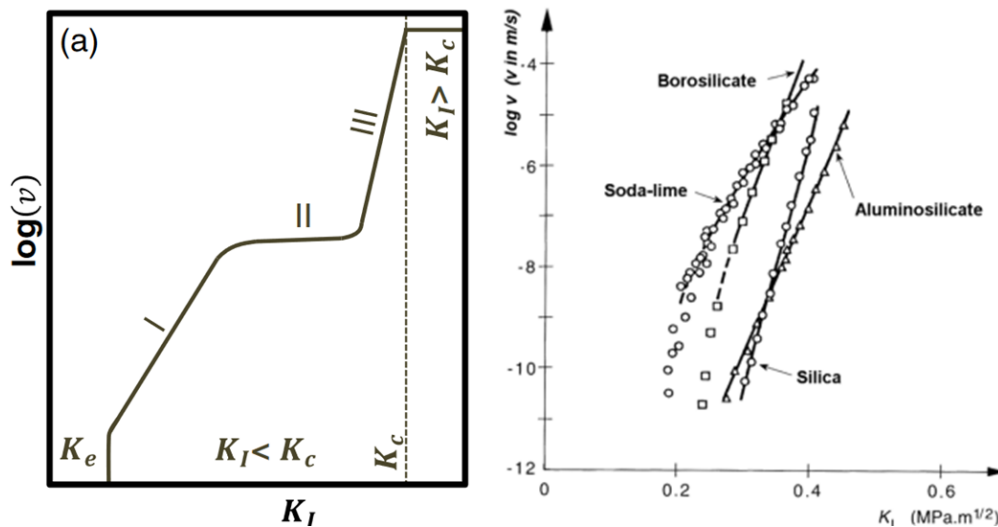


FIGURE 1.5: (a) Schematic of  $K$ - $v$  curves for glasses with the three-regions of sub-critical cracking from [13, 35] and (b) effect of glass compositions on  $K$ - $v$  curves in the region I in water (taken from [33]).

- Region I: The slope of region I mostly depends on the time for the chemical reaction. Consequently, the higher the slope of region I, the more susceptible the glass is to stress corrosion. This mechanism of stress corrosion is described, for the case of pure amorphous silica, in Fig. 1.6. It shows that, under stress, water molecules tend to penetrate the structure and break siloxane bonds which is going to ease the crack propagation.
- Region II: The crack front velocity is limited by the time for the reactant to reach the crack front.
- Region III: The velocity of the crack is too fast to be impacted by the stress corrosion and it doesn't allow time for the reactant to reach the crack tip. However,  $K$  is still less than  $K_c$ .

Some glasses also exhibit a threshold  $K_e$  associated with the environmental limit where the stress at the crack tip is insufficient to induce stress corrosion and where the crack does not propagate.  $K_e$  is usually called the "propagation threshold".

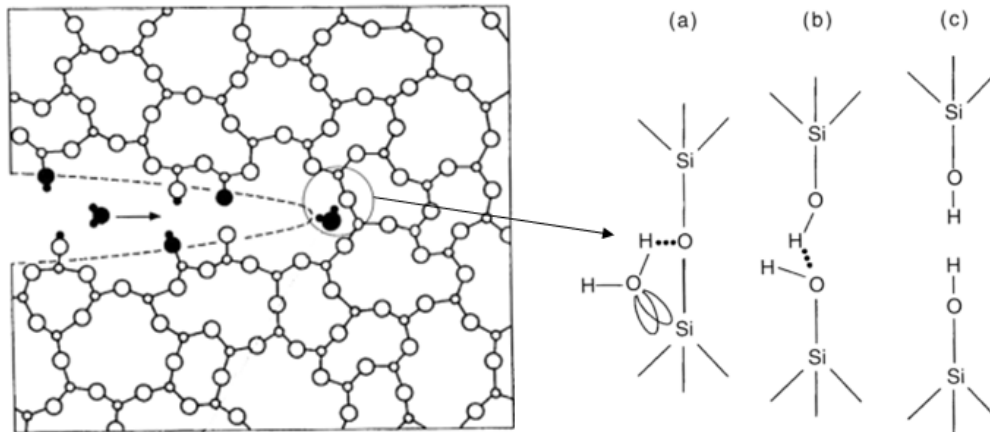


FIGURE 1.6: Mechanism of the stress-corrosion reaction adapted from [35, 36].

The glass composition can also affect the crack growth. For example, based on measurements by Wiederhorn [34], no sub-critical crack growth is observed under an inert atmosphere or vacuum (mode III) for some materials, such as silica glass or low-alkali borosilicate glasses which are glasses with anomalous elastic properties. However, glasses with normal elastic properties such as soda-lime silicate or aluminosilicate glasses display a sub-critical crack growth under vacuum. It indicates that the number of network modifiers in the structure might play a role in the type of crack growth.

A lot of attention has been devoted to the relation between Poisson ratio and the rupture properties of glasses in general (Fig. 1.7). In particular, Lewandowski *et al.* [37] reported a correlation between the fracture energy and the Poisson ratio of several types of glasses. They showed, as Fig. 1.7 also does, that higher values of  $\nu$  give higher fracture energy and that the transition between brittle and tough regimes is for  $\nu_c = 0.31 - 0.32$ . From this correlation, Poisson ratio has been used to try to explain the different breaking properties of glasses. However, despite the rather clear trend for metallic glasses, it appears that this coefficient can not explain everything since little variation is registered within given families, particularly concerning silicate glasses, where the fracture toughness values are not influenced by their composition (Fig. 1.5.b). For example, silica, with a very low Poisson ratio, displays approximately the same fracture toughness as soda-lime silicate or borate glasses. We can therefore say that the role of Poisson ratio, which has nevertheless been much highlighted, is not as clear for silicate as for metallic glasses.

This entire discussion centers on crack propagation from preexisting flaws in the structure. On the other hand, another relevant aspect of fracture is investigating what happens if care is taken to suppress these flaws.

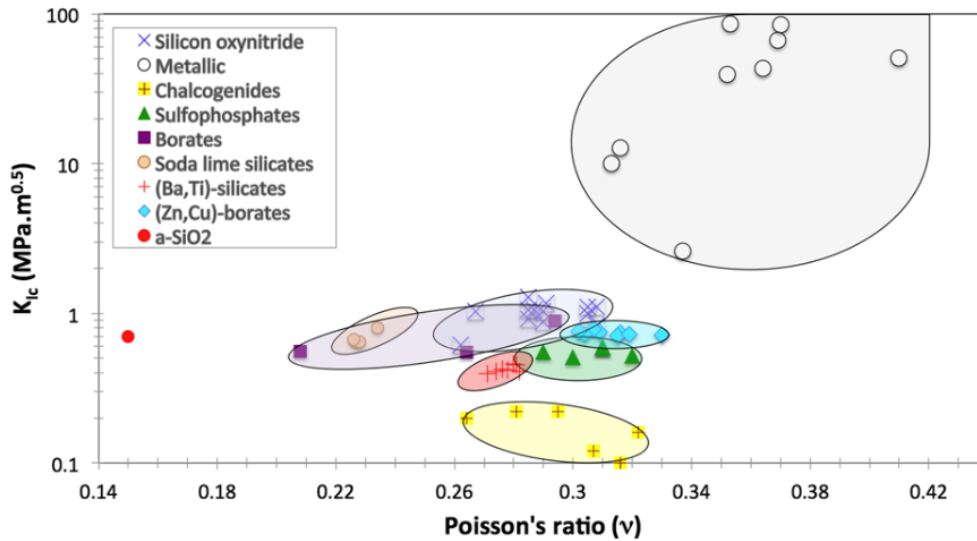


FIGURE 1.7: Apparent fracture toughness of glasses as a function of Poisson ratio from [38].

### 1.1.3.b Intrinsic strength of glass

As we discussed just before, it is known that the practical strength or fracture toughness of glasses is defined by the ability of the glass to resist the propagation of a pre-existing crack (Inglis and Griffith theory). However, very high tensile strengths on carefully prepared pristine E-glass (defect-free glass designed for electrical application [39]), tested under liquid N<sub>2</sub> temperature (77 K), have been measured in the past [40, 41, 42]. Later Kurkjian, Paek, and Gupta [43, 44] argued that these measured fiber strength values were "intrinsic strengths". It is called intrinsic because the stress to rupture is no longer controlled by the size of extrinsic flaws. Initially, uniaxial tension tests were performed but experimental difficulties due to gripping limited its use. In more recent works [45, 46, 47, 48], the two-point bending technique has been used. This method involves constraining a bent fiber between two faceplates which are brought until the fiber breaks. A computer-controlled stepper motor brings one faceplate to the other (Fig. 1.8.a). The motor stops when the fiber fracture is sensed by an acoustic detector. The failure strain is then calculated from the remaining distance between the two faces. This method gets rid of gripping issues and the setup can easily be immersed in a liquid-nitrogen bath or other inert environment to avoid the effect of moisture. The main drawback comes from the difficulty of assessing the failure stress from the large failure strain (over 10%) since the constitutive law corresponds to a non-linear elastic behavior in this range. However, some works proposed a theory to evaluate this failure stress from the measured strain [49, 50].

Fig. 1.8.b shows the failure strain of E-glass and pure silica glass in an inert environment. The narrow and sharply peaked distributions of both E-glass and silica in this graph indicate that these materials have very consistent failure strains. This consistency suggests that the observed failure strains are largely determined by the intrinsic properties of the material rather than by extrinsic factors such as defects or variations in the material structure and manufacturing. In comparison with fracture toughness, where all these compositions displayed approximately the same value between 0.3 and 1 MPa.m<sup>1/2</sup>, the failure strain of pure silica is higher than the failure strain of

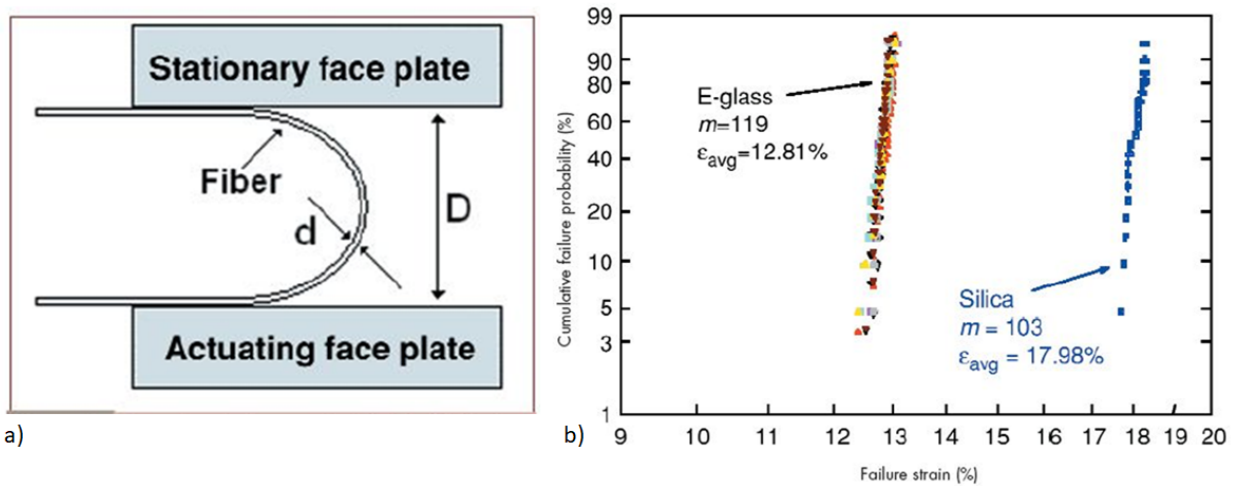


FIGURE 1.8: (a) Schematic of the two-point bending technique and (b) Weibull plot of inert failure strains from E-glass and silica glass fibers at 77K from [48].

E-glasses which means that defect-less carefully prepared silica fibers are significantly tougher than other glass compositions. But in all cases, they exhibit intrinsic strengths of several GPa [51]. It has also been seen that intrinsic strength is also dependent on the temperature as Fig. 1.9 shows. Performing two-point bending experiments at a very low temperature will limit the water activity. Consequently, the stress corrosion reaction is going to be frozen and the strength of the glass increases.

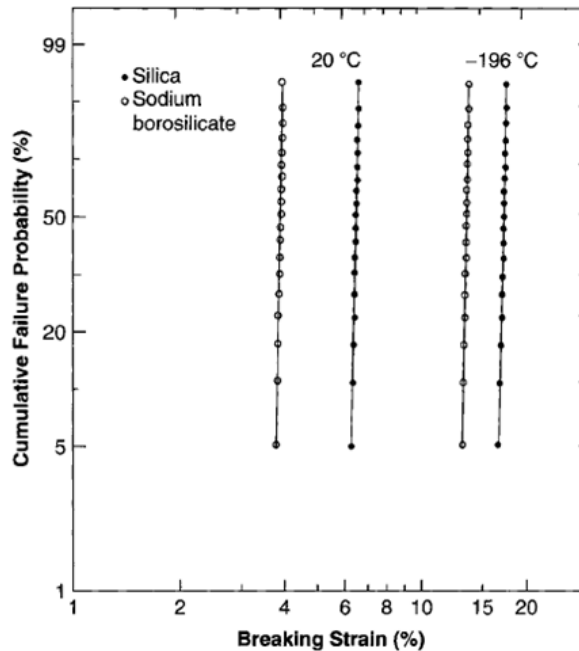


FIGURE 1.9: Failure strain of sodium borosilicate and silica glass fibers at room temperature and in liquid nitrogen from [52].

## 1.2 Plasticity in oxide glasses

### 1.2.1 Brittle to ductile transition: lengthscales

At the macroscopic scale, silicate glasses are generally considered the archetype of brittle materials, which break without plastic deformation. As a consequence, no energy dissipation is expected to take place during fracture, and the energy release rate should exactly compensate for the creation of two free surfaces [29], which is not the case (1.1.3.a) for silicate glasses. Indeed, at a scale of the order of micrometers, it is well-known that silicate glasses *do* undergo plastic deformation [53, 54, 55]. For example, indentation, which measures the hardness of a material (see section 1.1.1.a), has revealed evidence of plastic deformation in glasses at a local scale. Fig. 1.10 shows that for lower loads, the glass exhibits a permanent imprint, which reflects an irreversible deformation, but little or no cracking. By increasing the load and consequently the size of the print, the indentation generates cracking, especially along the diagonals (radial cracks).

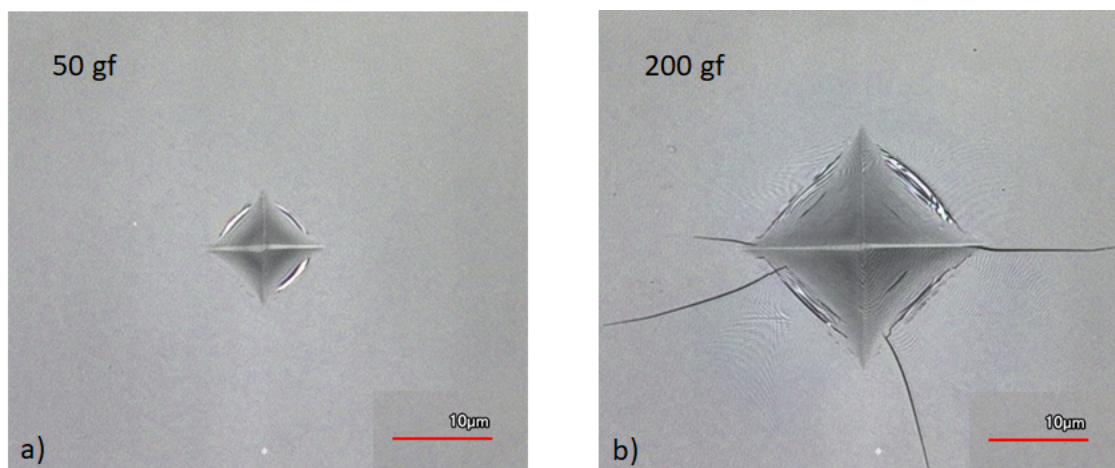


FIGURE 1.10: Vickers indents in a calcio-aluminoborosilicate glass at (a) 50 gf and (b) 200 gf

Other pieces of evidence of plastic deformation in silicate glasses have been published over the past years. For example, in 1964, Marsh [54] reported plastic scratches on a glass surface (Fig. 1.11.a). But one of the most spectacular illustrations of the connection between plastic flow and fracture in silicate glasses was detailed by Puttick *et al.* [56] in 1989. When a single-point diamond machines a silica glass surface, in very special conditions, it generates "machine turnings" as shown in Fig. 1.11.b. The twisted shapes of these turnings definitely suggest some plastic deformation has occurred along with the fracture.

Then, the indentation technique was widely used over the years to study in more detail this local plasticity. To better understand the indentation cracking of silicate glasses and the role played by the plastic strain, we need a detailed description of the indentation-induced stress fields and the deformation mechanisms below the indent. Once plastic deformation under indentation is described and characterized in section 1.2.3, we will show its correlation with the indentation cracking in section 1.2.4 to try to understand why some glasses are more crack-resistant than others.

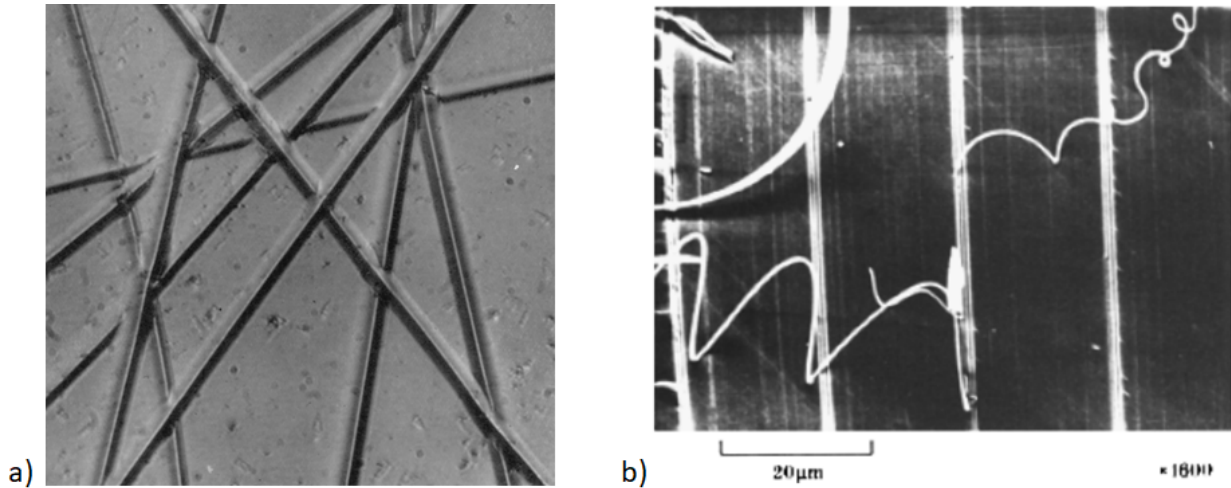


FIGURE 1.11: Plastic scratches produced by trailing a hard point over a glass surface (taken from [54]), and detail of detachment of spiral ribbons from "Machine turnings" from machined grooves by a single-point diamond in silica glass (from[56])

### 1.2.2 First approach to the indentation stress fields - Yoffe model

As described by Hertz [57], when a relatively blunt object like a sphere is used to load glass, the stresses induced do not reach the yield stress and the glass only undergoes elastic deformation. In the case of a small sphere's radius or a sharper indenter, plastic deformation can occur and the elastic-plastic behavior of the glass becomes apparent [58]. Thus, the glass undergoes permanent deformation such as densification and/or shearing, which will be discussed in the following sections. This results in a sort of hemispherical zone of compacted and/or shear-flowed material around the indent [59, 60, 61]. A portion of the work of indentation is used for this plastic deformation, while the rest is elastically recovered during the "spring-back" effect after unloading [58]. The plastically deformed zone prevents some of the elastically deformed material around it from returning to its original, undeformed state. Roughly speaking, this leaves the plastically deformed area with residual compressive stresses due to the permanent deformation it has undergone. In contrast, the surrounding elastic zone, now free from the applied load, experiences residual tensile stresses. These tensions can lead to the formation of cracks, especially near the boundary with the plastic zone, where the material tries to return to its original shape. Yoffe [62] proposed an approximate elastic-plastic analysis of the indentation problem for a conical indenter. This analysis is commonly used to understand crack patterns. The Yoffe equations are given as

$$\sigma_r = \left[ \frac{P}{4\pi r^2} \right] [1 - 7 \cos \theta] + \left[ \frac{B}{r^3} \right] [19 \cos^2 \theta - 7] \quad (1.12)$$

$$\sigma_\theta = \left[ \frac{P}{4\pi r^2} \right] \left[ \frac{\cos^2 \theta}{(1 + \cos \theta)} \right] - \left[ \frac{B}{r^3} \right] \cos^2 \theta \quad (1.13)$$

$$\sigma_\phi = \left[ \frac{P}{4\pi r^2} \right] \left[ \cos \theta - \left\{ \frac{1}{(1 + \cos \theta)} \right\} \right] + \left[ \frac{B}{r^3} \right] [2 - 3 \cos^2 \theta] \quad (1.14)$$

$$\tau_{r\theta} = \left[ \frac{P}{4\pi r^2} \right] \left[ \frac{\sin \theta \cos \theta}{(1 + \cos \theta)} \right] + \left[ \frac{B}{r^3} \right] [5 \sin \theta \cos \theta] \quad (1.15)$$

$$\tau_{r\phi} = \tau_{\phi\theta} = 0 \quad (1.16)$$

The normal and shear stresses are expressed in polar coordinates  $(r, \theta, \phi)$ . These stresses are influenced by the normal load  $P$  and the so-called "blister field"  $B$ , with the values of  $P$  and  $B$  determining if the stresses are tensile or compressive in the key locations around the indent. Tensile stresses can drive crack formation. The blister field introduced by Yoffe, which is equivalent to force doublets along the surface and the vertical axis, represents the strength of the "spring-back" effect retained by the hemispherical plastic zone [63]. In Yoffe's model,  $B$  is the only material-dependent parameter. Its value and how it depends upon the glass composition will be discussed at more length below (see section 1.2.4.a) after we have discussed some specificities of the plastic deformation of amorphous silicates.

### 1.2.3 Plastic deformation mechanisms: densification vs shear flow

The plastic deformation in glass under indentation is mostly governed by two mechanisms: shear flow and densification [64]. Early indentation results have shown [53, 65] that glass can deform plastically under sharp-contact loading, in a manner apparently similar to more usual ductile materials like metals, ie by homogeneous shear flow. On the other hand, densification, a process where the glass atomic network becomes more tightly packed without necessarily breaking bonds, has been observed in amorphous silicates under high-pressure conditions, as shown by Bridgman and Simon [66, 67] for example. Ernsberger demonstrated that indentation of amorphous silica also results in densification [68]. The study of different glass compositions by Peter [69] showed that both densification and shear flow can occur, with the mode of deformation depending on the chemical composition of the glass. Thus, this section will deal with the mechanical response of oxide glasses to indentation by either shear flow or densification, which can be influenced by experimental conditions and glass compositions.

#### 1.2.3.a Structural changes induced by densification

Densification involves the compaction of the glass structure under applied hydrostatic stress, reducing the overall volume of the material without a corresponding loss of mass. To characterize the densification independently from the shear deformation, silica glass has to be tested under hydrostatic pressure. High-pressure techniques were first necessary for geophysical applications to model pressure and temperature conditions prevailing deep down in the Earth's interior [70] and Diamond Anvil Cell (DAC) experiments have finally been developed.

The principle of the DAC experiment is straightforward. A sample placed between the flat parallel faces of two opposed diamond anvils, surrounded by a metallic seal (see Fig. 1.13.a), and immersed in a mixture of methanol-ethanol, is subjected to pressure when a force pushes the two opposed anvils together. A small piece of ruby is introduced to monitor the pressure level using the shift of the R1 luminescence band.

This technique is usually coupled with advanced spectroscopic techniques to allow indirect observations of the structural changes associated with densification in silicate glasses. Raman

spectroscopy, in particular, has been useful in monitoring how the internal structure of silicate glasses adapts under hydrostatic pressure or indentation. Shifts in Raman peaks corresponding to the Si-O bond vibrations provide insight into the strain state within the glass and the degree of structural reorganization.

Densification in amorphous silica has been largely studied in the past, especially by Raman scattering [71]. Between 200 and 750  $\text{cm}^{-1}$  the Raman spectrum of silica glass consists of three bands (Fig. 1.12.a) The main band at 440  $\text{cm}^{-1}$  results from the symmetric stretching mode of Si-O-Si. This intense band is affected by the densification process through the reduction of the inter-tetrahedral angles Si-O-Si [72] and thus its stiffening leading to a shift toward higher wavenumbers. The defect lines  $D_1$  and  $D_2$ , at 492 and 605  $\text{cm}^{-1}$ , are respectively attributed to the breathing modes of the four-membered and three-membered rings [73, 74]. As Fig. 1.12.b shows, the  $D_2$  and  $D_1$  bands shift in position toward higher wavenumbers with increasing pressure and consequently density. However, the intensity of the  $D_1$  band decreases with pressure. These structural changes are associated with an increase in the number of three-membered rings but a decrease in the number of four-membered rings which is consistent with a general decrease in the free volume of the glass.

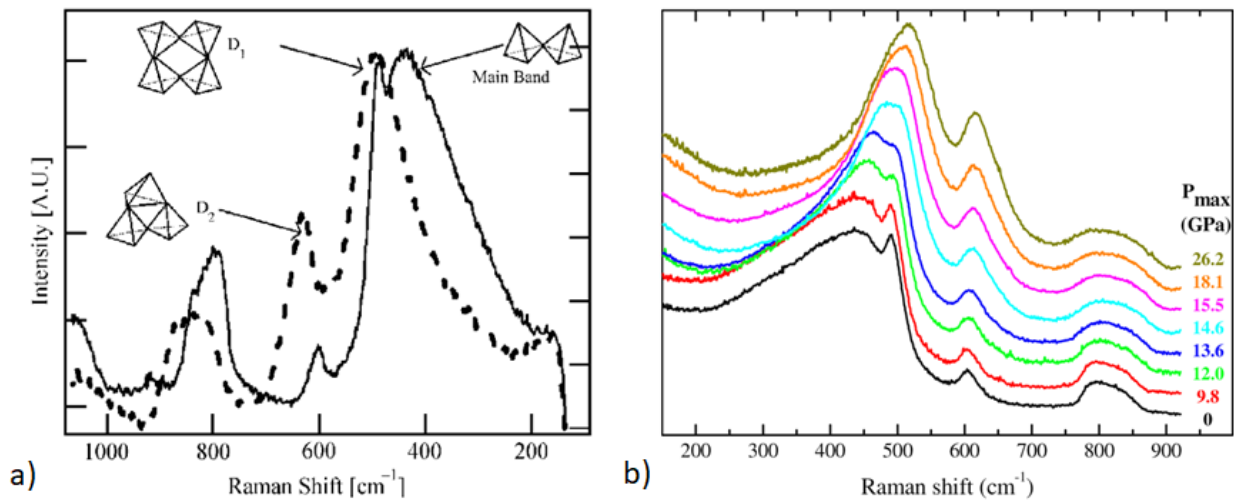


FIGURE 1.12: (a) Raman spectra for pristine (solid line) and indentation-densified (dash line) amorphous silica from [75]. (b) Ex situ Raman spectra of the non-densified and gradually densified silica glasses by DAC from [76]. The spectra are vertically shifted for a better visualization. The x-axis is reversed for graph (a).

Since the shift of the  $D_2$  line was described to be independent of the elastic stress, it has been used to estimate the densification under pressure in DAC following the relation [77]:

$$\frac{\Delta\omega_{D_2}}{\omega_{D_2}} \simeq \left( \frac{\Delta\rho}{\rho} \right)^{0.14} \quad (1.17)$$

Fig. 1.13.b shows the final density after unloading as a function of the maximum pressure reached in the experiment. Pure amorphous silica glass appears to be elastic up to around 10 GPa and exhibits densification at higher pressure: permanent densification up to the densification at saturation  $\Delta\rho_{sat} = 20\%$  can be observed.

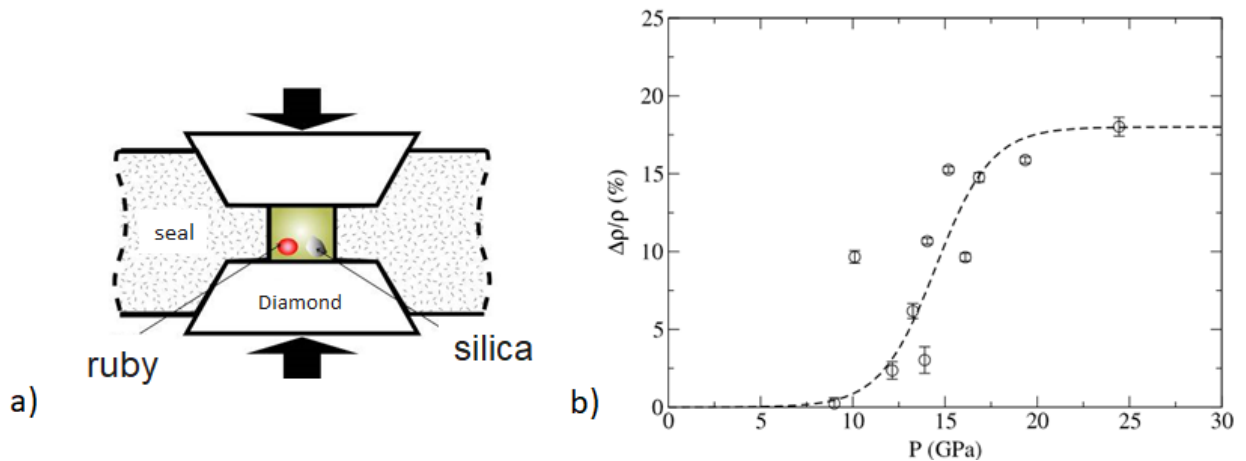


FIGURE 1.13: (a) Schematic of the Diamond Anvill Cell compression. The  $R_1$  luminescence band of ruby is used to infer the initial pressure. (b) Evolution of the residual densification versus the maximum pressure of the pressure cycle. The dashed line is an indicative sigmoidal curve corresponding to 18% of maximum densification. (adapted from [77])

Densification is possible due to the open structure of the amorphous silica network, which typically consists of tetrahedrally coordinated silicon atoms linked by oxygen bridges, with a decrease of the average Si-O-Si angle as described previously. Under hydrostatic pressure, these tetrahedral units are pushed closer together, resulting in tighter packing [78] and decreased free volume, which is associated with the space between molecules in the glass. During the densification process, several key structural changes occur:

- **Bond Angle Reduction:** From 10 GPa, the angles between bonds in the silica network are reduced, making the network more compact.
- **Coordination Number Increase:** From 20 GPa, there is an increase in the coordination number of silicon, as the network condenses under pressure. This means that each silicon atom may be coordinated by more oxygen atoms than under normal conditions, leading to a more interconnected network structure.

This network compaction leads to changes in the physical properties of the glass, such as increased refractive index [55] and enhanced mechanical properties. For example, Poisson ratio and elastic moduli increase with densification ratio [79].

Finally, when modifier oxides, like  $\text{Na}_2\text{O}$  or  $\text{CaO}$ , are added to amorphous silica, they cause depolymerization of the silica network and reduce its large free volume, which affects the glass deformation mechanisms under stress. For instance, in soda lime silica (window glass), Raman spectroscopy reveals more complex features compared to pure silica [80] due to the presence of various silica-oxygen bonding environments ( $Q^2$ ,  $Q^3$ ,  $Q^4$  - see section 1.1.2.b). Under pressure, the abundance of simpler  $Q^2$  units increases at the expense of more complex  $Q^3$  units, inducing a shift in the spectra and reflecting depolymerization that facilitates densification [81, 82]. This contrasts with glasses formed by  $\text{Al}_2\text{O}_3$  or  $\text{B}_2\text{O}_3$ , where the addition results in a structural response more similar to amorphous silica, emphasizing the stability of the silica network and the redistribution of ring structures rather than significant depolymerization.

### 1.2.3.b Experimental techniques to characterize densification under indentation

A method to study indentation-induced densification under micro-indentation is confocal microscopy, as with DAC measurements [75]. Interestingly, very different methods have also been proposed.

Neely and Mackenzie [83] suggested that deformation mechanisms described previously and induced by densification could be partially reversible through thermal annealing at moderate temperatures. They concluded that silica glass deforms mainly through densification rather than shear flow, which requires much more energy to recover. The idea to evaluate densification is to use atomic force microscopic observations coupled with thermal annealing. This method involves capturing topographic images of the indentation site before and after its heat treatment at  $0.9 \times T_g$ . This procedure makes it possible to quantify the size reduction of the indentation cavity after annealing. As pointed out in [83], the activation energy associated with the volume recovery is supposed to be less than the activation energy required for shear flow. Thus, only densified structures will be recovered by annealing below  $T_g$  [84], and the volume displaced by shear flow should be unaffected by annealing at  $0.9 \times T_g$  for 2h [85]. Under these conditions, the temperature is sufficiently low to disregard the impact of viscous flow but the duration is adequate to ensure full recovery of the densified region. Instead of assessing the full volume recovered [59], a measurement of the Recovery of Indentation Depth (RID) before and after heat treatment has also been considered to bring a first evaluation of the densification under indentation [86, 87, 88, 89].

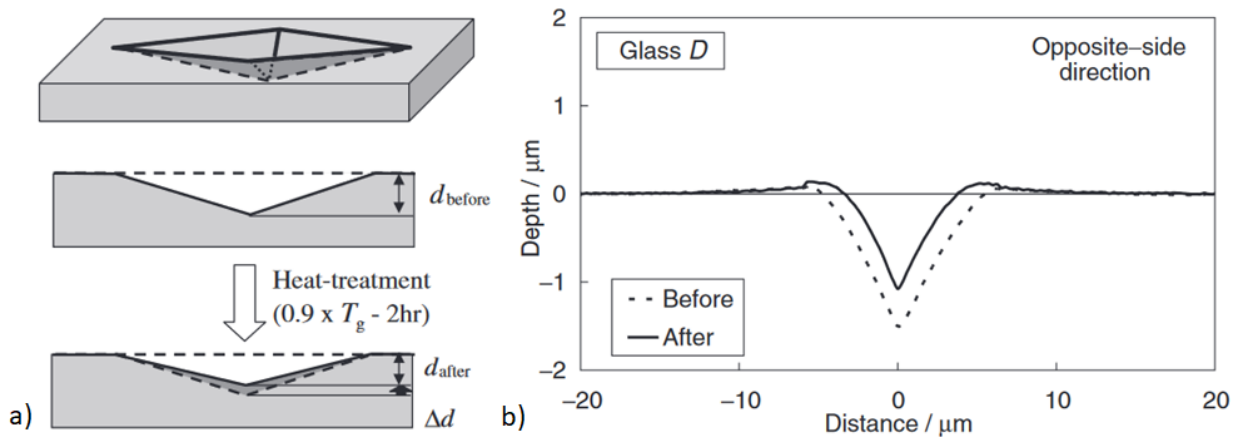


FIGURE 1.14: (a) Schematic of the method to measure the recovery of indentation depth (RID) and (b) example of cross-section profiles in opposite-side direction before and after heat treatment from a 100 gf Vickers indentation on an aluminoborosilicate glass. The thermal annealing has been performed at  $0.9 \times T_g$  (°C) for 2h. (adapted from [89])

As Fig. 1.14 shows, the indentation depth before annealing  $d_{before}$  is first measured. Once the annealing is done, a second measurement  $d_{after}$  is performed. RID is then defined by the following equation:

$$RID = \frac{d_{before} - d_{after}}{d_{before}} \quad (1.18)$$

The remaining indentation depth should result from plastic flow or residual elastic strain in or outside the plastic zone. However, the reliability of this experimental technique will be discussed

and questioned in the section 3.5.1.

On the other hand, an alternative and novel approach to characterize densification under indentation in silica glass is the chemical dissolution technique. This method, as described by Guin *et al.* [90], leverages the increased dissolution rate of densified zones compared to non-densified regions in a controlled chemical environment. Specifically, the technique involves immersing an indented silica glass sample in a NaOH solution, where the densified material beneath the indentation dissolves at a faster rate than the surrounding non-densified glass. This method provides a high spatial resolution, capable of detecting nanometer-scale changes in the residual imprint's geometry using Atomic Force Microscopy (AFM). By periodically measuring the dissolution depth of the indent, it is possible to determine the size and homogeneity of the densified zone. The dissolution rate of the glass in its pristine state is first established using an indent-free sample. Then, the evolution of the imprint depth is monitored over time to map the densified region's boundary. Finally, the chemical dissolution technique, combined with AFM imaging, provides a robust and sensitive method for characterizing densification in silica glass.

### 1.2.3.c Shear flow

In silicate glasses subjected to indentation testing, shear flow emerges as another plastic deformation mechanism alongside densification. Such shear flow is actually the standard plastic deformation process, which operates at constant density, for example in metals. In glasses, this flow involves the disruption and reformation of the network, and we can expect that it is influenced by the presence of network modifiers such as sodium or calcium. These modifiers break the continuity of the silica network, reducing its overall rigidity and allowing for greater atomic mobility under stress.

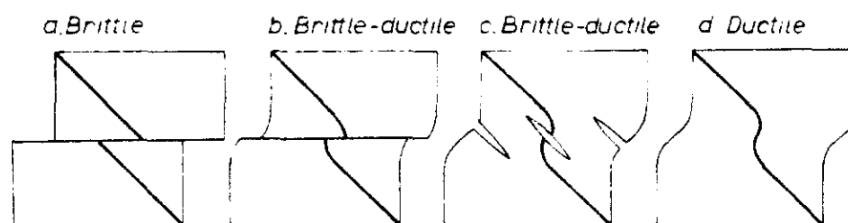


FIGURE 1.15: Types of shear zones (taken from [91])

Although shear flow can be homogeneous, as in many metals or polymers, in glasses it is often microscopically manifested through the formation of shear bands [1, 92]. These bands are zones where the glass material has undergone a large shear flow locally. Shear bands manifest themselves as thin lines or striations that appear around the indent, in the plastic deformation "hemisphere". They are indicative of the material's response by localized strain, where the glass network has yielded and flowed plastically. By increasing the load, these shear bands generally turn into shear faults but the difference between them is not always clear. In the literature, it is said that shear bands are localized zones of deformation that may act as precursors to the formation of shear faults. Shear faults, on the other hand, are fractures or planes of slip where relative displacement occurs between adjacent surfaces [93]. The difference between shear bands

and shear faults can be clearly observed in terms of discontinuities where Fig. 1.15.d representing shear bands without discontinuity and Fig. 1.15.a illustrating shear faults with a discontinuity. In chapter 3, we will see that distinguishing between the two is not straightforward in the observations of indentation cross-sections. Therefore, we will uniformly refer to any shear-induced plastic localization as "Shear bands."

The study and observation of shear bands, especially from indent cross sections [1, 94], provide valuable insights into the plastic response of the material. Techniques such as scanning electron microscopy (SEM) are commonly employed to visualize these deformations. SEM images reveal the detailed structure of shear bands, showing how the glass accommodates shear flow at the microscopic level. As is obvious from Fig. 1.16, the shear localization pattern under indentation strongly depends on the glass composition. Soda-lime silicate glass tends to exhibit bigger shear bands that have turned into shear faults than calcio-aluminoborosilicate glasses with high boron content which contain very thin and dense shear bands.

However, the formation of shear bands in silicate glasses and their relation to cracking resistance (section 1.2.4.b) are not fully understood yet. Gross *et al.* highlighted that the density and characteristics of shear bands are greatly influenced by the glass composition. For example, soda lime silica glass, which contains a significant number of non-bridging oxygens (NBOs), tends to develop well-defined shear faults (Fig. 1.16.a)) with substantial spacing between them. This contrasts with glasses that have fewer NBOs, like certain calcium aluminoborosilicates, where shear bands are less pronounced and denser by increasing boron content (Fig. 1.16.b, c, and d). However, the correlation between non-bridging oxygens and significant shear bands has not yet been clearly proved.

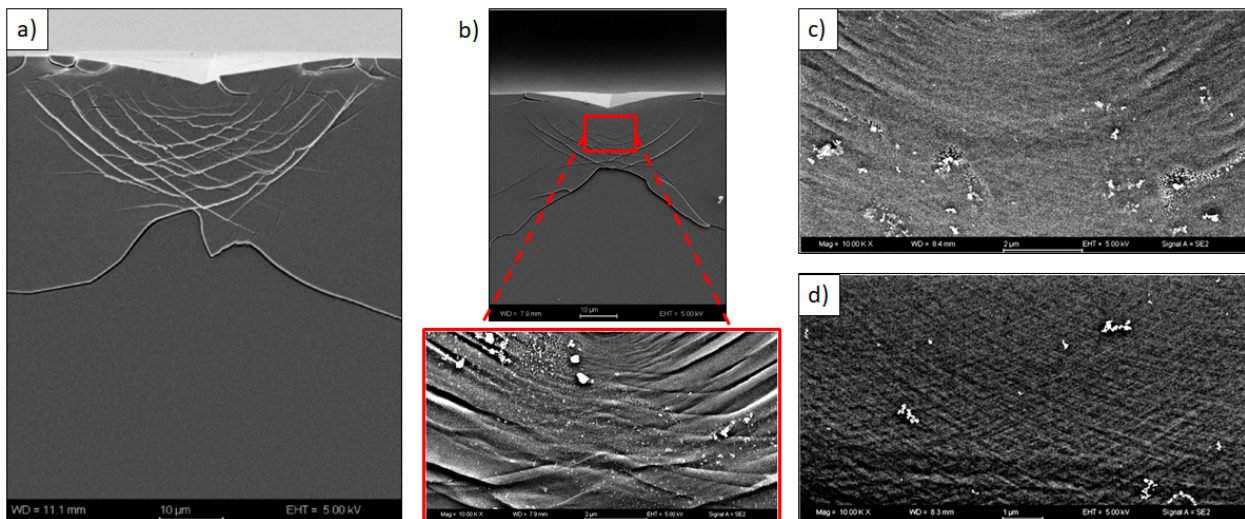


FIGURE 1.16: cross-section view of Vickers indentations in (a) soda-lime-silica glass and calcio-aluminoborosilicate glasses with (b) 5%mol of boron, (c) 15%mol of boron, and (d) 25%mol of boron. (adapted from [94])

The conditions under which indentation testing is conducted also affect the occurrence of shear flow. Factors such as the speed of indentation or the geometry of the indenter (section 1.2.3.f) play critical roles. A sharper indenter and faster indentation speeds are more likely to increase the shear band formation according to [95], as they enhance the shear strain. However, Gross *et al.*

[94] mentioned that shear band formation could have an impact on the driving force for crack initiation, depending on the size or the density of shear localizations, where a plastic deformation zone containing significant shear faulting damage should initiate larger lateral cracks. In oxide glasses, shear flow can manifest as localized shear, where deformation is concentrated in specific regions or zones, leading to significant shear strain that may appear as visible lines or bands where the material has yielded more than in other areas. However, shear flow can also occur more homogeneously, where the material deforms uniformly under shear without distinct bands or lines. This homogeneous deformation is particularly evident during the compression of silica pillars [96]. Furthermore, it is important to consider the continuum of shear band morphologies, which can vary in terms of displacement, thickness, and density. In some cases, these shear bands may be very thin and densely packed, only becoming visible at smaller scales, as shown in Fig. 1.15.d.

### 1.2.3.d Role of Poisson ratio

The contribution of densification to indentation deformation varies depending on the chemical composition of the glass. In particular, an interesting observation is a correlation between the Poisson ratio  $\nu$  and densification ability obtained either from the volume recovery ratio ( $VR$ ) measurement [59] or from the maximum density change measured by Raman spectroscopy [97].

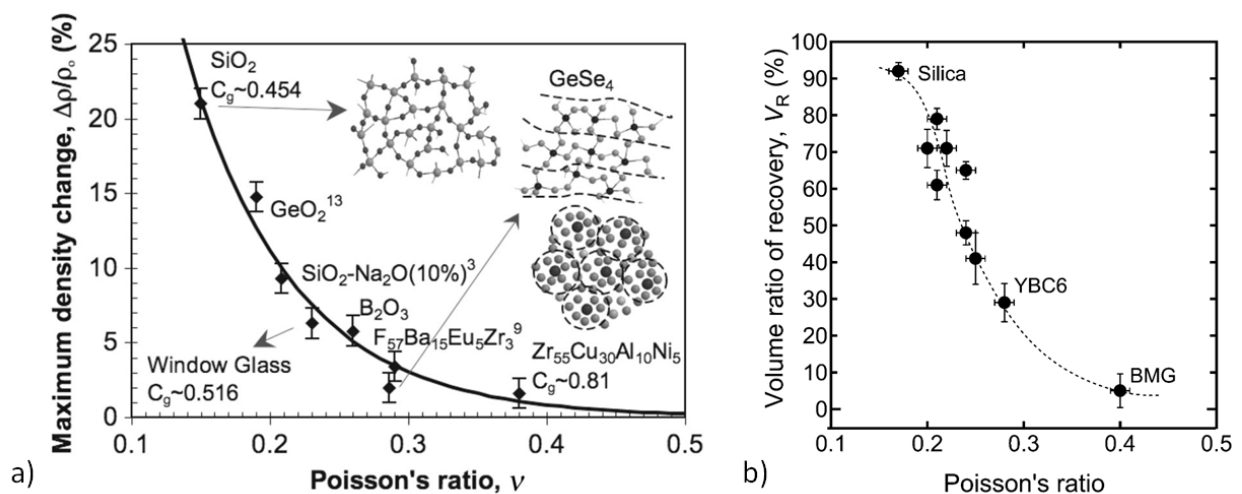


FIGURE 1.17: (a) Maximum density change and (b) volume recovery ratio as a function of Poisson ratio for several glass compositions. The solid line on the left is a fit expressed in [97] and the dashed line on the right is a guide for eyes [59].

Fig. 1.17 shows that the higher  $\nu$ , the smaller the densification. Indeed, Poisson ratio is proposed to be strongly dependent on the glass atomic network organization. For instance, after thermal annealing, amorphous silica recovers more than 90% of its deformed volume under indentation (Fig. 1.17.b) since its rather open structure (low packing density  $C_g$  or  $V_t$ , cf section 1.1.1.b) leads to a strong resistance toward contraction in the transverse direction. Accordingly, silica glass exhibits a low Poisson ratio. On the other hand, higher values of  $\nu$ , which are known to be linked to higher atomic packing densities [98], lead to increased resistance to volume shrinkage. When modifiers are added to the glass network, such as in soda lime silica glass where  $VR$  is about

60% against 90% for amorphous silica, the network connectivity degree decreases, and the atomic packing density increases. Densification is lower and  $\nu$  higher (Fig 1.17.a).

### 1.2.3.e Role of the glass composition

As already mentioned in the previous sections, the chemical composition plays an important role in determining the mechanism acting on plastic deformation. Both glass formers and modifiers can generate different mechanical properties and lead to different plastic mechanisms. The first part of this section will deal with the effect on densification and shear flow of the substitution of a glass former by another. The second part will deal with the impact of network modifiers.

First, the substitution of silica by boron particularly influences the densification. Kato *et al.* [88] investigated the compositional dependence of deformation mechanisms in borosilicate glasses, focusing particularly on how these compositions influence densification during indentation. They discovered that the recovery of indentation depth (*RID*), is highly sensitive to variations in composition. Several studies have also shown that boron coordination tends to increase from trigonal to tetrahedral in glass composition with a significant amount of modifiers (and therefore of NBOs) when pressure increases with an increasing density [99, 100, 101]. Moreover, when the field strength of the modifier cation is relatively large, structural changes with pressure can be as large in low NBO glasses as in NBO-rich compositions since the formation of NBO is promoted by higher field strength [99, 102]. Thus, this densification-induced structural change should occur during indentation. Finally, when silica is fully replaced by boron, a borate glass, such as sodium borate glasses, is obtained. These compositions have also been investigated by Raman spectroscopy and it has been shown that the densification mechanism differs markedly from silicate glasses [103]. Raman studies show changes in the intensity and width of bands associated with boroxol and  $\text{BO}_4$ -containing rings, suggesting a transformation of borate structures under pressure. These structural changes indicate a shift towards higher coordination of boron, highlighting a fundamental difference in how borate and silicate glasses respond to mechanical stress.

Concerning the impact of modifiers, the accepted picture is that glasses with high concentrations of network-modifying oxides tend to deform through shear flow, whereas those with lower concentrations primarily deform through densification. More particularly, the excess modifiers create non-bridging oxygens (NBOs) and form weaker, less directional, ionic bonds within the glass network, which have been proposed as initiation sites for shear deformation [69, 1, 68]. Additionally, the modified random network model suggests that these NBO-forming modifiers align along percolation channels [104], and this alignment of weaker bonds along these channels facilitates the formation of shear faults. For instance, some investigation into  $x\text{Na}_2\text{O}\cdot(100-x)\cdot\text{B}_2\text{O}_3$  glasses showed that at high modifiers concentrations, the formation of non-bridging oxygens (NBOs) enables more pronounced shear, and lowers the volume recovery ratio *VR* [103]. It means a more depolymerized glass will tend to deform through shear flow at a lower stress. This has been further supported by quantitative analyses and molecular dynamic simulations [105].

Additionally, depending on the glass composition and glass formers, the mixed modifier effect may occur when several modifiers are included in the structure. It refers to the nonlinear variations of glass properties when mixing different types of modifier ions [106, 107]. The effect plays an important role since it can be applied to design glasses with controlled properties. The impact of this effect on deformation mechanisms in aluminosilicate glasses was also investigated by Kjeldsen *et al.* [108, 109], showing that around the composition with an equal molar concentration between the two modifiers, densification is minimum. Moreover, the amount of shear flow varies significantly depending on the relative ratio of modifiers.

On the other hand, the formation of shear bands is significantly impacted when the glass network is fully connected, meaning it contains no non-bridging oxygens (NBOs). This increased connectivity gives the glass greater resistance to shear deformation because there are no weak bonds or fragile areas where deformation could easily concentrate. In such a connected network, shear is less likely to localize into distinct regions, reducing the formation of well-defined shear bands. Instead, the glass may exhibit more homogeneous deformation or shear distributed over a larger area, without the development of significant shear faults [94].

All these findings underscore the complex interplay between glass composition, structural organization, and mechanical properties, illustrating that predicting the mechanical behavior of glass based on composition requires a nuanced understanding of its structural chemistry.

#### 1.2.3.f Role of the indenter geometry

During indentation tests, the indent geometry, particularly the shape and sharpness of the tip, plays a crucial role in determining how the glass will deform under applied pressure, influencing the stress distribution beneath. For instance, it will be reflected in the blister field  $B$  introduced by Yoffe [62] (sec. 1.2.2).

When using a sharp indenter, such as a Vickers or a cube corner, the stress distribution promotes shear flow as the primary deformation mechanism [69]. Indeed, Lee *et al.* [110] explained that the characteristic indentation strain is proportional to  $\tan^{-1}(\beta)$ , where  $\beta$  represents the half-included angle. In the stress-strain curve, a larger strain value indicates a deeper excursion into the plastic regime. Conversely, using a blunter indenter, like a spherical tip, for example, results in low characteristic strain but tends to increase pressure, favoring densification rather than shear flow [111]. Different indenter geometries don't affect only the predominant deformation mode but also affect other related properties such as crack initiation and propagation. For instance, sharper indenters, while promoting shear flow, may also lead to more pronounced and immediate cracking patterns. Furthermore, since indenters such as Vickers or conical indenters are self-similar, the size of the shear deformation zone only depends on the applied load. On the other hand, blunter indenters might lead to fewer and less severe cracks due to the more distributed stress, which allows the glass to densify and absorb some of the impact energy more effectively.

The geometry of the indenter is eventually a critical factor in assessing the mechanical response of glass during indentation tests, influencing whether shear flow or densification will dominate as the primary deformation mechanism and it will play a significant role in the cracking process.

## 1.2.4 Indentation cracking

### 1.2.4.a Cracking morphology

Depending on the glass composition and the indenter geometry, different indentation cracking patterns can be found in oxide glasses. Most of them are shown in Fig. 1.18. Arora *et al.* [112] observed that the cracking pattern of one given glass composition is directly related to its normal or anomalous behavior. For instance, amorphous silica, which is known as an anomalous glass, mostly displays ring cracks and cone cracks (Fig. 1.18.e) under a sharp Vickers indenter [113]. In contrast, window glass (soda-lime silicate glass) exhibits radial/median cracks from the corners and lateral cracks below the plastic deformation zone of the indentation [114].

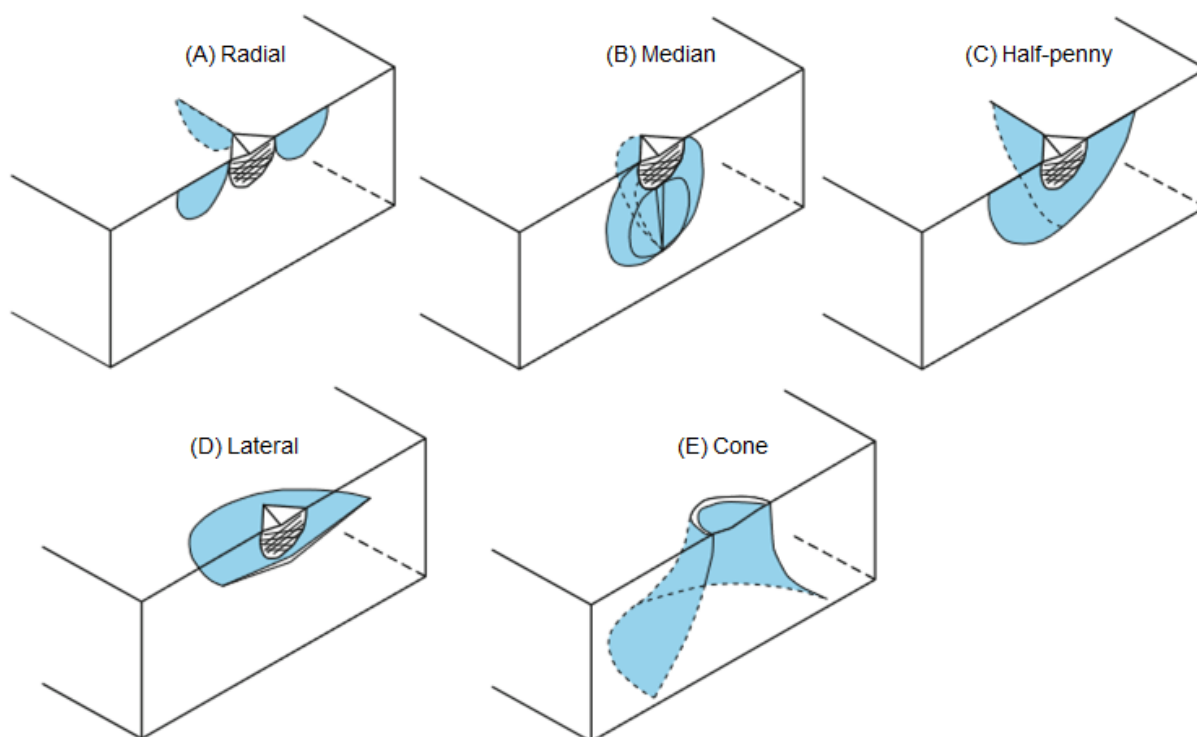


FIGURE 1.18: Schematic sections of crack morphologies from indentations: (a) radial crack, (b) median cracks, (c) half-penny cracks, (d) lateral crack, (e) cone crack and associated ring crack (taken from [115] and adapted from [116]).

The normal or anomalous feature of glass and its impact on crack morphologies is also identified by looking at the Vickers indentation cross-section of a soda-lime silicate glass or an amorphous silica glass (Fig. 1.19). It appears that the subsurface damage in normal glass is more likely to be linked to shear flow, resulting in radial or median cracks. Conversely, anomalous glasses tend to deform more homogeneously, through densification, and generate ring or cone cracks [112, 117].

The moment when a crack initiates in glass upon indentation is also different depending on the normal or anomalous feature. Cook and Pharr [116] recorded and marked on load-displacement curves cracks nucleating upon indentation (Fig. 1.20) and they noticed that radial/median cracks in normal glasses tend to initiate upon unloading. In contrast, ring/cone cracks, in anomalous

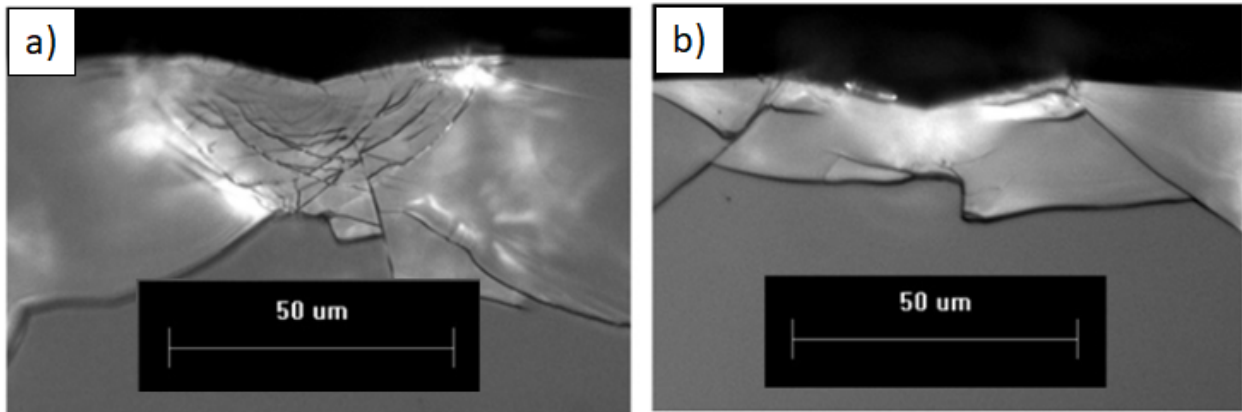


FIGURE 1.19: Cross sectional view of 1 kgf Vickers indentation in (a) soda lime silicate and (b) silica (adapted from [117]).

glasses, nucleate upon loading. However, during unloading in silica, additional radial and lateral cracks appear afterward.

The accepted picture follows Yoffe [62] (sec. 1.2.2) who explains that the cracking pattern during the indentation of brittle materials is significantly influenced by the value of the blister field  $B$  (see section 1.2.2) which is proportional to the extra volume maintained within the deformed zone. This volume is reduced by densification or by using a larger indenter angle. When  $B$  is small, typical for highly densifying materials, such as amorphous silica glass, or those indented by large-angle indenters (or equivalent, such as a spherical indenter for example), the highest tensile stress occurs at the surface, leading to ring and cone cracks near the contact edge. As  $B$  increases, due to less densification or a more pointed indenter, the axial tensile stress becomes dominant, shifting the crack formation to median cracks beneath the surface. For even higher  $B$  values, the axial stress decreases, but circumferential surface stress increases, causing radial cracks. After unloading, these stresses can cause lateral cracks beneath the indentation and upward propagation of median or radial cracks.

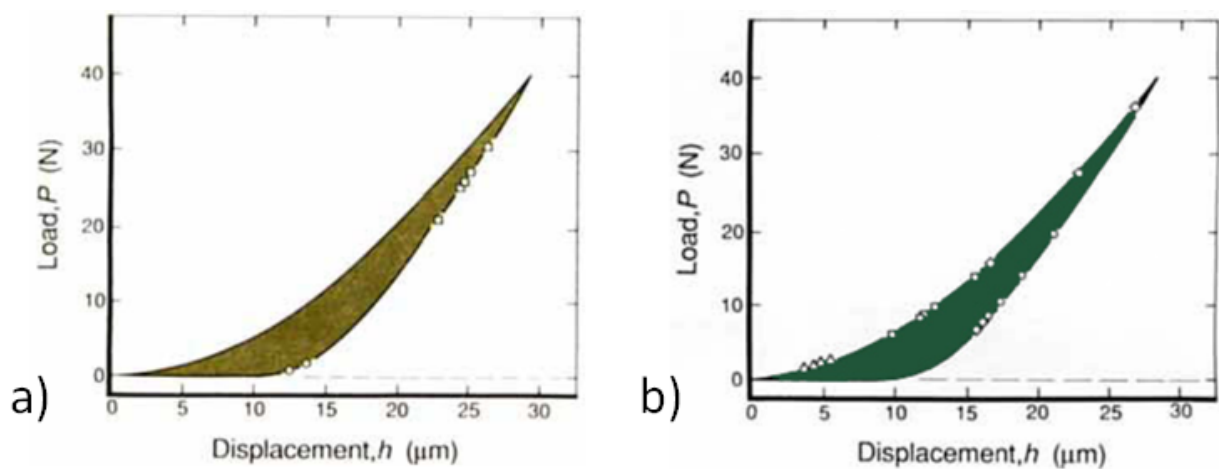


FIGURE 1.20: Load-displacement curves for Vickers indentation of (a) soda-lime silicate glass and (b) fused silica. Markers represent cracks nucleation (adapted from [116]).

In a refinement of this approach, Sellapan *et al.* [118] proposed a way to evaluate the strength of the blister field in the context of Vickers indentation. They define  $B$  as

$$B = \frac{3E}{4\pi(1+\nu)(1-2\nu)}(1 - V_R - V_P)V_i^- \quad (1.19)$$

where  $E$  is Young's modulus,  $\nu$  is the Poisson ratio,  $V_R$  is the volume recovery ratio from sub- $T_g$  annealing (sec. 1.2.3.b),  $V_P$  is the proportion of material pile-up, and  $V_i^-$  is the volume of the indentation cavity. Measurements of  $V_R$ ,  $V_P$ , and  $V_i^-$  are detailed in [59]. For example, we have seen (Fig. 1.17.b) that the volume recovery for silica is about 90%, which means that the term  $(1 - V_R - V_P)$  governing the blister field strength is low and induces a small  $B$ , leading to conical or ring crack patterns as described previously. However, this model, which is obviously approximate, has been developed for Vickers indentation. Thus, one drawback of this Blister field approach is the lack of a method to quantitatively assess its strength for other indenter geometries.

#### 1.2.4.b Crack resistance

Indentation has been largely used to assess the ability of glass to resist cracking. Wada *et al.* proposed a method to measure the crack resistance of glasses that display radial cracks from Vickers indentation [119]. Several Vickers indentations are performed at increasing load and the number of radial cracks emanating from the corners of the residual imprints are counted. Then, the probability of crack initiation ( $PCI$ ) is defined as the ratio between the number of corners where a crack was formed and the total number of corners (4 for a Vickers indentation). The crack resistance is defined as the load corresponding to 50% of  $PCI$  (Fig. 1.21.a).

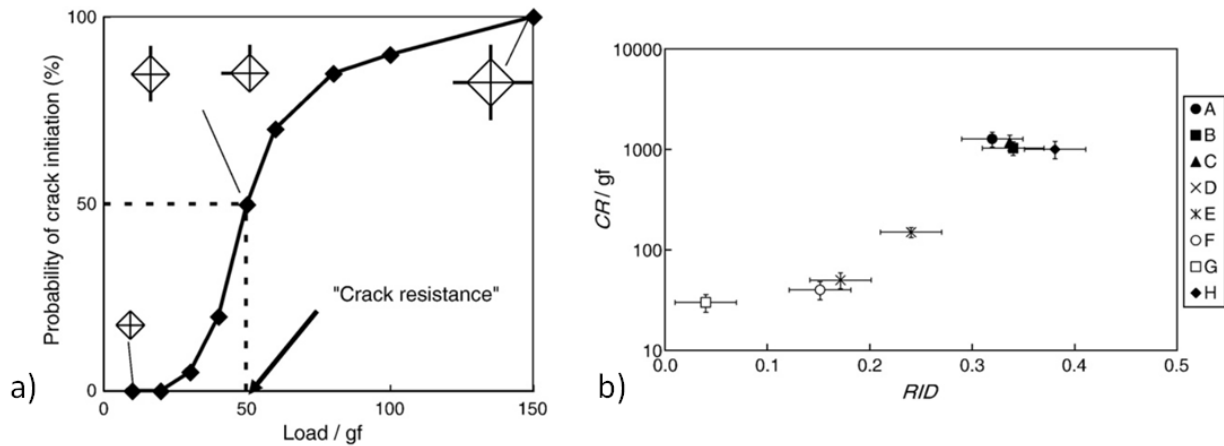


FIGURE 1.21: (a) Schematic of the measurement of crack resistance and (b) Relationship between  $CR$  and the recovery of indentation depth ( $RID$ ) for several compositions presented in Table 1.3 (taken from [87])

Important  $CR$  results were obtained by Kato *et al.* [87] who investigated several series of glass compositions, shown in Table 1.3. They found that crack resistance varies over nearly 2 decades, although, as we mentioned at the beginning of section 1.2.1 all glasses otherwise display more or less the same standard mechanical properties including eg Young's modulus, hardness, and

fracture toughness. To understand this puzzling observation, more arcane variables have been invoked. Notably, following the idea that densification reduces the blister field, and hence cracking, attention has been caught by densification, and its correlation with Poisson's ratio. Since it is expected  $RID$  somehow reflects densification, a correlation has been looked for, and found, between  $RID$  and  $CR$  (Fig. 1.21.b). However, this correlation does not hold for every system [88, 64]. Other parameters must be interrogated. For example, a relation between crack resistance and shear flow has not been investigated yet.

TABLE 1.3: Glass compositions studied by Kato *et al.* [87] and their properties.

Name	General composition (mol%)	$\rho$ (g/cm <sup>3</sup> )	$T_g$ (°C)	$K_{Ic}$ (MPa·m <sup>1/2</sup> )	$E$ (GPa)	$K$ (GPa)
A	70SiO <sub>2</sub> - 20B <sub>2</sub> O <sub>3</sub> - 5K <sub>2</sub> O	2.28	500	0.73	64	40
B	75SiO <sub>2</sub> - 10B <sub>2</sub> O <sub>3</sub> - 5Na <sub>2</sub> O	2.36	570	0.76	71	37
C	70SiO <sub>2</sub> - 10Al <sub>2</sub> O <sub>3</sub> - 10B <sub>2</sub> O <sub>3</sub>	2.48	710	0.79	70	40
D	70SiO <sub>2</sub> - 10Na <sub>2</sub> O - 10CaO	2.49	540	0.75	72	47
E	70SiO <sub>2</sub> - 10Na <sub>2</sub> O - 5SrO	2.76	520	0.71	68	40
F	70SiO <sub>2</sub> - 5SrO - 5K <sub>2</sub> O	2.81	630	0.73	77	43
G	60SiO <sub>2</sub> - 25PbO - 5B <sub>2</sub> O <sub>3</sub>	4.44	470	0.66	63	44
H	70SiO <sub>2</sub> - 15Al <sub>2</sub> O <sub>3</sub> - 10Li <sub>2</sub> O	2.43	710	0.84	81	39

Despite its apparent simplicity,  $CR$  is a difficult measurement. For example, we can notice that  $CR$  can not be defined for an anomalous glass, like silica, which mainly exhibits cone cracks and generally no radial cracks, at least under Vickers indentation. However, a first approximation of the crack resistance of silica can be made if the indentation is performed under an inert environment (Fig. 1.22) to avoid stress corrosion, detailed in section 1.1.3.a).

Indeed, Gross *et al.* [92] have shown that silica exhibits residual Vickers imprints of 1kgf load without cracking under dry N<sub>2</sub> atmosphere, which means its crack resistance should be at least 1 kgf  $\approx$  10N in the conditions used during this test. This result shows that the stress corrosion (section 1.1.3.a) plays a role in the measurement of the crack resistance, especially for pure amorphous silica. To compare anomalous glasses with normal glasses, experiments under an inert environment should be performed and the radial cracks should be counted under the same atmosphere as during the indentation. It is important to keep in mind that the crack resistance measurement reflects both experimental conditions and the glass characteristics. It is therefore difficult to compare the crack resistance values obtained from different studies since the experimental conditions (loading rate, relative humidity, temperature, etc...) and the time elapsed before counting the radial cracks are not necessarily the same [120].

### 1.2.5 Constitutive relations and other numerical models developed for oxide glasses

Januchta and Smedskjaer [64] point to difficulties with the use of Yoffe's stress field calculations [62]. The strength of the approach is that it is analytical, but it lacks parameters that quantify the material's resistance to crack propagation (sec. 1.1.3). As a result, although these calculations can

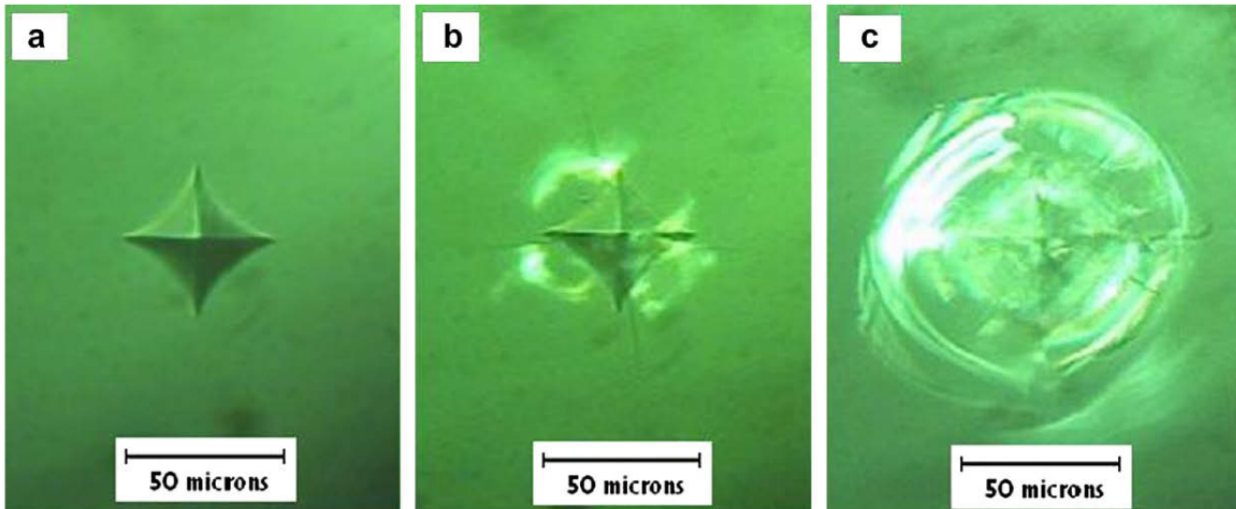


FIGURE 1.22: 1 kgf load Vickers indentation under (a) dry nitrogen atmosphere and kept in the same environment, (b) dry nitrogen atmosphere and then moved into air atmosphere, and (c) air atmosphere (taken from [92]).

predict characteristic cracking patterns, they have limited composition- or property-dependent predictive power. In addition, Yoffe's model is only an approximation and its accuracy has not been assessed. To address these limitations, some works have developed more quantitative models with continuum scale descriptions aimed at predicted indentation stress fields using finite element simulations.

In parallel, molecular dynamics enable a more detailed description of material mechanics by considering atomic-scale deformation mechanisms. These models offer better insights into energy dissipation and crack resistance by accounting for intrinsic material properties, such as chemical composition and bond strength, which significantly influence resistance to indentation-induced fractures. Interestingly, they can be used to work out constitutive relations for the continuum scale calculations.

### 1.2.5.a Constitutive relations

Faced with this unconventional plastic deformation, the issue of measuring it correctly, and the need for stress fields to understand fracture generation and propagation in glasses, alternative strategies were developed. One solution is to use numerical calculations as a more elaborate tool than Yoffe's equation, which encapsulates all the plastic effects in the single parameter  $B$ , to establish the stress field. To run these simulations, it is important to identify an appropriate constitutive law to account for the material response to mechanical tests, such as indentation, and get as close as possible to the deformation mechanisms in silicate glasses. Yield criteria such as Von Mises criterion, Mohr-Coulomb criterion, or Drucker-Prager criterion have been largely employed to describe indentation deformation in multiple studies such as in porous material by Shima and Oyane [121] or such as frictional materials by Khan *et al.* [122]. One relevant constitutive model has been developed by Kermouche *et al.* [123], drawing inspiration from the models previously described [124], and has been tested over the last decade. This model assumes linear isotropic elasticity characterized by Young's modulus and Poisson's ratio. Plastic strain is initiated by an

elliptical criterion dependent on hydrostatic pressure and shear stress. This criterion involves the flow stress  $\tau_c$  (or uniaxial Mises stress), which triggers plastic shear flow, and the volumetric yield stress or yield pressure  $p_c$ , marking the onset of densification under hydrostatic compression. Thus, the proposed yield criterion is:

$$f(\sigma_{ij}) = \left(\frac{\tau}{\tau_c}\right)^2 + \left(\frac{p}{p_c}\right)^2 - 1 \quad (1.20)$$

As Fig. 1.23.a shows, following the DAC data (Fig.1.13 b),  $p_c$  increases with density until reaching a saturation point, without any hardening or softening for the shear flow with a constant  $\tau_c$ . The partition of plastic strain between densification and shear flow depends on the loading state through the orientation of the normal to the yield surface (associated plasticity). The key parameters in this model are Young's modulus, the flow stress, and the yield pressure and its relationship to material density. Finally, regarding negative pressure, a simple Von Mises criterion is assumed. This model has been experimentally validated for pure amorphous silica [96] with various micromechanics experiments including micropillar compression. The same model has also been applied to other glass compositions, but there is less experimental validation available and we assume it only gives a first approximation of the mechanical response.

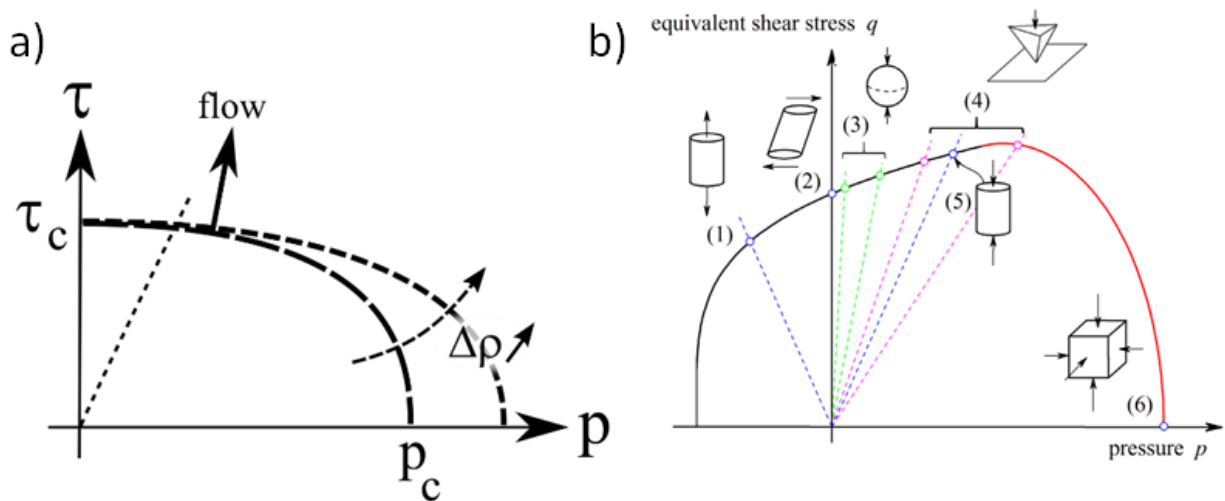


FIGURE 1.23: (a) Elliptic yield criterion for the plastic response of silicate glasses (The dashed straight line represents uniaxial compression)[123, 125] and (b) elliptic yield criterion extended with Drucker-Prager function with different set of possible experiments reported on it [126].

A few years later, Molnár *et al.* [126] proposed an evolution of the yield surface of the Kermouche's model. Instead of assuming a Von Mises criterion for the tensile side (negative pressure), the yield surface is modeled by an extended Drucker–Prager model (Fig. 1.23.b). A strong limitation in practice is that there are no real tensile testing results available. But, once again, this model is specifically developed for pure amorphous silica. However, we expect it could be easily extended to other compositions in the future. The main issue with other glass compositions is the calibration (on ad hoc experiments) and their validations (on other experiments) for those other compositions, which will require extensive experimental work.

### 1.2.5.b Finite Element Analysis (FEA) to understand indentation of glasses

Once a constitutive model has been defined, it can be implemented in finite element software (such as ABAQUS®). For instance, calculations have been performed using an axisymmetric simulation to model cone indentation with Kermouche's model, and the densification map resulting from this analysis is plotted in Fig. 1.24 next to the experimental data from [75], derived from Raman mappings of the D2 band position (sec. 1.2.3.a) and presented as a densification map (Fig. 1.24).

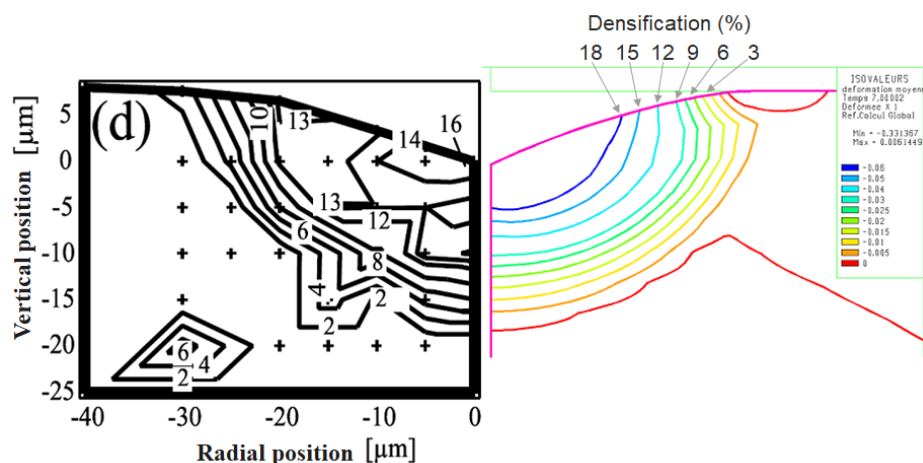


FIGURE 1.24: (Left) Raman densification map of Vickers indentation in pure amorphous silica (from [75]). (Right) Densification map from FEA simulation (adapted from [123]).

This figure displays a good agreement between experiments and simulations. Thus, the indentation-induced densification process of silica was considered to be successfully reproduced by the constitutive model. However, more recent experimental works, using techniques such as chemical dissolution [90, 127] (see section 1.2.3.b) or Brillouin spectroscopy [128] to probe the densified region underneath an indentation imprint in silica glass, have shown that the maximum densification (Brillouin method) or the densification ratio along the depth of the indent (chemical dissolution technique), seem to differ from the results shown in Fig. 1.24, with a much sharper gradient. These results can be used to provide a new set of data for improving the previous numerical models or developing new ones to simulate glass indentation.

On the other hand, FEA simulation can also be a good method to verify whether analytical models, such as the Yoffe model [62] (see section 1.2.2), are consistent with experimental evidence. Indeed, Davis *et al.* [129] used FEA simulation with both Kermouche's [123] and Molnar's models [126] to compare the stress fields generated by FEA with the analytical solutions from Yoffe [62]. They found that Yoffe's model is not completely suitable for calculating crack driving stresses at the elastic-plastic boundary in silicate glass sharp indentation. It is actually not possible to use a single tunable parameter (blister field coefficient  $B$ ) to account for the FEA predictions. Since the constitutive models have shown their reliability against many micro-mechanics experiments (nanoindentation, DAC, and pillar compression - and of course the predicted stress distributions align closely with the crack patterns appearing under indentation), they can also be used to evaluate the impact of more clearly defined parameters (densification threshold, densification saturation, shear flow stress, Young's modulus) on indentation-induced stress fields. As we described

in previous sections, densification has been largely proposed to play a significant role in indentation response. However, Barthel *et al.* [125] have shown, based on Kermouche's constitutive relation, that the contribution of the latter has been overrated. They calculated stress fields and modified both densification and shear flow stress (Fig. 1.25) and they demonstrated that changing densification at saturation doesn't impact noticeably the overall stress level. In contrast, when the flow stress is lower, the general stress level decreases significantly, as required by the notion of hardness (section 1.1.1.a).

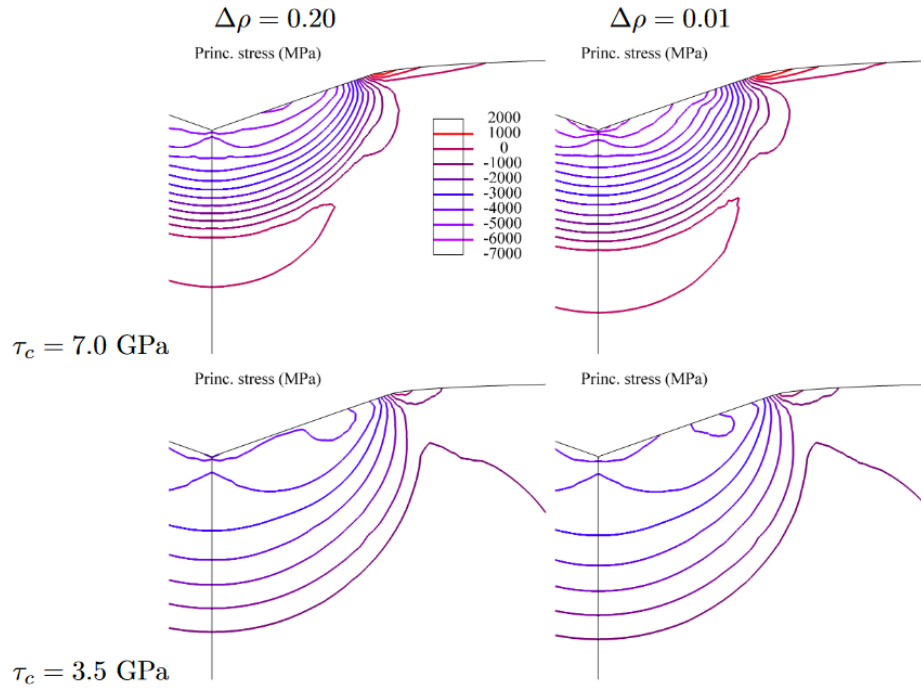


FIGURE 1.25: Maximum principal stress distribution for a Vickers equivalent cone indentation under load with two conditions of flow stress  $\tau_c$  and densification at saturation  $\Delta\rho_{sat}$  (taken from [125]).

Based on these results, it was concluded that flow stress is the determining parameter for indentation response and crack driving stresses. By the way, it seems this idea had already been mentioned by Marsh fifty years ago [54] but has largely been discounted in the glass mechanics community. Finally, if the shear flow is the main factor, the material damage resulting from plastic shear flow, and especially instabilities like shear localizations, might play a role in crack initiation [1]. However, these shear localizations have not been investigated yet with the FEA method since they are difficult to implement. Indeed, there is currently no FEA model able to account for localized shear flow. Therefore, to deepen this idea, calculations of mechanical tests that we do not know how to perform experimentally have to be carried out with another method that can model local instabilities: Molecular Dynamics simulations.

### 1.2.5.c Molecular dynamics simulations

Molecular dynamics (MD) simulations provide a method to investigate material behaviors at an atomic level, predicting properties based on their composition and structure. In this approach,

atoms are modeled as point masses interacting through complex nonlinear forces, which mimic atomic bonds. The evolution of the system is governed by classical dynamics principles (Newton's laws), with added controls for temperature or pressure via thermostats or barostats. Due to computational limitations, especially the number of operations executable within a given time, these simulations typically cover only a few nanoseconds for a million atoms, representing a sub-micrometer sample size.

To probe mechanical responses, simple deformations are imposed on the sample, enabling analysis of stress and displacement from macro to atomic scales. This method is particularly interesting for amorphous materials since they do not have long-range order or rather intermediate lengthscales (eg dislocation in metals). In that way, representative results on the mechanical response of the material can be obtained by only investigating sub-micrometer samples. For instance, Mantisi *et al.* [130] have performed loading-unloading simulations on an amorphous sample of a few micrometers with increasing pressure. They plotted the results in a Von Mises vs hydrostatic pressure (Fig. 1.26) and they obtained a parabolic yield surface, which can be fitted with a simple buckling model proposed by Lambropoulos *et al.* [124], and also compared to the elliptical model proposed by Kermouche *et al.* [123] (sec. 1.2.5.a). It differs from Kermouche's model in the vicinity of pure shear loading with much higher flow stress exceeding the 7.5 GPa threshold for silica, experimentally validated [131], and a finite slope. However, the two models agree on the general shape of the yield surface and the yield pressure around 10 GPa.

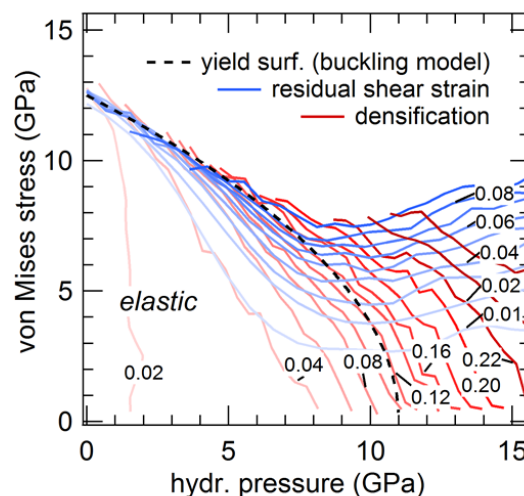


FIGURE 1.26: Distribution of residual volumetric strain (densification) and residual shear strain as a function of hydrostatic pressure and Von Mises stress. This map delineates a yield surface with strain hardening due to densification [130].

Moreover, compared to finite element simulations, this method also identifies local structural rearrangements, offering direct insight into the deformation processes at the atomic level which we will cover in more detail in Chapter 2. For example, in the same paper, Mantisi *et al.* [130] have shown the effect of pressure on the nature of the plastic rearrangements in the structure (Fig. 1.27). Under low or zero pressure, large plastic events occur whereas they become smaller and less heterogeneously distributed when pressure increases, allowing for a much more homogeneous deformation. The pressure effect on local deformation has also been investigated with

MD simulations by Molnar *et al.* [132] in soda silicate glasses and by Lee *et al.* [133] in borosilicate glasses with about 10% of cation modifiers. They found that ion modifiers have higher mobility in the structure during plastic deformation than glass formers and should play a significant role in local plastic rearrangements (see sec. 1.2.3.e). Moreover, they observed a shear-induced densification in all their compositions. However, at higher pressures, the difference between a composition with low and high network modifiers content vanishes. Eventually, the plasticity is accompanied by more homogeneous atom rearrangements. In conclusion, Molecular Dynamics should significantly help to compare with experimental results where both densification and shear flow can occur depending on the mechanical test performed. Nonetheless, results are strongly influenced by the numerical parameters of the material model, and an accurate representation of different types of silicate glasses remains challenging to this day.

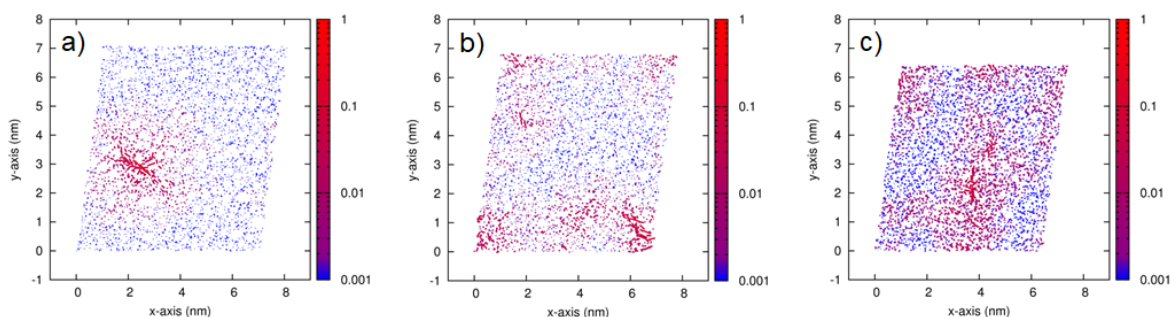


FIGURE 1.27: Maps of typical non-affine displacement fields taken at 7.5% shear strain for hydrostatic pressures equal to (a) 0 GPa, (b) 5 GPa, and (c) 10 GPa with  $N = 24,000$  particles (taken from [130]).

#### Short summary of the chapter

- Two mechanisms concomitantly govern the plastic deformation under indentation in silicate glasses: densification and shear flow. Their mutual contributions have been measured and discussed for a long time but the question is still open.
- Constitutive relations developed in recent years provide predictions at the continuum length-scale but they still have to be improved and calibrated. Both experiments and numerical calculations can be useful.
- The atomic-scale mechanisms that rule the plasticity of silicate glasses are still elusive. We will provide new insight based on quasi-static dynamic measurements which bring an original viewpoint in chapter 2.
- The relationship between densification and resistance to crack initiation has often been mentioned and measured, but it is still open to questions. In particular, recent FEA modeling has claimed that indentation cracking is preferentially directed by the shear flow instead of densification.
- The correlation between shear flow and crack resistance has not yet been investigated in depth. A first correlation will be brought in chapter 3.

## Conclusion

This chapter has highlighted the intricate interplay between plasticity and fracture in oxide glasses.

At the macroscopic scale, this chapter has emphasized the role that plastic deformation plays in controlling the stress fields that drive crack formation. The plastically deformed zone governs the stress distribution around indentations and, consequently, the initiation and propagation of cracks. The composition of glass and the geometry of the indenter significantly affect how plastic flow occurs, with different compositions showing varying tendencies towards densification or shear flow. While correlations with Poisson's ratio and the Recovery of Indentation Depth *RID* have provided some understanding of the role of densification, they remain far from comprehensive.

At the atomic scale, the significant difference between fracture energy and surface energy serves as evidence of plastic deformation in oxide glasses. The excess energy is dissipated through plastic processes such as shear flow, confirming that these materials, though traditionally considered brittle, do undergo plastic deformation even at this very local scale level. Moreover, the detailed mechanics of shear band formation, which play a crucial role in the shear flow of glasses, has often been neglected in existing models. A more profound understanding of these shear bands is essential, particularly to better understand their relation to the overall crack resistance of glasses. Advanced simulation techniques, such as finite element modeling and molecular dynamics, hold promise for better capturing these localized shear phenomena, potentially offering a more complete picture of how glass densification and shear localization interact under stress. Moving forward, these simulation methods could prove very useful for modeling shear localizations such as shear bands, while simultaneously dealing with glass densification, and enable a deeper and more comprehensive understanding of plasticity in oxide glasses.

However advanced models can be developed only with reference to reliable experimental data. It is to this task that this research work contributes. In a first part (ch. 2), we report original room temperature viscoplasticity measurements on three different silicate glasses. Through the contrasted dynamics, we try to better understand the plasticity mechanisms and how they depend upon the silicate glass structure. In a second part, we provide an in-depth investigation of indentation cracking in an extensive family of borosilicate glasses. We show that the complex deformation patterns observed correlate with indentation cracking and can be accounted for mainly by shear flow.

## Chapter 2

# Effect of irradiation on silicate glass plasticity - In-situ micromechanical testing

### Contents

---

<b>2.1</b>	<b>Material and methods</b> . . . . .	<b>44</b>
<b>2.2</b>	<b>In situ micropillar compression</b> . . . . .	<b>49</b>
2.2.1	Mechanical behavior under irradiation and strain rate sensitivity . . . . .	49
2.2.2	Residual geometry of compressed micropillars with and without electron irradiation . . . . .	51
<b>2.3</b>	<b>Electron irradiation and viscoplastic deformation</b> . . . . .	<b>53</b>
2.3.1	Relaxation tests . . . . .	53
2.3.2	Strain rate description . . . . .	56
2.3.3	Application and comparison with other glass compositions . . . . .	58
<b>2.4</b>	<b>Physical description of the phenomenon</b> . . . . .	<b>59</b>
2.4.1	Glass plasticity and activation model . . . . .	59
2.4.2	Impact of irradiation . . . . .	61
2.4.3	Two relaxation mechanisms: analogy with dynamic measurements . . . . .	63
2.4.4	From strain rate to relaxation . . . . .	65

---

## Introduction

Silicate glasses are traditionally considered brittle, as evidenced by everyday observations. However, at small scales, these materials exhibit ductile behavior [54]. Progress in understanding this ductility through plastic deformation is crucial for reducing the fragility of silicate glasses. The methodological challenge lies in investigating the plastic deformation of silicates at the small scales where ductility is observed. Typically, the brittle-to-ductile transition occurs at the micron scale for amorphous silicates, as explained in section 1.2.1. Early experiments identified phenomenological aspects of irreversible deformation, such as densification and shear flow during sharp indentation, but could not quantify the constitutive relation of the material. Indeed, the main issue with instrumented indentation is that the stress-strain field underneath the indenter is highly complex and depends on the specific indenter tip geometry. For example, the simple uniaxial stress-strain response cannot be predicted from indentation. Experiments with simpler and more controlled loading conditions are required to investigate the yield properties accurately.

Recent advances in the study of plastic response in metals at small scales offer valuable insights: micropillar compression experiments have been proposed as an approximation to uniaxial loading. For amorphous silica, recent micro-compression works have been carried out by Lacroix *et al.* [131] on pillars to investigate precisely the plastic flow of the materials under uniaxial conditions and measure the yield stress. They compared their experimental results with Kermouche's constitutive relation [123] from FEM simulation and found a good agreement.

Traditionally, temperature and strain rate are two key parameters impacting plasticity. However, results on silicate glasses are scarce, because it is generally thought that the effects are weak. Very recently, Widmer *et al.* [134] investigated the impact of the temperature and strain rate on the strength and plasticity of fused silica micropillars. They found that the mechanical behavior shows a non-linear temperature dependence of yield stress and strain rate sensitivities. At 600°C, a significant decrease in yield stress and an increase in strain rate sensitivity were observed.

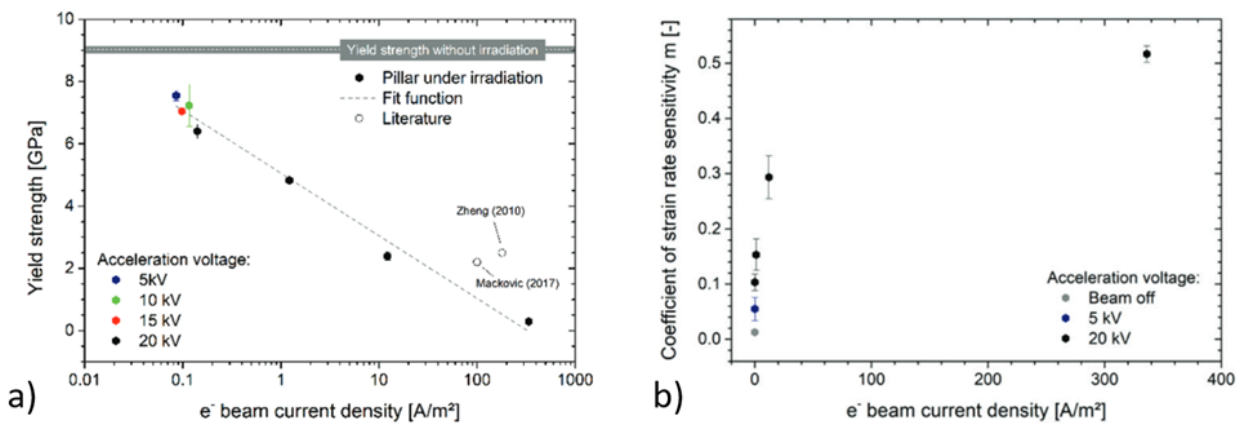


FIGURE 2.1: (a) yield stress as a function of the current density for different acceleration voltage and (b) coefficient of strain rate sensitivity  $m$  upon electron irradiation (taken from [135]).

Recently, significant electron irradiation effects have been evidenced in the microplasticity of silicate glasses [136, 137, 138]. For example, Bruns *et al.* [135] performed micro-compression experiments on amorphous silica but instead of increasing the temperature, they changed the electron

flux that the pillar undergoes in the scanning electron microscope chamber at room temperature. As Fig. 2.1.a shows, electron irradiation decreases the yield stress by roughly 6 GPa in the case of 20 kV. These results are consistent with previous literature [137]. In addition, they investigated the strain rate sensitivity as a function of the current density. They find a remarkable curve (Fig. 2.1.b) but do not provide any physical ground for this evolution.

Based on this paper, we will see how we can further explain what happens during microcompression under electron irradiation. Thus, in this chapter, we will delve into the effects of irradiation on the plasticity of silicate glasses through in-situ micromechanical tests. We will explore the mechanical behavior of the micropillars under varying conditions of irradiation and strain rates. We will discuss the residual geometries of the compressed micropillars with and without electron irradiation, highlighting the effects of irradiation on their structural integrity. As Widmer *et al.* [134] and Bruns *et al.* [135] did, we will perform these tests on pure amorphous silica but also on a soda-lime silicate glass and an aluminoborosilicate glass to evaluate the effect of irradiation on normal glasses, which has not been investigated yet.

Following this, we will investigate the influence of electron irradiation on the dynamics of the plastic deformation of the glasses. This includes a series of tests conducted under different irradiation conditions to observe stress relaxation over time.

Finally, we will try to provide a physical description of the phenomena observed and explain in more detail the remarkable curve from Bruns *et al.* (Fig. 2.1.b). We will discuss the activation model for glass plasticity, which could explain the mechanism during plastic deformation in amorphous materials. The impact of irradiation on these deformation mechanisms is also discussed, particularly how it alters the activation energy and facilitates plastic flow in both anomalous and normal glasses.

## 2.1 Material and methods

### Micropillars manufacturing

#### Glass compositions

Three kinds of glasses produced by Nippon Electric Glass Co.,Ltd were used in this study. Two are commercial glasses: an aluminoborosilicate glass and a soda-lime silicate glass, and the last one is pure amorphous silica. The general compositions of the three glasses are shown in Table 2.1. Some of their basic properties are also displayed in the table.

TABLE 2.1: Glass general compositions and their properties, density ( $\rho$ ), glass transition temperature ( $T_g$ ), fracture toughness ( $K_{IC}$ ), Young's modulus ( $E$ ), and bulk modulus ( $K$ ) (adapted from [89]).

Name	General composition (mol%)	$\rho$ (g/cm <sup>3</sup> )	$T_g$ (°C)	$K_{IC}$ (MPa · m <sup>1/2</sup> )	$E$ (GPa)	$K$ (GPa)
SiO <sub>2</sub>	99.9SiO <sub>2</sub>	2.22	1210	0.7	72	38
ABS	70SiO <sub>2</sub> - 10Al <sub>2</sub> O <sub>3</sub> - 10B <sub>2</sub> O <sub>3</sub> - 10 others	2.48	710	0.79	70	40
SLS	70SiO <sub>2</sub> - 10Na <sub>2</sub> O - 10CaO - 10 others	2.49	540	0.75	72	47

Mole fractions of minor components in glass composition are omitted.

Experimental method and uncertainties are as follows: Density  $\rho$  ( $\pm 0.01 \text{ g/cm}^3$ ) was measured by Archimedes method. Glass transition temperature  $T_g$  ( $\pm 2^\circ\text{C}$ ) was determined by using a dilatometer. Fracture toughness ( $\pm 0.05 \text{ MPa} \cdot \text{m}^{1/2}$ ) was measured by the SEPB method. Young's modulus  $E$  ( $\pm 1 \text{ GPa}$ ) and shear modulus  $G$  ( $\pm 1 \text{ GPa}$ ), were determined by resonance method. Bulk modulus  $K$  ( $\pm 1 \text{ GPa}$ ) was calculated by using the values of  $E$  and  $G$ .

#### Reactive Ion Etching (RIE)

Glass plates of 30 mm x 30 mm x 1.0 mm were prepared which were used as substrate for pillar fabrication. The fabrication was carried out by Gustavo Rosales-Sosa and Yoshinari Kato, from Nippon Electric Glass Co.,Ltd, either at the National Institute of Advanced Industrial Science and Technology (AIST) at Kyoto University for silica or at Kyoto University Nanohub for ABS and SLS glass. The pure silica, soda-lime-silicate, and aluminoborosilicate glass pillars were fabricated by the deposition of a patterned metal film followed by reactive ion etching (RIE) process. Details of the process are different for silica and for the other glasses.

*Silica pillar case:* A photo-resist layer and a lift-off resist (LOR) layer were formed on the surface by spin-coating processes. The photo-resist layer was exposed to a pattern of intense light with a maskless lithography system and a Ni metal layer was deposited on the patterned photo-resist layer surface with an electron beam evaporation system. The LOR layer with Ni layer was removed with a pressure jet lift-off system, to leave an array of circular dots of Ni layer on the plate surface as a mask of the following RIE process. The glass surface was etched using CHF<sub>3</sub> gas by using a multiple ICP plasma etching system (RIE-101iPHS-L, SUMCO, Japan). After resolving the

remaining Ni layer, an array of straight silica pillars with  $5\ \mu\text{m}$  in diameter and  $4\ \mu\text{m}$  in height was obtained. An example of a silica glass pillar is shown in Fig. 2.2 below:

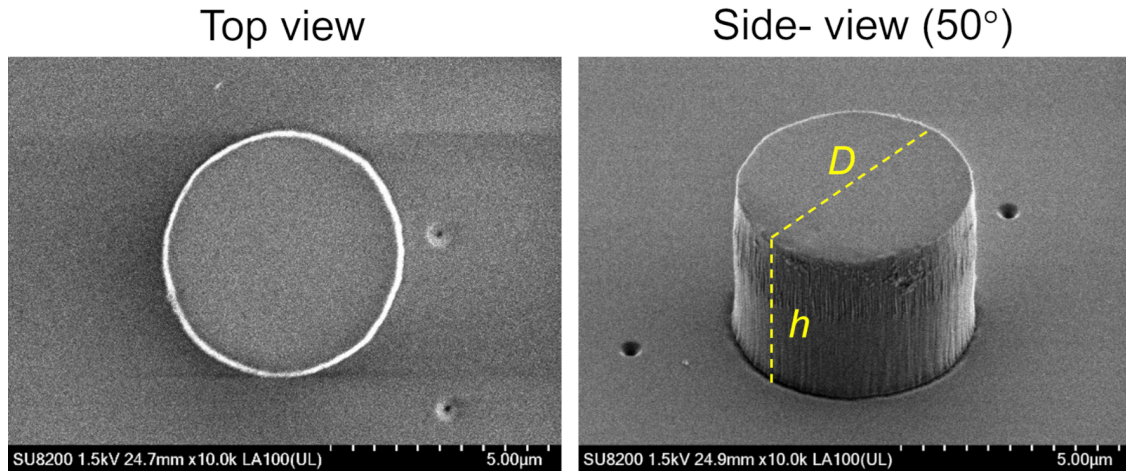


FIGURE 2.2: Scanning Electron Microscopy (SEM) images of RIE processed  $\text{SiO}_2$  micropillars. The dashed yellow lines represent the diameter  $D$  and height  $h$ .

*ABS and SLS cases:* After cleaning the sample surface, a Cr layer was deposited on a sample surface with an electron beam evaporation system. A photo-resist layer was coated by a spin-coating process, exposed to a pattern of intense light with a UV exposure system with a photomask, and then developed. Then the sample was etched with a Cr etcher solution to leave an array of circular dots of Cr/photo-resist layer on the plate surface as a mask of the following RIE process. The glass surface was etched using a mixture gas of  $\text{Ar}/\text{O}_2/\text{CHF}_3/\text{C}_4\text{F}_8$  by using a dry etching system (NLD-5700, ULVAC, Japan). After removing the remaining Cr/photo-resist layers, an array of conical glass pillars was obtained. ABS glass pillars have a top diameter of  $4.4\ \mu\text{m}$ , a bottom diameter of  $7.4\ \mu\text{m}$ , and a height of  $4.20\ \mu\text{m}$ . SLS glass pillars have a top diameter of  $5.4\ \mu\text{m}$ , a bottom diameter of  $9.0\ \mu\text{m}$ , and a height of  $3.8\ \mu\text{m}$ . Their geometries are presented respectively in Fig. 2.3.a and Fig. 2.4.a.

The description of those two processes has been provided by Yoshinari Kato from Nippon Electric Glass Co.,Ltd.

### Focused Ion Beam (FIB)

As Fig. 2.3.a and Fig. 2.4.a show, ABS glass pillars, and SLS glass pillars have a conical shape after manufacturing from RIE. We assume that ionized oxides in the structure, such as  $\text{Na}^+$  or  $\text{Ca}^{2+}$  would limit the efficiency of the RIE process. Preliminary experiments have shown that the data for conical pillars is very difficult to analyze. To make straight pillars, the conical pillars have been trimmed by Focused Ion Beam (FIB) milling. The device was a FIB/SEM Thermo Scientific Helios NanoLab DualBeam 600i. The machining was annular from outside to inside with two beam conditions:

- 30 kV and 790 pA for shaping the pillar.
- 30 kV and 230 pA for cleaning and finishing.

After this second processing, relatively straight pillars can be obtained, as represented by SEM images in Fig. 2.3.b and Fig. 2.4.b. The FIB processing was performed by Sergio Sao-Jao at Mines de Saint-Etienne.

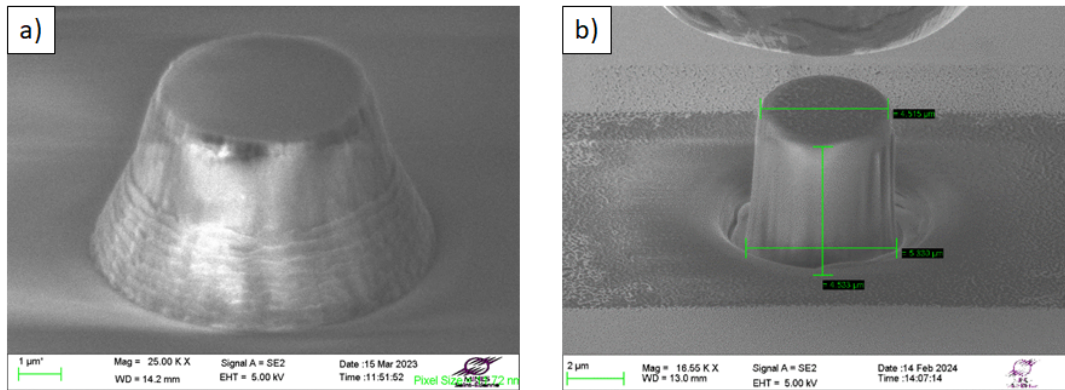


FIGURE 2.3: (a) Scanning Electron Microscopy (SEM) images of RIE processed ABS micropillars and (b) trimmed pillar by Focused Ion Beam (FIB).

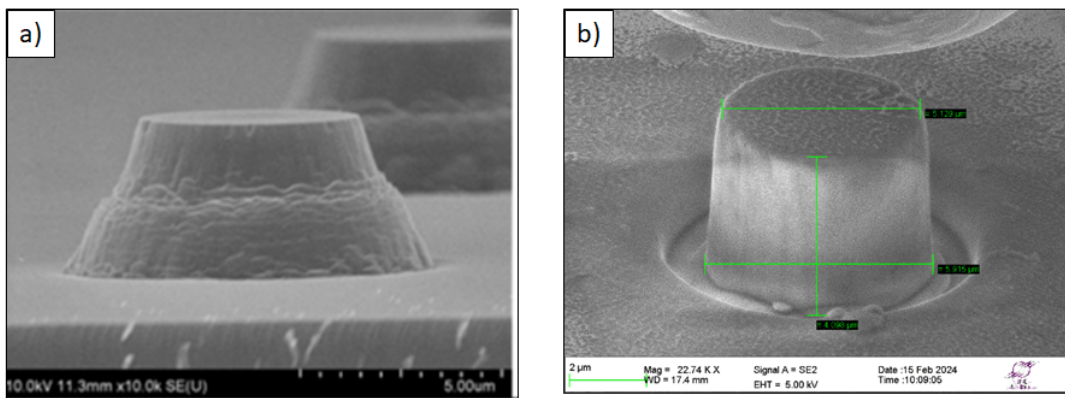


FIGURE 2.4: (a) Scanning Electron Microscopy (SEM) images of RIE processed SLS micropillars and (b) trimmed pillar by Focused Ion Beam (FIB).

After FIB milling, ABS glass pillars have a top diameter of 4.5 μm and a bottom diameter of 5.3 μm. SLS glass pillars have a top diameter of 5.1 μm and a bottom diameter of 5.9 μm. The height is more complicated to measure since the setup is tilted and the FIB has dug into the bulk around the pillar, thus increasing its height. By using tools from the scanning electron microscope, the projected height can be measured and the true height is deduced with trigonometric relations. We eventually obtain  $h_{ABS}=5.2 \mu\text{m}$  and  $h_{SLS}=4.6$ .

## Microscopy techniques

### Scanning Electron Microscopy (SEM)

For the in-situ micro-compression under e-beam, the indenter was installed in a Zeiss Supra 55 VP Scanning Electron Microscope. To change irradiation conditions, we played on current density  $J$  by playing both on the magnification and the diaphragm aperture. Changing the aperture affects the current  $I$ . The larger the diaphragm, the larger the current. Once the current is known, it has

to be divided by the size of the image to obtain the current density following the equation below:

$$J = \frac{I}{S} = \frac{I}{s_{pixel}n_{pixel}} \quad (2.1)$$

where  $S$  is the size of the image,  $s_{pixel}$  is the size of one pixel and  $n_{pixel}$  is the number of pixels of the SEM image. The size of the pillars was used to determine the size of one pixel which thus depends on the magnification. The entirety of the pillar must be observable to allow homogeneous irradiation of the latter. Consequently, the magnification can not exceed x30k. The irradiation conditions used in the experiments are gathered in Table 2.2.

Diaphragm aperture ( $\mu\text{m}$ )	Magnification (x1000)			
		7.5	15	30
7.5		0.03	0.11	0.45
30		0.45	1.79	7.15
60		1.79	7.15	28.6
120		7.15	28.6	114

TABLE 2.2: Current density conditions in  $A/m^2$  as a function of the diaphragm aperture and the magnification in the Scanning Electron Microscope.

On the other hand, based on electron trajectories calculated by Monte Carlo simulation in the literature [135] (Fig. 2.5), the minimum acceleration voltage allowing homogeneous irradiation of the pillar is around 20kV. Below this value, electrons will not diffuse within the full pillar. Given this assumption, the acceleration voltage was set at 20kV. Beyond 20 kV there is also a risk of damaging the materials [136]. This simulation has been carried out only for silica but it would be useful to do this calculation for other glasses in a flat system to get an idea of the effect of the composition of the glass on the penetration of electrons in matter.

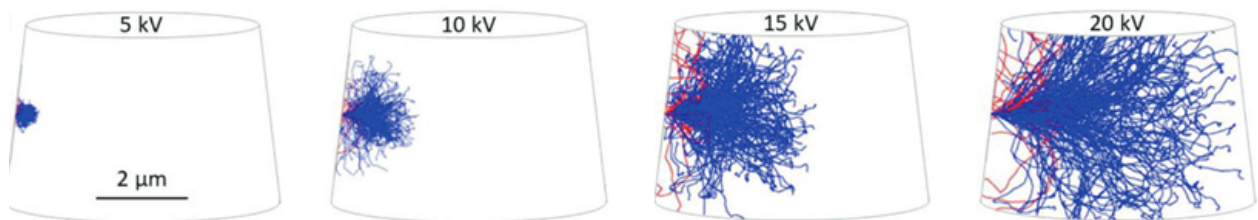


FIGURE 2.5: Electron trajectories inside the micropillar for different acceleration voltages calculated by Win X-ray software Monte Carlo simulations (taken from [135]).

Finally, one can wonder whether electron irradiation could increase the temperature which can also affect the plastic response of the material, as described in the introduction of this chapter. By using the following equation [139]:

$$\Delta T = \frac{1.5IV_0}{\pi kR} \quad (2.2)$$

with the intensity  $I$ , the acceleration voltage  $V_0$ , the thermal conductivity of the material  $k$ , and the electron range  $R$ , an increase in temperature of about 10 K is estimated which could be considered as negligible in our experiments.

## Mechanical analysis

### Micro-compression setup

The indenter was an Alemnis Standard Assembly (ASA) device, which can easily be placed within an SEM chamber to perform in-situ micro-mechanical tests such as indentation, micropillar compression, bending beam, tensile testing, or even fatigue and scratch testing. It operates with a true displacement control that allows sudden load excursions, load drops, compression artifacts or strain rate jumps to be monitored by a Mini Load Cell MLC-1.5 ( $k=1100$  mN/ $\mu\text{m}$ ) in real-time, with a load range up to 1.5N (typ.8  $\mu\text{N}$  RMS noise).

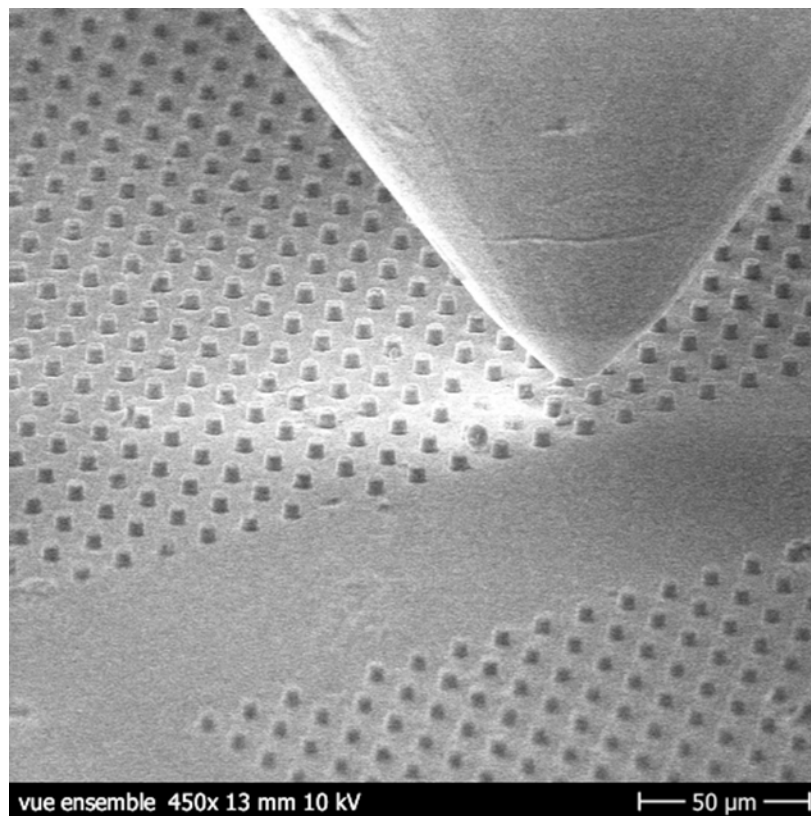


FIGURE 2.6: Scanning electron image of the micropillar compression setup. This setup is 30°-tilted within a Scanning Electron Microscope (SEM) to allow simultaneous SEM observation and pillar micro-compression. This image has been taken at the Laboratory for Mechanics of Materials and Nanostructures at Thun in Switzerland by G. Guillonéau, J. Michler, and G. Kermouche.

A flat punch made of a "conductive" diamond with a diameter of 10  $\mu\text{m}$  was fixed. Thus, the flat punch is large enough to maintain uniaxial compression despite increasing pillar sections. In the SEM chamber, the Alemnis device is tilted at 30° to allow good observation of the pillar and the most homogeneous irradiation possible during the micro-compression test. Fig. 2.6 is an

SEM picture showing the flat punch above the array of silica pillars. With this setup, both micro-compression tests and relaxation tests were carried out. All the experimental microcompression tests were performed with a displacement speed between 10 nm/s and 100  $\mu\text{m}/\text{s}$  at loading and unloading, with a maximum controlled displacement of 1.5  $\mu\text{m}$ , and at room temperature. Once the flat punch is set just above the pillar, an auto-approach has to be done to detect the top of the pillar and set the exact zero position. When the test is running, the load is recorded during all the mechanical testing and Load-Displacement curves are directly available from the Alemn software.

## 2.2 In situ micropillar compression

### 2.2.1 Mechanical behavior under irradiation and strain rate sensitivity

During the compression experiment, the flat punch is moving downwards, loading and deforming the pillar before moving upwards to release the deformed micropillar. The force vs indenter displacement curves are recorded. However, determining true stress-strain curves with pillar compression experiments is a difficult issue in the case of silicate glasses. The first issue is the elastic contribution of the substrate and the compliance of the device. Sneddon [140] provides an analytical formula to subtract the elastic sink-in depth  $U_{\text{Sneddon}}$  from the total displacement  $U_{\text{tot}}$ :

$$\Delta U = U_{\text{tot}} - U_{\text{Device}} - U_{\text{Sneddon}} = U_{\text{tot}} - \frac{F}{G_{\text{Device}}} - \frac{(1 - \nu^2)F}{2aE} \quad (2.3)$$

where  $F$  is the measured force,  $G_{\text{Device}}$  is the compliance of the machine,  $a$  is the radius of the micropillar,  $E$  is the elastic modulus, and  $\nu$  is the Poisson ratio.

The second issue is the change in the pillar section during straining. At first, the well-known basic expressions for the true stress  $\sigma_T$  and the true axial strain  $\epsilon_T$  are applied:

$$\sigma_T = \frac{F}{S_i} \quad (2.4)$$

$$\epsilon_T = -\ln \left( 1 - \frac{\Delta U}{U_0} \right) \quad (2.5)$$

where  $S_i$  is the actual area of the pillar during deformation and  $U_0$  is the initial height of the pillar. However, for crystalline metals, plastic deformation is volume-conservative, so  $S_i$  directly derives from  $\Delta U$  and the yield stress is small so that the compliance corrections are negligible, simplifying the calculation of pillar deformation through equations 2.4 and 2.5. In contrast, for silicate glasses, substantial plastic densification can occur (sec. 1.2.3.a), and the yield stress is high so that elastic deformation is not negligible. By following the method developed by Kermouche *et al.* [96], the radial deformation  $\epsilon_r$ , used to evaluate the true section of the pillar, is decomposed into elastic and plastic parts, and the radial strain rate during tests follows the equation below:

$$\dot{\epsilon}_r = -(\nu \dot{\epsilon}_T^e + k \dot{\epsilon}_T^p) \quad (2.6)$$

where  $\epsilon_T^e$  is the elastic axial deformation,  $\epsilon_T^p$  is the plastic axial deformation, and  $k$  is the ratio of the plastic radial expansion over axial plastic deformation. In previous experiments, it was shown that the densification in uniaxial compression is small (less than ten 10%) [141] so that in these experiments, we assume an isochoric plasticity with  $k = 0.5$  (constant volume). This model might be improved by a better estimation of  $k$  using FEM simulation and by taking into account the densification in the pillar [141].

Fig. 2.7.a exhibits stress-strain curves from micro-compression of pure silica, aluminoborosilicate, and soda-lime silicate glass pillars at several displacement speeds without irradiation. The stress increases with strain, reaching a peak before decreasing, indicating the yield stress and subsequent apparent softening. SiO<sub>2</sub> glass exhibits the highest yield stress up to 6-6.5 GPa (which is slightly lower than the value found by Bruns *et al.*), ABS displays a yield stress of 4.5-5 GPa, and SLS shows the lowest yield stress with 3.2-3.5 GPa, depending on the tip speed. This figure shows that those compositions are not strain rate sensitive under these testing conditions since the mechanical behaviors are quite similar whatever the tip speed. We can also notice a slight negative slope on the plastic part of the mechanical response for all compositions which could suggest a strain softening of the material. In fact, this is an artefact from the measurement resulting from inaccurate pillar surface correction. For these experiments, silica has been tested at lower tip speeds than the other glasses because of the difference in strain rate sensitivity with ABS or SLS (see below).

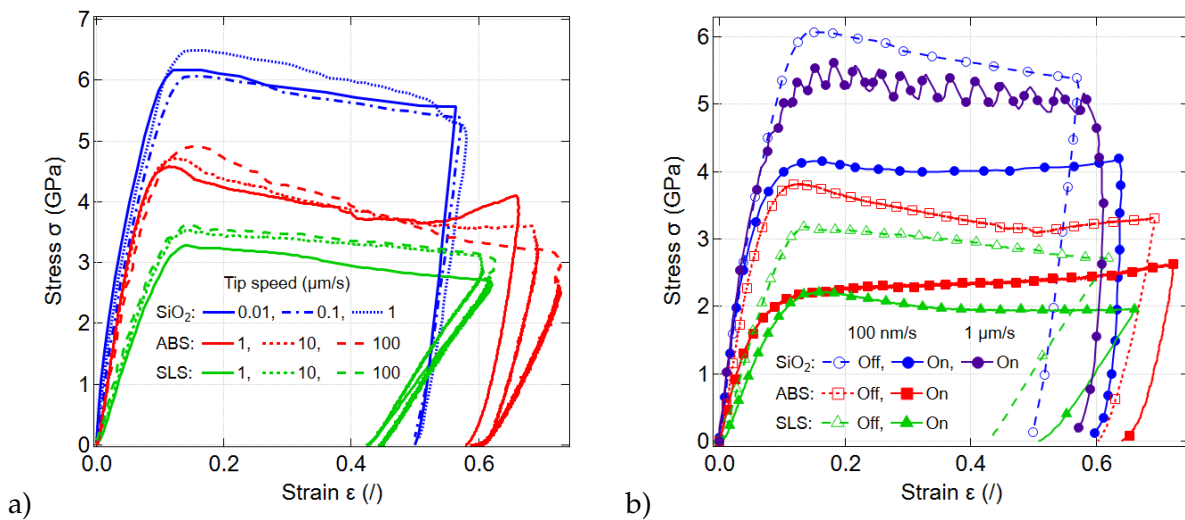


FIGURE 2.7: (a) Micro-pillars compression of SiO<sub>2</sub>, ABS and SLS glasses for several tip speeds without electron irradiation. (b) Micro-pillars compression of SiO<sub>2</sub>, ABS, and SLS glasses at 100 nm/s (or 1  $\mu\text{m/s}$  for SiO<sub>2</sub>) with (full marks) or without (empty marks) electron irradiation (marker every 4 data values).

The results obtained under beam-on conditions with an acceleration voltage of 20 kV and a current density of 114 A/m<sup>2</sup> (X30-120 $\mu\text{m}$  in Table 2.2) are shown in Fig. 2.7.b for a loading velocity of 100 nm/s. Clearly, all three compositions are irradiation sensitive: the yield stress decreases from 6 GPa to 4 GPa for silica, from 3.8 GPa to 2 GPa for ABS glass, and from 3 GPa to 2 GPa for SLS glass. Another interesting feature we can notice in this figure is this jerky plastic flow on the silica stress-strain curve at 1  $\mu\text{m/s}$  under irradiation. These features appear for tip speeds in

the range of 1 to 10  $\mu\text{m/s}$ . In fact, we noticed a perfect match between the periodicity of these oscillations and the scanning time of the SEM. It means this flow is characterized by alternative relaxation induced by alternative e-beam off/on conditions.

Our results, which for silica are fully in agreement with the micropillar compression performed under irradiation by Bruns *et al.* [135], demonstrate that normal silicate glasses present a similar behavior under irradiation.

### 2.2.2 Residual geometry of compressed micropillars with and without electron irradiation

We also investigated the residual geometry of the pillars resulting from the compression under beam-on or beam-off conditions. Fig. 2.8 presents SEM images of compressed  $\text{SiO}_2$  micropillars under varying levels of maximum applied axial strain ( $\epsilon_{z,max}$ ). In the top row, where the e-beam is off, the micropillars display a progressive increase in damage as the strain increases. At 21% maximum strain, the micropillar remains largely intact, but as the strain increases, minor cracks begin to appear. These cracks become more prominent and extend further at larger maximum strain while the structure shows significant damage with widened cracks. At very large maximum strain, severe cracking with large fractures is visible and the micropillar is heavily damaged with multiple large cracks and significant fragmentation.

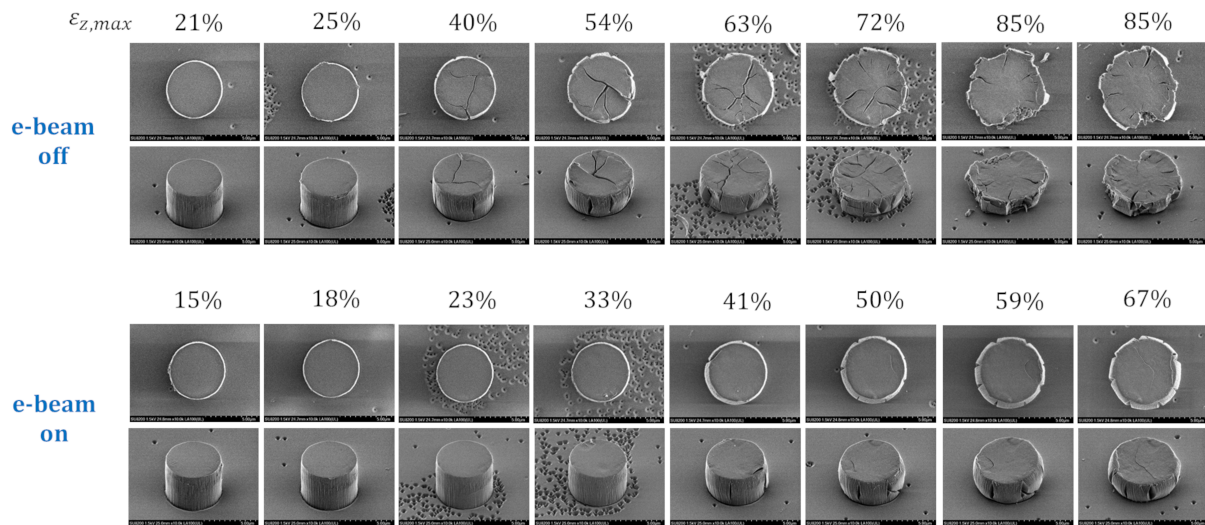


FIGURE 2.8: Field-Emission SEM images of compressed  $\text{SiO}_2$  micropillars with and without e-beam irradiation. The values above the images represent the maximum applied axial strain  $\epsilon_{z,max}$ .

In contrast, the bottom row, where the e-beam is on, shows that the micropillars tend to exhibit less severe cracking at equivalent or even higher maximum strain levels. At 15% maximum strain, the micropillar remains intact, showing no visible damage. As the maximum strain increases, some radial cracks begin to form, though they remain relatively small. When the maximum strain goes over 50%, the pillar exhibits visible damage and significant radial cracking is evident on the edges. However, no crack can be observed on the top of the pillar. Moreover, no direct correlation

can be deduced between the number of radial cracks and the strain applied. Overall, the comparison between the two sets of images suggests that e-beam irradiation has a mitigating effect on the structural damage caused by compression. The micropillars subjected to e-beam irradiation show less severe cracking and better structural integrity at comparable strain levels compared to those not subjected to e-beam irradiation. These results confirm that electron irradiation can promote plastic flow by lowering the yield stress in amorphous silica, as previous work highlighted [135].

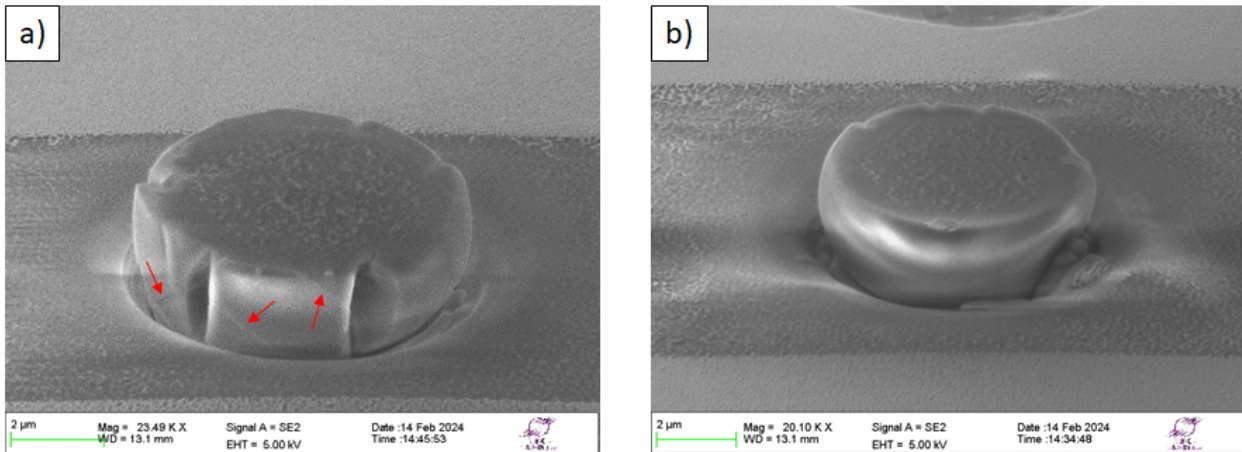


FIGURE 2.9: Scanning electron images of compressed ABS micropillars with (a) and without (b) e-beam irradiation. Red arrows show shear localizations on the pillar.

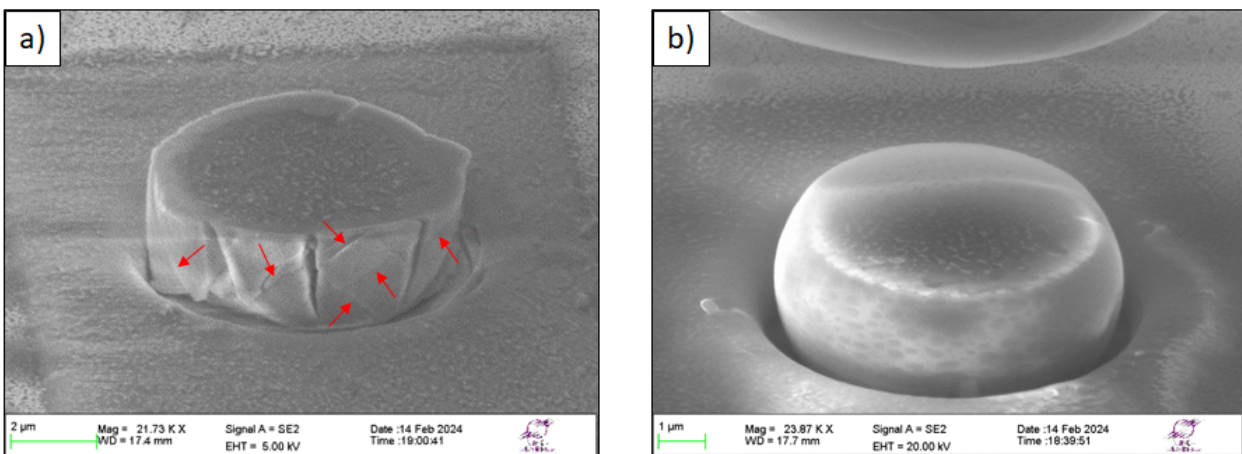


FIGURE 2.10: Scanning electron images of compressed SLS micropillars with (a) and without (b) e-beam irradiation. Red arrows show shear localizations on the pillar.

The same work has been done on ABS and SLS glass micropillars after compression with or without irradiation. Unlike silica glass pillars, this characterization of residual geometries has been only performed for one displacement at  $2\ \mu\text{m}$ , or about 40% maximum applied axial strain for both ABS and SLS glasses. When the beam is off (Fig. 2.9.a and Fig. 2.10.a), both compositions exhibit significant deformation and cracking around the pillar circumference, indicating substantial structural damage due to compression. Additionally, some traces of shear localizations are observed along the micropillar periphery (red arrows). In contrast, micropillars compressed under irradiation (Fig. 2.9.b and Fig. 2.10.b) display a more uniform surface without any cracking

pattern, and no more shear localizations. It clearly indicates that electron irradiation promotes a more homogeneous plastic deformation in other silicates as well.

To have a more precise characterization of the viscoplasticity of the glass under irradiation and the relation between stress, strain rate, and electron irradiation we have performed relaxation tests.

## 2.3 Electron irradiation and viscoplastic deformation

### 2.3.1 Relaxation tests

A relaxation test consists in applying a given strain and keeping it constant over time. In the meantime, the stress relaxation is monitored. In the example of Fig. 2.11, the pillar is first compressed to 2  $\mu\text{m}$  with a tip speed of 100 nm/s. The loading time is noted  $t_0$ . Once the final position is reached, the displacement and the electron beam are maintained and the load is recorded over a time of 300 s.

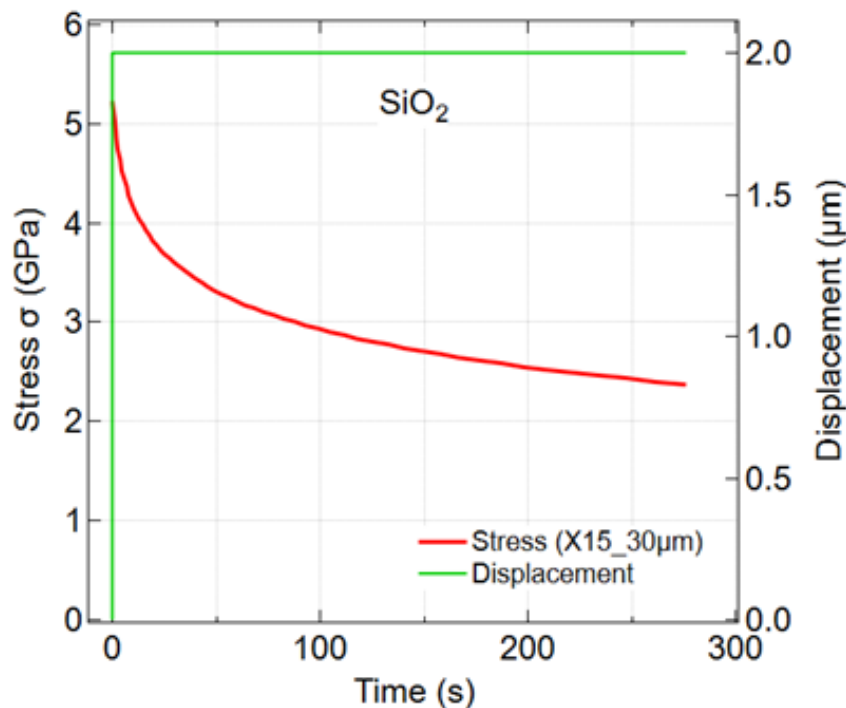


FIGURE 2.11:  $\text{SiO}_2$  pillar relaxation measurement: evolution of stress (left-hand axis) at constant displacement (right-hand axis). These data were taken under irradiation for a magnification of 15k and a diaphragm aperture of 30  $\mu\text{m}$ .

Then, the determination of  $\sigma$ - $\epsilon$  curves from F-U curves is based on the method described previously in section 2.2.1.

#### 2.3.1.a Rescaling time with current density

The stress relaxation was carried out with different irradiation conditions. Since the tip position is constant during a relaxation test, it makes it possible to maintain the same irradiated volume

of the pillar over time (in comparison with a simple micro-compression of the pillar where the irradiated volume changes upon the test), to more precisely evaluate the impact of the electron beam on the mechanical response of the glass.

The different irradiation conditions are given in Table.2.2 and the resulting stress-time curves are plotted in Fig. 2.12.a. The curves show a gradual decrease in stress over time, indicating material relaxation. It is observed that higher current densities lead to faster stress relaxation compared to lower current densities. Interestingly, all the plots have similar shapes of relaxation functions. As a result, from Fig. 2.12.a, we can try to rescale all the curves to the highest current density curve (X30A120) to obtain one single master curve presented in Fig. 2.12.b. The rescaling is given by the following equation:

$$t_N = \frac{t - t_0}{S_J} \quad (2.7)$$

where  $t_N$  is the normalized time,  $t$  is the time,  $t_0$  is the initial time and  $S_J$  (or *Shift(J)*) is the shift factor which is chosen to optimize the match between rescaled curves.

This excellent rescaling of all the relaxation curves underscores the exact impact of current density on the plastic properties of SiO<sub>2</sub> pillars, with higher densities accelerating stress relaxation which results in a lower apparent yield stress. Irradiation only affects the time scale without changing the relaxation process. This superposition in time-current density is in some way similar to the principle of time-temperature equivalence found in polymers where the shift factor  $a_T$  is defined by the WLF law [142].

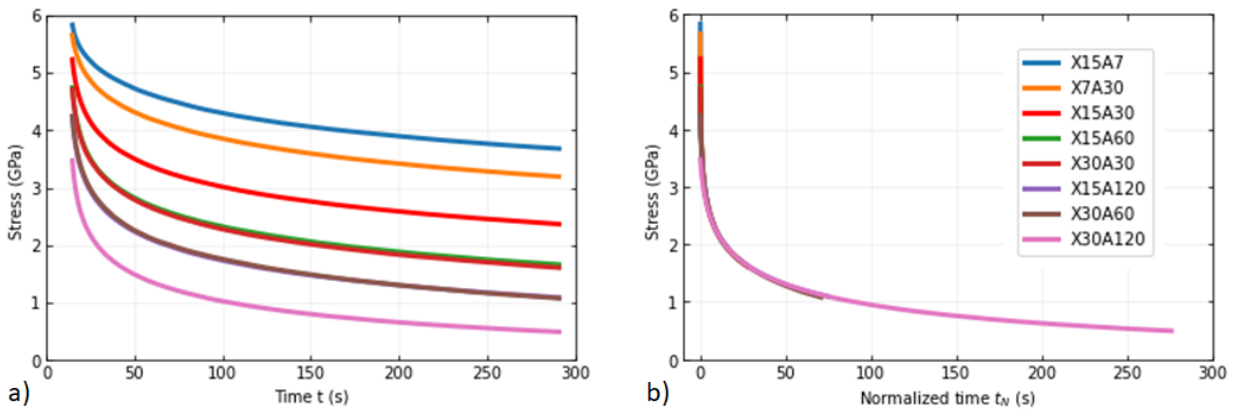


FIGURE 2.12: (a) SiO<sub>2</sub> pillar relaxation under e-beam irradiation for different current density conditions and (b) rescaled with a shift factor. The blue one is the smallest current density and the pink one is the highest condition of the batch.

For clarity and to avoid redundancies, only the case of silica is reported in this section. Since the data processing is the same for the three compositions, that of ABS and SLS is reported in Appendix 1 and we observe the same trend as for pure amorphous silica with higher current densities leading to faster stress relaxation, and all data rescaling into a single master curve.

The second important aspect of the rescaling is the shift factors. For all three glass compositions, the dependence of the shift factor with current density is plotted in Fig. 2.13.

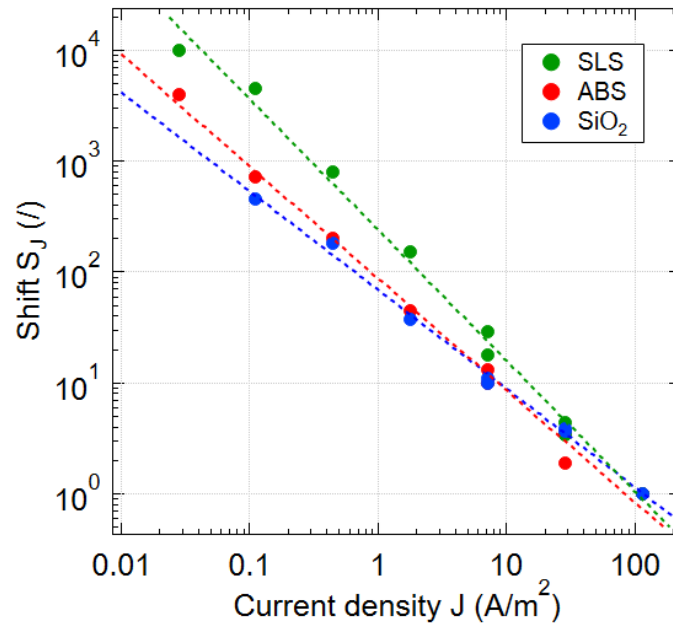


FIGURE 2.13: Shift factor  $S_J$  as a function of the current density for  $\text{SiO}_2$ , ABS and SLS glasses. Each composition is fitted with a power law function. By definition, the three points at the highest current density overlap.

Data have been fitted with a power law function which is defined by:

$$S_J = \frac{A}{J^B} \quad (2.8)$$

with  $J$  the current density, and  $A$  and  $B$  the two fitting parameters displayed in Table.2.3 for the three glass compositions. Interestingly, the values of all slopes are around 1. This approximately linear dependence over nearly 4 decades will be discussed in section 2.4.2.

	$\text{SiO}_2$	ABS	SLS
A	69.1	87.8	240.7
B	0.89	1.01	1.18

TABLE 2.3: Fitting parameters of the power law function depending on the glass composition. The corresponding fits are represented on Fig. 2.13.

### 2.3.1.b Time description - the stretched exponential model

A highly successful description of relaxation in disordered systems is the stretched exponential model initially proposed by Kohlrausch in 1847 for electric charges [143] and reviewed by Phillips [144, 145]. The function is:

$$\sigma(t) = \sigma_0 \exp[-(t/\tau)^\beta] \quad (2.9)$$

where  $\sigma_0$  is the initial stress. The relaxation time  $\tau$  and the dimensionless stretching fraction  $\beta$ , (with  $0 < \beta \leq 1$ ) are two free parameters. When  $\beta = 1$ , it corresponds to a simple exponential

function with a single relaxation time whereas  $\beta < 1$  indicates a nonexponential relaxation behavior which reflects a distribution of relaxation times or more complex relaxation phenomena. This model has been proved to provide a good description of the relaxation behavior of homogeneous glass systems [146].

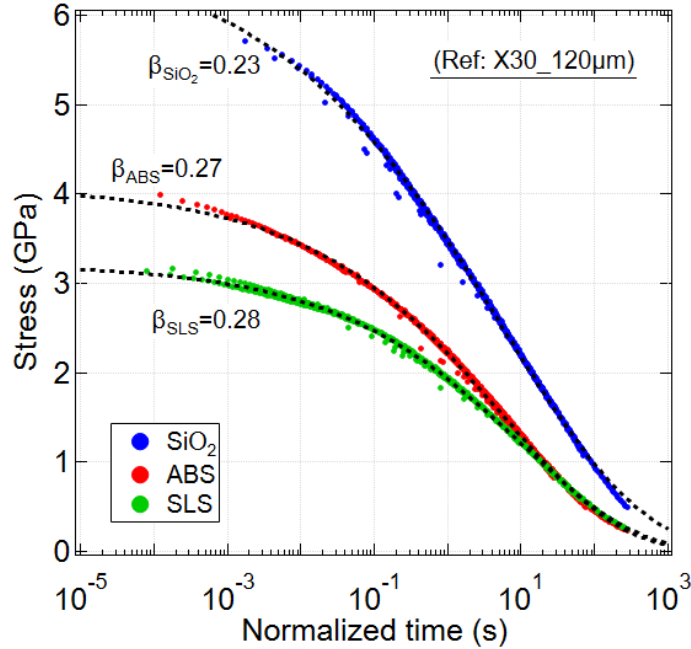


FIGURE 2.14: (a) Stress *vs* Time master curves for all glass compositions fitted with the stretched exponential model [146].

Fig. 2.14 shows the master curves for the three glass compositions fitted with the stretched exponential model. Good fits are obtained with  $\beta_{SiO_2} = 0.23$ ,  $\beta_{ABS} = 0.27$  and  $\beta_{SLS} = 0.28$ .

However, another description based on a strain rate analysis, as Bruns *et al.* did, is also possible to provide a different interpretation of the irradiation effect on the mechanical response of the glass.

### 2.3.2 Strain rate description

Based on the same data, we can also plot the stress as a function of the viscoplastic strain rate  $\dot{\epsilon}_p$ . In analogy with the uniaxial relaxation test, Baral *et al.* [147] proposed a method to calculate the plastic strain rate  $\dot{\epsilon}_{vp}$  during relaxation. Fig. 2.15 gives a simple representation of the relaxation test of an elastic-viscoplastic material.

Thus, we can write the relation between  $\dot{\epsilon}_{vp}$  and  $\sigma$ . Since the strain is constant we have the following relation:

$$\epsilon = \epsilon_e + \epsilon_{vp} = cst \quad (2.10)$$

and the stress is only determined by the elastic deformation (since the plasticity is a flow or a strain) and can be written as:

$$\sigma = E\epsilon_e \quad (2.11)$$

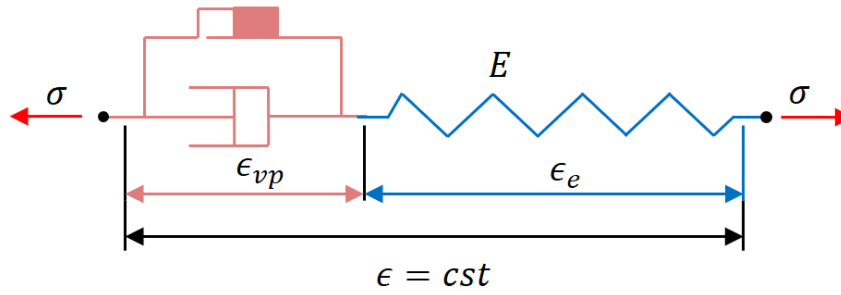


FIGURE 2.15: Rheological model of an elastic–viscoplastic solids.  $\sigma$  is the stress,  $\epsilon$  is the constant strain,  $\sigma_y$  is the yield stress,  $\epsilon_e$  is the elastic deformation, and  $\epsilon_{vp}$  is the viscoplastic deformation.  $\epsilon_{vp}$  gradually increases over time while  $\epsilon_e$  decreases during stress relaxation.

Finally, by combining equations 2.10 and 2.11, the relationship between the viscoplastic strain rate and the stress obeys:

$$\dot{\epsilon}_e = -\dot{\epsilon}_{vp} = \frac{\dot{\sigma}}{E} \quad (2.12)$$

with  $E$  the Young's modulus and  $\sigma$  the monitored stress. However, in practice, the strain is not constant. Indeed, the pillar is not completely blocked from both sides (sec. 2.2.1). It is slightly pushed back by the substrate which rises during the relaxation test. Eventually, the correct expression of the plastic strain rate follows the equation:

$$\dot{\epsilon}_{vp} = \dot{\epsilon}_T - \frac{\dot{\sigma}}{E} \quad (2.13)$$

where  $\dot{\epsilon}_T$  is the true strain defined in section 2.2.1.

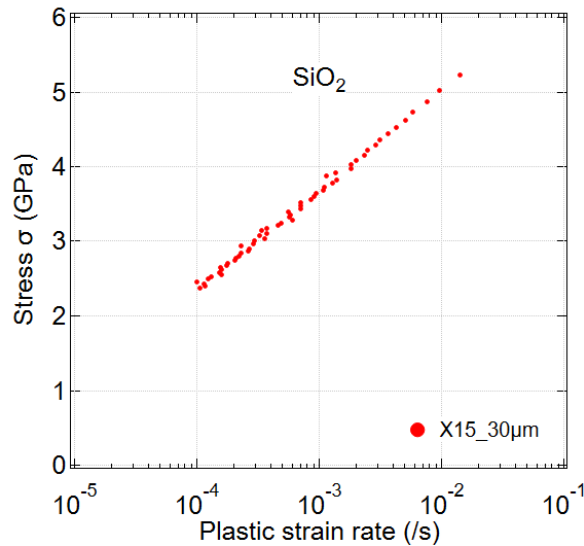


FIGURE 2.16: SiO<sub>2</sub> pillar relaxation measurement for a magnification of 15k and a diaphragm aperture of 30  $\mu\text{m}$ . The stress was plotted as a function of the plastic strain rate.

From equation 2.12, the stress as a function of time in Fig. 2.11 can be converted into stress as a function of plastic strain rate represented in Fig. 2.16. With this transformation, we obtain a full stress *vs* strain rate curve in one experiment, which can be compared with the results obtained by Bruns [135] with point-by-point experiments. For 20 kV and a current density of 1 A/m<sup>2</sup>, they

found a yield stress of about 4.5 GPa for a strain rate of  $5 \cdot 10^{-3} \text{ s}^{-1}$  which is consistent with Fig. 2.16 ( $J=1.8 \text{ A/m}^2$ ) where the yield stress is about 4.7 GPa for the same strain rate. Furthermore, this alternative data processing can be applied to all the current density conditions to obtain Fig. 2.17.a.

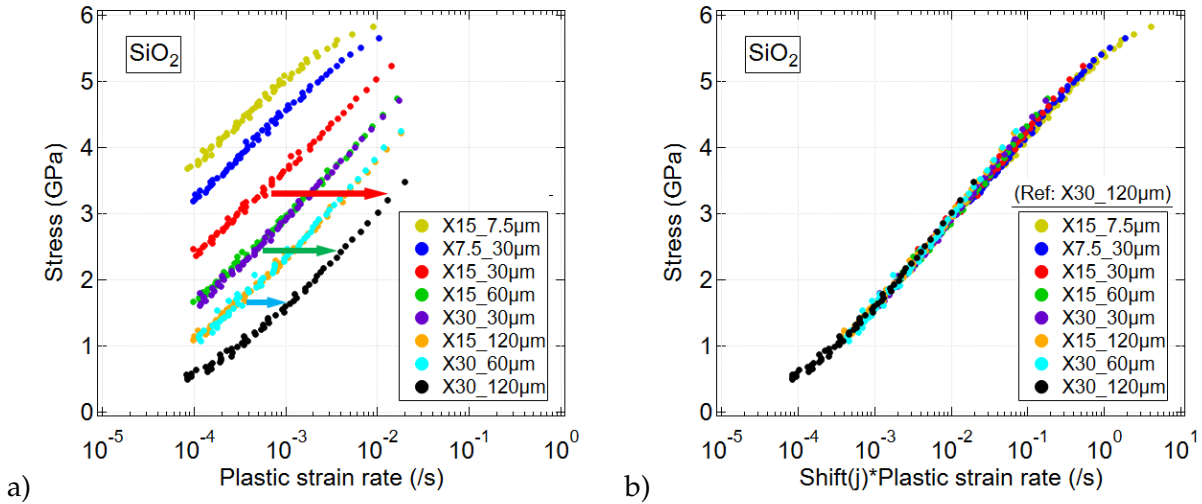


FIGURE 2.17: Silica pillars compression under e-beam irradiation. Relaxation curves (a) and rescaling by shift factor  $S_j$  (b) to get the  $\text{SiO}_2$  master curve. The highest current density condition is the reference and is not shifted.

As for Fig. 2.12.a, it shows that the yield stress decreases with higher current density conditions over the same range of plastic strain rate. Here, in log-log scale, it seems even clearer that we can shift the curves to obtain a single master curve reflecting a time (or strain rate)-current density superposition, similar to the time-temperature superposition for polymers [148], described in section 2.3.1.a. By using the highest current density as a reference condition and applying the same shift factors  $S_j$  determined in section 2.3.1.a, for each current density condition, we find a single master curve (Fig. 2.17.b). This master curve allows us to characterize the strain rate dependence of the yield stress over nearly 5 decades of strain rates.

### 2.3.3 Application and comparison with other glass compositions

Similarly, these experiments have been reproduced for ABS glass and SLS glass, and the respective master curves have been plotted together with silica in Fig. 2.18 with the same reference (identical highest current density). We observe that in contrast to silica glass which seems to display one single strain rate regime, ABS and SLS master curves exhibit two different regimes of strain rates. The low strain rate regime, below  $10^{-1} \text{ s}^{-1}$ , seems to be common with silica glass, as it will be detailed later in the discussion part. Above a strain rate of *ca.*  $10^{-1} \text{ s}^{-1}$ , a second regime with a much smaller slope appears for both ABS and SLS which suggests a different plastic mechanism is involved at a high strain rate.

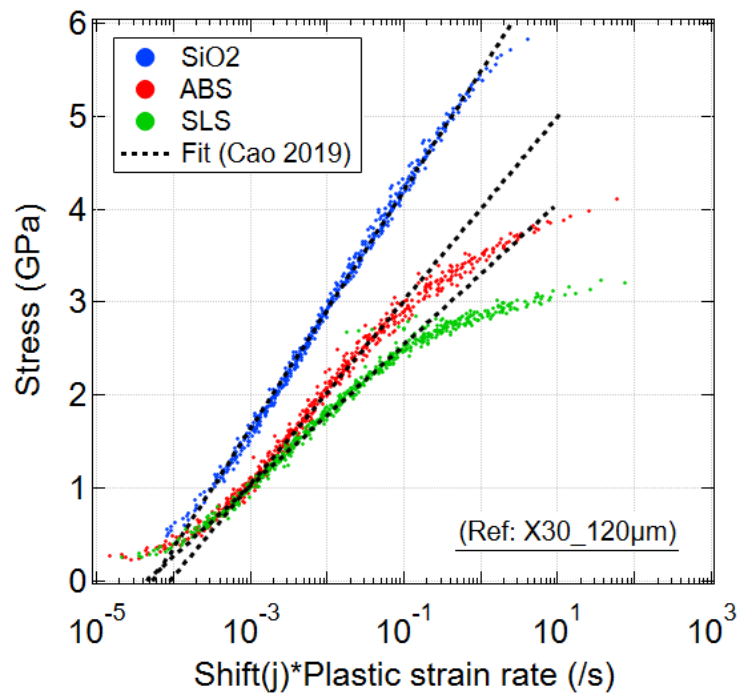


FIGURE 2.18: Superposition of the master curves for silica, ABS glass, and SLS glass show the generality of the time - current density equivalence. Each glass composition is fitted with an Eyring model taken from [149]. For normal glasses (ABS and SLS), the model only fits with the first part of the plot. Above  $10^{-1} s^{-1}$ , another regime appears.

## 2.4 Physical description of the phenomenon

### 2.4.1 Glass plasticity and activation model

Plasticity in ordered crystalline environments, such as metals, is primarily governed by dislocation-based mechanisms. In a crystalline solid, atoms are arranged in a highly ordered and periodic lattice structure. When stress is applied, the deformation of these materials is facilitated by the movement of dislocations, which are line defects within the crystal lattice. These dislocations allow layers of atoms to slip past one another at much lower stress levels than would be required for the entire lattice to shift simultaneously. Plastic processes involve the generation, movement, and interaction of dislocations, which can form complex networks and patterns within the crystal. The mobility of these dislocations is influenced by various factors, including the crystal structure, temperature, and the presence of impurities or other defects.

These mechanisms, however, do not directly account for the plasticity of silicate glasses (sec. 1.2.3) due to their amorphous nature. Unlike crystalline solids, amorphous materials lack a periodic structure, meaning dislocations are absent, necessitating a different approach to describe their plasticity at a molecular level. Since the pioneering works of Spaepen and Argon [150, 151] in the late 1970s, it has been established that plastic flow in amorphous solids occurs through shear stress-induced localized rearrangements of small clusters of particles. Argon [151], and later Falk and Langer [152], identified these clusters as shear transformation zones (STZs), where localized stresses lead to rearrangements. A similar phenomenon can be observed in foams, known as T1

local rearrangements [153]: foams are composed of bubbles or cells surrounded by thin films. When a foam is subjected to deformation, the cells can reorganize their structure through local rearrangements. Upon deformation, such as compression or extension, the bubbles can move closer or farther apart. In a T1 rearrangement, two adjacent bubbles (e.g., C and D) begin to separate while the other two (A and B) move closer together (see Fig. 2.19 below).

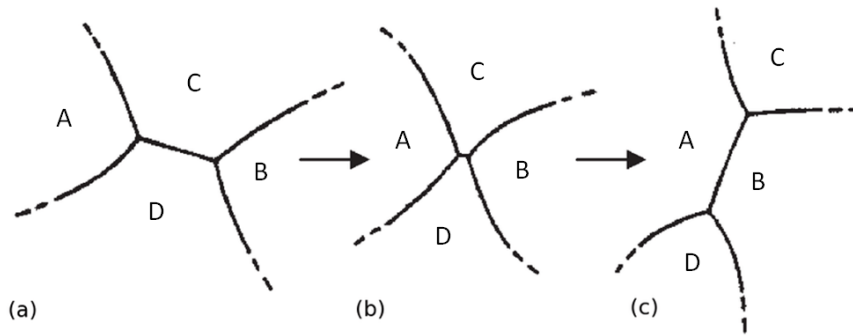


FIGURE 2.19: T1 process in two dimensions in liquid foams. A, B, C, and D are bubbles in contact (adapted from [153]).

By focusing on a smaller scale for silicate glasses in these STZs, the glass plasticity can even be described at the atomic scale. At this scale, bond-switching events occur [154, 155, 156, 137]. When stress is applied to the glass, it can induce local rearrangements. The energy from the stress causes certain bonds to break and new bonds to form. Initially, atoms are connected in a specific manner, forming bonds with their neighboring atoms (Fig. 2.20.a). As the stress increases, the atoms begin to shift positions, breaking stable bonds and moving closer to forming new connections (Fig. 2.20.b). Eventually, new bonds are established between different sets of neighboring atoms, rearranging the structure but maintaining the overall amorphous nature of the material (Fig. 2.20.c). This bond-switching mechanism allows the glass to deform plastically. Instead of cracking or breaking, the material can absorb and dissipate energy by rearranging its atomic structure. This ability to switch bonds enables the material to flow under stress, above a certain threshold, which is the yield stress. Because of the localized nature of the STZ, the yield stress in amorphous materials is typically larger than in crystalline materials. Those localized rearrangements can be modeled by using Molecular Dynamics simulations discussed in section 1.2.5.c.

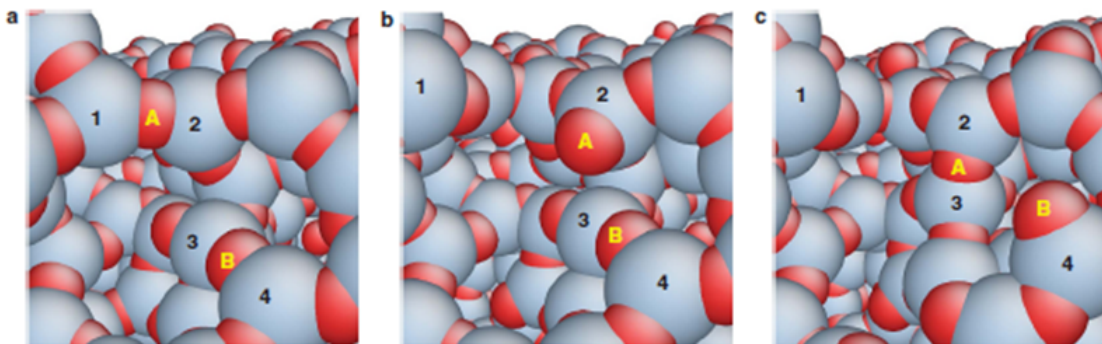


FIGURE 2.20: A representative bond-switching event in pure amorphous silica (adapted from [137]).

The temperature dependence of the yield stress described by Widmer *et al.* [134] suggests that this plastic deformation mechanism is thermally activated. The standard model to describe such a phenomenon is the Eyring equation (see *e.g.* [149]):

$$\dot{\epsilon} = \dot{\epsilon}_0 \exp\left(-\frac{E_0 - \sigma\Omega}{kT}\right) \quad (2.14)$$

or

$$\sigma = \frac{E_0}{\Omega} + \frac{kT}{\Omega} \ln \frac{\dot{\epsilon}}{\dot{\epsilon}_0} \quad (2.15)$$

where  $\dot{\epsilon}$  is the strain rate,  $\dot{\epsilon}_0$  is the product of attempt frequency and average shear strain per successful attempt,  $E_0$  the activation energy,  $\sigma$  the shear stress,  $kT$  the thermal energy, and  $\Omega$  some activation volume. This volume is a parameter that cannot be linked to any characteristic size of the material. According to the Eyring equation, when stress is applied, the activation energy is reduced by the elastic energy supplied by the stress. Beyond the yield stress, the energy barrier becomes sufficiently low to trigger local rearrangements, leading to plastic deformation in the material, and the flow rate depends on the stress.

### 2.4.2 Impact of irradiation

The data show that electron irradiation affects the bond-switching mechanism in silicate glasses. When electrons penetrate the material, we assume they act as catalysts, effectively lowering the activation energy required for bond switching from  $E_0$  to  $E_1$ . Then at constant  $\sigma$  we have:

$$E_0 + kT \ln \frac{\dot{\epsilon}}{\dot{\epsilon}_0} = E_1 + kT \ln \frac{\dot{\epsilon}_1}{\dot{\epsilon}_0} \quad (2.16)$$

or

$$\ln\left(\frac{\dot{\epsilon}}{\dot{\epsilon}_1}\right) = \frac{E_1 - E_0}{kT} = \frac{\Delta E}{kT} \quad (2.17)$$

*i.e.* the dynamics is shifted: if  $E_1 < E_0$ , then  $\dot{\epsilon}_1 > \dot{\epsilon}$ . In other words, under irradiation and for the same stress value, plastic flow occurs at a faster strain rate.  $E_1 - E_0$  will depend upon the details of the chemical bonds and their interactions with the impinging electrons. This reduction in activation energy shifts the dynamics, as depicted in Fig. 2.21 where the energy barrier  $E_0$  without irradiation is higher compared to the lower energy state  $E_1$  with irradiation.

Fig. 2.18 exhibits the master curves, for all the glass compositions investigated, fitted with the model described previously. Thus, the fitting model is defined by:

$$\sigma = C \ln(\dot{\epsilon}/D) \quad (2.18)$$

$$C = \frac{kT}{\Omega} \quad (2.19)$$

$$D = \dot{\epsilon}_0 \exp\left(\frac{-E_0}{kT}\right) \quad (2.20)$$

with  $C$  and  $D$  the fitting parameters. Since  $T$  is unchanged in the experiments,  $E_0$  and  $\dot{\epsilon}_0$  can not

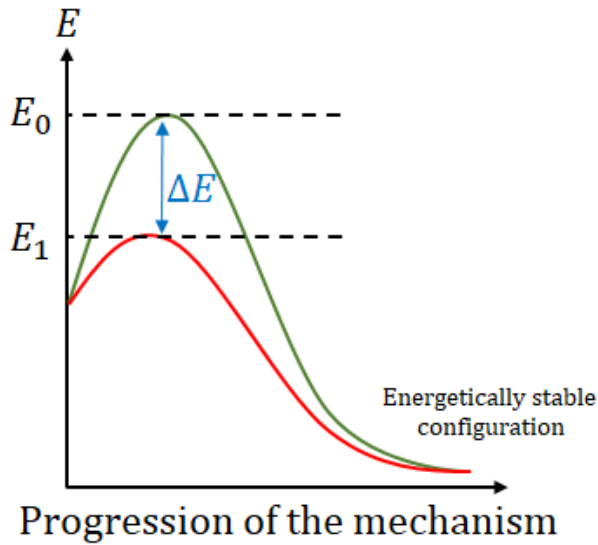


FIGURE 2.21: Diagram representing the activation energy for bond switching mechanism with and without irradiation. Under e-beam irradiation, the mechanism triggers at a lower energy state  $E_1$  than the initial activation energy  $E_0$  without irradiation.

be dissociated and the fit is a two-fitting parameters model instead of three. However, in the literature, the activation energy  $E_0$  required to detach and reattach a siloxane bond is usually around 90 kcal, which is nearly twice the bond energy [154]. Their values for each glass composition are displayed in Table 2.4.

	SiO <sub>2</sub>	ABS	SLS
C (GPa)	0.56	0.43	0.33
D (s <sup>-1</sup> )	$5.3 \times 10^{-5}$	$9 \times 10^{-5}$	$4.5 \times 10^{-5}$

TABLE 2.4: Fitting parameters of the Eyring model depending on the glass composition. The corresponding fits are represented in Fig. 2.18.

With the C values, an activation volume can be calculated for each glass. At room temperature, we obtained  $\Omega_{Silica} = 7 \text{ \AA}^3$ ,  $\Omega_{ABS} = 10 \text{ \AA}^3$ , and  $\Omega_{SLS} = 12 \text{ \AA}^3$  which is consistent with the value ( $9.7 \text{ \AA}^3$ ) obtained for amorphous silica by Kang *et al.* [138] with Transmission Electron Microscope (TEM) in-situ experiments on silica. However, the physical interpretation of these values has not yet been fully explored.

In Fig. 2.18, on the blue curve corresponding to pure silica (SiO<sub>2</sub>), the dotted black line representing the model fits well with the experimental data in the central region. However, there are noticeable deviations on both the left and right sides of the fitting model. A deviation on the right side, at high strain rates, corresponds to a saturation of the yield stress. At these high strain rates, the irradiation levels are low and do not significantly affect the material's plasticity. Consequently, the yield stress cannot exceed that of the original, unirradiated material, which has weak strain-rate dependence [157, 134]. Moreover, the strain rate probably exceeds the range where Eyring's model is valid which is based on activated plastic events with a limited maximum frequency. At high strain rates, the required frequency of plastic events surpasses what the model

can capture, leading to a poor fit with experimental data. We are therefore governed by a different mechanism. On the left side, at low strain rates, we find that Eyring's model doesn't fit the experimental data either, and another model could be more relevant. For instance, a different physics in the stretched exponential model ("fat tail"), described in section 2.3.1.b, fits well in this part of the plot (long times), especially concerning the normal glasses. In brief, in our case, the Eyring model is limited to a certain range of strain rates. Apart from these minor deviations, the model fits the silica quite well, which means that plasticity induced by thermally/mechanically activated bond-switching seems to describe the overall plastic deformation of the material particularly well.

Furthermore, these time-irradiation equivalences show us that theoretically, by applying a low strain rate (such as  $10^{-3}$  or  $10^{-4}s^{-1}$  on the curve), the material is capable of flowing at much lower yield stress than its initial value, without irradiation. Conversely, irradiation will allow the material to flow at lower yield stress if the strain rate is significant. We also have to keep in mind that the strain rate range depends on the reference current density condition initially chosen to shift the raw data. For example, by choosing the lowest current density condition as a reference, the strain rate range would have been from  $10^{-9}$  to  $10^{-2}s^{-1}$ . In this case, it means that silica can flow at 300 MPa if we wait for 30 years ( $10^9$  seconds), which is more plausible. Assuming that the time-current density equivalence is perfect, this choice is completely arbitrary. In terms of dynamics, whatever the reference, the interpretation is unchanged.

Finally, Fig. 2.13 exhibits an interesting relation between the shift factor  $S_J$  and the current density  $J$  with a slope of about 1 for the three glass compositions studied (Table 2.3). This direct proportionality indicates that the strain rate increases linearly with the current density, implying that the number of plastic events (bond-switching) is proportional to the number of electrons impinging on the pillar. The same plastic deformation (*i.e.* the same number of plastic events) is reached in half the time if the current density doubles. In on-going discussions, Morgan Rusinowicz pointed out that his linearity opens the door for another interpretation of the data, in which plastic events are directly triggered by the interaction with one/some electron with a plastic strain proportional to the charge. Experiments at elevated temperatures would help differentiate from the jump probability and activation energy approach involved in the Eyring model described in the present section.

### 2.4.3 Two relaxation mechanisms: analogy with dynamic measurements

In contrast to pure silica, a single Eyring model does not (almost) fully fit the master curves for ABS and SLS glasses as shown in Fig. 2.18. The model only matches one of the two strain rate regimes described in section 2.3.3. In the case of normal glasses, we observe a second regime, not (or much less) catalyzed by electron irradiation, at higher strain rates, which, in our opinion, reveal more "rapid" relaxation events. Since this regime doesn't exist in silica, we suggest that it involves the mobility of the network modifiers present in the structure of normal glasses and not in silica. Consequently, we ascribe the first regime, characterized by a relatively "slow" (*i.e.* "highly irradiated") relaxation, to the plasticity of the  $\text{SiO}_2$  matrix. As described in pure amorphous silica in the previous section, in this regime, irradiation catalyzes bond-switching events thus facilitating stress relaxation through the activation of plasticity in the material at a lower strain rate. As a first approach, we note that the ABS and SLS glass contain 70%  $\text{SiO}_2$  so that a strict proportionality

rule would predict a slope  $C$  reduced from 0.56 for silica to 0.39 for these two glasses which qualitatively agrees with the measured values (0.43 and 0.33). On the other hand, we observe that the more network glass formers (Si, B, Al) present in the glass, the higher the slope of the first regime. It is therefore likely that this initial regime describes not only the plasticity of the silica matrix but also that of the other network glass formers which would also be affected by irradiation.

As described in section 1.1.2.b, normal glasses contain a significant amount of network modifiers. Their presence leads to network depolymerization, which directly affects the material's thermal and mechanical properties. Other tests published in the literature have demonstrated the existence of two relaxation mechanisms, notably through the use of internal friction [158, 159].

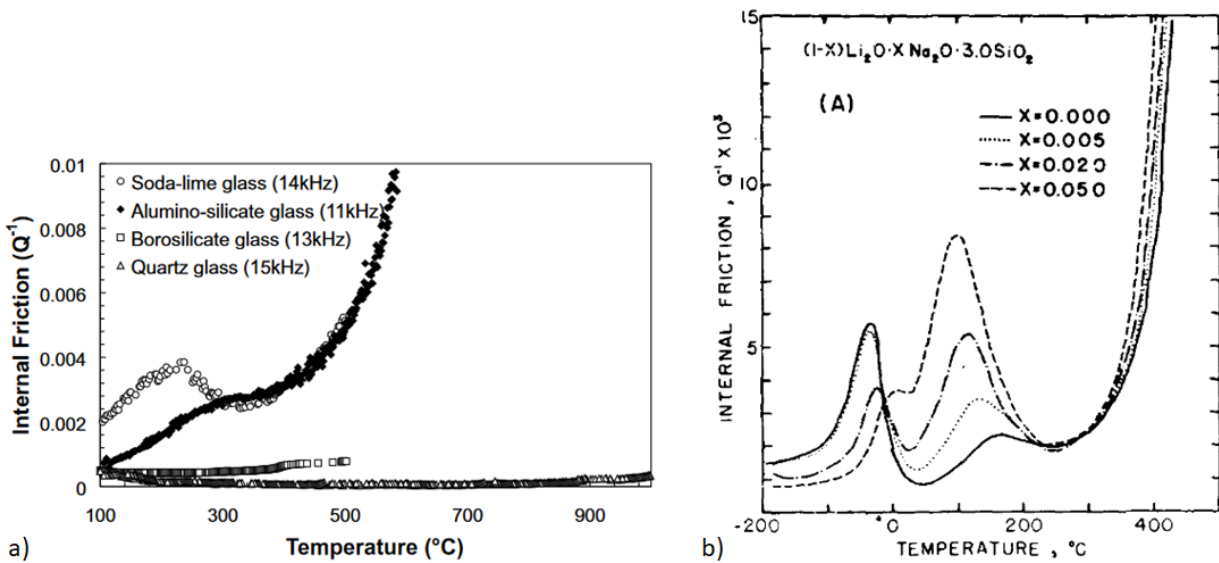


FIGURE 2.22: (a) Internal friction ( $Q^{-1}$ ) of four kinds of glasses as a function of the temperature (taken from [159]) and (b) progressive changes of the internal friction curves during gradual substitution of alkalis in  $(1-x)Li_2O \cdot xNa_2O \cdot SiO_2$  glasses (taken from [158]).

Internal friction evaluates the dissipation of mechanical energy when a glass sample is subjected to periodic, small strain, deformations (vibrations). These tests are carried out through temperature sweeps and the identification of the viscoelastic properties and especially the relaxation modes provide insight into atomic network structure and phase transitions. Fig. 2.22 displays two sets of internal friction measurements as a function of temperature for different silicate glasses. In this case, the temperature plays the same role as electron irradiation in our measurements since by increasing the temperature the energy ratio in the exponential from Eyring's equation (Equation 2.14) decreases. These experiments show that glasses containing a significant amount of network modifiers (SLS and AS) exhibit two regimes of dissipation. One peak at very high temperatures (at least over  $400^{\circ}C$ ) corresponds to the  $\alpha$  relaxation of the glass formers from the matrix, which is closely related to the glass transition. This  $\alpha$  relaxation represents the point at which the material undergoes significant molecular rearrangements as it transitions from a rigid, glassy state to a more flexible and dynamic state, marking the onset of viscoelastic behavior. Other peaks at lower temperatures correspond to the  $\beta$  relaxation of the network modifiers, which are clearly associated

with the localized motions of these modifiers within the structure. For example, since the borosilicate and the "quartz glass" (amorphous silica) in Fig. 2.22.a lack such network modifiers, they do not exhibit this secondary relaxation regime. Moreover, by substituting a network modifier for another (Fig. 2.22.b), the position of the peak corresponding to this relaxation  $\beta$  changes while the  $\alpha$  peak at 400°C does not change.

In analogy to these experiments, our interpretation of the relaxation experiments for normal glass involves two mechanisms: one governed by the matrix and the other one governed by the ions. Network modifiers, which have ionic bonding with lower dissociation energies (150 to 400 kJ/mol) compared to covalent bonds (200 to 1000 kJ/mol) [160], are expected to play a different role in the plasticity of ABS and SLS glasses. Our data suggest that these mechanisms are: 1) more easily activated by stress, which lowers the yield stress compared to silica; 2) less sensitive to electron irradiation, which seems reasonable given their ionic nature. In brief, our results suggest a direct connection between the small strain/low-stress relaxation mechanisms and the large strain/high-stress mechanisms of plasticity. In particular, they show that the dominant mechanism at room temperature in normal glasses is associated with the network modifiers.

#### 2.4.4 From strain rate to relaxation

Finally, we will establish a connection between the strain rate description as shown by Bruns (fig. 2.1b) and the time-dependent (relaxation) approach that we addressed using the stretched exponential model in section 2.3.1.b.

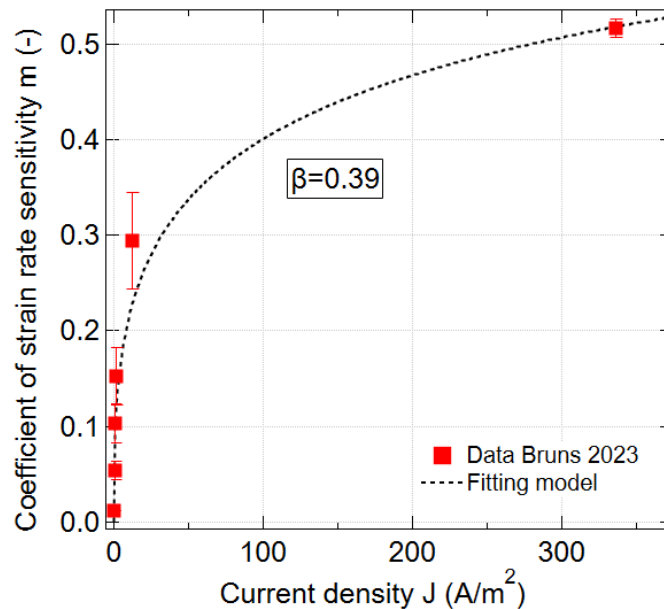


FIGURE 2.23: Data from Fig. 2.1.b [135] fitted with a law based on the stretched exponential model.

Indeed, the shift factor  $S_J$  scales the characteristic relaxation time  $\tau$ . Moreover, according to Fig. 2.13, we know that this shift factor  $S_J$  is inversely proportional to the current density  $J$  (considering a slope of 1). So we have  $\tau \sim S_J = \frac{\alpha}{J}$  with  $\alpha$  a constant. Moreover, the definition of the

coefficient of strain rate sensitivity [161] is given by:

$$m = \frac{\partial \ln \sigma}{\partial \ln \dot{\epsilon}_{vp}} = \frac{\partial \ln \sigma}{\partial \ln (-\dot{\sigma})} \quad (2.21)$$

where  $\dot{\epsilon}_{vp}$  is defined by the equation 2.12. Starting from equation 2.9 of the stretched exponential model and expressing  $t$  as a function of  $\sigma$ , we have:

$$\dot{\sigma} = -\frac{\sigma_0 \beta t^{\beta-1}}{\tau^\beta} \exp[-(t/\tau)^\beta] = -\frac{\beta t^{\beta-1}}{\tau^\beta} \sigma = -\frac{\beta}{\tau} \sigma \left( -\ln \left( \frac{\sigma}{\sigma_0} \right) \right)^{\frac{\beta-1}{\beta}} \quad (2.22)$$

Thus, we have to express  $\ln(-\dot{\sigma})$  as a function of  $\ln \sigma$ :

$$\ln(-\dot{\sigma}) = \ln \left( \frac{\beta}{\tau} \exp(\ln \sigma) \left( -\ln \left( \frac{\sigma}{\sigma_0} \right) \right)^{\frac{\beta-1}{\beta}} \right) = \ln \left( \frac{\beta}{\tau} \right) + \ln \sigma + \frac{\beta-1}{\beta} \ln \left( -\ln \left( \frac{\sigma}{\sigma_0} \right) \right) \quad (2.23)$$

Then, we can express equation 2.21 as:

$$\frac{1}{m} = \frac{\partial \ln(-\dot{\sigma})}{\partial \ln \sigma} = 1 + \frac{1-\beta}{\beta} \left( -\ln \left( \frac{\sigma}{\sigma_0} \right) \right)^{-1} = 1 + \frac{1-\beta}{\beta} \left( \frac{t}{\tau} \right)^{-\beta} \quad (2.24)$$

Finally, the expression of  $m$  as a function of  $J$  is:

$$m = \frac{1}{1 + \frac{1-\beta}{\beta} \left( \frac{t}{\tau} \right)^{-\beta}} = \frac{t^\beta}{t^\beta + \frac{1-\beta}{\beta} \tau^\beta} = \frac{t^\beta}{t^\beta + \frac{1-\beta}{\beta} \left( \frac{\alpha}{J} \right)^\beta} \quad (2.25)$$

which provides an expression for the strain rate sensitivity  $m$  as a function of the stretching fraction (exponent of the stretched exponential fit)  $\beta$ . A fit of this model to Bruns' data (Fig. 2.23) gives  $\beta = 0.39$ , to be compared with our value 0.23 for silica.

In the literature [144], two values of  $\beta$  can be found:  $\beta = 3/5$  follows the diffusion-trap theory for short-range forces, while  $\beta = 3/7$  describes a relaxation governed by longer-range interactions, as structural relaxation [146]. However, in our case,  $\beta$  is systematically smaller than the mentioned values. Most probably, these discrepancies are related to the heterogeneity of the electron irradiation which will produce a spread of the relaxation times. Indeed, the shadowing by the flat punch during the relaxation test may influence the homogeneity of the irradiation in the pillar and consequently, the stress relaxation homogeneity. Another parameter that can affect the homogeneity of the irradiation is the penetration depth of the electrons, which is of the order of the pillar size (sec. 2.1). Consequently, the slightest inhomogeneity reduces the value of  $\beta$ , which can explain why all the coefficients we obtained are smaller than  $3/5$  or  $3/7$ . The value obtained in Fig. 2.23 is closer to those found in the literature [146] compared to the  $\beta$  values we previously determined for our silicate glasses, but is very much dependent on the value of one single point... To achieve a more accurate fit, additional data points should be added to this graph, which would alter the  $\beta$  value.

## Conclusion

In this chapter, we have examined the impact of electron irradiation on the dynamics of plastic flow in different types of silicate glasses. For that purpose, we have used original experimental conditions, namely relaxation measurements under different irradiation conditions within the chamber of an SEM for three different glass compositions.

In many respects, electron irradiation at room temperature in silicate glasses plays the same role as temperature in other types of amorphous materials. In particular, we have shown that we can apply time-current density equivalence in a manner reminiscent of time-temperature superposition in polymers. When the experimental times are rescaled, a stretched exponential model works well to fit the stress *vs.* time master curve. However, the physical interpretation of these fits remains unclear and requires further investigation. In particular, the low value of the exponent  $\beta$ , about 0.25, suggests it may be due to heterogeneities within the sample rather than some intrinsic relaxation time distribution.

The same data can also be analyzed as families of stress-*strain rate* curves that can of course also be rescaled into a single master curve by time-current density superposition. We find that for amorphous silica the strain rate sensitivity curve can be mostly fitted by an Eyring model over more than 3 decades of strain rate, with deviations both at high and low strain rates. However, this model no longer applies to normal glasses at high strain rates (low irradiation). Under these conditions, a second regime emerges, likely related to the plastic rearrangement involving network modifiers, which are much less sensitive to irradiation.

This study highlights the complexity of plastic deformation mechanisms in different glass compositions under irradiation, illustrating the different impacts of the network and of the modified regions in the plastic response, which are differently affected by irradiation. Future research should focus on relaxation experiments applied to other glass compositions such as lead silicate glass (60SiO<sub>2</sub> - 25PbO - 5B<sub>2</sub>O<sub>3</sub> - 10Others [89]) which contains lots of network modifiers or such as borosilicate with a very low amount of network modifiers.

Finally, it is important to recognize that electron irradiation can introduce side effects and potential sources of error, especially in micro-scale mechanical characterization performed in situ inside an SEM. These effects can significantly impact the assessment of plastic flow behavior and fracture toughness, making small-scale approaches particularly susceptible to irradiation influences.



## Chapter 3

# Characterization of indentation cracking in alkaline-earth aluminoborosilicate glasses: densification vs plastic shear flow

### Contents

---

<b>3.1</b>	<b>Material and methods</b> . . . . .	<b>71</b>
<b>3.2</b>	<b>Glass properties</b> . . . . .	<b>79</b>
3.2.1	Thermal properties . . . . .	79
3.2.2	Mechanical properties . . . . .	80
3.2.3	Crack resistance measurements . . . . .	83
<b>3.3</b>	<b>Indentation cross-sections and plastic flow characterization</b> . . . . .	<b>84</b>
<b>3.4</b>	<b>Roughness measurements of the plastically deformed region</b> . . . . .	<b>87</b>
<b>3.5</b>	<b>Understanding what rules indentation cracking</b> . . . . .	<b>90</b>
3.5.1	Impact of the volumetric change on crack resistance . . . . .	90
3.5.2	Shear localizations and cracking susceptibility . . . . .	93
3.5.3	Composition dependence of local rearrangements and crack resistance . . . . .	98

---

## Introduction

Surface flaws play a significant role in determining the mechanical strength of glasses, as established by Griffith [29] in 1921. In the context of silicate glasses, the tendency to crack under indentation, such as in a Vickers test, is influenced by several factors, including the chemical composition of the glass and the geometry of the indenter (sec. 1.2.4).

Traditionally, densification has been identified as a key factor influencing indentation cracking, with certain glass compositions exhibiting greater crack resistance due to their ability to densify [59, 87]. More recent studies suggest that another approach might be considered. Indeed, at the very end of their review, Januchta and Smedskjaer [64] pointed out that most of the reviewed works have focused on the densification contribution to the indentation-induced deformation and that greater focus is needed on understanding shear flow mechanisms, along with developing methods to quantify shear characteristics. Indeed, it was later shown numerically that densification impacts the residual stress field in indentation in a more limited manner than usually assumed [125]. Clear evidence of shear localizations in the plastically deformed region in silicate glasses beneath Vickers indents has been highlighted by Gross *et al.* [94] resulting in very different shear patterns and crack resistances depending on the composition of the glass. Concerning the crack resistance investigation, other studies have shown that the amount of  $\text{Al}_2\text{O}_3$  in aluminosilicate glasses [162], just like the rare-earth cation size in aluminate glasses [163], directly affects their cracking susceptibility. Therefore, understanding the link between glass composition, shear band formation, and crack initiation is essential for improving the mechanical resistance of glasses.

This chapter aims to explore this relation by evaluating the effect of mixed glass formers ( $\text{SiO}_2$ ,  $\text{B}_2\text{O}_3$ ) and mixed alkaline-earth modifiers ( $\text{CaO}$ ,  $\text{MgO}$ ) in a series of aluminoborosilicate (ABS) glasses on crack susceptibility under indentation. These compositions closely resemble display-type glass compositions, specifically alkali-free aluminoborosilicates, and are relatively easy to melt in particular due to the lower viscosity resulting from the high boron content. They have also demonstrated a clear dependence on composition for shear band formation and cracking susceptibility [94]. More generally,  $\text{MgO}$  is known to enhance crack resistance [164], but the corresponding shear patterns have not been established yet. The proposed compositions may help to clarify the effect of the substitution of glass formers and network modifiers on shear band formation and its relation to crack resistance. This study will take up some of the experimental methods described in the chapter 1 to quantify these effects and identify a general trend applicable to different glass compositions. These investigations will provide a deeper understanding of the mechanisms of shear band formation in ABS glasses, considering the effects of the applied load, glass composition, and indenter geometry in relation to glass rupture properties.

### 3.1 Material and methods

#### Sample preparation and glass compositions

Eighteen glass samples were melted with composition  $(15 - y)\text{CaO} \cdot y\text{MgO} \cdot 15\text{Al}_2\text{O}_3 \cdot x\text{B}_2\text{O}_3 \cdot (70 - x)\text{SiO}_2$ , with  $x = 0, 5, 15, 25$  (mol%) (**Table 3.1**). In the case where  $x$  is 5 or 15, the substitution of CaO by MgO follows  $y = 0, 2.5, 5, 7.5, 10, 12.5, 15$  (mol%) (**Table 3.2**). Batches were mixed to yield 500 g of glass using industrial grade raw materials: silicon oxide  $\text{SiO}_2$  (99.9%), boric acid  $\text{H}_3\text{BO}_3$  (56.8 wt%), aluminum oxide  $\text{Al}_2\text{O}_3$  (99.9 wt%), calcium carbonate  $\text{CaCO}_3$  (55.5 wt%) and magnesium oxide  $\text{MgO}$  (99.3 wt%). After batches were prepared, small amounts (0.1 wt% of the total batch) of fining agent  $\text{SnO}_2$  were added to allow the removal of gas bubbles from the melt. For each batch, weighted raw materials were first melted in a 300 cc Pt-Rh crucible for 15h at a temperature of 1500 °C in an electric furnace and stirred one first time using a platinum rod to improve the homogeneity of the melt. After letting melt overnight (around 15h), the batch materials were stirred periodically and melted again at  $T_m + 30$  °C for 3h. An approximation of their glass transition temperature  $T_g$  was determined by using the Facstage<sup>®</sup> and Interglad<sup>®</sup> softwares, based on the viscosity calculation of each melt. Melted glasses were poured onto a carbon plate and placed in an electric furnace to cool slowly. They were annealed at  $T_g + 30$  °C for 1h and then cooled at 3 °C/min up to room temperature to reduce residual thermal stresses. All obtained glasses were transparent except the composition  $15\text{MgO} \cdot 15\text{Al}_2\text{O}_3 \cdot 25\text{B}_2\text{O}_3 \cdot 45\text{SiO}_2$  which showed a "bluish" transparent color after annealing probably due to phase separation. Each annealed glass was then cut and processed into several different samples. The glass transition temperature was precisely determined by a dilatometer (see next section). Finally, samples of the glasses were heated up in an annealer at 5 °C/min up to  $T_g + 30$  °C, held for 30 min, cooled at 3 °C/min down to  $T_g - 150$  °C and then cooled at 5°C/min down to room temperature to reduce residual mechanical stresses from post-processing.

TABLE 3.1: Single alkaline earth aluminoborosilicate glass compositions

Glass	SiO <sub>2</sub> (mol %)	B <sub>2</sub> O <sub>3</sub> (mol %)	Al <sub>2</sub> O <sub>3</sub> (mol %)	CaO (mol %)	MgO (mol %)
CAS1	70	-	15	15	-
CABS2	65	5	15	15	-
CABS3	55	15	15	15	-
CABS4	45	25	15	15	-
MAS1	70	-	15	-	15
MABS2	65	5	15	-	15
MABS3	55	15	15	-	15
MABS4	45	25	15	-	15

TABLE 3.2: Dual alkaline earth aluminoborosilicate glass compositions.

Glass	SiO <sub>2</sub> (mol %)	B <sub>2</sub> O <sub>3</sub> (mol %)	Al <sub>2</sub> O <sub>3</sub> (mol %)	CaO (mol %)	MgO (mol %)
CMABS1	65	5	15	12.5	2.5
CMABS2	65	5	15	10	5
CMABS3	65	5	15	7.5	7.5
CMABS4	65	5	15	5	10
CMABS5	65	5	15	2.5	12.5
CMABS6	55	15	15	12.5	2.5
CMABS7	55	15	15	10	5
CMABS8	55	15 </td <td>15</td> <td>7.5</td> <td>7.5</td>	15	7.5	7.5
CMABS9	55	15	15	5	10
CMABS10	55	15	15	2.5	12.5

## Measurement of glass properties

### Thermal properties

The glass transition temperature  $T_g$  and coefficient of thermal expansion  $CTE$  were estimated with thermomechanical analysis (TMA) by using a Bruker AXS TD5000SA machine (differential dilatometer) under He gas flow. The maximum temperature that can be reached is around 900°C and a heating rate of 3°C/min was applied. Those measurements have been performed by a technician from NEG company.

### Mechanical properties

Mechanical properties were measured. Density was determined using Archimedes' method (water displacement) with an uncertainty of  $\pm 0.0002 \text{ g/cm}^3$ .

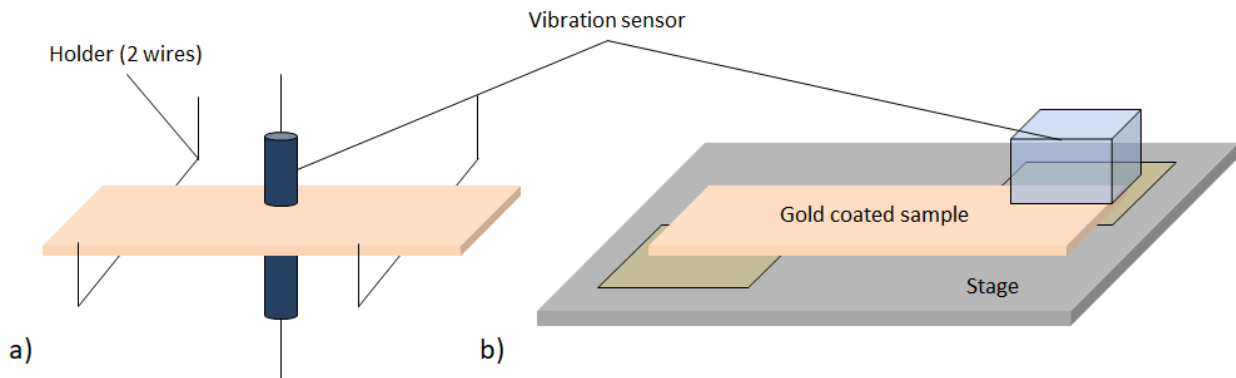


FIGURE 3.1: Diagram of the resonance method for measuring (a) the Young's modulus  $E$  and (b) the shear modulus  $G$ .

Young's modulus ( $E$ ) and shear modulus ( $G$ ) were measured by resonance method using the ASTM standard issued under the fixed designation E1875-08, with  $40 \times 20 \times 2 \text{ mm}^3$  samples. A

Japan Techno-Plus JE-RT3 with Young's modulus (JR-RT) and Shear Modulus (JG) modules were used to estimate these two elastic moduli. Each sample has first been gold coated for 2 min. The diagram of the method is shown in Fig. 3.1 above. The frequency at which the measured intensity is highest is defined as the resonance frequency  $f$ . From this value, we can calculate Young's modulus  $E$  and shear modulus  $G$  from the sample dimensions with the following equations:

$$E = 0.9465 \cdot \frac{Mf^2}{w} \cdot \left(\frac{L}{t}\right)^3 \cdot \left(1 + 6.59 \left(\frac{t}{L}\right)^2\right) \quad (3.1)$$

$$G = 3.933 \cdot \frac{MLf^2}{wt} \cdot \left(\frac{s + 1/s}{4s - 2.52s^2 + 0.21s^6}\right) \quad (3.2)$$

where  $L$  is the length of the sample,  $t$  is the thickness,  $w$  is the width,  $M$  is the weight, and  $s = t/w$ . The bulk modulus ( $K$ ) and the Poisson ratio ( $\nu$ ) were then calculated using the standard relations ([10]):

$$K = \frac{EG}{(9G - 3E)} \quad (3.3)$$

$$\nu = \frac{E}{2G} - 1 \quad (3.4)$$

Reduced Young's modulus  $E_r$  values were also measured by nanoindentation by extracting the slope upon unloading [165], as Fig. 3.2 shows:

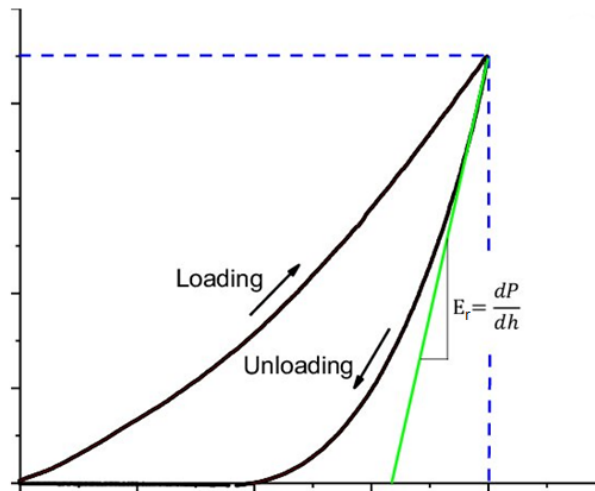


FIGURE 3.2: Typical nanoindentation mechanical response. The slope of the curve upon unloading is indicative of the stiffness and can be used to calculate the reduced Young's Modulus.

Then Young's Modulus  $E$  is extracted by:

$$\frac{1}{E_r} = \frac{1 - \nu_i^2}{E_i} + \frac{1 - \nu^2}{E} \quad (3.5)$$

where  $\nu_i$  and  $E_i$  are respectively the Poisson ratio and Young's modulus of the indenter, and  $\nu$  is the Poisson ratio of the glass. These values were compared with those obtained by resonance, and the two methods appear to provide very similar results, as shown in Fig. 4.6 in the appendix 2.

To determine Vickers hardness, 30 indents were made at 100 gf and a dwelling time of 15 s with a microhardness tester (MXT50, Matsuzawa Seiki Corp., Japan). Diagonals for each indent were measured and the Vickers hardness ( $HV$ ) values were then calculated using the following equation:

$$HV = \frac{2 \sin\left(\frac{\theta}{2}\right) \cdot F}{D^2} = \frac{1.8544 \cdot F}{D^2} \quad (3.6)$$

where  $F$  is the applied load,  $\theta$  is the  $136^\circ$  angle between opposite faces of the Vickers tip, and  $D$  is the diagonal length of the indent. The hardness unit is  $HV$  (or  $\text{kgf}/\text{mm}^2$ ). To convert  $HV$  to GPa, we have to multiply by 0.009807.

Some details of the method to measure crack resistance have been given in section 1.2.4.b. In brief, to estimate the value of crack resistance ( $CR$ ), the glass sample is indented by a Vickers indenter under a controlled atmosphere ( $25^\circ\text{C}$  and 30% relative humidity) and the corners where radial cracks appear are counted. The load is gradually increased from 100 gf to 6 kgf and 40 indents were performed for each applied load. The probability of crack initiation ( $PCI$ ) can be calculated by dividing the total number of radial cracks  $n_{RC}$  by the total number of corners  $n_{corners}$ . Finally, the load at which  $PCI = 50\%$  is determined as  $CR$  ([166]).

### Recovery of Indentation Depth

To evaluate densification, we have measured the recovery of indentation depth ( $RID$  - [59, 87]) as described in sec. 1.2.3.b. In short, Vickers indentation depths  $d_{before}$  and  $d_{after}$  are measured before and after annealing at  $0.9 \times T_g$  (K) for 2h and the  $RID$  is defined by

$$RID = \frac{d_{before} - d_{after}}{d_{before}} \quad (3.7)$$

To assess the indentation deformation mechanism of the glasses, we also measured the recovery of the indent side length. Like  $RID$  measurements, this method involves capturing topographic pictures of the indent size both before and after thermal treatment at  $0.9 \times T_g$  for 2 hours (Fig. 3.3). This process measures how much the side length of the indent cavity contracts upon annealing. For each specimen, we analyzed 3 indents with a load of 100 gf with a dwell time of 10 seconds

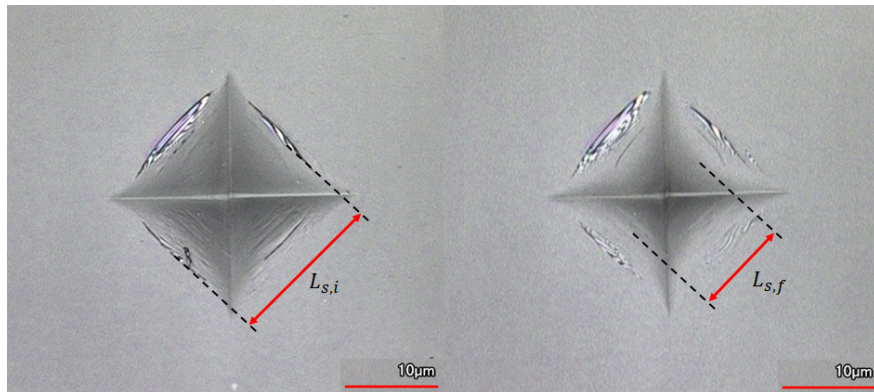


FIGURE 3.3: Laser scanning microscope pictures of indents produced at 100 gf on the surface of the CABS4 glass compositions before and after annealing at  $0.9 \times T_g$  for 2 hours.

and the indentation side length was measured using a laser scanning microscope before ( $L_{s,i}$ ) and after ( $L_{s,f}$ ) annealing. Similar to the recovery of indentation volume as per Yoshida's method [59], the densification contribution to the overall indentation deformation is estimated from the temperature-induced side length recovery ( $L_{SR}$ ):

$$L_{SR} = \frac{L_{s,i} - L_{s,f}}{L_{s,i}} \quad (3.8)$$

## Plastic flow characterization

### Cross-section preparation

Cross-sections of 500 gf and 1 kgf Vickers indents were prepared by using Peter's method [69] which has been used later by Hagan [167, 168, 1] and more recently by Gross [94]. This technique involves indenting across a pre-existing crack introduced into a  $25 \times 5 \times 1 \text{ mm}^3$  glass specimen by performing a line of dozen indentations at 1 kgf. The crack is slowly propagated with a 3-point bending setup until it reaches 1 mm in length from each side of the indents line. When the load is released, a part of the crack becomes invisible. Indentations at several loads were then made along the crack at different positions and each new indent reveals a visible part of the crack, as illustrated in Fig. 3.4.

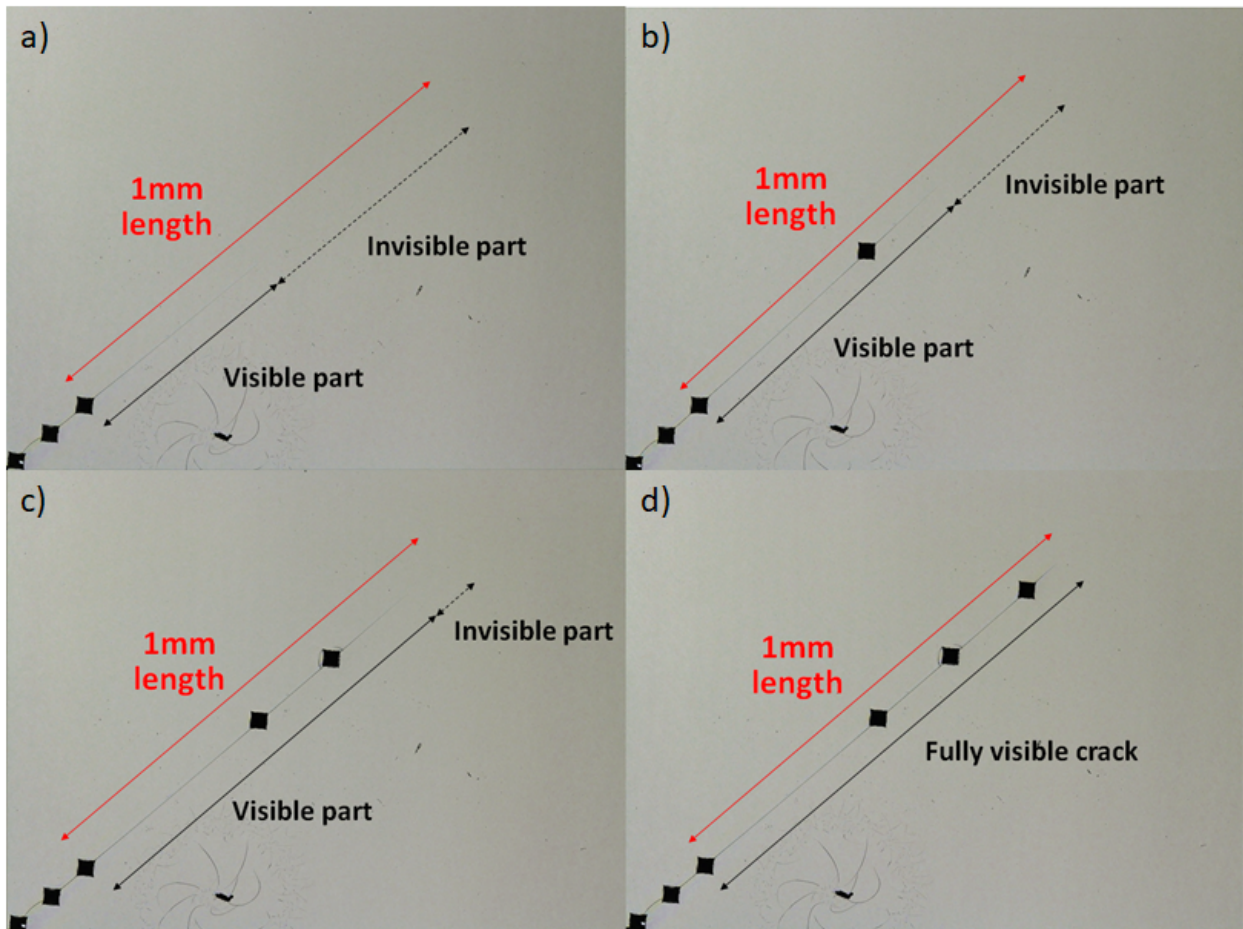


FIGURE 3.4: Gradual indentation process along the propagated main crack revealing the latter. Pictures were taken with a Laser Scanning Microscope.

The distance between two indents must be at least  $100\ \mu\text{m}$  to prevent the stress field of the previous indent from affecting the indentation pattern of the next one. The two faces of the glass specimen are finally separated by fully propagating the pre-existing crack with the same 3-point bending setup.

### Laser Scanning Microscope (LSM)

The indentation cross-sections from both sides have been observed at the Nippon Electric Glass Co.,Ltd. with a VK-X250K/X260K Laser Scanning Microscope from KEYENCE company. The observation was performed with the highest magnification (X28k) and a single scan mode was used. Samples were fixed vertically on the holder with double-face tape to observe their edges where the plastically deformed region of the indentation cross-section is located. Fig. 3.5 gives a concrete overview of the area observed after separating the two faces.

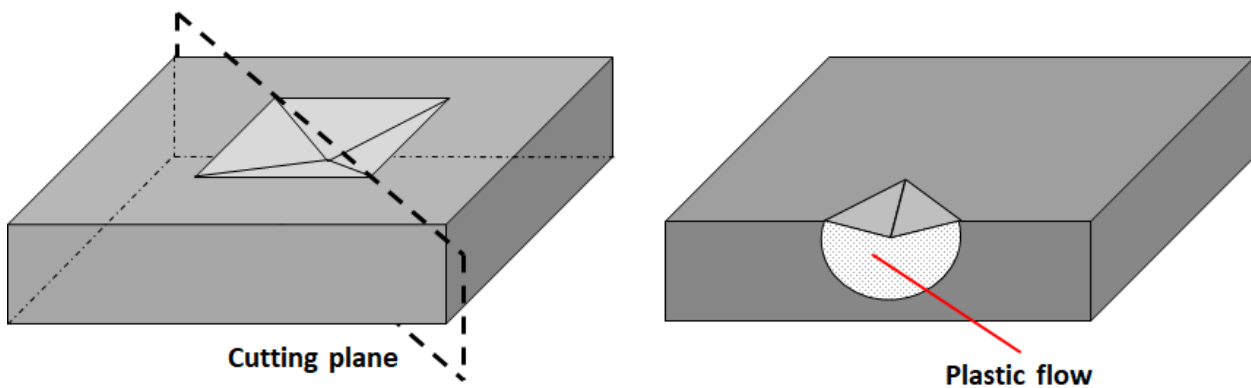


FIGURE 3.5: Visualization of plastic deformation under an indentation load, showing the cutting plane of the imprint (left) and the plastic flow in the surrounding material (right)

### Roughness and spacing measurements

The roughness of the plastically deformed region under indents was determined by using the multi-line roughness measurement from the MultiFileAnalyzer software (VK-H1XME, KEYENCE).

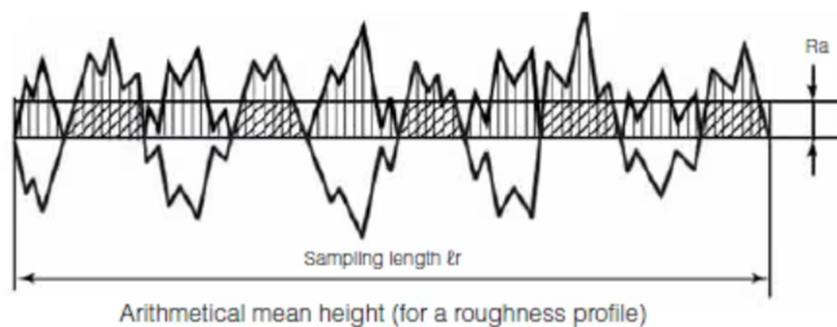


FIGURE 3.6: Roughness measurement process performed by KEYENCE software.  $R_a$  is referred to as the arithmetic mean roughness.

This function sets multiple measurement lines parallel to an initial line given by the user and calculates the roughness  $Ra$  of each line with (see Fig. 3.6)

$$Ra = \frac{1}{l_r} \int_0^{l_r} |Z(x) - \bar{Z}| dx \quad (3.9)$$

Similarly, the characteristic length between roughness features was measured from (see Fig. 3.7)

$$Rsm = \frac{1}{m} \sum_{i=1}^m X_{si} \quad (3.10)$$

Concerning the  $Rsm$  value,  $X_{si}$  is the length of a single profile element. The peaks (valley) will be treated as noise and considered a part of the preceding valley (peak) if the height (depth) is less than 10% of the maximum height or the length is less than 1% of the segment length.

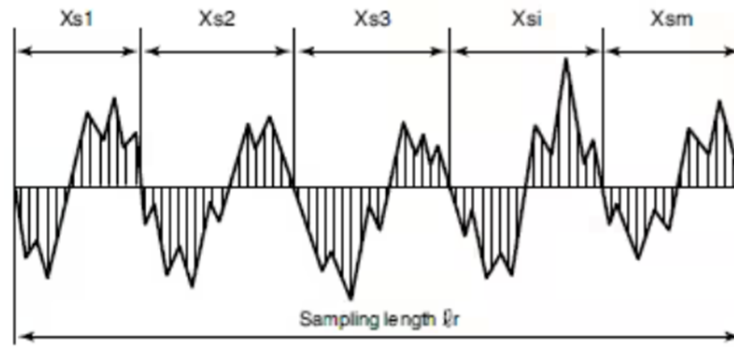


FIGURE 3.7: Spacing measurement process performed by KEYENCE software.

### Scanning Electron Microscopy (SEM)

The indentation cross-sections on soda-lime silicate glass were observed in ESPCI with a Quattro Environmental Scanning Electron Microscope (ESEM - ThermoFisher®). Observations were conducted at room temperature and in a low vacuum mode under a 100 Pa atmosphere. This mode allows the observation of the sample without gold coating.

### Finite Element modelling

We have modeled the indentation process by FEA (ABAQUS 2016) to better understand the distribution of plastic flow and the stress fields in silicates. We used an axisymmetric geometry and elastic properties used for the indenter and the glass are  $E_{indenter} = 1000$  GPa,  $\nu_{indenter} = 0.07$ ,  $E_{glass} = 72$  GPa and  $\nu_{glass} = 0.18$ . the plastic deformation was described by a no-hardening plasticity with a yield stress  $\sigma_{y_{glass}} = 6.5$  GPa. We applied a load of 1 kgf. A large strain formulation was used, and the contact was modeled using the penalty method in frictionless conditions. Four-node fully integrated elements (CAX4) were used for both the indenter and the glass. A high mesh density was used near the contact area with an average element size of 0.25  $\mu\text{m}$  (Fig. 3.8).

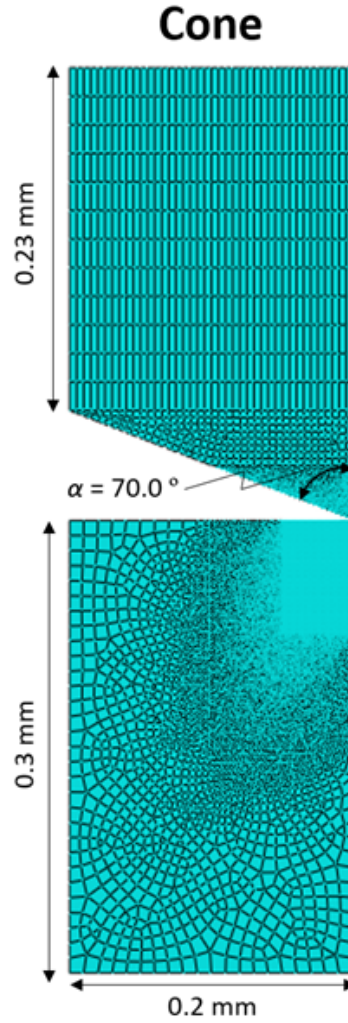


FIGURE 3.8: FEA solid model used for obtaining the pressure and strain fields as well as fitting nanoindentation experimental results using cone indenter. The cone indenter semi-angle  $\alpha$  is indicated in the figure.

Even though the pressure-dependant yield criteria has been found effective in predicting the elastoplastic behavior of silica glass [123], in our case, this constitutive model has not been calibrated for the investigated glass compositions (sec. 1.2.5.b). For this reason, given the moderate free volume of glasses considered here, we use the Von Mises criterion as a first approximation [125]. The yield surface is described as

$$\sigma_y = \sqrt{3J_2} = \sqrt{\frac{1}{2}((\sigma_{11} - \sigma_{22})^2 + (\sigma_{22} - \sigma_{33})^2 + (\sigma_{33} - \sigma_{11})^2) + 3\sigma_{12}^2} \quad (3.11)$$

where  $J_2$  is the second invariant of the deviatoric stress tensor. With this constitutive relation, we will use the results to derive the material flow stress  $\sigma_y$  from nanoindentation load-displacement measurements. In parallel, the flow stress was also determined directly from micro-hardness values by using a phenomenological model [169, 125] which predicts:

$$\frac{H_V}{\sigma_y} = \frac{\zeta_1 \tan \beta}{(1 - \zeta_2) \frac{\sigma_y}{E} + \zeta_3 \tan \beta} \quad (3.12)$$

where the constants  $\beta$  and  $\zeta$  depend on the tip geometry. This relation was derived from FEA calculations using a J2 yield criterion as well. Then it is possible to compare flow stresses determined by nanoindentation and those determined by micro-indentation.

## 3.2 Glass properties

### 3.2.1 Thermal properties

Knowing the glass transition temperature  $T_g$  is important for annealing glass samples that have been cut into the required shape for mechanical or thermal testing but also to measure the *RID* according to the specifications by annealing at  $0.9 \times T_g$ . The results of the glass transition temperature measurements of all glasses are displayed in Fig. 3.9.

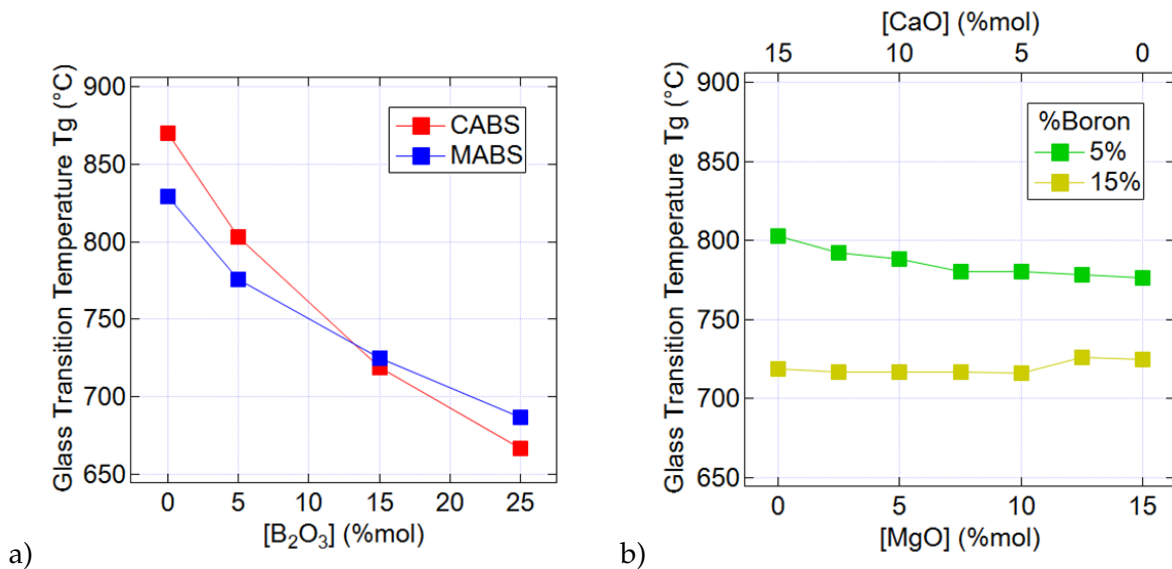


FIGURE 3.9: Glass transition temperature  $T_g$  of (a) single alkaline earth ABS glasses as a function of  $B_2O_3$  content and (b) mixed alkaline earth ABS glasses as a function of MgO/CaO content. Error bars are smaller than the markers' size.

The left graph (a) shows  $T_g$  as a function of boron content (which is substituting silica) in mol%, comparing single alkaline earth network modifier glasses (CABS and MABS). It reveals a clear decreasing trend in  $T_g$  with increasing boron concentration, where CABS glasses exhibit slightly higher  $T_g$  values than MABS glasses from 0 to 15% of boron. However, at higher than 15% of boron content, MABS glasses exhibit higher  $T_g$  than CABS. The right graph (b) depicts  $T_g$  as a function of magnesium concentration in the mixed calcium-magnesium glasses, for two different boron concentrations (5% and 15%). This graph indicates that the  $T_g$  remains relatively constant (or decreases slightly in the case of 5% boron) with increasing MgO content. The evolution of the glass transition temperature in Fig. 3.9.a and Fig. 3.9.b will be further discussed when we consider the possible atomic rearrangement mechanisms in section 3.5.3.

### 3.2.2 Mechanical properties

#### 3.2.2.a Elastic moduli

The measured values of Young's modulus and Poisson ratios are shown in Fig. 3.10 and also given in the appendix (Table 4.1).

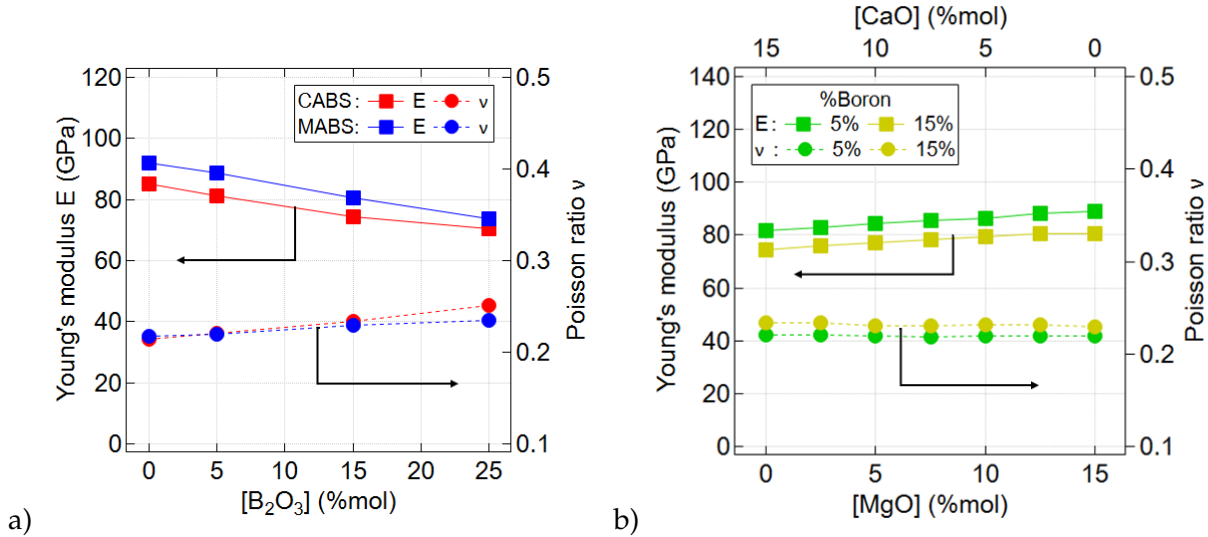


FIGURE 3.10: Young's Modulus  $E$  and Poisson ratio  $\nu$  of (a) single alkaline earth ABS glasses and (b) mixed alkaline earth ABS glasses. Error bars are smaller than the markers' size.

The left graph (a) shows the effect of  $B_2O_3$  content on both  $E$  and  $\nu$  for CABS and MABS. As the boron content increases, Young's Modulus decreases for both CABS and MABS, indicating a reduction in the stiffness of the material. Meanwhile, the Poisson ratio remains relatively stable, with CABS showing slightly higher values than MABS across the range of  $B_2O_3$  concentrations. On the other hand, the right graph (b) examines the influence of the substitution of calcium by magnesium on  $E$  and  $\nu$ . Young's Modulus slightly increases with increasing  $MgO$  content. There is no effect of the substitution of network modifiers on the Poisson ratio.

These experimental results can be compared to the Makishima-Mackenzie model [8, 9] (see section 1.1.1.b) which predicts Young's modulus from the atomic packing density and the dissociation energy. We considered the ionic radius and the dissociation energy of either a 3-coordinated boron (0.01 Å, and 15.6 kJ/cm<sup>3</sup> respectively) or a 4-coordinated boron (0.11 Å, and 82.8 kJ/cm<sup>3</sup> respectively) [24, 9]. This comparison is shown in Fig. 3.11. The prediction for Boron III closely follows the experimental data, while the predictions for Boron IV go in the opposite direction. Similarly, on the right (b), experimental results are closer to the predictions from 3-coordinated boron than from 4-coordinated boron although the agreement is not as good. From these comparisons, we conclude that boron is predominantly 3-coordinated in the structure of all the glasses investigated. However, it is possible that the substitution of calcium by magnesium in the case of 5% boron could lead to a change in boron coordination. We will attempt to develop this discussion in the section 3.5.3.

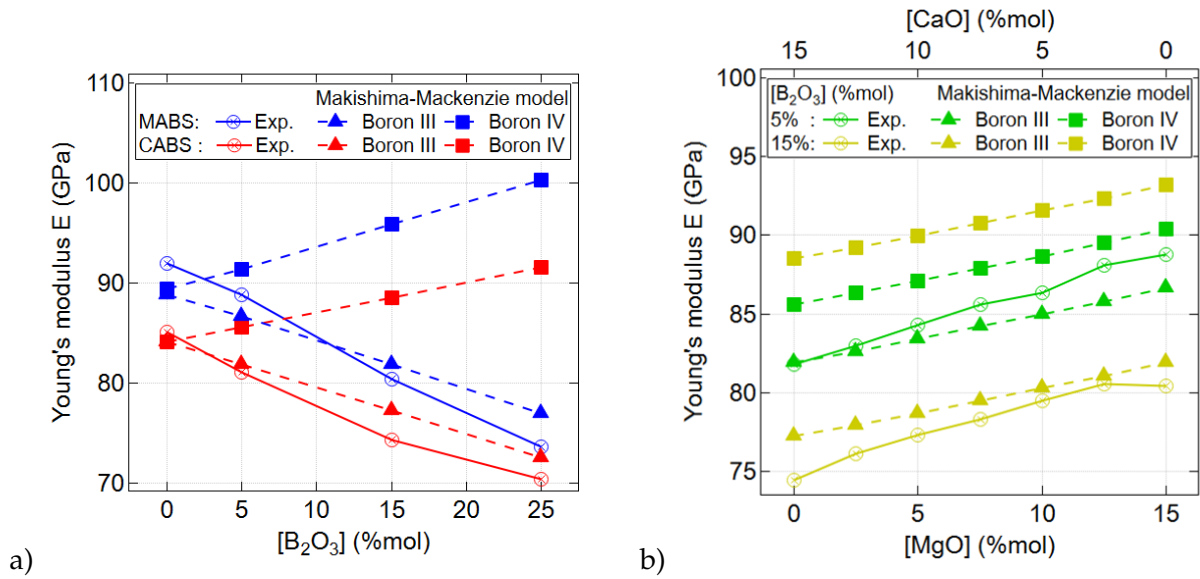


FIGURE 3.11: Comparison of Young's modulus obtained experimentally with Makishima-Mackenzie model depending on the boron coordination for (a) single alkaline earth ABS glasses and (b) mixed alkaline earth ABS glasses.

### 3.2.2.b Hardness and flow stress

As explained in sec. 1.1.1, Vickers micro-hardness is a technique that allows a first approach to characterizing the plasticity of silicate glasses.

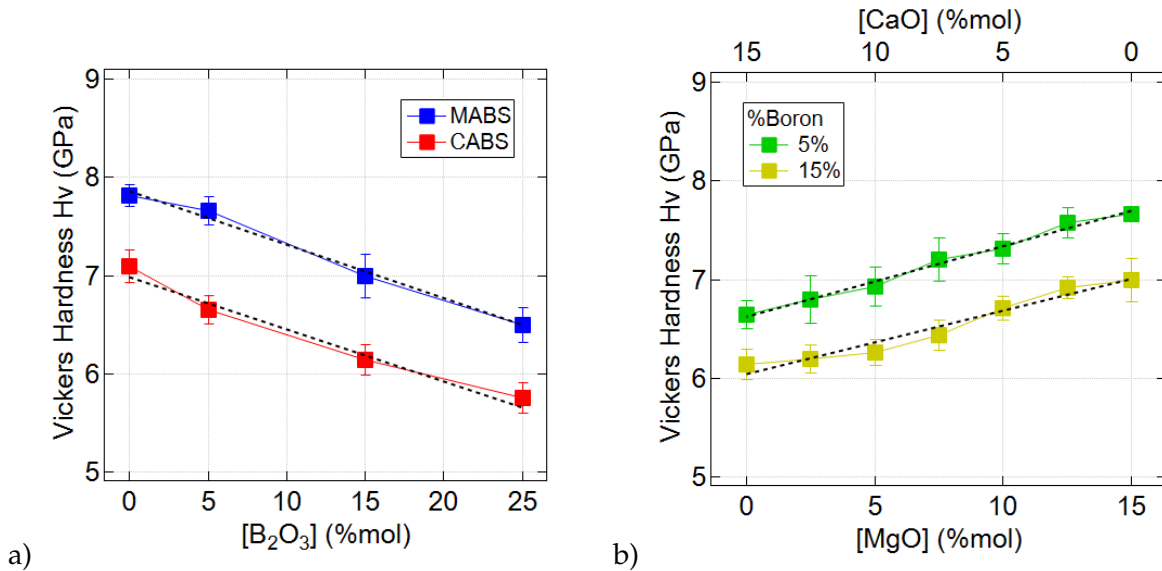


FIGURE 3.12: Vickers hardness  $H_V$  measured by micro-indentation of (a) single alkaline earth ABS glasses and (b) mixed alkaline earth ABS glasses. Error bars could be smaller than the markers' size.

Fig. 3.12 illustrates the variation in Vickers hardness  $H_V$  as a function of glass composition for (a) glasses with a single network modifier, and (b) glasses with mixed network modifiers. The hardness decreases linearly (a) with increasing boron content for both MABS and CABS glass compositions. MABS glasses exhibit higher hardness values than CABS glasses across all  $B_2O_3$

concentrations. Consequently, it is not surprising that the hardness increases with the substitution of calcium by MgO in glasses containing two network modifiers (b), regardless of the boron content. We also note that the evolution is linear.

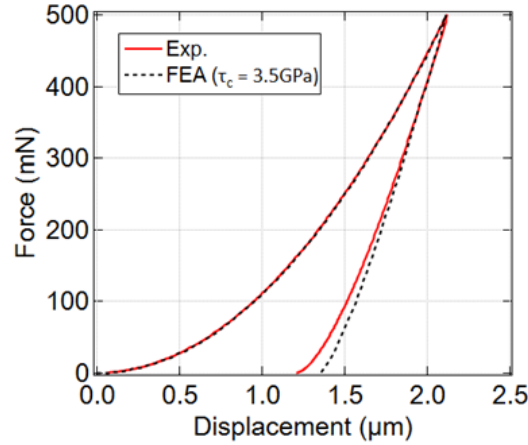


FIGURE 3.13: An example of nanoindentation experiments fitted with FEA calculations for CAS1 composition.

These data can be used to estimate the flow stress of the material by using the J2 plasticity phenomenological model [169, 125] described in section 3.1. Additionally, we can also extract the flow stress from nanoindentation experiments by fitting experimental and calculated mechanical responses, as Fig. 3.13 shows. The fit is mainly done with the loading part of the experimental result. Consequently, this fit shows some discrepancies upon unloading, especially concerning the residual indentation depth which is overestimated by the FEA calculation. This difference comes from the Von Mises model which does not perfectly describe the plasticity of our materials. However, as explained in sec. 1.2.5.a, we think it is a useful approximation.

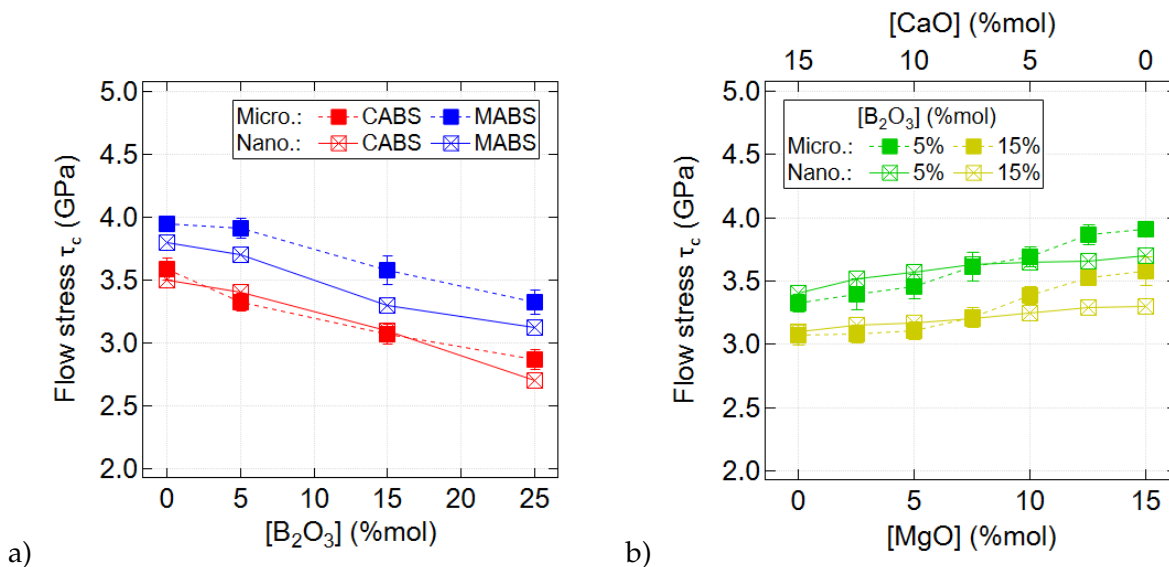


FIGURE 3.14: Flow stresses  $\tau_c$  obtained from experimental Vickers hardness by using a J2 plasticity phenomenological model and comparison with flow stresses determined from FEA calculation for (a) single alkaline modifier ABS glasses and (b) mixed alkaline earth ABS glasses.

The flow stress, in Fig. 3.14 in both single and double network modifiers compositions follows the same trends as the Vickers hardness and as expected, nanoindentation and micro-indentation results are generally in agreement. Most interestingly, We also notice that there is a slight difference for high boron content in CABS and for high magnesium content at all boron content. This result suggests that these glasses have a different size effect than the others.

### 3.2.3 Crack resistance measurements

The relationship between CR and compositions is plotted in Fig. 3.15 and the values are given in Table 4.1 in appendix 2. For CABS (Fig. 3.15.a),  $B_2O_3$  has a strong impact and the crack resistance increases sharply from 3N to 25N between a boron-free composition and 25%  $B_2O_3$ . When calcium is replaced by magnesium, the CR is high throughout the range with a very moderate increase from 27N to 33N, ie for MgO,  $B_2O_3$  does not affect CR. In the case of compositions with mixed modifiers (Fig. 3.15.b), with 5%  $B_2O_3$ , the presence of MgO enhances crack resistance. However, with 15%  $B_2O_3$ , CR is high, the substitution of CaO by MgO has a very limited effect and the crack resistance remains constant around 30 N, regardless of the amount of magnesium added. These results suggest that the substitution of silica for boron and the substitution of calcium for magnesium represent two different strengthening mechanisms that we will discuss in section 3.5.3.

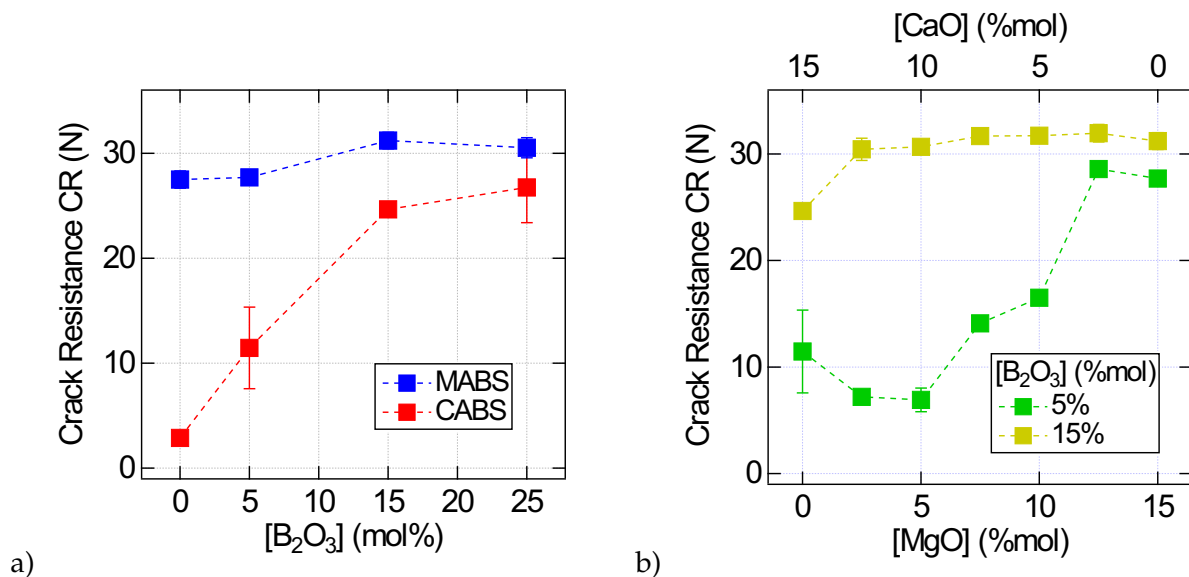


FIGURE 3.15: Crack resistance CR of (a) single alkaline earth ABS glasses and (b) mixed alkaline earth ABS glasses. Error bars could be larger or smaller than the marker's size.

### 3.3 Indentation cross-sections and plastic flow characterization

To characterize plastic deformation under Vickers indentation, 0.5 and 1 kgf indentation cross-sections have been prepared. For visual clarity, only cross-sectional views of the deformation zones for 1 kgf indents are presented in this section. Similar results were found on the 0.5 kg indents.

Fig. 3.16 shows an indentation cross-section in soda-lime glass observed under the environmental scanning electron microscope. Significant shear localization appears in this picture.

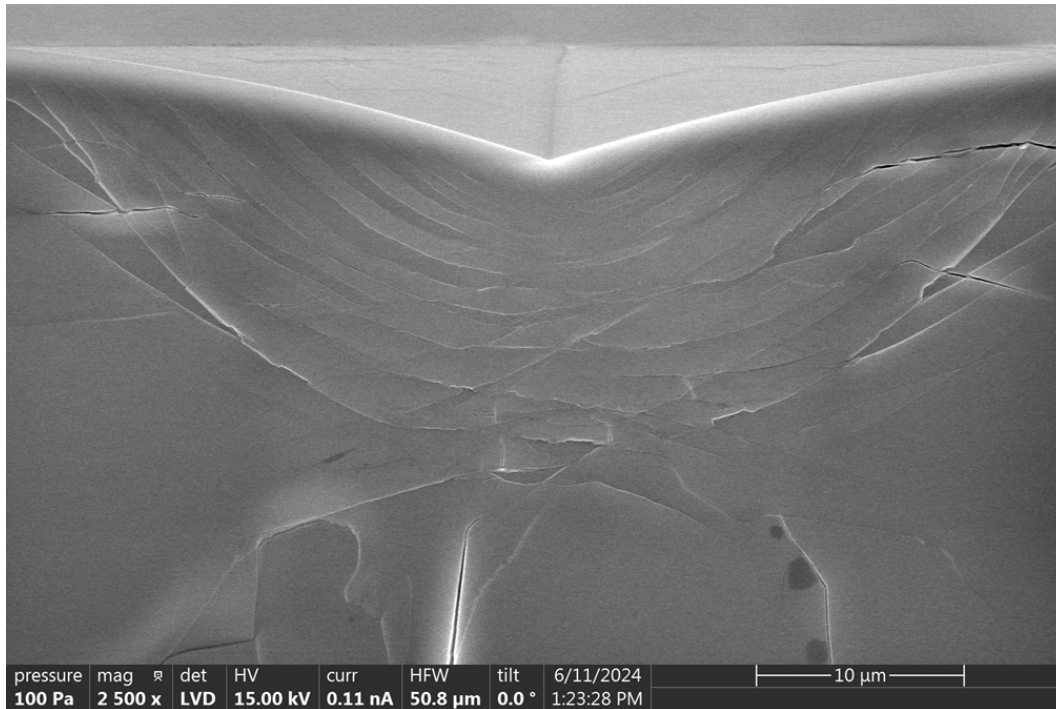


FIGURE 3.16: Scanning Electron picture of 1 kgf Vickers indentation cross-section in soda-lime silicate glass. Contrasts from shear bands and cracks are different.

Moreover, optimized environmental and electronic conditions clearly reveal the presence of both open cracks and shear bands. A crack is surrounded by a white contrast, and a gap is observed, while shear bands exhibit a more subtle and diffuse contrast without any gap in between.

The cross-sections in both series of glasses have been systematically observed at lower resolution by laser scanning microscopy. Fig. 3.17 contrasts low (CAS1 - a top) and high (CABS4 - a bottom)  $B_2O_3$  glasses as well as Ca (CAS1 - a top) and Mg (MAS1 - b) glasses. The measured CR is also given in each graph. One first notable observation in Fig. 3.17.a is that the size of the plastically deformed area below the indentation increases with higher levels of boron content which is consistent with the trend of the flow stress discussed in section 3.2.2.b. Composition CAS1 without  $B_2O_3$  exhibits significant shear localization over the full plastically deformed region and a low crack resistance. When we substitute  $SiO_2$  by  $B_2O_3$  (Fig. 3.17.a), the crack resistance increases almost by a factor of 9, and shear localization has been significantly reduced, especially in the middle of the plastically deformed region. It is still visible on the edges. Remarkably, when calcium (CAS1) is substituted by magnesium (MAS1) in a boron-free glass (Fig. 3.17.b), we find that the shear bands are also less visible, although they are still present in the middle region of the

plastically deformed zone. In this case,  $CR$  has also increased very significantly and is as large as for the Boron-rich sample.

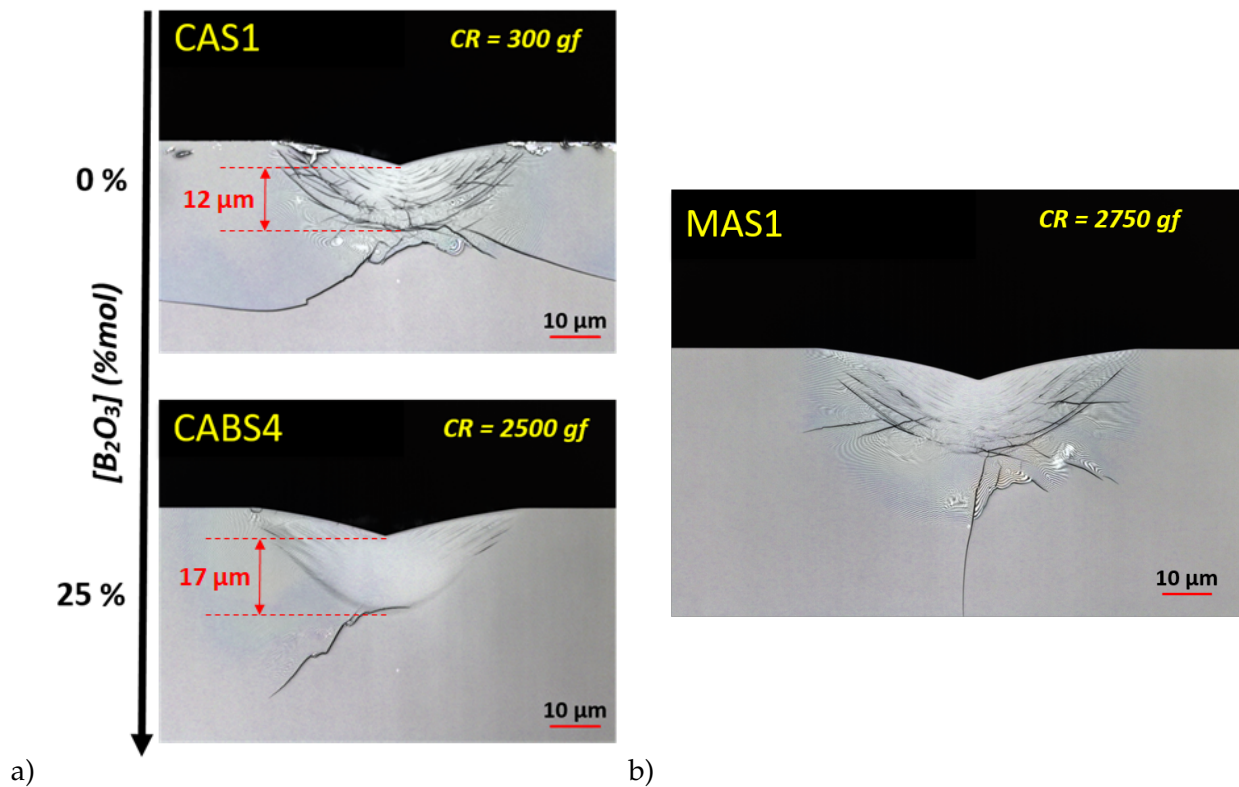


FIGURE 3.17: Cross-sections through 1 kgf Vickers indents in (a) calcio-aluminoborosilicate glasses and (b) magnesio-aluminosilicate glass.

The same trends are observed throughout the composition range investigated. For example, Fig. 3.18 shows indentation cross sections for mixed network modifiers glasses. In the magnesium-free glass with 5% B<sub>2</sub>O<sub>3</sub> (CABS2), significant shear bands are observed over all the plastically deformed area and the crack resistance is about 900 gf. For a substitution of 10% of calcium by magnesium (CMABS4), the crack resistance doubles and the center of the plastically deformed region contains less visible shear bands whereas the same shear patterns appear on the edges in both cases. A similar morphology is observed when increasing the boron content from 5% (CABS2) to 15% (CABS3) in the calcium glass and the crack resistances are also very close. Finally, for an increase from 5% (CMABS4) to 15% (CMABS9) boron in the 10% magnesium glass, the sides of the plastically deformed region still remain somewhat affected by shear bands but the middle region gets even smoother and no lateral crack is visible below the plastically deformed area. The crack resistance increases again, by approximately 1 kgf.

A panel including cross-sections of Vickers indent for all the compositions is presented in appendix 3. It shows the gradual decrease of the amount of shear bands in the middle of the plastically deformed region with the increase of boron content (columns) while  $CR$  increases. The same trend is observed for the substitution of CaO by MgO (rows). In all cases, lateral cracks below the plastically deformed region also gradually vanish with the increase of crack resistance and the disappearance of significant shear bands over the middle of the plastically deformed area.

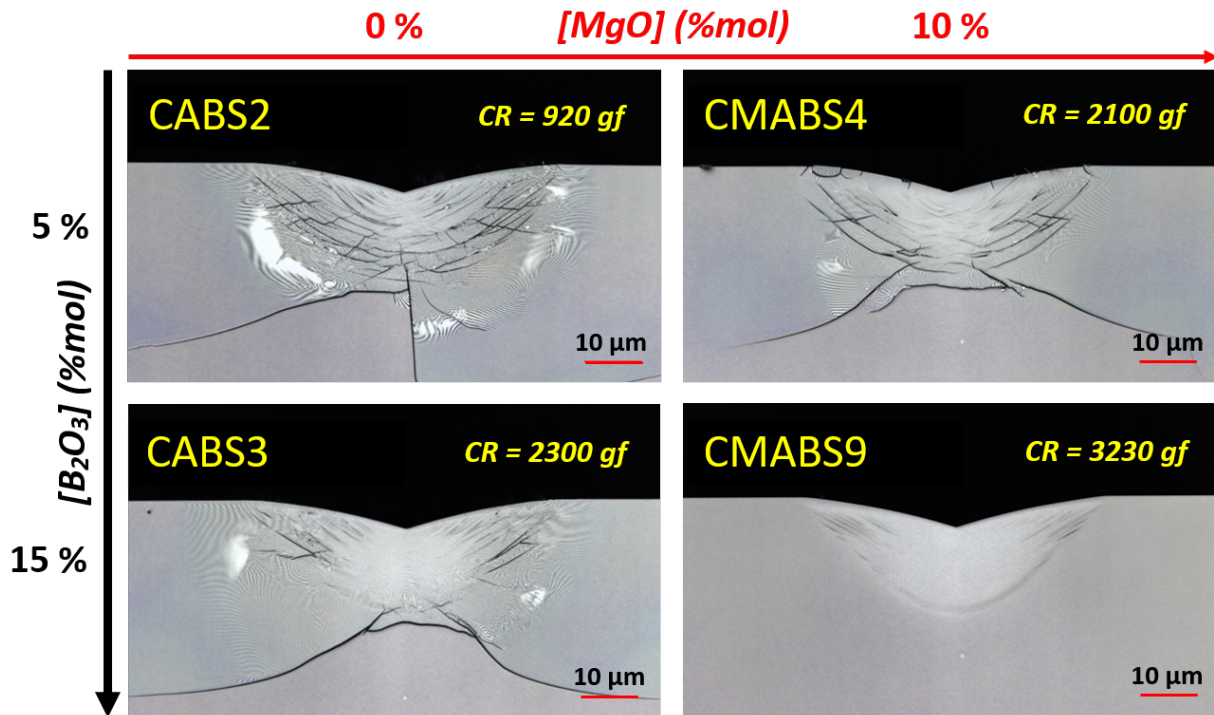


FIGURE 3.18: Cross-sections through 1 kgf Vickers indents in (a) CABS2, (b) CMABS4, (c) CABS3 and (d) CMABS9 glasses.

Appendix 3 also contains two other cross-section panels for indents made with either a conical tip of  $140^\circ$ -angle or a spherical tip with a radius of  $50\ \mu\text{m}$  both at 1 kgf. The conical tip cross-section panel exhibits the same trend as the Vickers tip panel even though the progressive vanishing of the shear localizations overall occurs over the entire plastically deformed region (middle + edges), compared to the Vickers tip panel described previously. Also, intriguingly, lateral cracks appear for all compositions. On the other hand, in the case of the spherical tip at 1 kgf, no shear bands are observed in the plastically deformed region regardless of the glass composition. As explained in section 1.2.3.f, the spherical tip involves less shear than the Vickers or conical tip, and from the cross sections, it seems not to produce shear bands synonymous with localized plastic deformation. It is important to remember that the crack resistance  $CR$  is defined by the indentation of the glass by a Vickers tip ( $146^\circ$ -angle, so close to the cone tip angle at  $140^\circ$ ). Therefore, the comparison between the characterization of the plastic deformation of a spherical indentation cross-section and the crack resistance remains debatable. In the rest of the section, we will only consider the cross sections of the Vickers indentations.

To better connect our results with the existing literature, we have made cross-sections on some of the glass compositions previously studied by Kato *et al.* (see section 1.2.4.b). These cross-sections are shown in Fig. 3.19. The crack resistance values are their values and have not been measured again for the present work. The ABS glass (Fig. 3.19.a) does not show any shear localization within the plastically deformed area and exhibits a homogeneous plastic strain. Note however, that this glass is more sensitive to cracking (1200 gf) than a 25%  $\text{B}_2\text{O}_3$  glass (CABS4 for instance - 2500 gf) whose plastically deformed region does not show any shear pattern as well. On the other hand, soda-lime silicate glass (Fig. 3.19.b) and lead silicate glass (Fig. 3.19.c) exhibit

significant shear localization over all their plastically deformed regions and have also very low crack resistances. Clearly, this series of experiments confirms the trend inferred from our series of glasses.

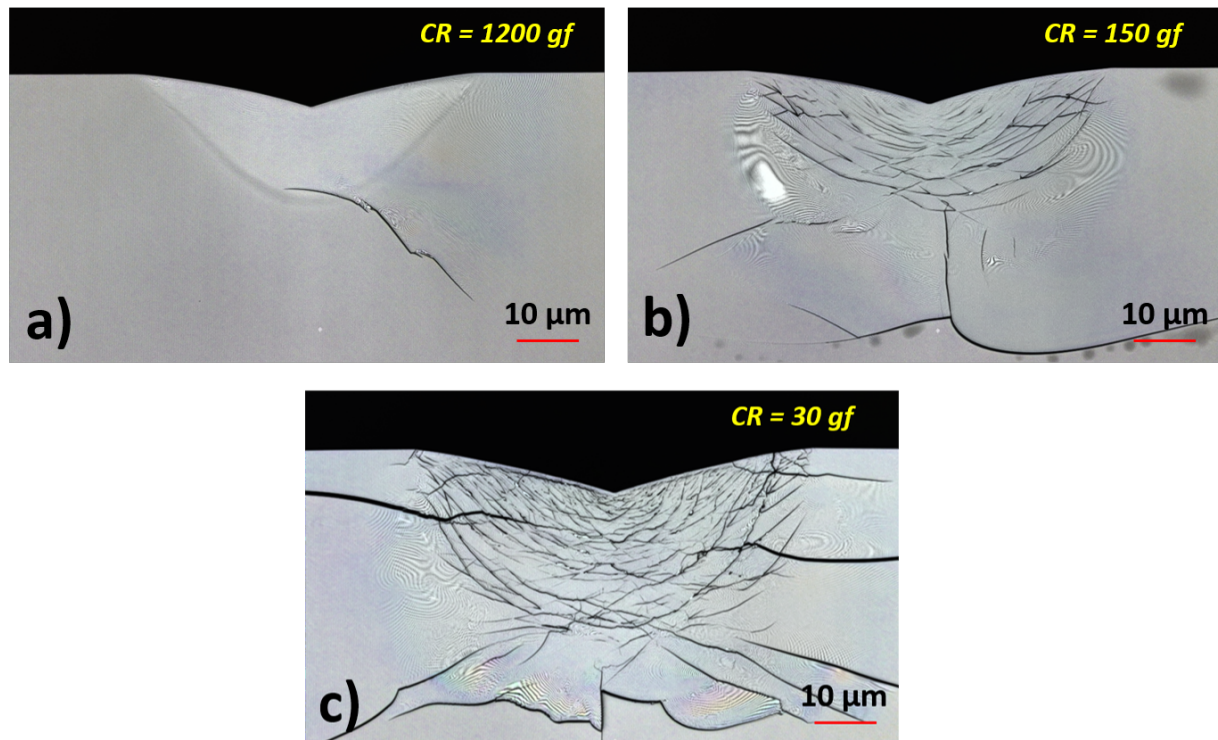


FIGURE 3.19: Cross-sections through 1 kgf Vickers indents in (a) aluminoborosilicate, (b) soda-lime silicate and (c) lead silicate glasses.

### 3.4 Roughness measurements of the plastically deformed region

We have highlighted a correlation between the presence of shear bands and low crack resistance through the observation of indentation cross-sections. For a more quantitative approach, we have characterized the morphology of the surface of the cross-sections.

SEM images of the cross section of a 1 kgf Vickers indentation on soda lime silicate are shown in Fig. 3.20. The low magnification view (Fig. 3.20.a) reveals the overall deformation pattern, including shear (or slip) bands and cracks. Fig. 3.20.b is a high magnification view taken with a 35° tilt of the center of the plastically deformed region (area highlighted by the red box in (a)). The shear bands clearly appear as a succession of steps, with distinct step heights and distinct pitch between steps, creating a staircase pattern, with two networks of steps crossing at an angle. Through roughness measurements, we expect to obtain a direct quantification of the step features. However, the density of shear localization and their size cannot be completely dissociated by a simple measurement of the amplitude of the roughness. Indeed, one could imagine that an indentation cross-section of strongly sheared bands with low density displays the same roughness as a cross-section with a high density of weakly-sheared bands. The stronger and more localized the shear deformation, the higher and the more widely spaced the steps. We therefore need to

measure both the amplitude of the roughness, which must reflect the relative displacement along the shear bands, and some characteristic distance in the roughness reflecting the typical distance between bands.

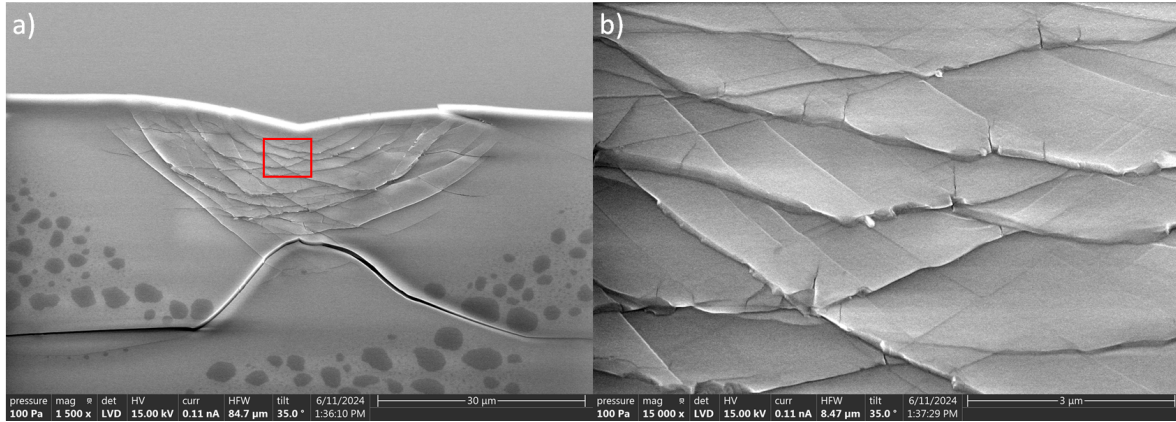


FIGURE 3.20: (a) Scanning Electron picture of 1kgf Vickers indentation cross-section in soda-lime silicate glass and (b) magnified picture on shear bands from the cross-section. The sample has been tilted to 35° to observe shear bands from the bottom.

We have measured the roughness in rectangular areas within the plastic deformation zone (Fig. 3.21). Within this area, the roughness measurement is conducted vertically (perpendicular to the direction of the shear bands) on the cross-section using 60 height profiles (which is the maximum number of profiles allowed by the software), and the average value is then calculated. To avoid skewing the roughness value, it is essential to ensure that the height profiles do not intersect a crack and in particular a lateral crack. Fig. 3.16 showed that the middle of the plastically deformed region does not contain cracks. Thus, in this region, the roughness measurements were conducted in the central part of the plastically deformed zone where we can characterize only the size of the shear bands without interference from potential cracks in the plastically deformed region.

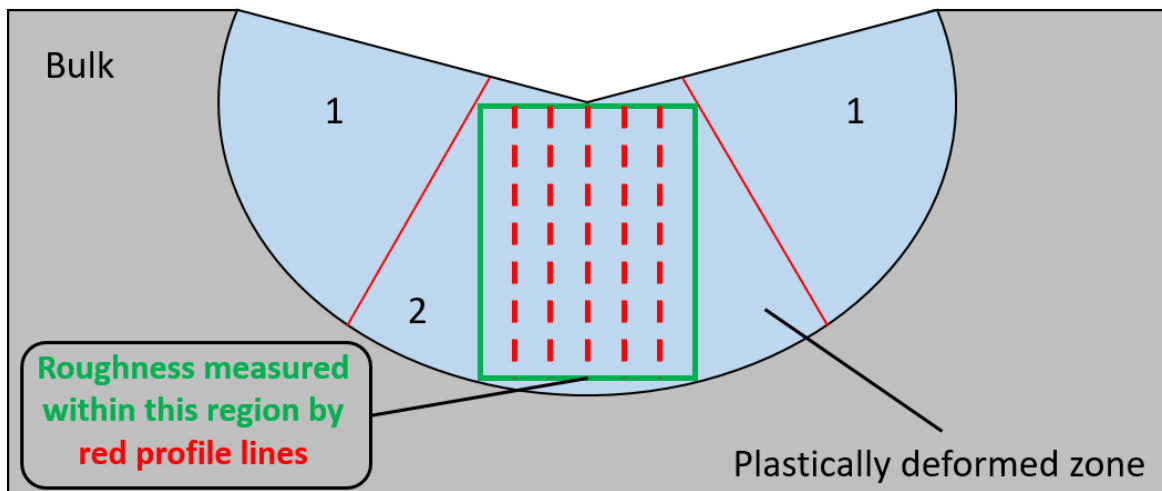


FIGURE 3.21: Diagram of an indentation cross-section. The plastically deformed region is divided into three regions: edges (1) and middle (2). The roughness is measured in the middle region.

Fig. 3.22 shows crack resistance  $CR$  as a function of the amplitude of the roughness  $Ra$  from cross-sections of both 500 gf or 1 kgf Vickers indents. The measured roughness increases from 5 to 20 nm as the crack resistance decreases from 30 to 1 N. Note that the ca 5 nm lower bound is due to the instrument resolution limit. Fig. 3.22.b also displays a sub-graph that considers the self-similarity of the indenter geometry. By multiplying the 500 gf roughness data by 1.2 (close to  $\sqrt{2}$ ) we obtain a good overlapping of the 1 kgf data and the 500 gf data. Despite a few stray points, there is a good correlation, with a roughly bi-linear shape. This correlation shows that a more crack-resistant glass will exhibit a lower roughness over the center of the plastically deformed region because it undergoes less shear localization. Concerning glass compositions that present more significant shear bands, the roughness will be higher at higher load, as Fig. 3.22.a shows with lead silicate glass for instance. Indeed, when a notable shear band is initiated within the plastically deformed region, its size can be enlarged by increasing the displacement (therefore the load). Consequently, the roughness will increase and the trend is clearer at 1 kgf than at 500 gf. Additionally, appendix 4 also shows the correlation between  $CR$  and  $Ra$  for conical and spherical indentation cross-sections. We obtain the same trend for the cone but no specific correlation between  $CR$  and  $Ra$  for the sphere, with the notable exception of the very brittle LS.

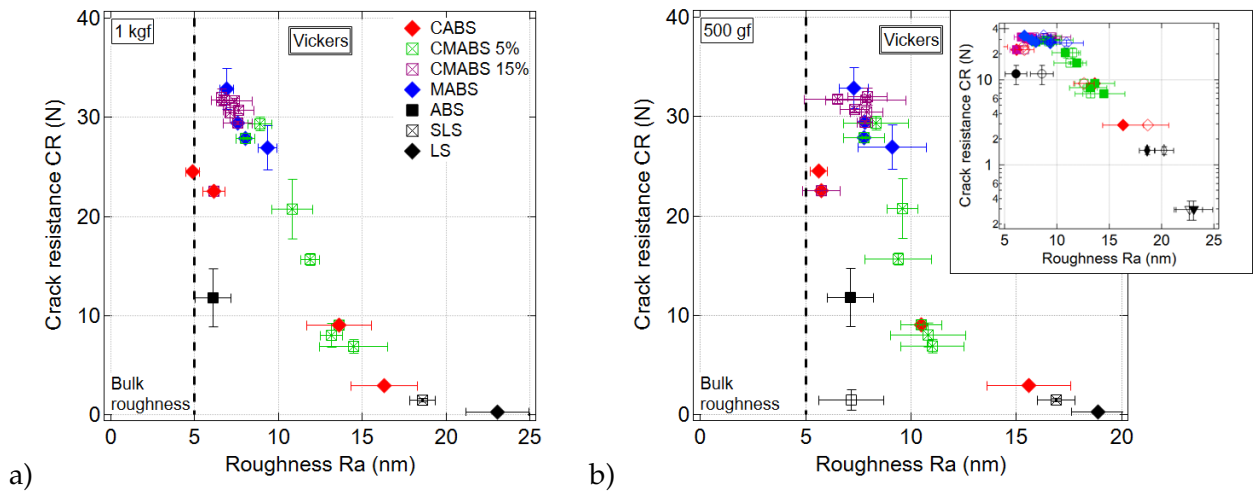


FIGURE 3.22: Relationship between crack resistance ( $CR$ ) and roughness ( $R_a$ ) for Vickers indentation cross-sections at (a) 1 kgf and (b) 500 gf including some compositions (black markers) from Kato *et al.* [87]. The sub-graph in (b) is plotted in log-lin and includes raw data from 1 kgf and data from 500 gf rescaled by 1.2. From self-similarity of the indenter geometry, we expect a rescaling by  $\sqrt{2} = 1.41\dots$ . The vertical dashed line is determined as the bulk roughness.

Crack resistance  $CR$  plotted as a function of the average spacing  $R_{Sm}$  between bands is presented in Fig. 3.23. Similar to the amplitude, we observe that the greater the spacing between the shear bands, the lower the crack resistance of the glass. Here again, as the profiles shown in Fig. 3.23 exemplify, the spacing measurement is overestimated at lower values. For example, for MABS3, the algorithm converges towards  $R_{Sm} = 0.5 \mu\text{m}$  while visual inspection suggests the correct value should be less than 100 nm. This comes from the measurement limits of the LSM which considers as noise (below the 10% threshold mentioned in section 3.1) the variations in height due to the relatively homogeneous and very poorly localized shear deformation for highly

crack-resistance glass compositions. In this case, the better resolution of atomic force microscopy should be used to characterize the roughness.

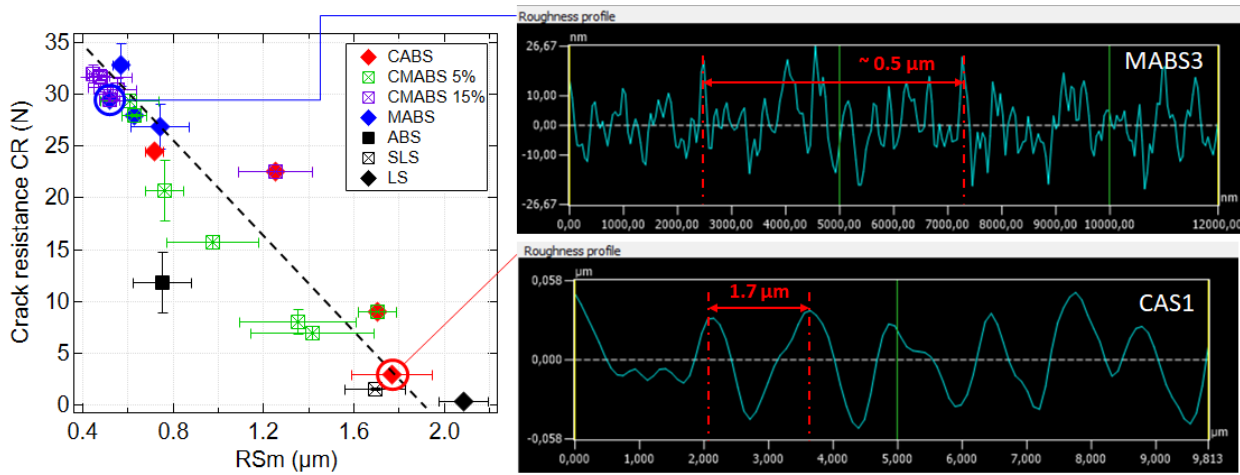


FIGURE 3.23: (Left) Crack resistance as a function of the average spacing between shear bands from Vickers indentation cross-sections at 1kgf for all glass compositions. (Right) Height profiles plotted vertically along the middle of the plastically deformed region for CAS1 glass (in red, low crack resistance) and MABS3 glass (in blue, high crack resistance).

For a given amount of shear, if the density of shear bands is lower, the slip in each band must be more intense. With these results, we can assert that, for the glass compositions investigated in this study, a glass with low crack resistance will exhibit a shear pattern consisting of large-slip shear bands in low density. For a high crack resistance, the cross-sections reveal a high density of smaller-slip shear bands, eventually leading to a generally homogeneous deformation throughout the plastically deformed region for most crack-resistant glass compositions.

### 3.5 Understanding what rules indentation cracking

Following currently accepted ideas, people have tried to establish correlations between crack resistance and parameters that are somehow linked to densification, namely  $RID$  and Poisson ratio (section 1.2.3). No correlation has been proposed with shear flow, which is the other main mechanism of plastic deformation under indentation in silicate glasses. In this section, we will first discuss our results in relation to the standard approach, focusing on densification, and then try to work out a connection with shear flow. Subsequently, we will examine our results in terms of glass composition, material structure, and plastic deformation mechanisms (shear band formations), in connection with the thermal ( $T_g$ ) and the mechanical properties ( $E$ ,  $H_V$ ).

#### 3.5.1 Impact of the volumetric change on crack resistance

On the series of glasses already mentioned, Kato *et al.* [89] found a strong *positive* correlation between  $CR$  and  $RID$ , which suggests that densification contributes to crack resistance. As presented in section 1.2.4.b, it was concluded that densification limits residual stresses and thus indentation cracking. We also measured  $RID$  for our glasses (Table 4.1). Some of the results are

shown as a bar chart in Fig. 3.24.a, for different materials (LS, SLS, ABS, CABS, CMABS, MABS): they evidence an opposite trend where the crack resistance increases roughly ten times while the  $RID$  decreases mildly. When we plot the results for all glass compositions in a single graph (Fig. 3.25) as a function of  $RID$  (or alternatively lateral recovery  $L_{SR}$ ), we no longer find the correlation between  $CR$  and  $RID$  which was apparent in a subset (Fig. 1.21.b).

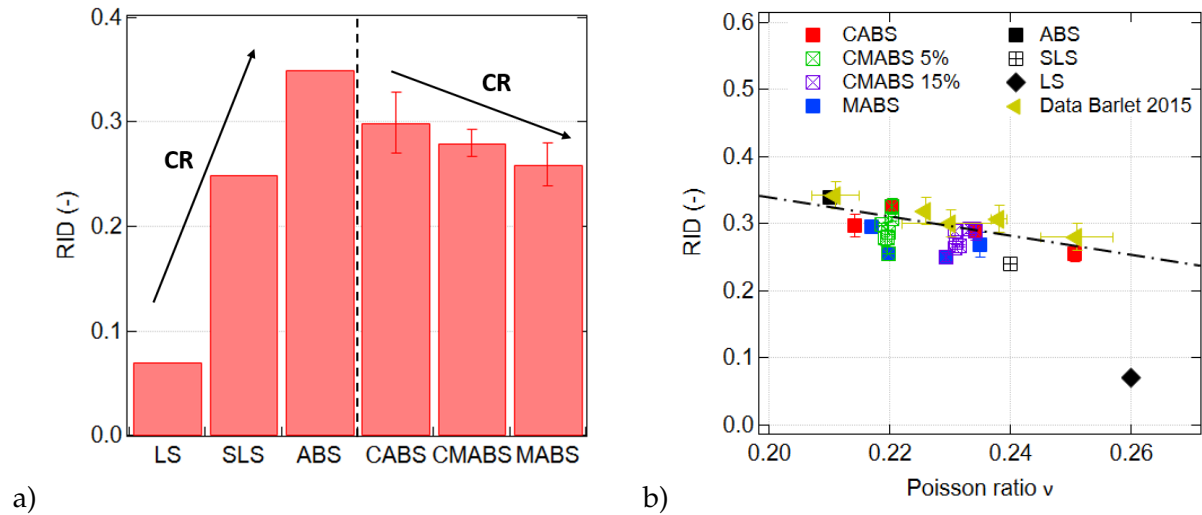


FIGURE 3.24: (a) The recovery of indentation depth for different silicate glasses compositions and (b) correlation between  $RID$  and Poisson ratio including some (LS, SLS, ABS) from Kato *et al* [89] and from Barlet *et al.* [170]. Arrows show how crack resistance increases with compositions.

We also measured  $RID$  for different tip geometries, a conical tip with an angle of  $140^\circ$  and a  $50\ \mu\text{m}$  radius spherical tip (appendix 5). Fig. 4.13 shows that recovery from Vickers and conical indentation are equivalent, regardless of the amount of boron or the type of modifier. When spherical indentation is considered, the respective recovery reaches between 60% and 80% depending on the boron content and network modifiers. In fact, spherical indentation induces a more hydrostatic stress state compared to Vickers or conical indentation (sec. 1.2.3.f) and favors densification, which leads to more recovered volume after thermal annealing. Alternatively, we propose that spherical indentation offers a more effective approach for assessing the recovery of the volume densified under indentation than Vickers, Berkovich, or conical tip which involve more shear flow than spherical indentation.

Yoshida and Rouxel pointed out a correlation between densification under indentation and Poisson ratio [59, 97]. To test how the Poisson ratio is related to the volumetric change in the material (see section 1.2.3.d), we have plotted the recovery of indentation depth  $RID$  (or the volume recovery of indentation  $V_R$ ) as a function of Poisson ratio and we have included the results of two others works [89, 170] in the same plot. Fig. 3.24.b shows that the volume recovery  $V_R$  slightly decreases with increasing Poisson ratio. Our data are completely consistent with the results of Barlet *et al.* [170] for an amount of boron between approximately 15 to 25% but with higher concentrations of network modifiers. It suggests that  $V_R$  is indeed related to the ratio  $\text{SiO}_2/\text{B}_2\text{O}_3$  in borosilicate glasses and that the higher the amount of  $\text{B}_2\text{O}_3$ , the higher Poisson ratio. However,

the variation we measured between  $V_R$  and  $\nu$  is moderate compared to the data shown by Sellapan *et al.* [118] or Yoshida *et al.* [59].

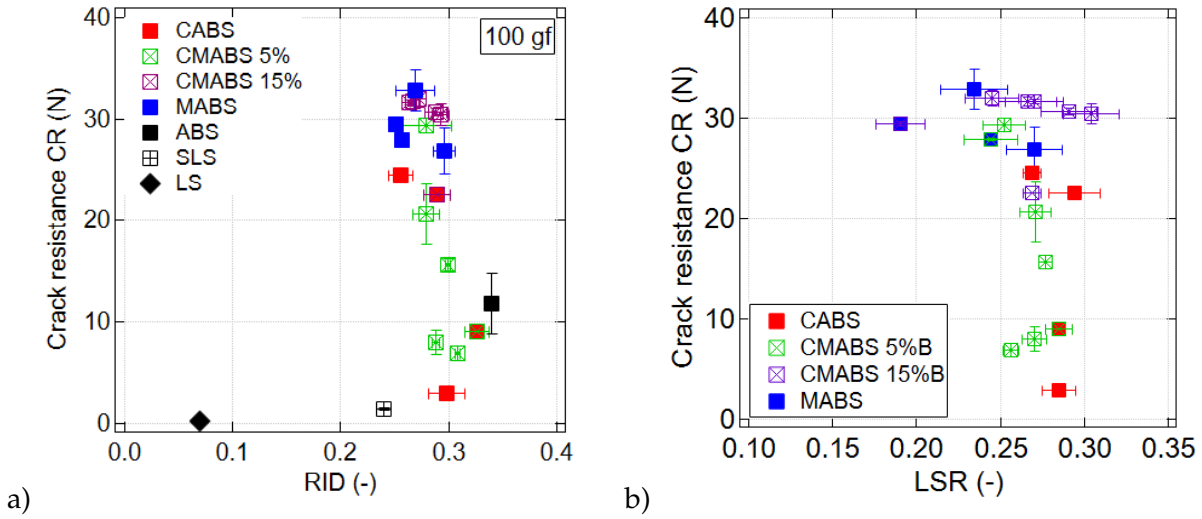


FIGURE 3.25: (a) Relationship between crack resistance ( $CR$ ) and the recovery of indentation depth ( $RID$ ) including some compositions (black markers) from Kato *et al.* [89] and (b) correlation between crack resistance ( $CR$ ) and indentation side recovery  $L_{SR}$ .

Altogether, our results challenge the commonly accepted idea that  $RID$  is a key parameter to understand  $CR$ . Firstly,  $RID$  is a very complex material parameter. Indeed even though the activation energy associated with the volume recovery after densification is assumed to be less than the energy required for shear flow, it is debatable that thermal annealing solely enables the recovery of the volume deformed by densification without any recovery from shear flow. Furthermore, there is no guarantee that after 2 hours of heat treatment, all the densified volume will have returned to a non-densified state. Therefore, the exact meaning of  $RID$  in terms of material properties is

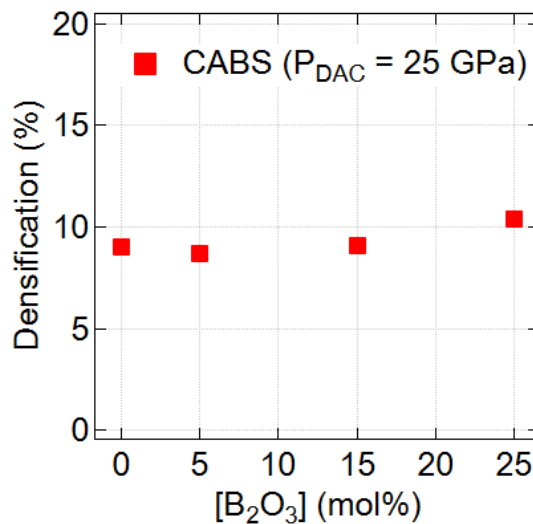


FIGURE 3.26: Measurements of the densification of CABS glass composition (CAS1, CAS2, CAS3 and CAS4) under 25 GPa carried out with Diamond Anvill Cell (DAC, see section 1.2.3.a).

difficult to assess. Secondly, there is certainly a relation between  $RID$  and densification, but, as already suggested, it is far from clear that densification is the primary parameter to understand  $CR$ .

In fact, measurements of the maximum densification under 25 GPa were performed by NEG company. The results are shown in Fig. 3.26. The saturation densification is approximately 10% for all compositions even though the crack resistance increases almost by a factor of 9 between 0% and 25% boron (Fig. 3.15.a). This result also casts doubts on the relevance of densification to explain the variation in crack resistance across the full composition range.

### 3.5.2 Shear localizations and cracking susceptibility

#### 3.5.2.a Shear bands formations

At a mesoscopic scale, shear bands are localized regions of intense plastic deformation that often form in materials under high stress [171]. The formation of shear bands is closely associated with the phenomenon of strain softening, where the material, after reaching the yield stress (aka flow stress)  $\tau_c$ , begins to soften rather than continuing to harden as plastic flow progresses. This behavior is illustrated in Fig. 3.27, where the stress initially increases elastically with strain up to the flow stress, after which the stress decreases, indicating the onset of softening. As the material deforms plastically, it can reach a critical state where further deformation leads to a decrease in the material's ability to withstand stress, resulting in the softening seen in the stress-strain curve. This softening destabilizes the uniform distribution of strain, causing it to localize into narrow regions

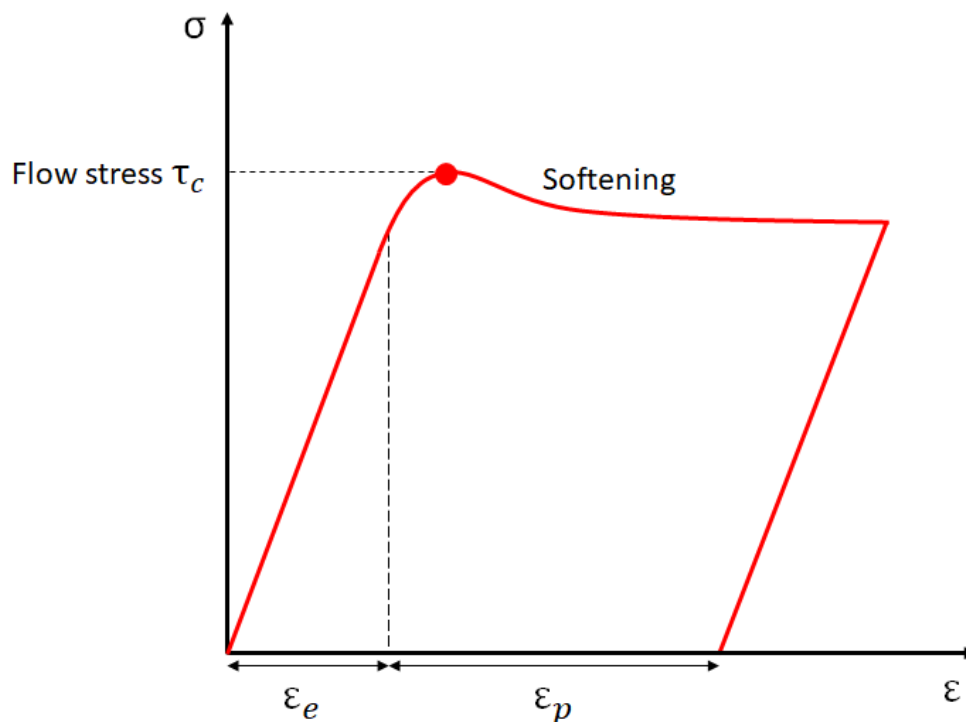


FIGURE 3.27: Stress-Strain curve illustrating the onset of shear band formation due to strain softening.  $\epsilon_e$  and  $\epsilon_p$  are respectively the elastic deformations and the plastic deformation.

or shear bands. These bands act as channels through which further deformation is concentrated, leading to rapid and possibly catastrophic failure in some materials. The local reduction in flow stress within these bands allows for easier deformation, exacerbating the localization. This process can be influenced by various factors, including material composition, strain rate, temperature, and the presence of microstructural defects, which can all affect the onset and propagation of shear bands. Under indentation, shear bands typically form beneath the indenter, where the material experiences a combination of high compressive and shear stresses. As the indenter penetrates the material, the stress state evolves, and once the material reaches the flow stress and begins to soften, shear bands may initiate.

In the current study, all indents made with Vickers tip showed normal cracking behavior (sec. 1.2.4.a), with well-defined subsurface lateral cracks and median or radial cracks propagating along the corners of the indent [112]. Fig. 3.17, 3.18, and 3.19 allow direct observations of these lateral cracks for the less crack-resistant compositions. Moreover, deformation occurs primarily by volume displacing shear since significant shear localizations are observed, but we do not notice any shear pattern for high crack-resistant glass compositions at this magnification. However, Gross has also investigated CABS4 at a higher magnification than we did in our study, and he showed that this glass composition exhibits a very high density of very thin shear bands over the middle of the plastically deformed region [94]. Clearly, a high density of shear bands does not necessarily mean low crack resistance since the crack resistance of the CABS4 glass is one of the highest in our batch compositions (2500 gf). As we pointed out with the roughness measurement, it is the morphology of the shear band (slip amplitude, spacing) that matters. Large 'steps' with wide spacing are characteristic of low crack-resistance glass in our study. For instance, CABS1 (Fig. 3.17.a) or SLS glasses (Fig. 3.19.b) exhibit a low density of large-slip shear bands and a crack resistance below 300 gf. In the LS glass case, the crack resistance is ten times lower than CABS1 (30 gf) and its indentation cross-section displays an even lower density of larger-slip shear bands. Due to the self-similarity of the geometry, the crack resistance is correlated to the slip amplitude of the shear bands and their density within the plastically deformed area. The higher density of small-slip shear bands causes less heterogeneous displacements along with shear and enhances the crack resistance. Conversely, a low crack resistance is correlated to a strong deformation heterogeneity causing a strong localization in shear with large-slip shear bands.

It can also be observed, especially in Fig. 3.20, that the shear bands intersect over the middle of the plastically deformed region. It might be reasonable to consider that these intersections locally weaken the material, making these sites favorable for crack initiation under the stress fields generated during the unloading of the indentation, which will be discussed in the following section. Furthermore, Hagan [1] has also pointed out that some short cracks form at the intersection point of flow lines within the plastically deformed area, probably helping to break up the material. Similarly, in polymer science, it has been shown that intersections of coarse slip bands in polystyrene lead to craze formation and damage the material [172].

Finally, it is useful to reconsider the special case of silica in the context of shear bands. No localization can be observed when considering the cross-sectional view of 1 kgf Vickers indentation in fused silica [117, 173]. By using the two-point bending method, Tang *et al.* [174] highlighted that the failure stress of fused silica can be between 1.5 and 2 times higher than the failure stress of

normal glasses depending on experimental conditions. Indeed, Gross and Tomozawa [92] have proposed a method to test the crack resistance of silica under dry nitrogen to avoid stress corrosion due to water. With these testing conditions, they proved that radial crack-free Vickers indentations at 1 kgf are possible. The cracking susceptibility of silica is mostly dependent on the experimental atmosphere (section 1.1.3.a). Consequently, silica should be at least as crack-resistant as ABS in Fig. 3.19.a which also does not display any heterogeneous shear flow over the plastically deformed region of its indentation cross-section.

### 3.5.2.b Crack initiation

Residual stress fields in materials post-indentation are critical in understanding crack initiation and propagation. A crucial aspect of these stress fields is the strong tensile stress that develops beneath the plastically deformed zone [125] (sec. 1.2.4.a). This tensile stress arises as the elastic half-space, previously compressed by the indenter, attempts to return to its original shape but is restrained by the plastically deformed core. The tensile stress is particularly pronounced directly under the area of maximum deformation, where it can reach levels high enough to initiate cracks. This tensile residual stress field, which appears right at the end of the unloading leg, is a key factor in initiating cracks [116]. It creates conditions where existing micro-defects or flaws within the material are prone to propagate, leading to crack initiation and growth. In silicate glasses, as we discussed, these flaws could indeed originate from the intersection of shear bands at the bottom of the plastically deformed zone, damaging the material. Additionally, a larger slip in a shear band implies more damage and consequently a more locally weakened material which can eventually initiate crack at lower load.

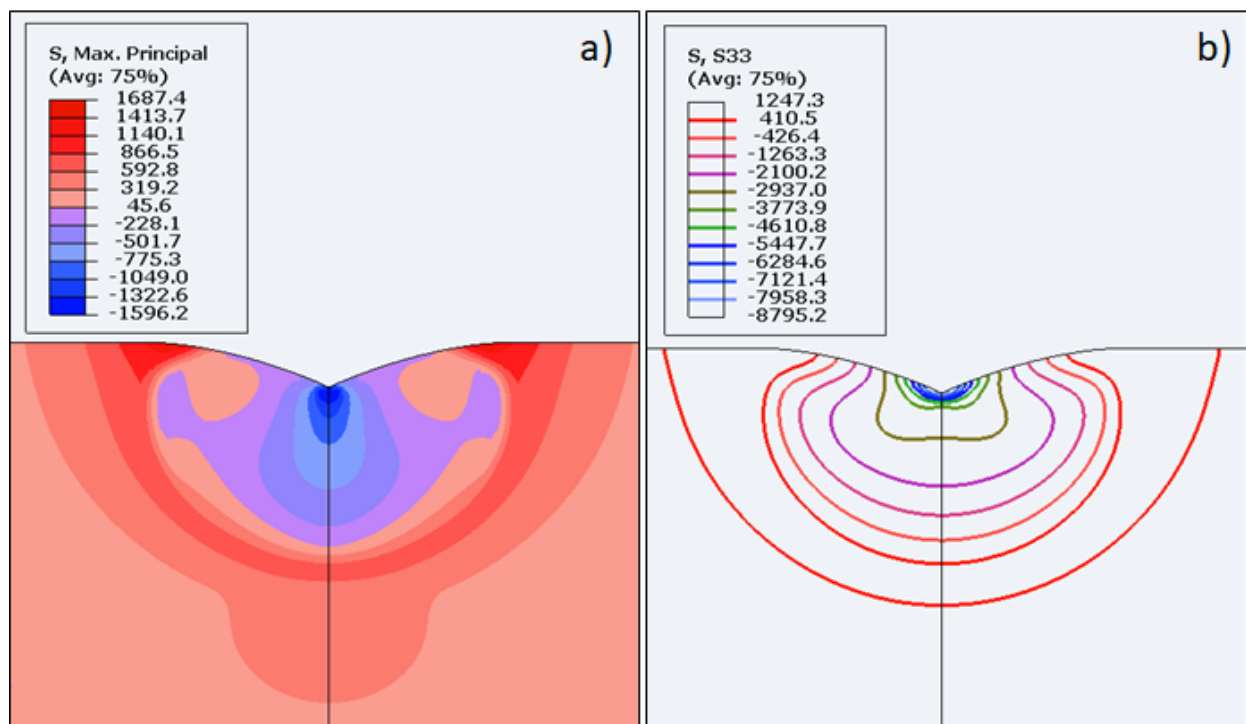


FIGURE 3.28: (a) Maximal principal stress field and (b) orthoradial stress field post-indentation using FEA model from section 3.1.

To better understand these residual stress fields after complete unloading, we conducted finite element simulations whose details are given in material and methods (see section 3.1). Fig. 3.28 (a) shows the first (maximum) principal stress field. The color gradient ranges from red, indicating areas of tensile maximum principal stress, to blue, showing regions of compressive maximum principal stress. In the center part of the plastically deformed core, there is a significant zone of compression, marked by a "blue core," surrounded by regions where the material experiences tensile stresses. In interpreting these stress fields, it is important to note that cracks will primarily propagate in regions where the maximum principal stress is in tension, excluding the highly compressed "blue core" beneath the indenter. Thus, the area of the material (the middle of the plastically deformed region) where the roughness has been measured corresponds to this compressed core, ensuring an accurate roughness measurement without interference from cracks.

The second and third principal stress components are crucial in understanding the propagation of indentation cracks, as they define planes normal to the maximum principal stress so that isovalue plots give a qualitative view of the crack trajectories (more precisely, one should calculate the stress trajectories: see refs. [175, 176] for the case of spherical indentation and cone cracks).

Fig. 3.28 (b) presents the orthoradial stress field (S33 - orthoradial stress), which turns out to be mostly the second principal stress component (not shown). The blue to orange areas indicate compression, the red lines indicating tension. Since S33 is mostly the second (mid) principal stress, the crack trajectories *in the plane* are suggested by the isovalues of the minimum principal stress.

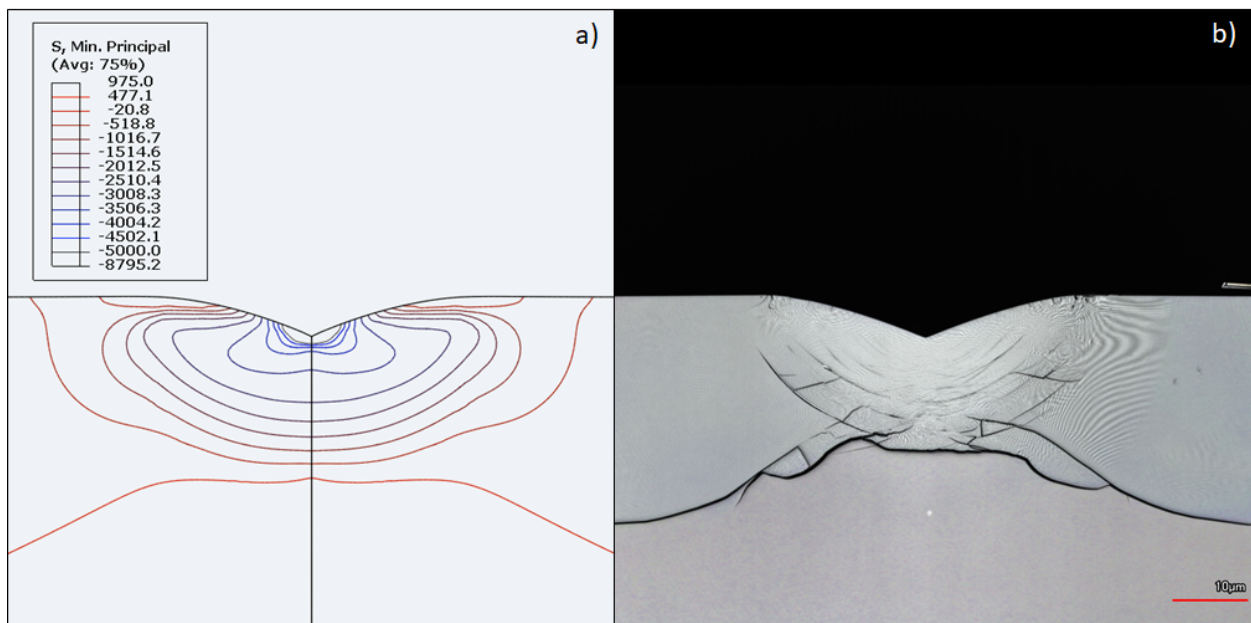


FIGURE 3.29: Comparison between (a) FEA simulation of minimum principal stress field and (b) conical indentation cross-section in CMABS1 glass at 1 kgf. The isostress lines are compared to the positions of the cracks on the cross-section.

Fig. 3.29 compares the calculated minimum principal stress field (left) with a cross-sectional view of a typical conical indentation in CMABS1 glass at 1 kgf (right). The left image shows isostress lines with blue representing compressive stresses and red representing tensile stresses. The right image displays cracks formed in the glass, revealing that the crack paths align with

the trajectories suggested by the FEA. Similarly, isostress lines in Fig. 3.29.a can predict the position of the lateral cracks and the cracks located on the sides of the plastically deformed region in Fig.3.29.b.

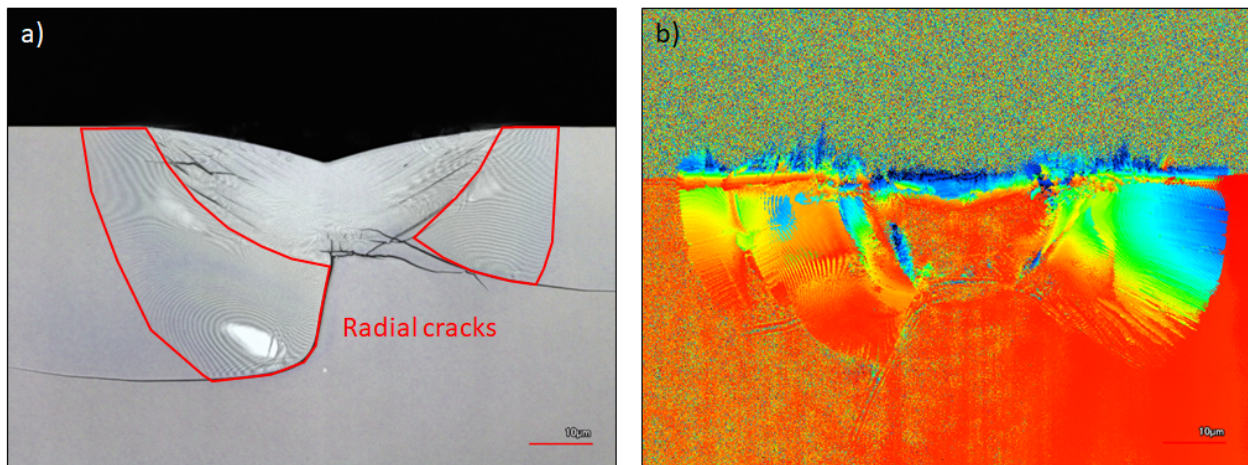


FIGURE 3.30: (a) Laser scanning microscope picture of 1 kgf Vickers indentation cross-section in CABS3 glass with radial/median crack appearing as interferences due to the laser reflections and (b) height diagram of a spherical indentation. All radian/median cracks, in both cases, seem to start from the lateral crack nucleating below the plastically deformed region and propagate up to the surface.

Finally, Fig. 3.30 presents two pictures taken with the laser scanning microscope, showcasing different aspects of crack formation and surface deformation due to indentation in CABS3 glass. On the left, The picture clearly shows radial and median cracks, highlighted by red lines, originating from the lateral cracks at the bottom of the plastically deformed region, and extending toward the glass surface. On the right, the height mode of the spherical indentation cross-section picture allows us to visualize the topography of the surface and beyond the surface, directly into the glass. It reveals a detailed view of the formed and extended radial/median cracks under indentation. Furthermore, we can assume that the lateral cracks observed in the material are likely the primary "driving force" behind the initiation of median cracks that propagate to the surface. These median cracks tend to emerge at points of tensile stress concentration (Fig. 3.28.b), and more specifically around the corners, concerning Vickers indentation. In these corners, residual stress concentrations are most pronounced, promoting the propagation of radial cracks toward these corners. The lateral cracks, forming below the plastically deformed region, act as the starting points for these radial cracks, which eventually reach the surface of the material. However, Cook and Pharr [116] have shown that the lateral cracks initiate after the radial or median cracks upon unloading which is the opposite chronology compared with our description. We assume that the pre-existing crack from the cross-section process affects the cracking chronology since we are not indenting in the bulk but on the pre-existing crack. It would be useful to visualize the crack formation process during indentation on a pre-existing crack to reach a more reliable description.

### 3.5.3 Composition dependence of local rearrangements and crack resistance

In this last section, we discuss more deeply the effect of composition on mechanical and thermal properties but also how it affects the shear flow. We first emphasize the impact of boron and then we will deal with the influence of the substitution of CaO by MgO.

#### Impact of Boron

Fig. 3.9 showed that the glass transition temperature decreases with increasing boron content because of the changes in the glass network structure and the decrease of overall connectivity within the glass matrix. Silica, when it forms a glass, creates a highly connected network of tetrahedral  $\text{SiO}_4$  units. This results in a more rigid structure, which requires high thermal energy to transition from a glassy to a liquid state, thus a higher  $T_g$ . When boron oxide is introduced into the glass network, it initially integrates into the structure as a trigonal  $\text{BO}_3$  unit. This integration reduces the overall connectivity and rigidity of the network because  $\text{BO}_3$  units have a lower coordination number than the  $\text{SiO}_4$  tetrahedra [177]. As more boron replaces silica, the network becomes increasingly less rigid and more flexible, reducing the thermal energy required for the glass transition, hence lowering  $T_g$ . This phenomenon is supported by the topological constraint theory [178], which suggests that the number of constraints in a glass network determines its rigidity. When silica is substituted by boron, the number of constraints decreases, leading to a decrease in  $T_g$ .

Concerning mechanical properties, the observation that substituting  $\text{SiO}_2$  by  $\text{B}_2\text{O}_3$  in glass *increases* the atomic packing density (see Table 4.2) while it *also decreases* Young's modulus and hardness (section 3.2.2) might seem counterintuitive at first sight since higher atomic packing density leads to a reduced free volume, and a more interconnected network structure which should contribute to greater resistance to deformation. However, the bond dissociation energy has also to be considered. Indeed, Table 4.3 shows that the dissociation energy of Si-O bonds in a  $\text{SiO}_2$  network is four times higher than the dissociation energy of B-O in the  $\text{B}_2\text{O}_3$  network (particularly in the  $\text{BO}_3$  trigonal units). It means that in the Makishima-Mackenzie model [8] (see section 1.1.1.b), the modulus is primarily directed by the dissociation energy rather than the atomic packing density, at least in the case of our glasses. These weaker B-O bonds result in a more flexible and less stiff glass.

Finally, the substitution of silica by boron has a significant impact on the formation of shear bands. One hypothesis is that the trigonal  $\text{BO}_3$  units may have a greater ability to rearrange and adapt around the looser ionic environments ( $\text{Ca}^+$  or  $\text{Mg}^+$ ) (see sec. 1.2.3.e) compared to the more rigid and geometrically constrained tetrahedral  $\text{SiO}_4$  units. This increased flexibility could allow the glass network to accommodate local stresses more evenly, which might prevent the nucleation of shear bands. The lower dissociation energy associated with B-O bonds, compared to Si-O bonds, may contribute to a glass network that deforms more gradually and homogeneously. Further support by spectroscopic studies (Raman spectroscopy or NMR) or detailed simulations (Molecular Dynamics) would be needed to understand the exact mechanisms at play.

### Impact of network modifiers

The substitution of CaO by MgO does not significantly affect the glass transition temperature (Fig. 3.9.b) or Young's modulus (Fig. 3.10.b). However, the Vickers hardness increases with increasing MgO content (Fig. 3.12.b). Table 4.2 shows that the atomic packing density is higher for glass compositions with higher magnesium content. Moreover, the dissociation energy of Mg is also higher than that of Ca. The combination of denser atomic packing, stronger Mg-O bonds, and a more rigid network structure might collectively lead to a significant increase in the hardness of the glass when calcium is replaced by magnesium.

More generally, the type of modifiers greatly affects shear band formation (Fig. 3.19). Lead silicate glass (Pb) and soda-lime silicate glass (Na) display significant visible shear localizations. In comparison, calcium-aluminoborosilicate glasses (Ca) show fewer visible shear bands over the plastically deformed region and magnesium-aluminoborosilicate glasses (Mg) display even less or none at all. This evolution correlates with the field strength  $FS$  (section 1.1.2.b) of the modifier which depends on the ion size (ionic radius). Table 1.2 gives  $FS_{Mg} > FS_{Ca} > FS_{Pb} > FS_{Na}$ . It means that nucleation of large-slip shear bands is promoted by a large ion modifier with low field strength. The incorporation of larger ions into the glass network creates free volume within the glass where more ionic bonding and the loss of network connectivity let atoms move more easily. Under stress, these regions are more likely to experience localized plastic rearrangements, which can lead to the formation of shear bands. Moreover, the distribution of modifier cations within the structure is not necessarily uniform. Certain regions may have a higher concentration of these ions, leading to the formation of ion-rich clusters [179]. These clusters probably promote shear localization. Finally, the structure of glasses with a large concentration of modifiers, such as LS glass or SLS glass, contains non-bridging oxygens NBO. As discussed in section 1.2.3.e, some papers propose that modifiers in the glass network serve as initiation sites for shear deformation, under stress, due to weaker ionic bonds from NBO [180, 181]. The formation of a shear band might be due to the response of these more weakly bonded zones under indentation stress [104]. Once again, these assumptions would have to be confirmed by a deeper experimental characterization of the glass structure and by numerical simulations to model the structural rearrangements under mechanical testing.

## Conclusion

In this chapter, we have explored the underlying mechanisms of indentation cracking in alkaline-earth aluminoborosilicate glasses by investigating indentation-induced densification and plastic shear flow, as well as the influence of different glass compositions on these mechanisms. A comprehensive set of characterizations was also performed to obtain a better understanding of the effect of composition on thermal and mechanical properties.

The most significant contribution of this work is the systematic observation of the plastic zone generated by indentation, which involves performing cross-sections of indentations. This approach allowed us to directly characterize shear bands and the plastically deformed zone, providing clear evidence of the strong impact of composition on the extent of shear flow. Moreover, we have proposed a method to quantitatively evaluate the characteristics of the shear bands through roughness measurements in the central part of the plastically deformed area. These measurements were correlated with the crack resistance of each glass, demonstrating a clear relationship between shear flow and crack resistance. In contrast, indentation-induced densification was also explored, but the correlation we found with crack resistance proved to be much less convincing than the shear bands, and at any rate, does not align with the trends postulated in the literature.

Finite element simulations provided additional insight into the initiation and propagation of cracks, highlighting the importance of residual stress fields in these processes. The simulations revealed a region of compressive maximum principal stress in the middle of the plastically deformed zone surrounded by a shell of tensile maximum principal stress. The calculated stress field matches the observed indentation features very well and can predict the path and shape of radial/median cracks. From the minimum principal stress component, we determine that the observed crack patterns at the periphery of the plastic core, which qualitatively aligns with the isostress, appear at the very end of unloading. Finally, the compressive core is the part less affected by cracking, as expected: this observation justifies the area selected for the roughness measurements.

Finally, through the analysis of the dissociation energies and the atomic packing densities, we have attempted to interpret the effects of glass composition on the observed trends in plasticity mechanisms. However, more in-depth experimental characterizations and simulations of the structure will be required to validate the proposed hypotheses and refine our atomic-scale understanding of the plastic deformation mechanism, shear band formation and damage in borosilicate glasses.

# Conclusions and general outlooks

This work aimed at providing more understanding of plasticity in borosilicate glasses in relation to their fracture properties and more precisely their crack resistance. Due to the limited array of experimental tools available to study the plasticity of brittle amorphous materials, two micromechanical techniques were chosen and glass composition was used as a key variable. The systems we selected were thought as representative for generic silicate glasses and the conclusions on the relation between composition, structure, viscoplasticity, shear band formation and crack initiation should generalize to other compositions as well.

## Main results and future improvements

We have first carried out an extensive study of the viscoplasticity of silicate glasses under electron irradiation. Earlier experiments had shown that irradiation can promote plastic flow by lowering the yield stress, even below 1 GPa, a phenomenon analogous to the effect of temperature [134]. We have been able to significantly extend this analogy using stress relaxation measurements. From the extensive amount of stress vs strain rate data generated by this new approach, we have demonstrated that the yield stress dependence upon plastic strain rate obeys a time-current density superposition similar to the time-temperature equivalence in polymers. The application of Eyring's model [149] and comparison with internal friction experiments [158] have highlighted the existence of two different relaxation regimes depending on glass composition: one regime governed by the network-forming matrix and another by the mobility of ionic modifiers. These results have directly demonstrated that it is the network modifiers which control the short-time dynamics in the plastic response of normal silicate glasses.

Indentation cross-sections were made on an extensive series of borosilicate glasses. They have allowed for direct observation of the plastically deformed zone. We have found that the plastic deformation was characterized by the presence of shear localizations, or shear bands, which were more or less intense depending on the glass composition, and accompanied by more or less extensive cracking, particularly at the periphery of the plastically deformed region. To quantify the morphology of the shear bands in the cross-sectional area, roughness measurements were used to characterize the slip amplitude and the spacing between shear bands. The results obtained showed a direct correlation between the characteristics of the shear bands and the crack resistance of glasses. For the least resistant glasses, large-slip shear bands with a significant spacing between them were observed, with roughness amplitudes reaching up to 25 nm. For high crack resistance glasses, the shear band morphologies were below the detection limit of the profilometer. In contrast, densification, which is thought as a key parameter for crack resistance [87], did not show

as clear a correlation as shear flow. In our systems, we found a trend that is opposite to previous studies: the thermal recovery of the indented volume decreases as glasses exhibit better crack resistance.

With the cross-section technique, we also found direct evidence of the major role played by the glass composition in the formation of shear bands. The size of the ion network modifiers appears to be a key parameter. It was found that silicate glasses containing network modifiers with large ionic radii and low field strength  $FS$  show intense localization while for modifiers with small ionic radii, and therefore high  $FS$  (section 1.1.2.b), the glasses exhibit relatively homogeneous shear flow without particularly pronounced localizations throughout the plastically deformed zone. The same phenomenon is observed when the matrix is modified, particularly when silica is substituted by 25% boron. Large shear bands likely damage the material locally, especially at the intersections of shear bands in the middle of the plastically deformed region.

These observations are consistent with the stress field predicted by FEA modelling. Besides the radial cracks, which allow crack resistance to be measured, we have shown that the observed crack pattern mostly agrees with the isostress lines of the minimum principal stress found after unloading, which suggest they formed with the lateral crack. All these results provide a consistent picture of the links between glass composition, shear band formation, and crack resistance.

## Optimizations and long-term perspectives

The results of this thesis provide additional insights into the question: how can glass be made as resistant as possible to cracking? Several optimizations emerge from this research. Optimizing glass composition appears to be a direct practical application. By adapting the chosen network formers and modifiers, it could be possible to develop glasses with mechanical properties tailored to specific applications. For example, borosilicate glasses incorporating network modifiers with high field strength, such as magnesium, could be developed for uses requiring better crack resistance. Experimentally, it would be useful to more precisely measure the characteristic lengths discussed in section 3.4. The use of AFM could notably allow for precise characterization of the size and spacing of thin shear bands present in the plastically deformed zone of the most crack-resistant glass indentation cross-sections.

Regarding the irradiation studies, this thesis first reminds us that in situ SEM or TEM tests are subject to irradiation, which can alter the material behavior. It is therefore imperative to ensure that the acceleration voltage and electron current density are relatively low to avoid significantly impacting the mechanical response. From a practical perspective, one could consider using irradiation, leveraging the time-irradiation equivalence developed in this work, as a means to perform tests equivalent to an extremely slow strain rate without having to wait several days for a single experiment, by applying a sufficiently high electron current density. Finally, these irradiation-induced relaxation tests should be applied to a broader range of glass compositions, including silicate glasses with very few network modifiers, or conversely, a large amount of network modifiers (like LS glass), to observe their effect on the two relaxation regimes mentioned in this research.

The long-term perspectives of this project also include the further development of finite element simulations or molecular dynamics simulations to model the different types of shear localization discussed in this manuscript (low density of large shear bands or high density of thin shear bands), which implies confirming and/or improving the constitutive relations used. To do this, new experiments, such as Brillouin spectroscopy [128] or chemical dissolution [90], must be developed to better understand the contribution of densification under indentation and that of plastic shear flow. During this project, we also used the birefringence [182, 183] to assess the stress fields under indentation by measuring the retardation and the rotation of the light passing through the glass and we compared those fields with indentation-induced photoelastic patterns calculated from Kermouche's constitutive relation [123].

Finally, the use of glassy polymers such as polystyrene could also help in understanding shear localization mechanisms [184, 172, 185]. In polymers, these mechanisms are a thousand times larger than in glasses, making them easier to observe and characterize. Thus, polymers offer a unique opportunity to study these phenomena on a more accessible scale, providing valuable insights that could be applied to the study of inorganic glasses.



# Bibliography

- [1] JT Hagan. Shear deformation under pyramidal indentations in soda-lime glass. *Journal of Materials Science*, 15:1417–1424, 1980.
- [2] Michael F. Ashby. *Material Selection in Mechanical Design*. Third Edition, 2004.
- [3] William D Callister and David G Rethwisch. *Materials science and engineering: an introduction*. Wiley New York, 1999.
- [4] Jing Tian, Yaxian Zhao, Yiping Huang, Yuan Li, Chong Zhang, Shou Peng, Gaorong Han, and Yong Liu. Theoretical Prediction of Vickers Hardness for Oxide Glasses: Machine Learning Model, Interpretability Analysis, and Experimental Validation. *Materialia*, 33:102006, 2024.
- [5] Pascal Richet and Yan Bottinga. Verres, liquides et transition vitreuse. *Bulletin de Minéralogie*, 106(1):147–168, 1983.
- [6] I. Avramov, TS. Vassilev, and I. Penkov. The glass transition temperature of silicate and borate glasses. *Journal of non-crystalline solids*, 351(6-7):472–476, 2005.
- [7] Stephen W Hughes. Archimedes revisited: a faster, better, cheaper method of accurately measuring the volume of small objects. *Physics Education*, 40(5):468–474, September 2005.
- [8] A Makishima and J D Mackenzie. Direct calculation of Young’s modulus of glass. *Journal of Non-Crystalline Solids*, 12:35–45, 1973.
- [9] Seiji Inaba, Shigeru Fujino, and Kenji Morinaga. Young’s Modulus and Compositional Parameters of Oxide Glasses. *Journal of the American Ceramic Society*, 82(12):3501–3507, December 1999.
- [10] Akio Makishima and John D. Mackenzie. Calculation of bulk modulus, shear modulus and Poisson’s ratio of glass. *Journal of Non-Crystalline Solids*, 17:147–157, 1975.
- [11] W. H. Zachariasen. The atomic arrangement in glass. *Journal of the American Chemical Society*, 54(10):3841–3851, October 1932.
- [12] Jaroslav Šesták, Jiří J. Mareš, and Pavel Hubík. *Glassy, Amorphous and Nano-Crystalline Materials*, volume 8. Springer Netherlands, 2011.
- [13] Cindy L. Rountree. Recent progress to understand stress corrosion cracking in sodium borosilicate glasses: linking the chemical composition to structural, physical and fracture properties. *Journal of Physics D: Applied Physics*, 50(34):343002, 2017.

- [14] R. L. Mozzi and B. E. Warren. The structure of vitreous silica. *Journal of Applied Crystallography*, 2(4):164–172, 1969.
- [15] Adrian C. Wright. Neutron scattering from vitreous silica. *Journal of Non-Crystalline Solids*, 179:84–115, November 1994.
- [16] P. Vashishta, Rajiv K. Kalia, José P. Rino, and Ingvar Ebbsjö. Interaction potential for SiO<sub>2</sub>: A molecular-dynamics study of structural correlations. *Physical Review B*, 41(17):12197–12209, 1990.
- [17] Eric Le Bourhis. *Glass: mechanics and technology*. John Wiley & Sons, 2014.
- [18] Laurent Van Brutzel, Cindy L Rountree, Rajiv K Kalia, Aiichiro Nakano, and Priya Vashishta. Dynamic fracture mechanisms in nanostructured and amorphous silica glasses million-atom molecular dynamics simulations. *MRS Online Proceedings Library (OPL)*, 703:V3–9, 2001.
- [19] Pinshane Y. Huang, Simon Kurasch, Anchal Srivastava, Viera Skakalova, Jani Kotakoski, Arkady V. Krasheninnikov, Robert Hovden, Qingyun Mao, Jannik C. Meyer, Jurgen Smet, David A. Muller, and Ute Kaiser. Direct Imaging of a Two-Dimensional Silica Glass on Graphene. *Nano Letters*, 12(2):1081–1086, February 2012.
- [20] Kuan-Han Sun. Fundamental condition of glass formation. *Journal of the American Ceramic Society*, 30(9):277–281, September 1947.
- [21] M. Bouhadja, N. Jakse, and A. Pasturel. Striking role of non-bridging oxygen on glass transition temperature of calcium aluminosilicate glass-formers. *The Journal of Chemical Physics*, 140(23):234507, 2014.
- [22] Tobias K. Bechgaard, Ashutosh Goel, Randall E. Youngman, John C. Mauro, Sylwester J. Rzoska, Michal Bockowski, Lars R. Jensen, and Morten M. Smedskjaer. Structure and mechanical properties of compressed sodium aluminosilicate glasses: Role of non-bridging oxygens. *Journal of Non-Crystalline Solids*, 441:49–57, 2016.
- [23] A. Dietzel. Die Kationenfeldstärken und ihre Beziehungen zu Entglasungsvorgängen, zur Verbindungsbildung und zu den Schmelzpunkten von Silicaten. *Zeitschrift für Elektrochemie und angewandte physikalische Chemie*, 48(1):9–23, 1942.
- [24] R. D. Shannon. Revised effective ionic radii and systematic studies of interatomic distances in halides and chalcogenides. *Acta crystallographica*, A(32):751–767, 1976.
- [25] Bruce C. Bunker, R. James Kirkpatrick, and Richard K. Brow. Local structure of alkaline-earth boroaluminate crystals and glasses: I, crystal chemical concepts—structural predictions and comparisons to known crystal structures. *Journal of the American Ceramic Society*, 74(6):1425–1429, 1991.
- [26] Daniel R Neuville and Laurent Cormier. Le verre: un matériau d’hier, d’aujourd’hui et de demain. *Matériaux & Techniques*, 110(4):404, 2022.

- [27] Kacper Januchta, Randall E Youngman, Ashutosh Goel, Mathieu Bauchy, Sylwester J Rzoska, Michal Bockowski, and Morten M Smedskjaer. Structural origin of high crack resistance in sodium aluminoborate glasses. *Journal of Non-Crystalline Solids*, 460:54–65, 2017.
- [28] C Inglis. Stress in a plate due to the presence of sharp corners and cracks. *Trans. Roy. Inst. Naval Architects*, 60:219–241, 1913.
- [29] Alan Arnold Griffith. Vi. the phenomena of rupture and flow in solids. *Philosophical transactions of the royal society of london. Series A, containing papers of a mathematical or physical character*, 221(582-593):163–198, 1921.
- [30] GR Irwin. Analysis of stresses and strains near the end of a crack traversing a plate. *J. Appl. Mech.*, 24:361–364, 1957.
- [31] GR Irwin. Fracture. *encyclopaedia of physics*, vol. 6, 1958.
- [32] GR Irwin. Fundamental aspects of crack growth and fracture. In *Engineering fundamentals and environmental effects*, pages 1–46. Elsevier, 1971.
- [33] SM Wiederhorn and LH Bolz. Stress corrosion and static fatigue of glass. *Journal of the American ceramic society*, 53(10):543–548, 1970.
- [34] SM Wiederhorn, H Johnson, AM Diness, and AH Heuer. Fracture of glass in vacuum. *Journal of the American Ceramic Society*, 57(8):336–341, 1974.
- [35] Matteo Ciccotti. Stress-corrosion mechanisms in silicate glasses. *Journal of physics D: Applied physics*, 42(21):214006, 2009.
- [36] Terry A Michalske and Stephen W Freiman. A molecular mechanism for stress corrosion in vitreous silica. *Journal of the American Ceramic Society*, 66(4):284–288, 1983.
- [37] JJ Lewandowski, WH Wang, and AL Greer. Intrinsic plasticity or brittleness of metallic glasses. *Philosophical Magazine Letters*, 85(2):77–87, 2005.
- [38] Tanguy Rouxel and Satoshi Yoshida. The fracture toughness of inorganic glasses. *Journal of the American Ceramic Society*, 100(10):4374–4396, 2017.
- [39] Michael B Bever. *Encyclopedia of materials science and engineering*. Pergamon Press, Elmsford, NY, 1985.
- [40] William F Thomas. An investigation of the factors likely to affect the strength and properties of glass fibres. *Phys. Chem. Glasses*, 1(1):4–18, 1960.
- [41] BA Proctor, Ian Whitney, and JW Johnson. The strength of fused silica. *Proceedings of the Royal Society of London. Series A. Mathematical and Physical Sciences*, 297(1451):534–557, 1967.
- [42] NM Cameron. Effect of environment and temperature on strength of e-glass fibres. i. high vacuum and low temperature. *Glass Technology*, 9(1):14, 1968.

- [43] Charles R Kurkjian and UC Paek. Single-valued strength of perfect silica fibers. *Applied Physics Letters*, 42(3):251–253, 1983.
- [44] CR Kurkjian and PK Gupta. Intrinsic strength and the structure of glass. *Proc. Int. Congr.*, pages 11–18, 2001.
- [45] Charles R Kurkjian, PK Gupta, Richard K Brow, and N Lower. The intrinsic strength and fatigue of oxide glasses. *Journal of Non-Crystalline Solids*, 316(1):114–124, 2003.
- [46] Nathan P Lower, Richard K Brow, and Charles R Kurkjian. Inert failure strains of sodium aluminosilicate glass fibers. *Journal of non-crystalline solids*, 344(1-2):17–21, 2004.
- [47] Nathan P Lower, Richard K Brow, and Charles R Kurkjian. Inert failure strain studies of sodium silicate glass fibers. *Journal of non-crystalline solids*, 349:168–172, 2004.
- [48] Richard K Brow, Nathan P Lower, Charles R Kurkjian, and Hong Li. The effects of melt history on the failure characteristics of pristine glass fibres. *Physics and Chemistry of Glasses*, 50(1):31–33, 2009.
- [49] Prabhat K Gupta and Charles R Kurkjian. Intrinsic failure and non-linear elastic behavior of glasses. *Journal of non-crystalline solids*, 351(27-29):2324–2328, 2005.
- [50] Michael Guerette, Charles R Kurkjian, Sergey Semjonov, and Liping Huang. Nonlinear elasticity of silica glass. *Journal of the American Ceramic Society*, 99(3):841–848, 2016.
- [51] Charles R. Kurkjian, Prabhat K. Gupta, and Richard K. Brow. The Strength of Silicate Glasses: What Do We Know, What Do We Need to Know? *International Journal of Applied Glass Science*, 1(1):27–37, March 2010.
- [52] WJ Duncan, PW France, and SP Craig. The effect of environment on the strength of optical fiber. *Strength of inorganic glass*, pages 309–328, 1983.
- [53] E Wilfred Taylor. Plastic deformation of optical glass. *Nature*, 163(4139):323–323, 1949.
- [54] DM Marsh. Plastic Flow and Fracture of Glass. *Proceedings of the Royal Society of London. Series A, Mathematical and Physical Sciences*, 282(1388):33–43, 1964.
- [55] FM Ernsberger. Role of densification in deformation of glasses under point loading. *Journal of the American Ceramic Society*, 51(10):545–547, 1968.
- [56] KE Puttick, MR Rudman, KJ Smith, A Franks, and K Lindsey. Single-point diamond machining of glasses. *Proceedings of the Royal Society of London. A. Mathematical and Physical Sciences*, 426(1870):19–30, 1989.
- [57] Heinrich Hertz. The contact of elastic solids. *J Reine Angew, Math*, 92:156–171, 1881.
- [58] Arun K Varshneya. Stronger glass products: lessons learned and yet to be learned. *International Journal of Applied Glass Science*, 9(2):140–155, 2018.

- [59] Satoshi Yoshida, Jean-Christophe Sanglebœuf, and Tanguy Rouxel. Quantitative evaluation of indentation-induced densification in glass. *Journal of materials research*, 20(12):3404–3412, 2005.
- [60] Tanguy Rouxel, H Ji, JP Guin, F Augereau, and Benoit Rufflé. Indentation deformation mechanism in glass: densification versus shear flow. *Journal of applied physics*, 107(9), 2010.
- [61] Vincent Keryvin, Solène Gicquel, Ludovic Charleux, Jean Pierre Guin, Mariette Nivard, and Jean Christophe Sangleboeuf. Densification as the only mechanism at stake during indentation of silica glass? *Key Engineering Materials*, 606:53–60, 2014.
- [62] EH Yoffe. Elastic stress fields caused by indenting brittle materials. *Philosophical Magazine A*, 46(4):617–628, 1982.
- [63] Yoomin Ahn, TN Farris, and S Chandrasekar. Sliding microindentation fracture of brittle materials: Role of elastic stress fields. *Mechanics of Materials*, 29(3-4):143–152, 1998.
- [64] Kacper Januchta and Morten M Smedskjaer. Indentation deformation in oxide glasses: Quantification, structural changes, and relation to cracking. *Journal of Non-Crystalline Solids: X*, 1:100007, 2019.
- [65] RW Douglas. Some comments on indentation tests on glass. *J. Soc. Glass Technol*, 42(206):145–57T, 1958.
- [66] PW Bridgman. The effect of pressure on the tensile properties of several metals and other materials. *Journal of Applied Physics*, 24(5):560–570, 1953.
- [67] PW Bridgman and I Simon. Effects of very high pressures on glass. In *Papers 169-199*, pages 4291–4299. Harvard University Press, 1964.
- [68] F.M. Ernsberger. Mechanical properties of glass. *Journal of Non-Crystalline Solids*, 25:293–321, 1977.
- [69] KW Peter. Densification and flow phenomena of glass in indentation experiments. *Journal of Non-Crystalline Solids*, 5(2):103–115, 1970.
- [70] William A Bassett. The diamond cell and the nature of the earth’s mantle. *Annual Review of Earth and Planetary Sciences*, 7(1):357–384, 1979.
- [71] H Sugiura and T Yamadaya. Raman scattering in silica glass in the permanent densification region. *Journal of non-crystalline solids*, 144:151–158, 1992.
- [72] Sho-suke Mochizuki and Naoto Kawai. Lattice vibrational spectra of vitreous silica densified by pressure. *Solid State Communications*, 11(6):763–765, 1972.
- [73] Alfredo Pasquarello and Roberto Car. Identification of raman defect lines as signatures of ring structures in vitreous silica. *Physical Review Letters*, 80(23):5145, 1998.

- [74] Abdelali Rahmani, Magali Benoit, and Claude Benoit. Signature of small rings in the raman spectra of normal and compressed amorphous silica: A combined classical and ab initio study. *Physical Review B*, 68(18):184202, 2003.
- [75] Antoine Perriot, D Vandembroucq, E Barthel, V Martinez, L Grosvalet, Ch Martinet, and B Champagnon. Raman microspectroscopic characterization of amorphous silica plastic behavior. *Journal of the American Ceramic Society*, 89(2):596–601, 2006.
- [76] T Deschamps, A Kassir-Bodon, C Sonnevile, J Margueritat, C Martinet, D De Ligny, A Mermet, and B Champagnon. Permanent densification of compressed silica glass: a raman-density calibration curve. *Journal of Physics: Condensed Matter*, 25(2):025402, 2012.
- [77] Damien Vandembroucq, Thierry Deschamps, Camille Coussa, Antoine Perriot, Etienne Barthel, Bernard Champagnon, and Christine Martinet. Density hardening plasticity and mechanical ageing of silica glass under pressure: a raman spectroscopic study. *Journal of Physics: Condensed Matter*, 20(48):485221, 2008.
- [78] JD Mackenzie. High-pressure effects on oxide glasses: Ii, subsequent heat treatment. *Journal of the American Ceramic Society*, 46(10):470–476, 1963.
- [79] T Deschamps, J Margueritat, C Martinet, A Mermet, and B Champagnon. Elastic moduli of permanently densified silica glasses. *Scientific reports*, 4(1):7193, 2014.
- [80] T Deschamps, C Martinet, JL Bruneel, and B Champagnon. Soda-lime silicate glass under hydrostatic pressure and indentation: a micro-raman study. *Journal of Physics: Condensed Matter*, 23(3):035402, 2011.
- [81] Yoshinari Kato, Hiroki Yamazaki, Satoshi Yoshida, Jun Matsuoka, and Masami Kanzaki. Measurements of density distribution around vickers indentation on commercial aluminoborosilicate and soda-lime silicate glasses by using micro raman spectroscopy. *Journal of non-crystalline solids*, 358(24):3473–3480, 2012.
- [82] A Winterstein-Beckmann, D Möncke, Dimitris Palles, Efstratios I Kamitsos, and L Wondraczek. A raman-spectroscopic study of indentation-induced structural changes in technical alkali-borosilicate glasses with varying silicate network connectivity. *Journal of non-crystalline solids*, 405:196–206, 2014.
- [83] JE Neely and JD Mackenzie. Hardness and low-temperature deformation of silica glass. *Journal of Materials Science*, 3:603–609, 1968.
- [84] Hiroshi Sawasato, Satoshi Yoshida, Toru Sugawara, Yoshinari Miura, and Jun Matsuoka. Relaxation behaviors of vickers indentations in soda-lime glass. *Journal of the Ceramic Society of Japan*, 116(1356):864–868, 2008.
- [85] C Austen Angell. Formation of glasses from liquids and biopolymers. *Science*, 267(5206):1924–1935, 1995.

- [86] Satoshi Yoshida, Jean-Christophe Sangleboeuf, and Tanguy Rouxel. Indentation-induced densification of soda-lime silicate glass. *International journal of materials research*, 98(5):360–364, 2007.
- [87] Yoshinari Kato, Hiroki Yamazaki, Satoshi Yoshida, and Jun Matsuoka. Effect of densification on crack initiation under vickers indentation test. *Journal of Non-Crystalline Solids*, 356(35-36):1768–1773, 2010.
- [88] Yoshinari Kato, Hiroki Yamazaki, Yoshihiro Kubo, Satoshi Yoshida, Jun Matsuoka, and Tomoko Akai. Effect of  $\text{B}_2\text{O}_3$  content on crack initiation under vickers indentation test. *Journal of the Ceramic Society of Japan*, 118(1381):792–798, 2010.
- [89] Yoshinari Kato, Hiroki Yamazaki, Satoru Itakura, Satoshi Yoshida, and Jun Matsuoka. Load dependence of densification in glass during vickers indentation test. *Journal of the Ceramic Society of Japan*, 119(1386):110–115, 2011.
- [90] J-P Guin, V Keryvin, L Charleux, K Han, J-C Sangleboeuf, and M Ferry. A chemical dissolution technique for challenging existing constitutive models of the densification process beneath an indentation imprint in amorphous silica. *arXiv preprint arXiv:1601.06492*, 2016.
- [91] JGs Ramsay. Shear zone geometry: a review. *Journal of structural geology*, 2(1-2):83–99, 1980.
- [92] TM Gross and M Tomozawa. Indentation-induced microhardness changes in glasses: Possible fictive temperature increase caused by plastic deformation. *Journal of non-crystalline solids*, 354(34):4056–4062, 2008.
- [93] JS Tchalenko. Similarities between shear zones of different magnitudes. *Geological Society of America Bulletin*, 81(6):1625–1640, 1970.
- [94] TM Gross, J Wu, DE Baker, JJ Price, and R Yongsunthon. Crack-resistant glass with high shear band density. *Journal of Non-Crystalline Solids*, 494:13–20, 2018.
- [95] Riya Chakraborty, Arjun Dey, and Anoop Kumar Mukhopadhyay. Loading rate effect on nanohardness of soda-lime-silica glass. *Metallurgical and Materials Transactions A*, 41:1301–1312, 2010.
- [96] G Kermouche, G Guillonneau, J Michler, J Teisseire, and E Barthel. Perfectly plastic flow in silica glass. *Acta Materialia*, 114:146–153, 2016.
- [97] Tanguy Rouxel, H Ji, T Hammouda, and A Moréac. Poisson’s ratio and the densification of glass under high pressure. *Physical review letters*, 100(22):225501, 2008.
- [98] Tanguy Rouxel. Elastic properties and short-to medium-range order in glasses. *Journal of the American Ceramic Society*, 90(10):3019–3039, 2007.
- [99] Jingshi Wu and Jonathan F Stebbins. Temperature and modifier cation field strength effects on aluminoborosilicate glass network structure. *Journal of non-crystalline solids*, 362:73–81, 2013.

- [100] John C Mauro, Adama Tandia, K Deenamma Vargheese, Yihong Z Mauro, and Morten M Smedskjaer. Accelerating the design of functional glasses through modeling. *Chemistry of Materials*, 28(12):4267–4277, 2016.
- [101] Saurav Bista, Jonathan F Stebbins, Jingshi Wu, and Timothy M Gross. Structural changes in calcium aluminoborosilicate glasses recovered from pressures of 1.5 to 3 gpa: Interactions of two network species with coordination number increases. *Journal of Non-Crystalline Solids*, 478:50–57, 2017.
- [102] Hiroshi Yamashita, Kazuhiko Inoue, Takeshi Nakajin, Hyuma Inoue, and Takashi Maekawa. Nuclear magnetic resonance studies of  $0.139 \text{ mo (or m } 2\text{o)} \cdot 0.673 \text{ sio}_2 \cdot (0.188 - x) \text{ al}_2\text{o}_3 \cdot x\text{b}_2\text{o}_3$  ( $m = \text{mg, ca, sr and ba, m = na and k}$ ) glasses. *Journal of non-crystalline solids*, 331(1-3):128–136, 2003.
- [103] Satoshi Yoshida, Yasuhiro Hayashi, Akiko Konno, Toru Sugawara, Yoshinari Miura, and Jun Matsuoka. Indentation induced densification of sodium borate glasses. *Physics and Chemistry of Glasses-European Journal of Glass Science and Technology Part B*, 50(1):63–70, 2009.
- [104] GN Greaves. Exafs and the structure of glass. *Journal of Non-Crystalline Solids*, 71(1-3):203–217, 1985.
- [105] Gergely Molnár, Patrick Ganster, Anne Tanguy, Etienne Barthel, and Guillaume Kermouche. Densification dependent yield criteria for sodium silicate glasses—an atomistic simulation approach. *Acta Materialia*, 111:129–137, 2016.
- [106] Zhitao Shan, Changjiu Li, and Haizheng Tao. Mixed alkaline-earth effect on the mechanical and rheological properties of ca–mg silicate glasses. *Journal of the American Ceramic Society*, 100(10):4570–4580, 2017.
- [107] Jianchao Lu, Zhitao Shan, Jun Zhang, Yucai Su, Kangfeng Yi, Yanfei Zhang, and Qiuju Zheng. Mechanical properties of mixed modified oxide glasses. *Journal of Non-Crystalline Solids: X*, 16:100125, 2022.
- [108] Jonas Kjeldsen, Morten M Smedskjaer, John C Mauro, and Yuanzheng Yue. On the origin of the mixed alkali effect on indentation in silicate glasses. *Journal of non-crystalline solids*, 406:22–26, 2014.
- [109] Jonas Kjeldsen, Morten M Smedskjaer, John C Mauro, and Yuanzheng Yue. Hardness and incipient plasticity in silicate glasses: Origin of the mixed modifier effect. *Applied physics letters*, 104(5), 2014.
- [110] Dong-Hyun Lee, In-Chul Choi, Moo-Young Seok, Yakai Zhao, Jung-A Lee, and Jae-il Jang. Strain-dependent plasticity evolution of window glass. *Journal of the American Ceramic Society*, 98(1):186–189, 2015.
- [111] Satoshi Yoshida, Hiroshi Sawasato, Toru Sugawara, Yoshinari Miura, and Jun Matsuoka. Effects of indenter geometry on indentation-induced densification of soda-lime glass. *Journal of Materials Research*, 25(11):2203–2211, 2010.

- [112] A Arora, DB Marshall, BR Lawn, and MV Swain. Indentation deformation/fracture of normal and anomalous glasses. *Journal of Non-Crystalline Solids*, 31(3):415–428, 1979.
- [113] Peng Yao, Wei Wang, Chuan Zhen Huang, Jun Wang, Hong Tao Zhu, and Tunemoto Kuriyagawa. Indentation crack initiation and ductile to brittle transition behavior of fused silica. *Advanced Materials Research*, 797:667–672, 2013.
- [114] Ben R Whittle and Russell J Hand. Morphology of vickers indent flaws in soda–lime–silica glass. *Journal of the American Ceramic Society*, 84(10):2361–2365, 2001.
- [115] Étienne Barthel and Jean-Pierre Guin. Tribologie des verres silicatés frottement et endommagement superficiel. *Techniques de l'ingénieur: Frottement, usure et lubrification*, 2016.
- [116] Robert F Cook and George M Pharr. Direct observation and analysis of indentation cracking in glasses and ceramics. *Journal of the American Ceramic Society*, 73(4):787–817, 1990.
- [117] TM Gross. Deformation and cracking behavior of glasses indented with diamond tips of various sharpness. *Journal of Non-Crystalline Solids*, 358(24):3445–3452, 2012.
- [118] P Sellappan, Tanguy Rouxel, F Celarie, E Becker, Patrick Houizot, and RJAM Conradt. Composition dependence of indentation deformation and indentation cracking in glass. *Acta Materialia*, 61(16):5949–5965, 2013.
- [119] M Wada, H Furukawa, and K Fujita. Crack resistance of glass on vickers indentation. In *Proc. Int. Congr. Glass*, volume 11, pages 39–46, 1974.
- [120] Tobias K Bechgaard, John C Mauro, and Morten M Smedskjaer. Time and humidity dependence of indentation cracking in aluminosilicate glasses. *Journal of Non-Crystalline Solids*, 491:64–70, 2018.
- [121] S Shima and M Oyane. Plasticity theory for porous metals. *International Journal of Mechanical Sciences*, 18(6):285–291, 1976.
- [122] Akhtar S Khan and Sujian Huang. *Continuum theory of plasticity*. John Wiley & Sons, 1995.
- [123] Guillaume Kermouche, Etienne Barthel, D Vandembroucq, and Ph Dubujet. Mechanical modelling of indentation-induced densification in amorphous silica. *Acta Materialia*, 56(13):3222–3228, 2008.
- [124] John C Lambropoulos, Su Xu, and Tong Fang. Constitutive law for the densification of fused silica, with applications in polishing and microgrinding. *Journal of the American Ceramic Society*, 79(6):1441–1452, 1996.
- [125] Etienne Barthel, Vincent Keryvin, Gustavo Rosales-Sosa, and Guillaume Kermouche. Indentation cracking in silicate glasses is directed by shear flow, not by densification. *Acta Materialia*, 194:473–481, 2020.
- [126] Gergely Molnár, Guillaume Kermouche, and Etienne Barthel. Plastic response of amorphous silicates, from atomistic simulations to experiments—a general constitutive relation. *Mechanics of Materials*, 114:1–8, 2017.

- [127] J-P Guin, K Han, Ludovic Charleux, J-C Sangleboeuf, M Ferry, and Vincent Keryvin. A new nanometre resolution method for probing densification ratio at nanoindentation sites in glass: Unravelling discrepancies in the literature. *Acta Materialia*, 274:120005, 2024.
- [128] Alice Berthelot, Elodie Romeo, Xavier Dagany, Thierry Deschamps, Eliot Herry, Robin Kineider, Yannis De Leon, Emmeline Brassac, Guillaume Kermouche, Etienne Barthel, et al. Strength of Brillouin spectroscopy to identify spatial densification model in indented silica. *Journal of Non-Crystalline Solids*, 639:123058, 2024.
- [129] Brian C Davis, G Scott Glaesemann, and Ivar Reimanis. Sharp indentation stress fields in fused silica: Finite element analysis and Yoffe analytic model. *Journal of the American Ceramic Society*, 103(12):7135–7146, 2020.
- [130] B Mantsi, G Kermouche, E Barthel, and A Tanguy. Impact of pressure on plastic yield in amorphous solids with open structure. *Physical Review E*, 93(3):033001, 2016.
- [131] R Lacroix, G Kermouche, J Teisseire, and E Barthel. Plastic deformation and residual stresses in amorphous silica pillars under uniaxial loading. *Acta Materialia*, 60(15):5555–5566, 2012.
- [132] Gergely Molnár, Patrick Ganster, and Anne Tanguy. Effect of composition and pressure on the shear strength of sodium silicate glasses: An atomic scale simulation study. *Physical Review E*, 95(4):043001, 2017.
- [133] Kuo-Hao Lee, Yongjian Yang, Linfeng Ding, Benedikt Ziebarth, Mark J Davis, and John C Mauro. Pressure effects on shear deformation of borosilicate glasses. *Journal of the American Ceramic Society*, 104(7):3073–3086, 2021.
- [134] Remo N Widmer, Alexander Groetsch, Guillaume Kermouche, Ana Diaz, Gilles Pillonel, Manish Jain, Rajaprakash Ramachandramoorthy, Laszlo Pethö, Jakob Schwiedrzik, and Johann Michler. Temperature-dependent dynamic plasticity of micro-scale fused silica. *Materials & Design*, 215:110503, 2022.
- [135] Sebastian Bruns, Christian Minnert, Laszlo Pethö, Johann Michler, and Karsten Durst. Room temperature viscous flow of amorphous silica induced by electron beam irradiation. *Advanced Science*, 10(7):2205237, 2023.
- [136] Marion A. Stevens-Kalceff. Electron-Irradiation-Induced Radiolytic Oxygen Generation and Microsegregation in Silicon Dioxide Polymorphs. *Physical Review Letters*, 84(14):3137–3140, April 2000.
- [137] Kun Zheng, Chengcai Wang, Yong-Qiang Cheng, Yonghai Yue, Xiaodong Han, Ze Zhang, Zhiwei Shan, Scott X Mao, Miaomiao Ye, Yadong Yin, et al. Electron-beam-assisted superplastic shaping of nanoscale amorphous silica. *Nature communications*, 1(1):24, 2010.
- [138] Sung-gyu Kang, Kyeongjae Jeong, Woo Jin Cho, Jeongin Paeng, Jae-Pyeong Ahn, Steven Boles, Heung Nam Han, and In-Suk Choi. Glass shaping at nanoscale: Mechanical forming of brittle amorphous silica by engineered inelastic interaction of scanning electrons with matter. *arXiv preprint arXiv:2008.07746*, 2020.

- [139] RF Egerton, P Li, and M Malac. Radiation damage in the tem and sem. *Micron*, 35(6):399–409, 2004.
- [140] Ian N Sneddon. The relation between load and penetration in the axisymmetric boussinesq problem for a punch of arbitrary profile. *International journal of engineering science*, 3(1):47–57, 1965.
- [141] Christine Martinet, Manon Heili, Valérie Martinez, Guillaume Kermouche, Gergely Molnar, Nikita Shcheblanov, Etienne Barthel, and Anne Tanguy. Highlighting the impact of shear strain on the sio2 glass structure: From experiments to atomistic simulations. *Journal of Non-Crystalline Solids*, 533:119898, 2020.
- [142] Malcolm L. Williams, Robert F. Landel, and John D. Ferry. The Temperature Dependence of Relaxation Mechanisms in Amorphous Polymers and Other Glass-forming Liquids. *Journal of the American Chemical Society*, 77(14):3701–3707, 1955.
- [143] R Kohlrausch. Nachtrag uber die elastische nachwirkung beim cocon und glasladen. *Ann. Phys.(Leipzig)*, 72(393):7, 1847.
- [144] JC Phillips. Stretched exponential relaxation in molecular and electronic glasses. *Reports on Progress in Physics*, 59(9):1133, 1996.
- [145] JC Phillips. Microscopic aspects of stretched exponential relaxation (ser) in homogeneous molecular and network glasses and polymers. *Journal of Non-Crystalline Solids*, 357(22-23):3853–3865, 2011.
- [146] Marcel Potuzak, Roger C Welch, and John C Mauro. Topological origin of stretched exponential relaxation in glass. *The Journal of chemical physics*, 135(21), 2011.
- [147] P Baral, G Guillonneau, G Kermouche, J-M Bergheau, and J-L Loubet. A new long-term indentation relaxation method to measure creep properties at the micro-scale with application to fused silica and pmma. *Mechanics of Materials*, 137:103095, 2019.
- [148] Yu S Urzhumtsev. Time-temperature superposition. review. *Polymer Mechanics*, 11(1):57–72, 1975.
- [149] Penghui Cao, Michael P Short, and Sidney Yip. Potential energy landscape activations governing plastic flows in glass rheology. *Proceedings of the National Academy of Sciences*, 116(38):18790–18797, 2019.
- [150] Frans Spaepen. A microscopic mechanism for steady state inhomogeneous flow in metallic glasses. *Acta metallurgica*, 25(4):407–415, 1977.
- [151] AS Argon. Plastic deformation in metallic glasses. *Acta metallurgica*, 27(1):47–58, 1979.
- [152] Michael L Falk and James S Langer. Dynamics of viscoplastic deformation in amorphous solids. *Physical Review E*, 57(6):7192, 1998.

- [153] D Weaire, MF Vaz, PIC Teixeira, and MA Fortes. Instabilities in liquid foams. *Soft Matter*, 3(1):47–57, 2007.
- [154] NF Mott. The viscosity of vitreous silicon dioxide. *Philosophical Magazine B*, 56(2):257–262, 1987.
- [155] SG Mayr, Y Ashkenazy, K Albe, and RS Averback. Mechanisms of radiation-induced viscous flow: Role of point defects. *Physical review letters*, 90(5):055505, 2003.
- [156] Koichi Kajihara, Masahiro Hirano, Linards Skuja, and Hideo Hosono. Intrinsic defect formation in amorphous  $\text{SiO}_2$  by electronic excitation: bond dissociation versus frenkel mechanisms. *Physical Review B*, 78(9):094201, 2008.
- [157] Gaylord Guillonneau, Sergio Sao Joao, Benedicte Adogou, Simon Breumier, and Guillaume Kermouche. Plastic flow under shear-compression at the micron scale-application on amorphous silica at high strain rate. *Jom*, 74(6):2231–2237, 2022.
- [158] Wieslaw A Zdaniewski, Guy E Rindone, and Delbert E Day. The internal friction of glasses. *Journal of Materials Science*, 14:763–775, 1979.
- [159] Ren-Guan Duan, Gert Roebben, and Omer Van der Biest. Glass microstructure evaluations using high temperature mechanical spectroscopy measurements. *Journal of non-crystalline solids*, 316(1):138–145, 2003.
- [160] James E. Huheey, Ellen A. Keiter, and Richard L. Keiter. *Inorganic Chemistry: Principles of Structure and Reactivity*. HarperCollins College Publishers, 1993.
- [161] DL Goble and EG Wolff. Strain-rate sensitivity index of thermoplastics. *Journal of materials science*, 28(22):5986–5994, 1993.
- [162] Gustavo A Rosales-Sosa, Atsunobu Masuno, Yuji Higo, and Hiroyuki Inoue. Crack-resistant  $\text{Al}_2\text{O}_3$ - $\text{SiO}_2$  glasses. *Scientific reports*, 6(1):23620, 2016.
- [163] Gustavo A Rosales-Sosa, Atsunobu Masuno, Yuji Higo, Yasuhiro Watanabe, and Hiroyuki Inoue. Effect of rare-earth ion size on elasticity and crack initiation in rare-earth aluminate glasses. *Journal of the American Ceramic Society*, 101(11):5030–5036, 2018.
- [164] Xuefei Ke, Zhitao Shan, Zihuang Li, Yunhang Tao, Yuanzheng Yue, and Haizheng Tao. Toward hard and highly crack resistant magnesium aluminosilicate glasses and transparent glass-ceramics. *Journal of the American Ceramic Society*, 103(6):3600–3609, 2020.
- [165] Warren Carl Oliver and George Mathews Pharr. An improved technique for determining hardness and elastic modulus using load and displacement sensing indentation experiments. *Journal of materials research*, 7(6):1564–1583, 1992.
- [166] Aubrey L Fry, Christy George, Ian Slagle, Harry Hawbaker, Steve Feller, Seong H Kim, and John C Mauro. Field strength effect on structure, hardness, and crack resistance in single modifier aluminoborosilicate glasses. *Journal of the American Ceramic Society*, 106(2):951–966, 2023.

- [167] JT Hagan and Michael V Swain. The origin of median and lateral cracks around plastic indents in brittle materials. *Journal of Physics D: Applied Physics*, 11(15):2091, 1978.
- [168] JT Hagan. Cone cracks around vickers indentations in fused silica glass. *Journal of Materials Science*, 14:462–466, 1979.
- [169] Guillaume Kermouche, Jean-Luc Loubet, and Jean-Michel Bergheau. An approximate solution to the problem of cone or wedge indentation of elastoplastic solids. *Comptes Rendus Mécanique*, 333(5):389–395, 2005.
- [170] Marina Barlet, Jean-Marc Delaye, Thibault Charpentier, Mickael Gennisson, Daniel Bonamy, Tanguy Rouxel, and Cindy L Rountree. Hardness and toughness of sodium borosilicate glasses via vickers’s indentations. *Journal of Non-Crystalline Solids*, 417:66–79, 2015.
- [171] David Rodney, Anne Tanguy, and Damien Vandembroucq. Modeling the mechanics of amorphous solids at different length scale and time scale. *Modelling and Simulation in Materials Science and Engineering*, 19(8):083001, 2011.
- [172] JBC Wu and JCM Li. Slip processes in the deformation of polystyrene. *Journal of Materials Science*, 11:434–444, 1976.
- [173] Changsheng Li, Jianjun Ding, Liangchi Zhang, Chuhan Wu, Lin Sun, Qijing Lin, Yangpeng Liu, and Zhuangde Jiang. Densification effects on the fracture in fused silica under vickers indentation. *Ceramics International*, 48(7):9330–9341, 2022.
- [174] Zhongzhi Tang, Nathan P Lower, Prabhat K Gupta, Charles R Kurkjian, and Richard K Brow. Using the two-point bend technique to determine failure stress of pristine glass fibers. *Journal of Non-Crystalline Solids*, 428:98–104, 2015.
- [175] FC Frank and B\_R Lawn. On the theory of hertzian fracture. *Proceedings of the Royal Society of London A: Mathematical, Physical and Engineering Sciences*, 299(1458):291–306, 1967.
- [176] Jean-Pierre Guin and Etienne Barthel. Tribologie des verres silicatés-frottement et endommagement superficiel. *Techniques de l’Ingénieur*, (tri4575), 2016.
- [177] Katharina Schuhladden, Usanee Pantulap, Kristin Engel, Piotr Jeleń, Zbigniew Olejniczak, Leena Hupa, Maciej Sitarz, and Aldo R Boccaccini. Influence of the replacement of silica by boron trioxide on the properties of bioactive glass scaffolds. *International Journal of Applied Glass Science*, 12(3):293–312, 2021.
- [178] John C Mauro et al. Topological constraint theory of glass. *American Ceramic Society Bulletin*, 90(4):31, 2011.
- [179] T Deschamps, C Martinet, B Champagnon, G Molnár, and E Barthel. Memory effect in the plasticity of a silicate glass densified at room temperature. *Physical Review B*, 105(22):224206, 2022.
- [180] Arjun Dey, Riya Chakraborty, and Anoop K Mukhopadhyay. Enhancement in nanohardness of soda–lime–silica glass. *Journal of non-crystalline solids*, 357(15):2934–2940, 2011.

- [181] Payel Bandyopadhyay and Anoop K Mukhopadhyay. Role of shear stress in scratch deformation of soda-lime-silica glass. *Journal of non-crystalline solids*, 362:101–113, 2013.
- [182] Hillar K Aben. Optical phenomena in photoelastic models by the rotation of principal axes: Investigation shows that, using the matrix representation of the solution of the equations of photoelasticity, an adequate description of the complicated optical phenomena in three-dimensional photoelastic models can be obtained. *Experimental Mechanics*, 6:13–22, 1966.
- [183] Keisuke Asai, Satoshi Yoshida, Akihiro Yamada, Jun Matsuoka, Andrei Errapart, and Charles R Kurkjian. Micro-photoelastic evaluation of indentation-induced stress in glass. *Materials transactions*, 60(8):1423–1427, 2019.
- [184] Edward J Kramer. The growth of shear bands in polystyrene. *Journal of Polymer Science: Polymer Physics Edition*, 13(3):509–525, 1975.
- [185] CC Chau and JCM Li. Intersections of coarse shear bands in polystyrene. *Journal of Materials Science*, 14:2172–2182, 1979.

## Chapter 4

# Appendices

### Contents

---

1	Appendix: Time - Irradiation superposition . . . . .	120
2	Appendix: CMABS glass properties . . . . .	122
3	Appendix: Full mapping of indentation cross-sections . . . . .	124
4	Appendix: Roughness measurements of indentation cross-sections . . . . .	127
5	Appendix: Characterization of the densification ability by thermal recovery measurements . . . . .	128

---

# 1 Appendix: Time - Irradiation superposition

Pillar compression experiments were performed on SLS and ABS glass using the same experimental parameters as given in section 2.1 for silica. The resulting relaxation curves are shown in Figs. 4.1 and 4.3. The corresponding stress-plastic strain rate curves are given in Figs. 4.2 and 4.4

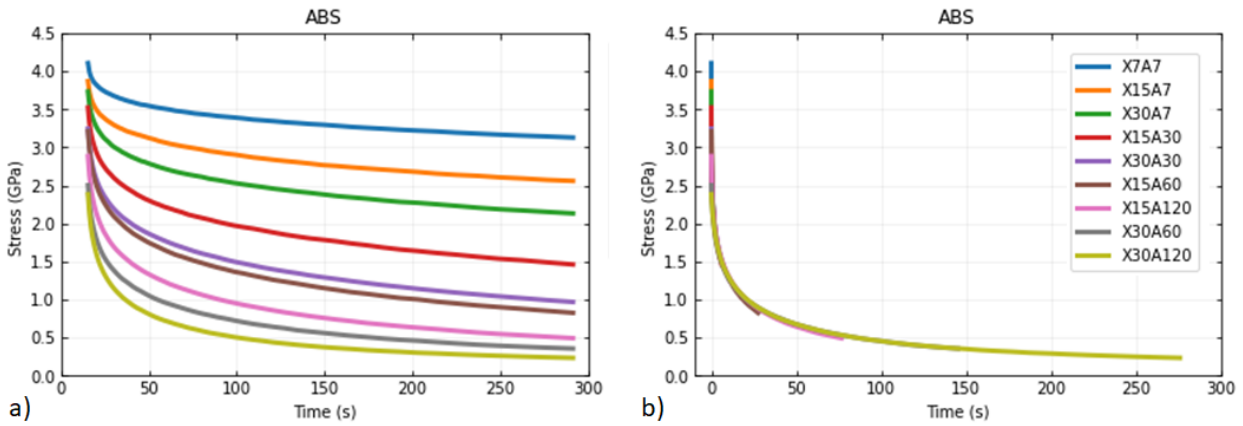


FIGURE 4.1: ABS glass pillars compression under e-beam irradiation. (a) Relaxation curves and (b) rescaling by shift factor  $S_j$ . The highest current density condition is the reference.

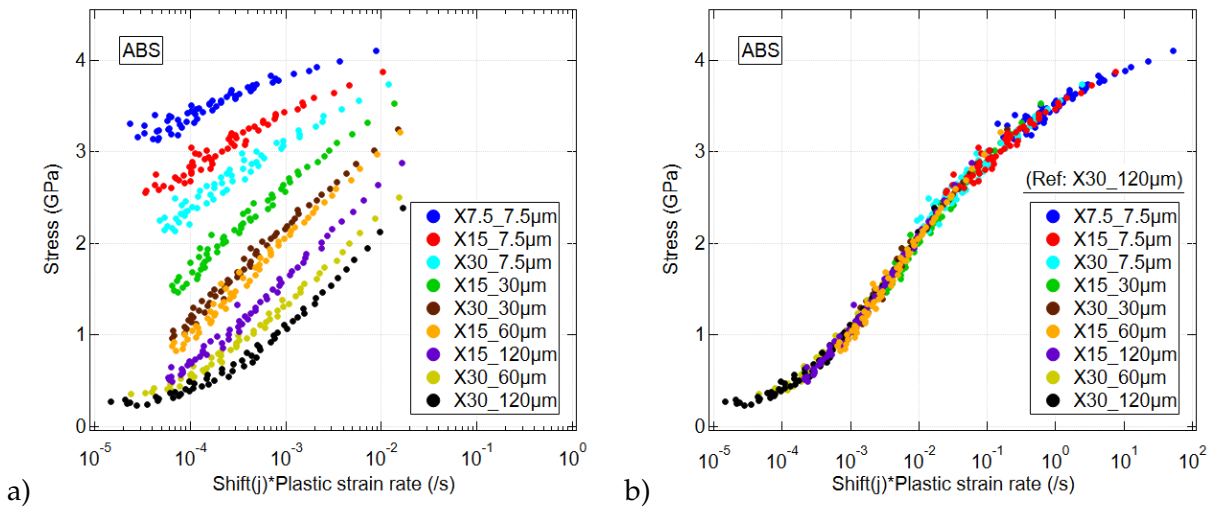


FIGURE 4.2: ABS glass pillars compression under e-beam irradiation. (a) Stress - Plastic strain rate curves and (b) rescaling by shift factor  $S_j$  to get the ABS master curve. The highest current density condition is the reference.

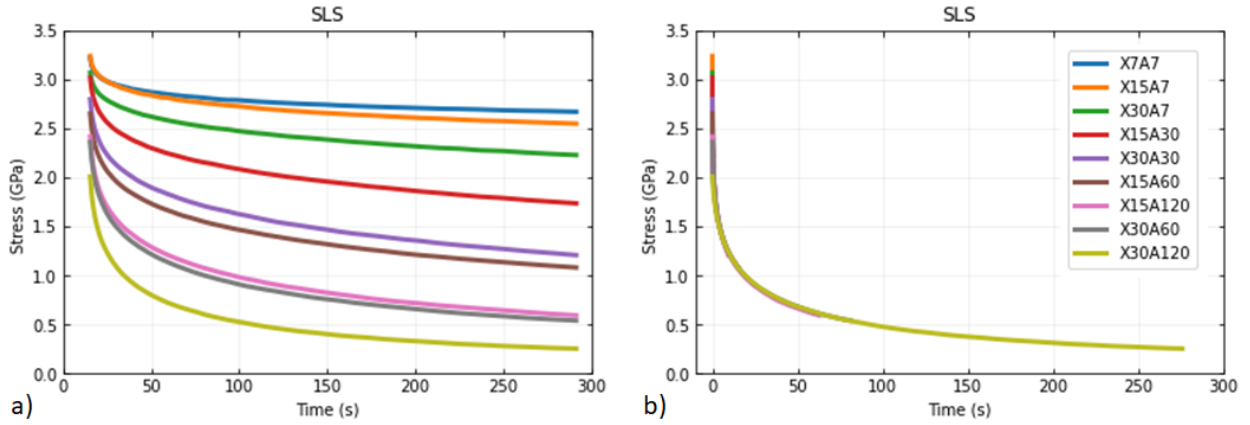


FIGURE 4.3: ABS glass pillars compression under e-beam irradiation. (a) Relaxation curves and (b) rescaling by shift factor  $S_j$ . The highest current density condition is the reference.

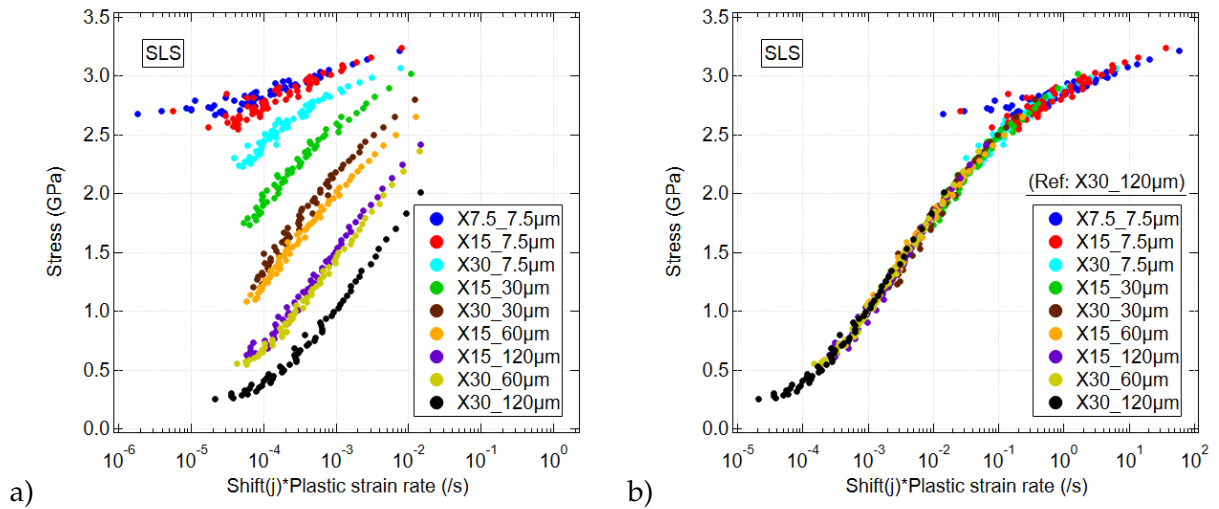


FIGURE 4.4: SLS glass pillars compression under e-beam irradiation. (a) Stress - Plastic strain rate curves and (b) rescaling by shift factor  $S_j$  to get the SLS master curve. The highest current density condition is the reference.

## 2 Appendix: CMABS glass properties

CTE measurements have been carried out for all the glass compositions (method described in section 3.1) and results are displayed in Fig. 4.5.

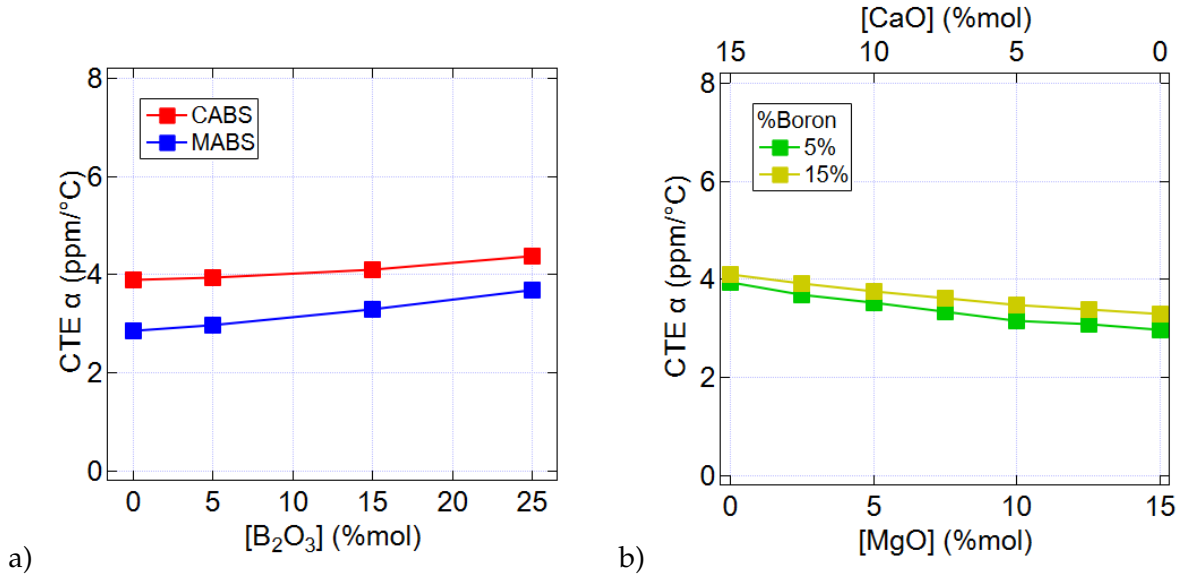


FIGURE 4.5: Coefficient of thermal expansion of (a) single alkaline earth ABS glasses and (b) mixed alkaline earth ABS glasses. Error bars are smaller than the markers' size.

Fig. 4.6 shows the comparison between Young's modulus values measured by nanoindentation and those measured by resonance method (see section 3.1).

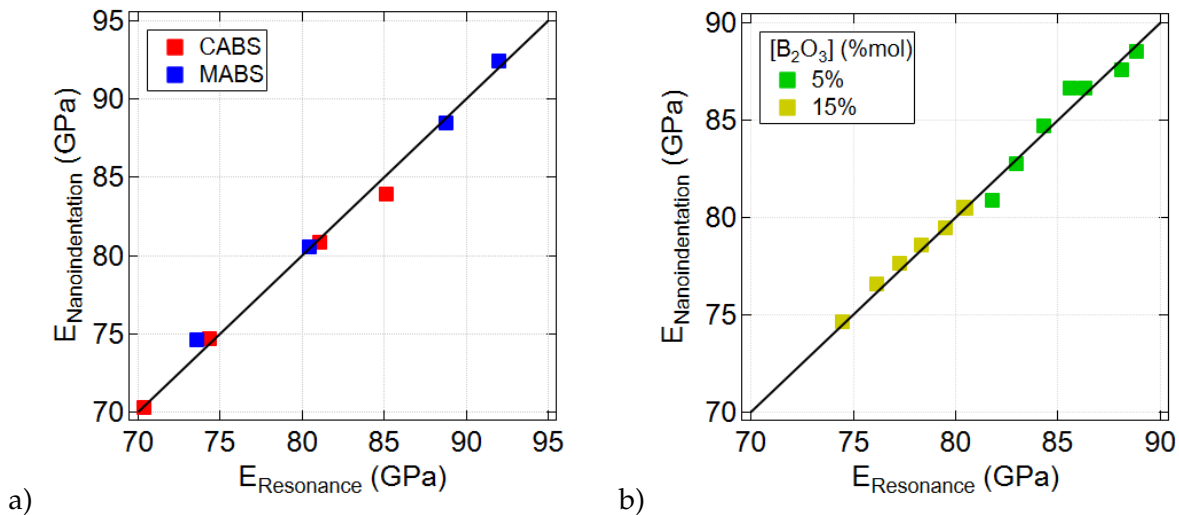


FIGURE 4.6: Comparison between Young's modulus measured by nanoindentation and resonance method for (a) single alkaline earth ABS glasses and (b) mixed alkaline earth ABS glasses. Error bars are smaller than the markers' size.

TABLE 4.1: Density ( $\rho$ ), Glass transition temperature ( $T_g$ ), Young's modulus ( $E$ ), Shear modulus ( $G$ ), Bulk modulus ( $K$ ), Poisson's ratio ( $\nu$ ), Vickers hardness ( $H_V$ ), Yield stress ( $\sigma_y$ ), Crack resistance ( $CR$ ) and Recovery of indentation depth ( $RID$ ) of single and mixed alkaline earth ABS glasses.

Glass	$\rho$ (g/cm <sup>3</sup> )	$T_g$ (°C)	$E$ (GPa)	$G$ (GPa)	$K$ (GPa)	$\nu$	$H_V$ (GPa)	$\sigma_y$ (GPa)	$CR$ (N)	$RID$ (%)
CAS1	2.52	870	85.1	35.1	49.6	0.21	7.1	3.5	3	30
CABS2	2.49	803	81.0	33.3	47.7	0.22	6.6	3.4	9	33
CABS3	2.45	719	74.4	30.1	46.9	0.24	6.1	3.1	23	29
CABS4	2.42	667	70.4	28.1	47.0	0.25	5.8	2.7	25	26
MAS1	2.48	829	92.0	37.8	54.2	0.22	7.8	3.8	27	30
MABS2	2.46	776	88.8	36.4	52.8	0.22	7.7	3.7	28	26
MABS3	2.41	725	80.4	32.7	49.5	0.23	7.0	3.3	29	25
MABS4	2.37	687	73.6	29.8	46.3	0.24	6.5	3.1	33	27
CMABS1	2.49	792	83.0	34.0	49.4	0.22	6.8	3.5	7	31
CMABS2	2.48	788	84.3	34.5	50.1	0.22	6.9	3.6	8	29
CMABS3	2.47	780	85.6	35.1	50.7	0.22	7.2	3.6	16	30
CMABS4	2.47	780	86.3	35.4	51.2	0.22	7.3	3.7	21	28
CMABS5	2.46	778	88.1	36.1	52.4	0.22	7.6	3.7	29	28
CMABS6	2.44	717	76.1	30.9	47.6	0.23	6.2	3.2	30	29
CMABS7	2.44	717	77.3	31.4	47.8	0.23	6.3	3.2	31	29
CMABS8	2.43	717	78.3	31.8	48.5	0.23	6.4	3.2	32	26
CMABS9	2.42	716	79.5	32.3	49.3	0.23	6.7	3.3	32	27
CMABS10	2.42	716	80.5	32.7	49.9	0.23	6.9	3.3	32	27

Experimental uncertainties are as follows:  $\rho$ :  $\pm 0.01$  g/cm<sup>3</sup>;  $T_g$ :  $\pm 2$  °C;  $E$ ,  $K$  and  $G$ :  $\pm 0.1$  GPa;  $\nu$ :  $\pm 0.01$ ;  $H_V$ :  $\pm 0.1$  GPa;  $\sigma_y$ :  $\pm 0.1$  GPa;  $CR$ :  $\pm 1$  N;  $RID$ :  $\pm 1$  %

TABLE 4.2: Atomic packing density  $V_t$  values calculated from equation 1.3 for single and double modifier glass compositions

Glass	CAS1	CABS2	CABS3	CABS4	MAS1	MABS2	MABS3	MABS4
$V_t$	0.547	0.552	0.560	0.569	0.550	0.555	0.562	0.569
Glass	CMABS1	CMABS2	CMABS3	CMABS4	CMABS5			
$V_t$	0.552	0.552	0.553	0.553	0.554			
Glass	CMABS6	CMABS7	CMABS8	CMABS9	CMABS10			
$V_t$	0.559	0.559	0.560	0.561	0.561			

TABLE 4.3: Dissociation Energy ( $G_i$ ) of oxides used in this work taken from [9].

Oxide	Oxygen Coordination Number (CN)	$G_i$ (kJ/cm <sup>3</sup> )
<i>Network formers</i>		
SiO <sub>2</sub>	(4)	68.0
B <sub>2</sub> O <sub>3</sub>	(3)	15.6
<i>Intermediate oxides</i>		
Al <sub>2</sub> O <sub>3</sub>	(4)	131.0
MgO		90.0
<i>Network modifiers</i>		
CaO		64.1

### 3 Appendix: Full mapping of indentation cross-sections

#### Vickers indentations

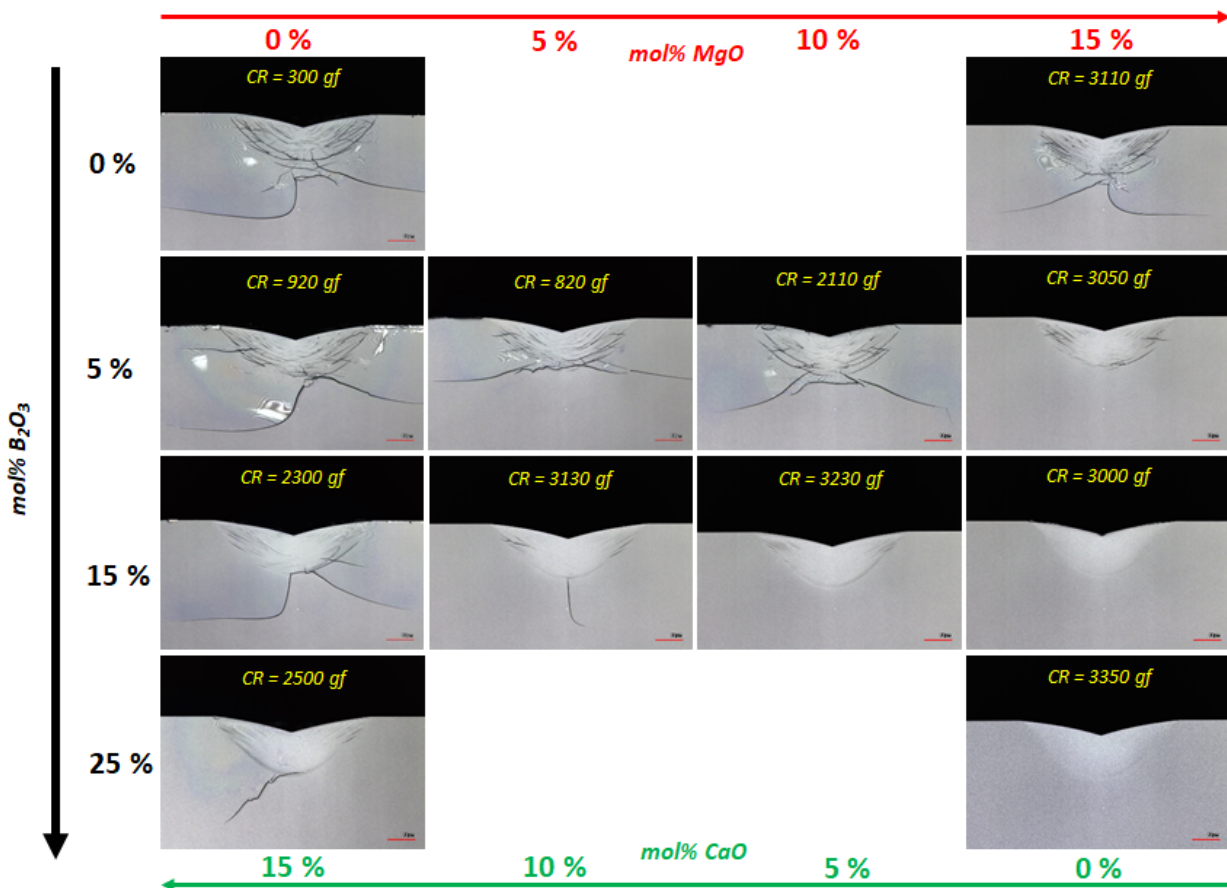


FIGURE 4.7: Full mapping of 1 kgf Vickers indentation cross-sections. Silica is gradually substituted by boron from top to bottom and calcium is gradually substituted by magnesium from left to right.

## Conical indentations

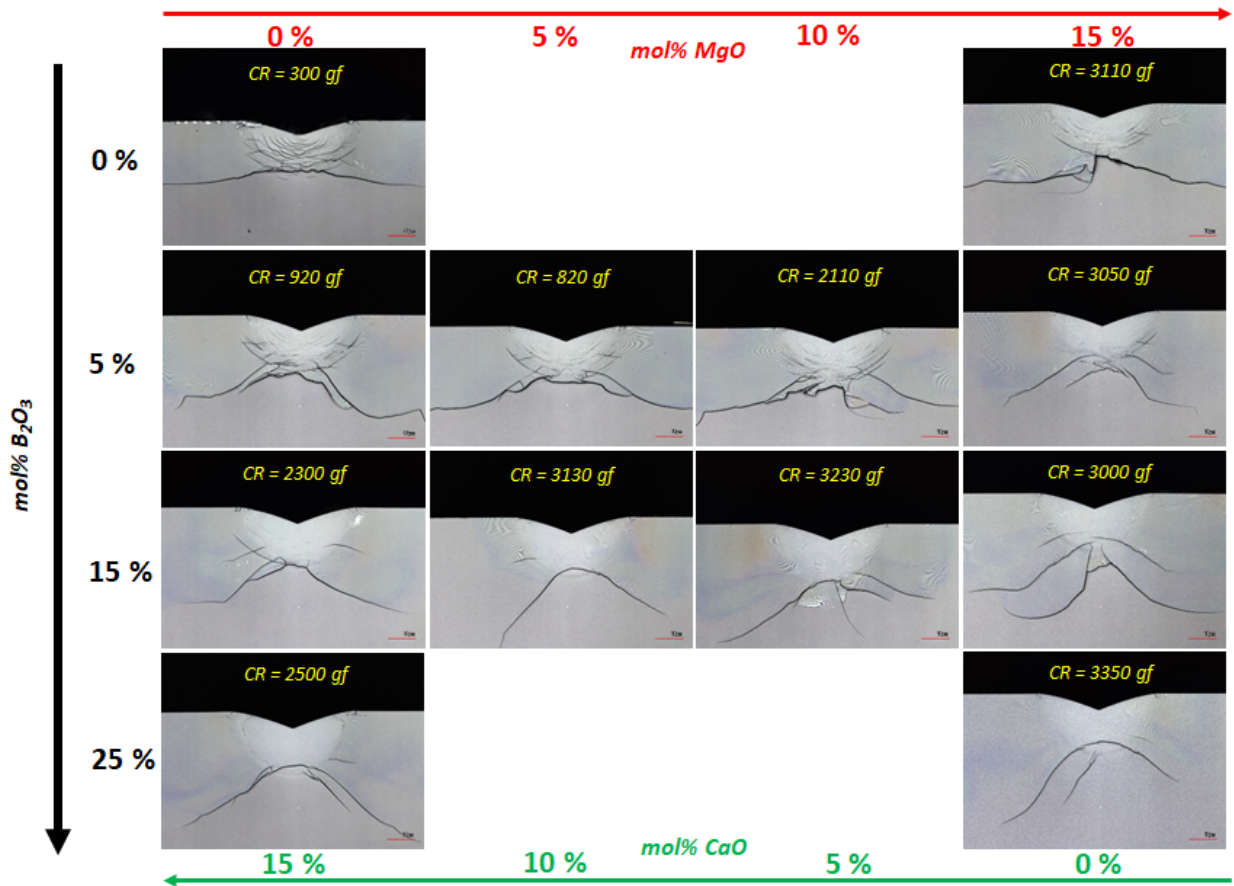


FIGURE 4.8: Full mapping of 1 kgf conical indentation cross-sections. Silica is gradually substituted by boron from top to bottom and calcium is gradually substituted by magnesium from left to right.

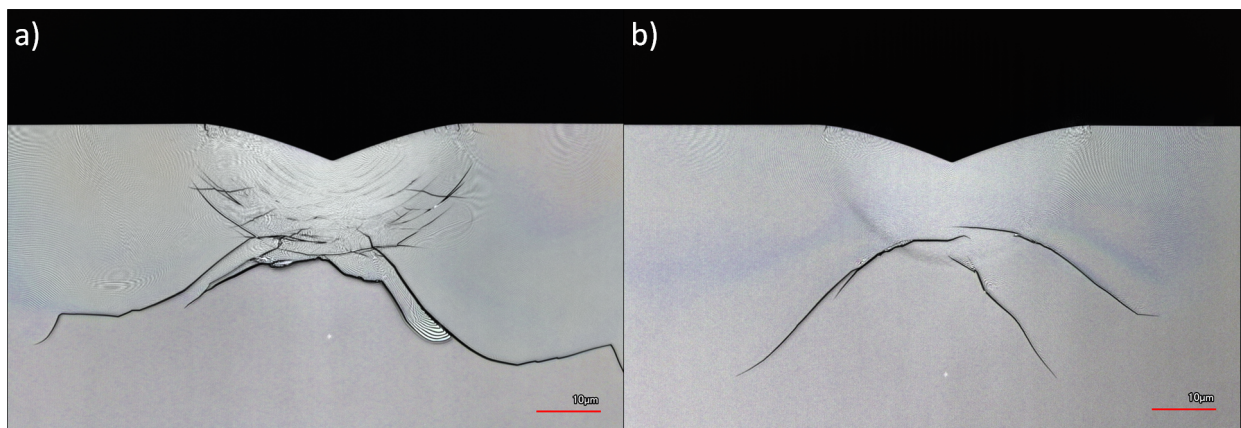


FIGURE 4.9: Cross-sections through 1 kgf conical indents in (a) calcio-aluminoborosilicate glass with 5%  $B_2O_3$  (CABS2) and (b) magnesio-aluminosilicate glass with 15%  $B_2O_3$  (MABS3).

## Spherical indentations

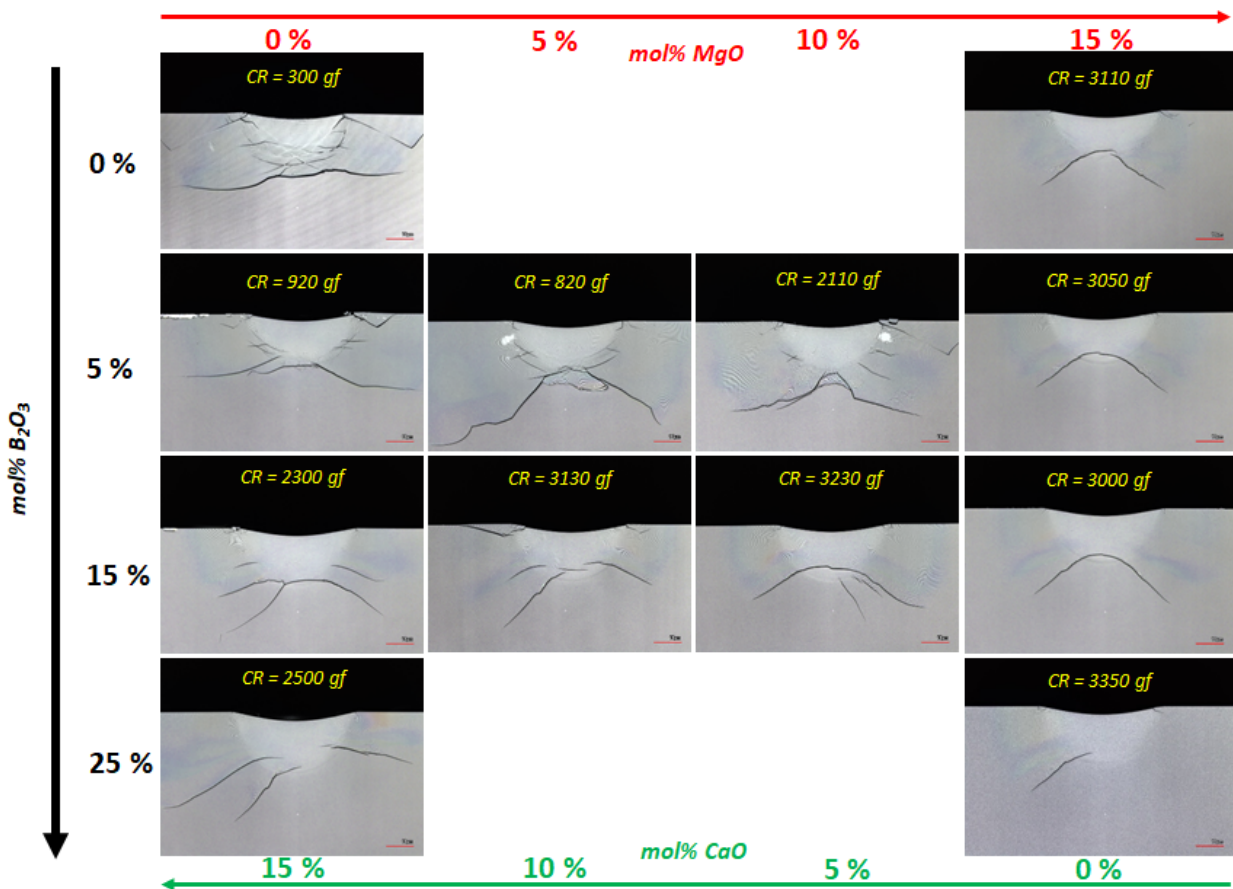


FIGURE 4.10: Full mapping of 1 kgf spherical indentation cross-sections. Silica is gradually substituted by boron from top to bottom and calcium is gradually substituted by magnesium from left to right.

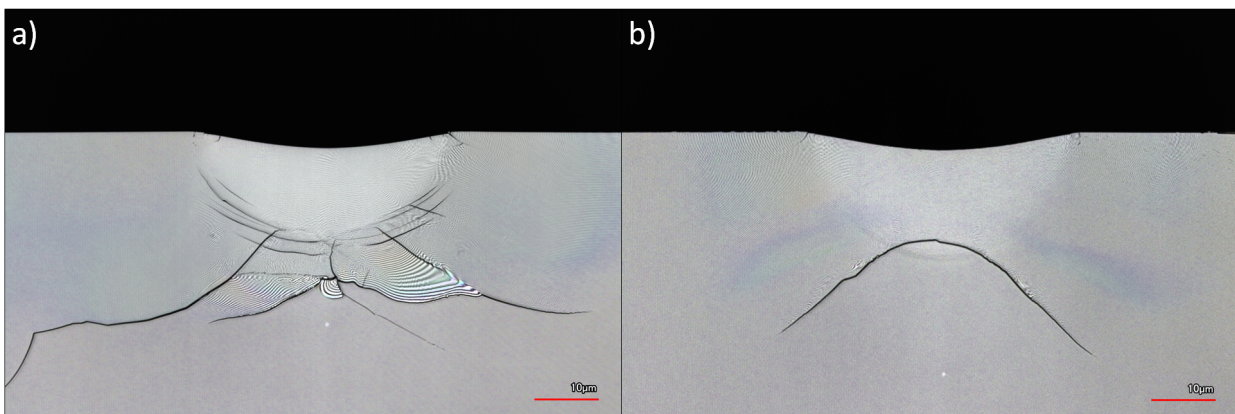


FIGURE 4.11: Cross-sections through 1 kgf spherical indents in (a) calcio-magnesium-aluminoborosilicate glass with 5%  $B_2O_3$  and 2.5%  $MgO$  (CMABS1) and (b) magnesium-aluminosilicate glass with 15%  $B_2O_3$  (MABS3).

## 4 Appendix: Roughness measurements of indentation cross-sections

Roughness measurements were performed from conical and spherical cross-sections using the same experimental parameters as given in section 3.1 and the correlation with the crack resistance is given in Fig. 4.12.

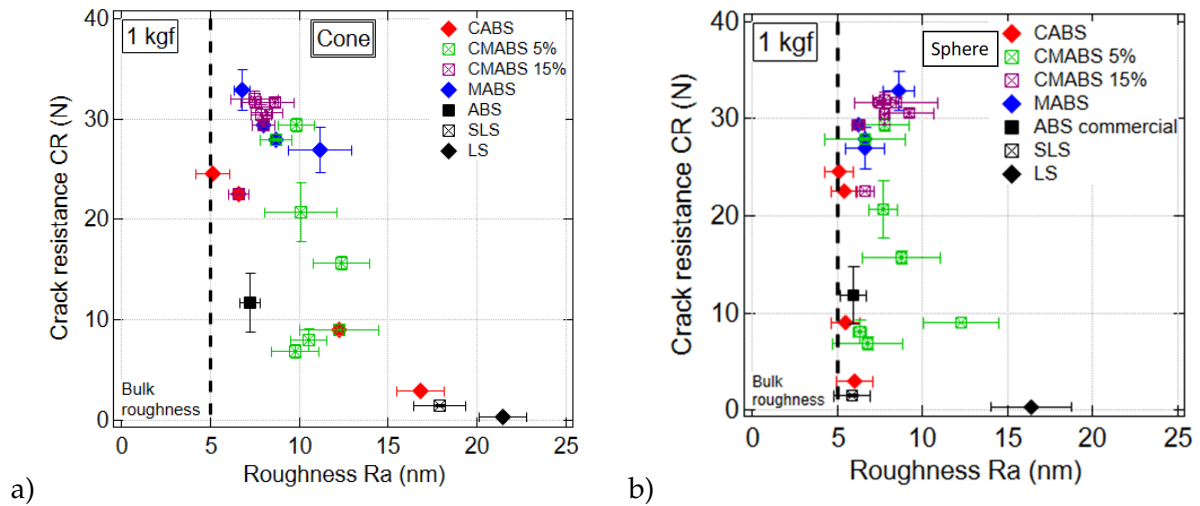


FIGURE 4.12: Relationship between crack resistance ( $CR$ ) and roughness ( $R_a$ ) for (a) conical indentation cross-sections and (b) spherical indentation cross-section at 1 kgf including some compositions (black markers) from Kato et al. [87]. The vertical dashed line is determined as the bulk roughness.

## 5 Appendix: Characterization of the densification ability by thermal recovery measurements

Volume recovery measurements were performed on all the glass compositions and results were used to plot the correlation between the crack resistance and the volume recovery in section 3.5.1 using the same experimental parameters as given in section 3.1.

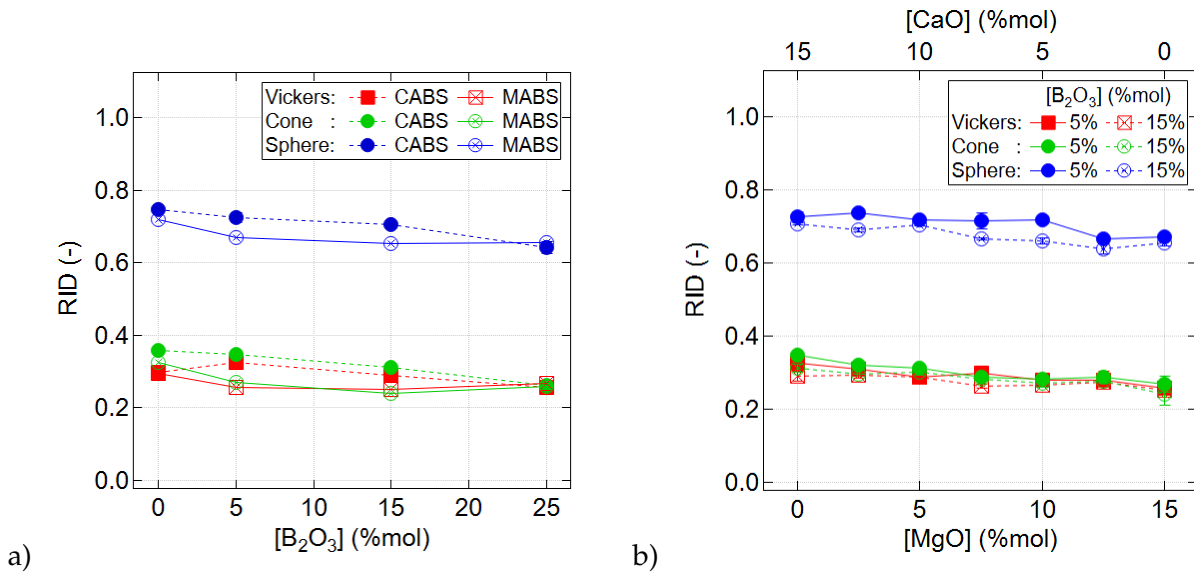


FIGURE 4.13: Recovery of indentation depth  $RID$  for several tip geometries of (a) single alkaline earth ABS glasses and (b) mixed alkaline earth ABS glasses. Error bars could be smaller than the markers' size.

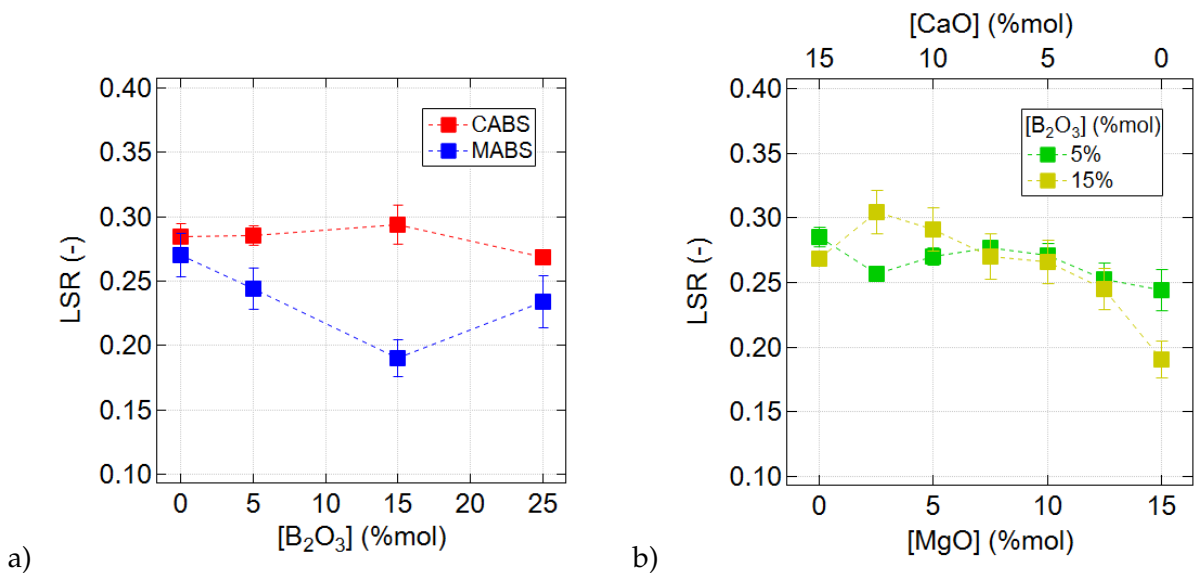


FIGURE 4.14: Indentation side recovery  $LSR$  of (a) single alkaline earth ABS glasses and (b) mixed alkaline earth ABS glasses. Error bars could be smaller than the markers' size.



Résumé :

Comprendre les mécanismes de rupture des verres est d'une importance cruciale en raison des vastes applications industrielles de ces matériaux et du rôle crucial de leurs propriétés mécaniques pour leurs performances et leur durabilité. Dans ce travail, des expériences originales ont permis d'explorer la réponse élastoplastique de verres aluminoborosilicatés jusqu'à la fissuration, sur de larges gammes de composition. Elles montrent que l'écoulement plastique localisé sous forme de bandes de cisaillement est fortement impacté par, d'une part, des modificateurs de réseau alcalino-terreux, et d'autre part un second formateur de réseau, le bore. Dans les deux cas nous trouvons une corrélation marquée entre le mode de formation de bandes de cisaillement et la résistance à l'initiation de fissures, ce qui nous permet de proposer un paradigme nouveau pour comprendre la fragilité des verres silicatés. Par ailleurs, il est bien connu que l'irradiation électronique est capable de catalyser les réarrangements structuraux sous contrainte, entraînant une nette diminution de la limite d'élasticité. Grâce à une procédure originale de superposition temps-irradiation, nos expériences ont exploré de façon fine le comportement viscoplastique de trois silicates, à température ambiante et sur une gamme de temps caractéristiques de déformation allant jusqu'à environ 1 siècle. Nous avons ainsi mis en évidence une évolution simple de la viscoplasticité du réseau tandis que l'ajout des modificateurs conduit à une saturation à haute vitesse. Ce comportement a été analysé par des modèles classiques de relaxation qui permettent d'en discuter les mécanismes. Ces travaux contribuent à la compréhension des processus de plasticité dans les verres et ouvrent la voie à des stratégies d'optimisation de leurs propriétés mécaniques, notamment en concevant des compositions spécifiques pour renforcer leur résistance dans des environnements industriels exigeants ou soumis à des conditions sévères.

Mots clés : Verres silicatés, Localisations en cisaillement, Fissuration sous indentation, Micromécaniques, Irradiation électronique, Relaxation

Abstract:

Understanding the fracture mechanisms of glass is of crucial importance due to the wide range of industrial applications of these materials and the critical role of their mechanical properties in their performance and durability. In this work, original experiments were conducted to explore the elastoplastic response of aluminoborosilicate glasses up to cracking, across a broad range of compositions. The results demonstrate that localized plastic flow in the form of shear bands is significantly influenced by, on one hand, alkali-earth network modifiers, and on the other hand, by a second network former, boron. In both cases, we found a strong correlation between the mode of shear band formation and the resistance to crack initiation, allowing us to propose a new paradigm for understanding the brittleness of silicate glasses. Moreover, it is well-known that electron irradiation can catalyze structural rearrangements under stress, leading to a significant reduction in the yield strength. Through an original time-irradiation superposition procedure, our experiments finely explored the viscoplastic behavior of three silicates at room temperature and over a range of characteristic deformation times extending up to about a century. We identified a simple evolution of network viscoplasticity, while the addition of modifiers led to a saturation at high strain rates. This behavior was analyzed using classical relaxation models, allowing us to discuss the underlying mechanisms. This work contributes to the understanding of plasticity processes in glass and paves the way for strategies to optimize their mechanical properties, particularly by designing specific compositions to enhance their resistance in demanding industrial environments or under severe conditions.

Keywords: Silicate glasses, Shear localizations, Indentation cracking, Micro-mechanics, Electron irradiation, Relaxation

